Titanium carbide-carbon porous nanocomposite materials for radioactive ion beam production: processing, sintering and isotope release properties

THÈSE N^{O} 7363 (2017)

PRÉSENTÉE LE 26 JANVIER 2017

À LA FACULTÉ DES SCIENCES ET TECHNIQUES DE L'INGÉNIEUR
LABORATOIRE DE TECHNOLOGIE DES POUDRES
PROGRAMME DOCTORAL EN SCIENCE ET GÉNIE DES MATÉRIAUX

ÉCOLE POLYTECHNIQUE FÉDÉRALE DE LAUSANNE

POUR L'OBTENTION DU GRADE DE DOCTEUR ÈS SCIENCES

PAR

João Pedro FERNANDES PINTO RAMOS

acceptée sur proposition du jury:

Prof. P. Muralt, président du jury
Prof. P. Bowen, Dr T. Stora, directeurs de thèse
Prof. A. M. Oliveira Rocha Senos, rapporteuse
Prof. L. Biasetto, rapporteuse
Prof. T. Graule, rapporteur

ÉCOLE POLYTECHNIQUE
FÉDÉRALE DE LAUSANNE
Suisse
2016

In any moment of decision,
the best thing you can do is the right thing,
the next best thing is the wrong thing,
and the worst thing you can do is nothing.
— Theodore Roosevelt

I dedicate this work to the love of my life, Diana,
and to my family...

Dedico este trabalho ao amor da minha vida, a Diana,
e à minha família...

Acknowledgements

I would like to, first of all, leave a very special thanks to my thesis directors, Prof. Paul Bowen (EPFL) and Dr. Thierry Stora (CERN), for believing in me and my skills, giving me the opportunity to work in their respective teams and to belong to such internationally renowned organizations. They were not only great mentors to me in their respective expertise fields, but also good friends that supported me through the most difficult phases of this work. I would also like to thank as well the opportunity given, to participate in many conferences, workshops and training courses allowing me to network and grow professionally. Thank you Thierry! Thank you Paul! I would also like to leave here a very special thanks to Prof. Ana Senos, which discussions and support were essential to this work. Thanks go also to CERN and EPFL for the financial support.

I had three different work places (CERN, EPFL and U. Aveiro) but most of my time was spent at CERN. I want to thank my team, the TISDs (Target and Ion Source Development team), for all the motivation and support during my PhD. Thank you Alex, Jochen, Julien, Tânia, Wonjoo, Melanie, Yisel, Ricardo and Christoph. I'm also grateful for the fact that you guys covered in for my ISOLDE responsibilities (yield checks) while I was writing my thesis. I promise to make it up for you very soon, in my new Fellow contract at CERN. Furthermore, I would like to leave a special thanks to my supervisee, Silvain Badie, for the dedication and work developing novel TiC-C nanocomposites with me. For the countless requested scientific articles readily delivered to me by the CERN Library staff, I big thanks to them.

At EPFL I would like to thank Carlos Morais for all the technical support and practical suggestions in the lab. I would also like to acknowledge Prof. Jacques Lemaître, Prof. Heinrich Hofmann, Prof. Sabien Sorin, Marijana Mionic and Prof. Yves Leterrier for the very interesting scientific discussions. I also leave here my thanks for the Zhangli Hu for the dedication in guidance and troubleshooting with the mercury intrusion porosimeter. Thanks as well to my colleagues at the LTP lab, for all the nice coffees and conversations during the free times at EPFL.

At Universidade de Aveiro, I want to thank those who supported me during the short and very intense experimental work periods: Prof. Ana Senos, Cristina Fernandes, Maria João Bastos, Carla Pinho, Célia Miranda, Artur Sarabando, Manuela Fernandes, Isabel Antunes and Filipe Oliveira.

At CERN I also had help from many specialists and colleagues, thank you Richard Catheral, Bernard Crepieux, Michael Owen, Matteo Vagnoni, Ermanno Barbero, Ana Paula Bernardes, Camille Lemesre, Ans Pardons, Joachim Vollaire, Uli Köster, the ISOLDE operators and the

physics group. A special thanks to the EN-MME-MM CERN group (namely Stefano Sgobba, Floriane Leaux and Barbora Bartova) for training and allowing me to operate their electron microscope.
I would like to thank the jury panel of my oral exam, for reading my work, provide very helpful comments that improved the current manuscript (and future work) and for the recommendation of my thesis for an EPFL doctoral prize.
To my friends here in Geneva area, Dora, Filipe, Gabriel, Luís, Paulo e Vítor, thank you so much for all the support, your unconditional friendship, fun, travels and dinners together. To my good friends and old office mates Alex, Monika and Wonjoo, for all the good moments and even though we are separated by more than 8000 km to the west (Vancouver, CA) and to the east (Daejeon, KR) we still keep our friendships strong and meeting each other around the globe. To Silvia and Elvis, EPFL external doctoral students at CERN, just like myself, thanks for all the nice conversations and support. Also, to my Portuguese friends who even though are in Portugal, is the same as if they were just here: thank you Pina, André, Francisco and Rogério.
To Diana, my beautiful and caring wife, which supported me, unconditionally and patiently through everything and specially through the thesis writing phase. Where, when I was down and tired, she cheered me up and took me out of my "writing cave" to see the sun or the moon. *Adoro-te! Obrigado!*
Last but not least, to my family (in Portuguese): *Aos meus pais, que me prepararam para a vida, me ensinaram os valores que defendo e suportaram a minha educação (superior) mesmo quando as dificuldades apertaram. Mesmo agora, aos 50+ anos quando a vida profissional lhes fechou portas, mostraram determinação, humildade, trabalho e espírito de sacrifício para trilhar novos caminhos e lutar por uma vida melhor. Aos meus irmãos, Paulo e Tiago, pelo apoio incondicional e por manterem os valores da família acima de tudo. Queria também deixar um agradecimento muito especial, pelo apoio constante durante esta fase: aos meus novos avós que me adotaram como neto, D. Evangelina e Sr. João; e aos meus sogros, Sr. Virgílio e D. Olinda. A todos vós, adoro-vos! Obrigado!*
To those who directly or indirectly contributed to this work and I've forgotten to include, please accept my apologies! Thank you all for making part of the dream of working and studying in such prestigious places, as is CERN and EPFL!

Geneva, 14th of November 2016 João Pedro Ramos

Résumé

ISOLDE - *Isotope Separator OnLine DEvice* - est une installation du CERN pour produire des faisceaux d'ions radioactifs pour des projets de recherche en physique avec la technique ISOL (*Isotope Separator OnLine*). Au CERN les protons sont accélérés à 1.4 GeV pour entrer en collision avec l'une des deux cibles d'ISOLDE. Lorsque les protons entrent en collision avec le matériel de la cible, des réactions nucléaires produisent des isotopes qui sont thermalisés à l'intérieur des grains du matériel de la cible. Pendant l'irradiation, la cible est maintenue à des températures élevées (jusqu'à 2300 °C) afin de promouvoir la diffusion et le transfert gazeuse des isotopes produits vers une source d'ions, pour produire un faisceau d'ions radioactifs.

Des cibles de feuilles de titane sont actuellement utilisées à ISOLDE pour produire des faisceaux de radioisotopes de K, Ca et Sc. Cependant à cause des températures élevées en opération, ces cibles se dégradent par frittage et/ou fusion, en réduisant l'intensité des faisceaux au fil du temps. Au cours des 10 dernières années, les matériaux nanostructurés ont montré des taux de libération plus élevés d'isotopes, en raison des courtes distances de diffusion et des porosités élevées.

Ici un nouveau matériel réfractaire à base de titane développé pour remplacer les feuilles de titane utilisées jusqu'ici. Le carbure de titane (TiC) nanométrique ne peut pas être maintenu à des températures élevées ($T > 1200\,°C$) en raison des phénomènes de frittage. Une nouvelle méthode de traitement a été développée pour produire des nanocomposites TiC-C plus stables où les allotropes de carbone utilisés étaient des particules du graphite, du noire de carbone ou des nanotubes multi couches (MWCNT). Le frittage des nanocomposites a été testé jusqu'à 1800 °C et les échantillons ont été caractérisés, en mesurent les variations dimensionnelles, la densité relative, les pertes de masse, leur surface spécifique, la taille des particules TiC et la morphologie de la microstructure.

Tous les allotropes de carbone ont eu un effet significatif de stabilisation du TiC nanométrique. Le meilleur résultat est obtenu pour un rapport de 1 : 1 de volume de TiC :noir de carbone. A 1800 °C les tailles de cristallite de TiC étaient de 76 nm (51 nm en vert) et la densité de 55 %, suivi part le TiC :MWCNT avec une taille de grain de TiC de 138 nm (58 % dense). Le traitement a introduit une fraction de ZrO_2 pendant le broyage, formant une phase de ZrC qui solubilise dans la phase TiC, en augmentant son paramètre de maille.

La cinétique du frittage de TiC a été étudiée en mesurent la courbe maîtresse de frittage peu laquelle l'énergie d'activation obtenue de 390 kJ mol^{-1} est proche des valeurs de la littérature. En utilisant la même méthode, l'énergie d'activation a été déterminée à 555 kJ mol^{-1} pour le composite synthétisé avec du noir de carbone, par réduction du nombre de coordination des

grains de TiC, ce qui rend le frittage plus difficile.
Les nanocomposites (dont le TiC) ont été irradiés et étudiés en termes de libération d'isotopes (Be, Na, Mg, K, Sc et Ca). Le nanocomposite TiC :noir de carbone qui présente la fraction des isotopes libérés la plus haute a été sélectionné pour produire une cible entière. Pour ce faire, le traitement a été modifié pour produire de plus grandes quantités et une cible prototype a été construite et testée à ISOLDE. Les intensités d'isotopes de Li, Na, et K et leur propriété de relâchement ont été mesurée. En comparaison avec des matériaux de référence à base de Ti, les intensités de faisceaux de Na et Li étaient plus élevées, et K et Ca étaient inférieurs.
Cette cible présente un temps de relâchement apparemment plus long, ce qui a déjà été vu dans d'autres cibles nanométriques, et qui est probablement lié aux propriétés de transport des isotopes dans la porosité du matériel. Contrairement, à la fin de cette thèse sont présentées des suggestions pour les travaux futurs qui comprennent le test d'un nouveau composite TiC-C déjà développé et la modélisation des propriétés de frittage et de relâchement d'isotopes.

Mots clefs : carbure de titane, cibles de spallation, applications à haute température, faisceaux d'ions radioactifs, nanocomposites, matériaux poreux, nanomatériaux, frittage, Isotope séparateur en ligne (ISOL), CERN-ISOLDE

Abstract

The Isotope Separator OnLine (ISOL) technique is used at the ISOLDE - Isotope Separator OnLine DEvice facility at CERN, to produce radioactive ion beams for physics research. At CERN protons are accelerated to 1.4 GeV and made to collide with one of two targets located at ISOLDE facility. When the protons collide with the target material, nuclear reactions produce isotopes which are thermalized in the bulk of the target material grains. During irradiation the target is kept at high temperatures (up to 2300 °C) to promote diffusion and effusion of the produced isotopes into an ion source, to produce a radioactive ion beam.

Ti-foils targets are currently used at ISOLDE to deliver beams of K, Ca and Sc, however they are operated at temperatures close to their melting point which brings target degradation, through sintering and/or melting which reduces the beam intensities over time. For the past 10 years, nanostructured target materials have been developed and have shown improved release rates of the produced isotopes, due to the short diffusion distances and high porosities.

In here a new Ti-based refractory material is developed to replace the currently used Ti-foils. Since nanometric TiC can't be maintained at high temperatures ($T > 1200$ °C) due to sintering, a processing route was developed to produce TiC-C nanocomposites where the carbon allotropes used were either graphite, carbon black or multi wall carbon nanotubes (MWCNT). The developed nanocomposites sinterability was tested up to 1800 °C and they were characterized according to dimensional changes, relative density, mass losses, surface area, TiC particle size and microstructure morphology.

All carbon allotropes had a significant effect on the stabilization of the nanometric TiC where the best result was obtained for a 1:1 volume ratio of TiC:carbon black at 1800 °C where TiC crystallite sizes were of 76 nm (from 51 nm) and density of 55 %, followed by TiC:MWCNT with TiC of 138 nm (58 % dense). The processing introduced a ZrO_2 contamination from the milling media, forming ZrC that solubilizes in the TiC phase, increasing its lattice parameter.

TiC sintering kinetics were studied through the master sintering curve and the activation energy determined for sintering, 390 kJ mol^{-1}, were close to the ones obtained in the literature. Using the same method, the calculated activation energy for TiC-carbon black was 555 kJ mol^{-1} resulting from the carbon which reduces the TiC sintering, reducing its coordination number.

The nanocomposites referred (and the TiC) were irradiated and studied in terms of isotope (Be, Na, Mg, K, Sc and Ca) release, where the nanocomposite with the highest isotope released fraction, TiC-carbon black was selected for the final target material. To produce a full target the processing was scaled up and a target prototype was build and tested at ISOLDE. Li, Na

and K isotope intensities and release time-structure were measured from the target prototype, where in comparison with Ti-based materials, Na and Li intensities were higher, K were slightly lower and Ca were lower.
The target presents an apparently longer release time structure when comparing with standard materials, as seen in other nanomaterial targets, which is likely related with effusion of the isotopes in the material porosity. Furthermore, contrarily to the Ti-foil targets, the obtained intensities were stable over the full operation time. At the end of this thesis suggestions for a future work which include a second iteration of the TiC-C nanocomposite (already developed) and modeling.

Keywords: titanium carbide, spallation targets, high temperature applications, radioactive ion beams, nanocomposites, porous materials, nanomaterials, sintering, isotope separator online, CERN-ISOLDE

Resumo

A técnica ISOL (*Isotope Separator OnLine*) é usada no ISOLDE (*Isotope Separator OnLine DEvice*) do CERN na produção de feixes de iões radioativos para estudos em física. No CERN, os protões são acelerados até 1.4 GeV para colidir com um dos dois alvos localizados nas instalações do ISOLDE. Quando os protões colidem com o material do alvo, produzem-se isótopos, por reações nucleares que são termalizados no interior dos grãos do material do alvo. Durante a irradiação, o alvo é mantido a altas temperaturas (até 2300 °C) para promover a difusão e efusão dos isótopos produzidos para uma fonte de iões e, originando assim, um feixe de iões radioativos.

São usados normalmente no ISOLDE alvos à base de folhas de Ti para produzir feixes de K, Ca e Sc. No entanto, devido às elevadas temperaturas de operação, estes alvos degradam-se, através de sinterização e/ou fusão, reduzindo a intensidade dos feixes ao longo do tempo. Por outro lado, os materiais nanoestruturados desenvolvidos nos últmos 10 anos, têm mostrado taxas de libertação mais altas de isótopos devido às curtas distâncias de difusão e porosidades elevadas.

Neste trabalho, desenvolveu-se um novo material refratário à base de Ti para substituir as folhas de Ti atualmente usadas. Dado que o TiC nanométrico não pode ser mantido a altas temperaturas (T> 1200 °C) devido a fenómenos de sinterização, um novo método de processamento foi desenvolvido para produzir nanocompósitos à base de TiC-C em que os alótropos de carbono utilizados foram a grafite, nanotubos de múltiplas paredes (MWCNT) ou negro de fumo. A sinterização dos nanocompósitos foi investigada testada até 1800 °C e as amostras foram caracterizadas de acordo com mudanças dimensionais, densidade relativa, perdas de massa, área superficial específica, tamanho de partícula do TiC e microestrutura.

Todos os alótropos de carbono tiveram um efeito positivo na estabilização microestrutural do TiC nanométrico, e, o melhor resultado encontrado foi o de 1:1 em volume, de TiC:negro de fumo, seguido do TiC-MWCNT. Estes compósitos permanecem nanométricos a 1800 °C: no primeiro caso com um tamanho de cristalite do TiC de 76 nm (partindo de 51 nm no compacto em verde) e densidade de 55 %, e, no segundo caso, com TiC de 138 nm e 58 % densidade relativa. O processamento introduziu uma contaminação de ZrO_2, proveniente da moagem, formando ZrC que solubiliza na fase de TiC, aumentando o seu parâmetro de rede.

A cinética de sinterização do TiC foi estudada através da curva de sinterização mestra e a energia de ativação aparente obtida de 390 kJ mol^{-1} que é próxima dos valores na literatura. Usando o mesmo método, a energia de ativação calculada para o TiC:negro de fumo foi de 555 kJ mol^{-1}, que resulta do facto do negro de fumo reduzir o número de coordenação do TiC,

dificultando a sinterização do mesmo.
Os nanocompósitos referidos (incluindo o TiC) foram irradiados e estudados em termos de libertação de isótopos (de Be, Na, Mg, K, SC e Ca), e aquele com a maior libertação de isótopos (TiC:negro de fumo) foi selecionado como alvo a ser testado. Dada a maior quantidade de material necessária para produzir um alvo completo ,o processamento desenvolvido foi modificado par este efeito de escala e produziu-se um alvo protótipo que foi testado no ISOLDE. As intensidades de isótopos de Li, Na e K foram medidas, bem como as suas curvas de libertação ao longo do tempo. E, em comparação com outros materiais à base de Ti, obtiveram-se intensidades superiores para os isótopos de Li e Na, enquanto as intensidades de K e Ca foram inferiores.
As curvas de libertação deste alvo têm uma libertação aparente longa, como visto anteriormente em outros alvos nanométricos e que está provavelmente relacionado com os longos tempos de efusão na porosidade do material. Contrariamente às folhas de Ti, as intensidades observadas foram estáveis ao longo do tempo de operação do alvo. No final desta tese são feitas sugestões de trabalho futuro que compreendem um novo compósito TiC-C (já desenvolvido) e modelação.

Palavras-chave: Carboneto de titânio, Alvos de espalação, Aplicações de alta temperatura, Feixes de iões radioactivos, nanocompósitos, Materiais porosos, nanomateriais, sinterização, Isotope separator online (ISOL), CERN-ISOLDE

Contents

Acknowledgements i

Abstract (Français/English/Português) iii

Contents ix

List of figures xiii

List of tables xix

Nomenclature xxi

Introduction 1

1 Literature review 5
- 1.1 Introduction to radioactive ion beams . . . 6
  - 1.1.1 Isotope Separator OnLine (ISOL) . . . 8
- 1.2 ISOLDE target and ion source system . . . 16
  - 1.2.1 Target materials . . . 18
  - 1.2.2 Transfer line . . . 21
  - 1.2.3 Ion sources . . . 23
- 1.3 Engineered microstructure ISOLDE target materials . . . 26
  - 1.3.1 Release efficiency: diffusion and effusion . . . 27
  - 1.3.2 (Sub)micrometric microstructure target materials . . . 29
  - 1.3.3 Nanostructured target materials development . . . 30
- 1.4 Sintering . . . 34
  - 1.4.1 Sintering stages . . . 36
  - 1.4.2 Sintering of porous ceramics . . . 37
  - 1.4.3 Constrained sintering . . . 38
  - 1.4.4 Irradiation influence on sintering . . . 40

2 Experimental Methods 43
- 2.1 Methods . . . 44
  - 2.1.1 Attrition milling . . . 44
  - 2.1.2 Thermal treatments . . . 45

2.1.3 Residual gas analysis . . . 47
2.1.4 Dilatometry . . . 48
2.2 Material characterization techniques . . . 50
2.2.1 Particle size distribution by laser diffraction . . . 50
2.2.2 Nitrogen physisorption isotherms . . . 51
2.2.3 Scanning electron microscopy . . . 52
2.2.4 Mercury Intrusion Porosimetry . . . 54
2.2.5 X-ray powder diffraction . . . 55
2.3 Isotope release studies . . . 57
2.3.1 Offline methods: gamma spectroscopy . . . 58
2.3.2 Online methods: tape station . . . 58

3 TiC-carbon nanocomposite development 61
3.1 TiO_2 and TiC preliminary studies . . . 62
3.1.1 Sintering studies . . . 62
3.1.2 Release studies . . . 64
3.2 Article: Development of a processing route for carbon allotrope-based TiC porous nanocomposites . . . 65
1. Introduction . . . 67
2. Materials and Methods . . . 69
3. Results and Discussions . . . 72
4. Conclusions . . . 82
3.3 Article: Stability of nanometric TiC-carbon composites: effects of carbon allotropes and Zr milling impurities . . . 86
1. Introduction . . . 89
2. Materials and Methods . . . 92
3. Results and Discussions . . . 93
4. Conclusions . . . 104
3.4 Summary of the TiC-carbon nanocomposite development . . . 107

4 TiC and TiC-carbon black sintering kinetics 109
4.1 Article: Master sintering curve determination of nanometric TiC and a TiC-carbon black nanocomposite . . . 109
1. Introduction . . . 111
1. Materials and Methods . . . 113
3. Results and Discussion . . . 115
4. Conclusions . . . 122
4.2 Further discussion and summary of the TiC and TiC-carbon black sintering kinetics . . . 125

5 Isotope release properties from TiC-carbon nanocomposites 127
5.1 Article: Constant isotope release properties measured for an online prototype TiC-carbon nanocomposite target material . . . 127

1. Introduction . . . 129
2. Materials and Methods . . . 133
3. Results and Discussion . . . 137
4. Conclusions . . . 142
5.2 Summary of the isotope release properties from TiC-carbon nanocomposites . . . 147

6 Conclusions and outlook **149**
6.1 Conclusions . . . 149
6.1.1 TiC-carbon nanocomposite development . . . 149
6.1.2 TiC and TiC-carbon black sintering kinetics . . . 150
6.1.3 Isotope release properties from TiC-carbon black nanocomposite . . . 150
6.2 Outlook . . . 151
6.2.1 Future of TiC-based nanocomposites at ISOLDE . . . 152
6.2.2 Modeling of release properties . . . 153

A Articles supplementary materials **159**
A.1 Development of a processing route for carbon allotrope-based TiC porous nanocomposites . . . 160
A.1.1 Parameter derivation . . . 160
A.1.2 Composites further characterizations . . . 162
A.2 Stability of nanometric TiC-carbon composites: effects of carbon allotropes and Zr milling impurities . . . 165
A.2.1 Parameter derivation . . . 168
A.3 Master sintering curve determination of nanometric TiC and a TiC-carbon black nanocomposite . . . 169
A.4 Constant isotope release properties measured for an online prototype TiC-carbon nanocomposite target material . . . 170

B TiC-MWCNT - carbothermal reduction from TiO_2 and MWCNT **177**

Bibliography **181**

Curriculum Vitae **197**

List of Figures

1.1 Karlsruhe Chart of Nuclides. 7
1.2 Schematic representation of spallation, fragmentation and fission reactions. . 9
1.3 Radioactive Ion Beam production: ISOL vs in flight separation. 10
1.4 Schematic representation of the ISOL method production, diffusion, effusion and ionization steps. 11
1.5 World Map representing the currently existing or under construction ISOL facilities. 12
1.6 Schematic of the CERN accelerator complex. 14
1.7 ISOLDE-CERN Facility Layout, including MEDICIS and HIE-ISOLDE. 15
1.8 Target and ion source system of ISOLDE. 17
1.9 Overview of ISOL studied materials for target application. 18
1.10 Periodic table representing the approximate temperatures at which each element has a vapor pressure of 0.01 mbar. 20
1.11 Types of transfer line used at ISOLDE. 22
1.12 Periodic table representing the currently available elements at ISOLDE and respective ionization mechanisms. 23
1.13 Ionization mechanisms used at ISOLDE: surface, laser and electron impact ionization. 24
1.14 Contaminant suppression techniques for laser ionized element beams: LIST and ToF-LIS 26
1.15 Different microstructured materials tested at ISOLDE: ThO_2 fibers and SiC foam. 30
1.16 Different microstructured materials developed at ISOLDE: SiC ice templating structure and micrometric BeO. 31
1.17 Yttria nanomaterial tested at ISOLDE before and after heat treatment. 31
1.18 Mesoporous nanometric CaO material developed for ISOLDE and its sintering behaviour. 32
1.19 Calcium oxide microstructure used before at ISOLDE and the newly developed nanometric CaO and respective release profiles. 33
1.20 Sintering basic phenomena (sintering and densification) due to driving force and main sintering mechanisms. 35
1.21 Geometrical models represeting the beginning, initial, intermediate and final stages of sintering. 36

1.22 Sintering mechanisms proposed by Grecovich and Lay for coarsening of porous ceramics. . . . 38
1.23 Radiation enhanced diffusion concept and experimental proof. . . . 40
1.24 SiC target microstructure post irradiation analysis after being operated at ISOLDE. 41
1.25 Radiation damage in nanomaterials (self-healing) vs in normal materials (swelling and embrittlement). . . . 42

2.1 Scheme of an attrition mill. . . . 44
2.2 Details of the ovens used for thermal treatments of TiC and respective composites. 46
2.3 Schematic of a quadrupole mass separator . . . 48
2.4 Setup used for the residual gas analysis. . . . 49
2.5 Dilatometer oven and cell used in the TiC/TiC-C composites. . . . 50
2.6 Bragg-Brentano geometry used normally in X-ray powder diffraction. . . . 55
2.7 ISOLDE tape station and its beta detector and representation of the pulse shape of a radioactive ion beam after proton impact. . . . 59

3.1 SEM microstructures obtained for the TiO_2 and TiC sintering studies. . . . 63
3.2 TiO_2 and TiC specific surface area and relative density evolution as a function of the 2 h heat treatment temperatures. . . . 63
3.3 Released fraction for Be, Na, Mg, k, Sc for TiO_2 at 1000 °C and for TiC from 1200 to 1450 °C. . . . 65
3.a1 SEM microstructures of the raw materials used in this study: TiC, graphite, carbon black and MWCNT. . . . 71
3.a2 Particle size distributions for different milling times and respective $D_{v,50}$ values for TiC, graphite, carbon black and MWCNT. . . . 74
3.a3 SEM microstructures of 75CNT as produced, heat treated at 1500 °C for 10 h and of 75CNTb (MWCNT not milled) as produced and heat treated at 1500 °C for 10 h. 75
3.a4 SEM microstructures of TiC heat treated at 1500 °C for 10 h and of TiC milled, TiCm, for 2 h and with the same heat treatment. . . . 75
3.a5 TiC, TiCm, 50Gr, 50CB and 75CNTb $\Delta\rho/\rho_0$ and $\Delta P_s/P_{s,0}$ for heat treatments at 1500 °C for 2 and 10 h obtained by ANOVA - analysis of variance. . . . 76
3.a6 Relative density and relative porosity ratios (below and above 200 nm) for the TiC, TiCm, 50Gr, 50CB and 75CNTb as produced and heat treated for 2 and 10h. 77
3.a7 Dilatometry of TiC, TiCm, 50Gr, 50CB and 75CNTb up to 1500 °C. . . . 77
3.a8 TiC, TiCm, 50Gr, 50CB and 75CNTb $\Delta S/S_0$ for heat treatments at 1500 °C for 2 and 10 h obtained by ANOVA - analysis of variance. . . . 79
3.a9 SEM microstructures of 50Gr before and after heat treatment at 1500 °C and of 50CB before and after the same heat treatment. . . . 80
3.4 TiCm, 50Gr, 50CB and 75CNTb results for heat treatments at 1500 °C for 10 h in two different ovens. . . . 86
3.b1 Mass losses of TiCm, 50Gr, 50CB and 75CNTb for heat treatments at 1500, 1650 and 1800 °C for 10 h. . . . 94

3.b2 Diffractograms obtained through XRPD for the TiC as supplied and 50Gr as-produced and heat treated for 1500, 1650 and 1800 °C. 95
3.b3 Mass spectrum shown in mass vs ion current, obtained by residual gas analysis of 50CB from 350 to 1500 °C and respective pressure evolution over temperature. 97
3.b4 Mass losses evolution with temperature extracted the RGA pressure evolution for TiC, TiCm and 50CB for comparison. 98
3.b5 Thermodynamical Ti-C-O (black) and Zr-C-O (grey) overlapped phase stability diagrams at 1200 °C, showing the calculated range of CO and O_2 partial pressures in the experimental setup. 98
3.b6 Phase diagram of TiC-ZrC. 99
3.b7 Diffractograms obtained through XRPD for the TiCm and 50Gr as-produced and heat treated for 1500, 1650 and 1800 °C revealing TiC peak shift for higher temperatures. 99
3.b8 SEM microstructures of TiC milled, TiCm and heat treated for 10 h at 1500, 1650 1800 °C. 100
3.b9 TiCm, 50Gr, 50CB and 75CNTb $\Delta\rho/\rho_0$ and $\Delta S/S_0$ for heat treatments at 1500, 1650 and 1800 °C for 10 h. 101
3.b10 Relative density and porosity (below and above 200 nm) for the TiCm, 50Gr, 50CB and 75CNTb as produced and heat treated for 10 h at 1500, 1650 and 1800 °C.101
3.b11 TiCm, 50Gr, 50CB and 75CNTb $\Delta P_S/P_{S,0}$ for heat treatments at 1500, 1650 and 1800 °C for 10 h. 103
3.b12 SEM microstructures of 50Gr, 50CB and 75CNTb as produced and the same composites but heat treated for 10 h at 1500, 1650 and 1800 °C. 104

4.a1 Dilatometric curves for nanometric TiC and respective derivative for different heating rates: 4, 8, 15 and 30 °C min^{-1}. 115
4.a2 MSC of nanometric TiC and reduced χ^2 minimization. 116
4.a3 Cumulative pore size distributions for the 8 °C min^{-1} dilatometry curves, as supplied, 1250, 1400 and 1500 °C, for TiC and TiC-CB. 117
4.a4 SEM fracture microstructures for the TiC 8 °C min^{-1} dilatometry curves: as-produced, 1250, 1400 and 1500 °C. 118
4.a5 Dilatometric curves for TiC-carbon black nanocomposite and respective derivative for different heating rates: 4, 8, 15 and 30 °C min^{-1}. 118
4.a6 Diffractograms obtained through XRPD for the TiC-CB 8 °C min^{-1} dilatometry curve stops: as-produced, 1200, 1400 and 1500 °C. 119
4.a7 MSC of TiC-CB nanocomposite and reduced χ^2 minimization. 120
4.a8 SEM fracture microstructures for the TiC-CB 8 °C min^{-1} dilatometry curves: as-produced, 1200, 1400 and 1500 °C. 121
4.1 MSC for late stage sintering of TiC-CB nanocomposite and reduced χ^2 minimization. 126

5.a1 Scanning electron microscopy microstructures of the selected samples: TiC-milled, TiC-CNT and TiC-CB. 133

5.a2 Scanning electron microscopy microstructures obtained for target material heat treated at 1800 and 2000 °C. . . . 136
5.a3 Release fraction for Be, Na, Mg, k, Sc and Ca for three different TiC microstructures at 1500 (TiC and TiC-CNT) and 1740 °C (TiC-CB) and comparison of TiC-CB release fraction with literature values. . . . 138
5.a4 $\varepsilon_{rel} \cdot \varepsilon_{is}$ for K, Na and Li. . . . 141
5.a5 Release profile for TiC-CB (1800 °C) and Ti foils (1450 °C) target materials for ^{37}K ($t_{1/2}$ = 1.22 s), ^{26}Na ($t_{1/2}$ = 1.07 s) and ^{8}Li ($t_{1/2}$ = 840.3 ms). . . . 142
5.1 Released fraction for Be, Na, Mg, K, Sc for all the TiC materials used during this work. . . . 147

6.1 $P_{\mu,\nu}(t)$ and $\varepsilon_{rel,\mu,\nu}(t_{1/2})$ Kirchner model with different effusion and diffusion time constants. . . . 154
6.2 Kirchner model $P_{\mu,\nu}(t)$ reproducing the release from nanomaterials. . . . 155
6.3 Ar and Ga simulated release efficiency as a function of the target grain size for different $t_{1/2}$. . . . 157

A.1.1 Statistical design used to study through ANOVA analysis of variance, the pore size variation, specific surface area variation and density variation of the materials produced. . . . 160
A.1.2 Especially designed double crucibles to avoid sample oxidation in the oven at high temperatures. In the picture, two sets of these crucibles are seen. . . . 161
A.1.3 X-ray powder diffraction showing the ZrO_2 contamination and its reduction, exemplified with the 50Gr, into ZrC. . . . 162
A.1.4 Relative density and relative porosity ratios (below and above 200 nm) for the TiC, TiCm, 50Gr, 50CB and 75CNTb as produced and heat treated for 2 and 10 h. 163
A.1.5 Dilatometry of 25Gr, 25CB and 75CB up to 1500 °C. TiC and TiCm are present for the sake of comparison. . . . 163
A.1.6 TiCm, 25Gr and 50Gr $\Delta\rho/\rho_0$, $\Delta S/S_0$ and $\Delta P_s/P_{s,0}$ for heat treatments at 1500 °C for 2 and 10 h obtained by ANOVA - analysis of variance. . . . 164
A.1.7 TiCm, 25CB, 50CB and 75CB $\Delta\rho/\rho_0$, $\Delta S/S_0$ and $\Delta P_s/P_{s,0}$ for heat treatments at 1500 °C for 2 and 10 h obtained by ANOVA - analysis of variance. . . . 164
A.1.8 TiCm, 25CNT, 50CNT, 75CNT and 75CNTb $\Delta\rho/\rho_0$, $\Delta S/S_0$ and $\Delta P_s/P_{s,0}$ for heat treatments at 1500 °C for 2 and 10 h obtained by ANOVA - analysis of variance. 164
A.2.1 Statistical design used to study through ANOVA analysis of variance, the pore size variation, specific surface area variation and density variation of the materials produced. . . . 165
A.2.2 Mass spectrum shown in mass vs ion current, obtained by residual gas analysis of TiC, TiCm, 50Gr and 75CNTb from 350 to 1500 °C and respective pressure evolution over temperature. . . . 166
A.2.3 Thermodynamical Ti-C-O and Zr-C-O phase stability diagrams at temperatures from 1200 to 1800 °C. . . . 167

A.2.4 XRPD diffractograms obtained for 50CB heat treated at 1800 °C for 10 h, showing phase segregation. 167
A.3.1 Relative mass losses for TiC and TiC-CB. 169
A.4.1 FLUKA simulation which estimates $H^*(10)$ at 10 cm of 3 pellets of 12 mm diameter and 1.5 mm thickness. 170
A.4.2 Irradiation stand design in 3D, built and sample tube opened showing the 9 samples for irradiation. 170
A.4.3 Target unit #527 with target, ion source, mass marker and CF_4 leak identified, TiC-CB pellets as-produced and graphite container with TiC-CB pellets ready to be inserted in the target unit oven. 171
A.4.4 Mass scan of the TiC-CB unit (#527) - target at 1800 °C and Re ion source at 2130 °C. 171

B.1 SEM microstructures of the as produced TiO_2 + MWCNT and resulting microstructures after thermal treatments (TiC + MWCNT) at 1700 °C and at 2100 °C for 1 h and 15 h. 178

List of Tables

1.1 List of the materials currently used and available at ISOLDE and respective fraction of targets built, melting point, maximum operation temperature and target thickness. 19

3.a1 Characteristics of the raw materials used in this study 70

3.a2 Density, SSA, median pore size, BJH pore volumes, SEM particle sizes determined with *ImageJ* and mass losses of TiC, TiCm, 50Gr, 50CB and 75CNTb as produced and after heat treatments at 1500 °C for 2 and 10 h. 78

3.b1 Crystallite sizes and stress determined by XRPD using the L.H.W. method and lattice parameter and phase ratios determined from Rietveld refinement. . . . 96

3.b2 C, N and O concentrations in TiC and TiC thermally treated at 1500 °C determined by combustion with infrared adsorption spectrometry and carrier gas hot extraction analysis. 96

3.b3 Density, SSA, median pore size and BJH pore volumes of TiCm, 50Gr, 50CB and 75CNTb as produced and after heat treatments for 10 h at 1500, 1650 and 1800 °C.102

4.a1 Activation energies for pressureless sintering of TiC, for C and Ti self-diffusion in TiC and for the MSC curves for TiC and TiC-carbon black composites (TiC-CB).116

4.a2 SSA, SEM particle size, XRPD crystallite size, for the TiC as supplied and heat at 8 °C min^{-1} up to 1250, 1400 and 1500 °C as well as for the TiC-CB as produced and heat treated at the same rate up to 1200, 1400 and 1500 °C. 119

5.a1 Titanium carbide and the nanocomposiste TiC-CNT and TiC-CB characteristics to be used in the release studies. 133

5.a2 Isotopes and respective half-lives ($t_{1/2}$), characteristic γ-ray energy (E_γ) and intensity used in the release studies of the different TiC microstructures. 134

5.a3 Comparison of sample and upscaled material processing and respective main characteristics of the obtained materials after 1800 °C for 10 h. 135

5.a4 Characteristics of the TiC-CB nanocomposite heat treated at 1800 and 2000 °C. 137

5.a5 Summary of the online yields for the studied isotopes on the TiC-CB prototype target, with target temperatures, in target production yield and comparison with ISOLDE and TRIUMF database yields (the later normalized to proton current). 140

A.1.1 Density, SSA, median pore size, BJH pore volumes and mass losses of 25Gr, 25CB, 75CB, 25CNT, 50CNT and 75CNT as produced and after heat treatments at 1500 °C for 2 and 10 h. 162
A.2.1 Characteristics of the raw materials used in this study. 165
A.4.1 Isotope in-target production yields in the TiC-CB, in μC^{-1}, when bombarding with 1.4 GeV protons. 172
A.4.2 Isotope production cross sections for the element Ti, in mb, when bombarding it with 1.4 GeV protons. 173
A.4.3 Ratio between the isotope production cross sections, in a Ti target, of CERN (1.4 GeV protons) and TRIUMF (500 MeV protons). 174
A.4.4 Isotope production cross sections for the element C, in mb, when bombarding it with 1.4 GeV protons. 175
A.4.5 Ratio between the isotope production cross sections, in a C target, at CERN (1.4 GeV protons) and at TRIUMF (500 MeV protons). 175

B.1 SSA, density, XRPD crystallite size and mass losses of the as produced samples and thermally treated at 1700 °C for 1 h and at 2100 °C for 1 and 15 h. 178

Nomenclature

Symbols

α	Weighting factor between the slow fall and fast fall components of the release function [%] 137
α_∞	Weighting factor between the slow fall and fast fall components of the release function for a stable element [%] 140
β^+	Type of β decay, positron emission 6
β^-	Type of β decay, electron emission 6
$\Delta\rho/\rho_0$	Density changes [%] 71
ΔH	Adsorption enthalpy [J mol^{-1}] 29
$\Delta l/l_0$	Linear shrinkage [%] 36
$\Delta l_{blank}(T)$	LVDT position variation due to expansion of the dilatometer cell [µm] 49
$\Delta l_{exp}(T)$	LVDT sample differential thermal expansion relatively to the blank [µm] 49
ΔM	Full width at half maximum of the separated ion beam [u e^{-1}] 11
$\Delta m/m_0$	Sample mass losses [%] 49
$\Delta P_S/P_{S,0}$	Pore size variation below 200 nm [%] 72
$\Delta S/S_0$	Specific surface area variations [%] 72
δ	Grain boundary thickness [Å] 113
ϵ	Type of β decay, electron capture 6
ϵ_{is}	Ionization efficiency [%] 24
ϵ_{rel}	Isotope release efficiency [%] 27
ϵ_{sep}	Isotope mass separation efficiency [%] 27
ϵ_{tranp}	Isotope beam transport efficiency [%] 27
γ	Specific surface energy [J m^{-2}] 34
γ_L	Liquid surface tension [N m^{-1}] 52
Γ_v	Sintering scaling parameters for volume diffusion 113
Γ_b	Sintering scaling parameters for surface diffusion 113

λ	Wavelength [Å] 55
λ_f	Release function fast fall time constant [s^{-1}] 137
λ_i	Decay constant [s^{-1}] 6
λ_r	Release function rise time constant [s^{-1}] 137
λ_s	Release function slow fall time constant [s^{-1}] 137
$\lambda_{f,\infty}$	Release function fast fall time constant for a stable element [s^{-1}] 140
$\lambda_{r,\infty}$	Release function rise time constant for a stable element [s^{-1}] 140
$\lambda_{s,\infty}$	Release function slow fall time constant for a stable element [s^{-1}] 140
μ	Diffusion time constante [s^{-1}] 28
ν	Effusion time constant [s^{-1}] 29
Ω	Atomic volume [m] 113
Φ	Work function [eV] 24
ϕ	XRPD peak-shape function, where it is normally Gaussian, Lorentzian, Pseudo-Voigt or Pearson VII 57
ρ	Density or geometrical density [$g\,cm^{-3}$] 28
ρ_0	Initial density [$cm\,g^{-3}$] 114
ρ_r	Relative density [%] 49
ρ_t	Theoretical density [$g\,cm^{-3}$] 37
σ	Isotope production cross section [mb] 27
σ_{mol}	Molecule cross section [m^2] 51
τ_0	Mean sticking time pre-exponential factor [s] 29
τ_a	Mean sticking time for a wall collision [s] 29
τ_f	Mean flight time between 2 wall collisions [s] 29
τ_ν	Effusion mean time [s] 29
Θ	Work of sintering [$s\,K^{-1}$] 113
θ	Incident angle of the X-ray beam [°] 55
θ_{Hg}	Hg contact angle [°] 54
A	Atomic number or number of protons in a nuclei [u] 6
a	Crystal lattice parameter [Å] 95
A_b	XRPD profile absorption factor 57
A_F	Powder agglomeration factor [dim] 70
B	XRPD peak broadening due to crystallite size [Å] 56
B^*	Reciprocal broadening [$Å^{-1}$] 56
C	Concentration [$mol\,m^3$] 35
c	Dilatometry heating rate [$°C\,min^{-1}$] 113
C_b	BET constant [dim] 52

C_g	Statistical constant regarding the ions and atoms quantum states [dim]	24
D	Diffusion coefficient [$m^2\,s^{-1}$]	27
d	Spacing between crystallographic planes [Å]	55
d^*	Reciprocal lattice [$Å^{-1}$]	56
D_0	Diffusion pre-exponential factor [$m^2\,s^{-1}$]	28
D_v	Grain boundary diffusion coefficient [$m^2\,s^{-1}$]	113
D_b	Surface diffusion coefficient [$m^2\,s^{-1}$]	113
$D_{Pv,50}$	Median pore size in volume [nm]	51
$D_{v,50}$	Median particle size in volume [nm]	50
E_A	Electron affinity [eV]	24
E_s	Surface free [J]	34
F	Released fraction of isotopes [%]	64
F_k	XRPD profile structure factor for the k^{th} Bragg reflection and contains the unit cell parameters	57
G	Mean grain size [Å]	113
G_{BET}	Particle size determined from the SSA [m]	70
G_{SEM}	Grain/particle size measured in SEM	71
H	Parameter containing geometrical, material and diffusion mechanism dependent parameters of initial stage sintering [s^{-1}]	36
h	XRPD crystallite size [Å]	56
$H^*(10)$	Ambient dose equivalent [µSv]	133
I	Primary beam intensity [µA]	21
j	Primary beam flux [cm^{-2}]	27
J_x	Flux of atoms [$J^{-1}\,s^{-1}$]	35
k	Boltzman constant [$J\,K^{-1}$]	24
K_h	Constant which depends on the crystallite shape [dim]	56
k_S	Constant depending on a particle shape [dim]	70
l_0	Initial size of the sample [µm]	49
L_k	XRPD profile parameter containing the Lorentz, polarization and multiplicity factors	57
$l_{LVDT,i}$	LVDT initial position [µm]	49
$l_{LVDT}(T)$	LVDT position as a function of temperature [µm]	49
M	Mass of the ions at the separator focal plane [$u\,e^{-1}$]	11
m	Exponent depending on initial stage sintering mechanism [dim]	36
m_0	Initial mass of the sample [g]	49
N	Neutron number or number of neutrons in a nucleus [u]	6

n	Exponent depending on initial stage sintering mechanism [dim]	36
n_+	Flux of ions leaving a surface [cm^{-2}]	24
n_0	Flux of neutrals leaving the surface [cm^{-2}]	24
N_A	Avogadro number [mol^{-1}]	51
n_C	Number of protons per µC of beam [μC^{-1}]	27
$N_i(t)$	Number of radioisotopes as a function of time [dim]	6
n_R	Order of the X-ray reflection [dim]	55
N_t	Number of target atoms exposed to the beam [dim]	27
$N_{i,0}$	Initial number of radioisotopes [dim]	6
n_{wc}	Number of wall collisions [dim]	29
P	Pressure [Pa]	51
P_0	Saturation pressure [Pa]	51
P_k	XRPD profile preferred orientation function	57
P_r	Relative porosity [%]	73
P_S	Median pore size in volume [nm]	50
$P_{\lambda_i}(t)$	Release function of a radioisotope from a TISS [dim]	137
$P_{\lambda_\infty}(t)$	Release function of a stable element from a TISS [dim]	140
P_{CO}	Partial pressure of CO.	45
P_{O_2}	Partial pressure of O_2	45
$P_{r,<200\,nm}$	Relative porosity below 200 nm [%]	73
$P_{r,>200\,nm}$	Relative porosity above 200 nm [%]	73
Q	Activation energy [$J\,mol^{-1}$]	28
q	Particle charge [e]	16
R	Ideal gas constant [$J\,K^{-1}\,mol^{-1}$]	28
r	Particle/grain radius [m]	28
r_c	Capillary radius [nm]	52
R_m	Separator mass resolving power [dim]	11
r_p	Pore radius in BJH model [nm]	52
S	Specific surface area [$m^2\,g^{-1}$]	51
s	Lattice stress [%]	56
S_A	Total surface area of the system [m^2]	34
S_{ph}	XRPD scale factor which will determine the fraction of a certain phase	57
T	Temperature [K]	27
t	Time [s]	6
t_c	Tape station collection time after proton impact [ms]	59

t_d	Tape station delay time after proton impact [ms]	59
T_m	Melting point temperature [°C]	18
t_m	Tape station measurement time [ms]	60
t_t	Tape station transport time from implantation to measurement spot [ms]	60
$t_{1/2}$	Half-life [s]	6
t_{ml}	Adsorbate monolayer thickness [nm]	52
$T_{op,max}$	Target material maximum operation temperature [°C]	18
V_0	Initial volume of the sample [cm^3]	49
V_a	Volume of adsorbate adsorbed [m^3]	52
V_m	Molar volume [m^3]	34
$V_{m,STP}$	Molar volume of a gas at STP [$m^3\,mol^{-1}$]	51
V_{ml}	Adsorbate monolayer volume [m^3]	51
$v_{P,BJH}$	Pore volume determined from the BJH model [$cm^3\,g^{-1}$]	70
W	Ionization potential [eV]	23
X	Target thickness [$g\,cm^{-2}$]	18
x	Particle neck radius [m]	36
Y	Yield [μC^{-1}]	26
$y_{b,i}$	XRPD background at the i^{th} step	57
$Y_{i,calc}$	XRPD intensity at an arbitrarily chosen point i	57
Y_{Prod}	In-target production yield [μC^{-1}]	27
$Y_{Ti,ISOLDE}$	Database yields for Ti-foils target at ISOLDE [μC^{-1}]	140
$Y_{TiC,ISAC}$	Database yields for TiC targets at ISAC-TRIUMF [μC^{-1}]	140
Z	Atomic mass number or number of protons and neutrons in a nucleus [u]	6

Acronyms

[dim]	Dimensionless unit	6
ABRABLA	Code to calculate nuclear reaction cross-sections using the ABLAsion-ABRAsion model.	27
ALTO	Accélérateur Linéaire et Tandem à Orsay	12
ANL	Argonne National Laboratory	12
ANOVA	ANalysis Of VAriance	67
ARIEL	Advanced Rare IsotopE Laboratory	13
BET	Brunaeur, Emmett and Teller mode	51
BJH	Barrett, Joyner and Hallenda model	51
BSE	Back scattered electrons	53
CARIBU	CAlifornium Rare Isotope Breeder Upgrade	12

CARIF	China Advanced Rare Ion beam Facility 13
CARR	Chinese Atomic Energy Commission 13
CASINO	monte CArlo SImulation of electroN trajectory in sOlids 53
CB	Carbon black 72
CE	Cluster emission 6
CERN	European Organization for Nuclear Research 1
CNT	Carbon nanotubes 33
cw	Continuous wave beam 21
EBIS	Electron beam ion source 16
EBSD	Electron BackScatter Diffraction 53
EDS	Energy-dispersive X-ray spectroscopy 53
EN-STI	ENgineering department - Sources, Targets and Interactions group at CERN 3
EPFL	École Polytechnique Fédérale de Lausanne 2
Err_S	Standard error of the mean - 95 % confidence interval 76
EURISOL	European ISOL facility 13
EXCYT	EXotics with CYclotron and Tandem 12
FCC	Face-Centered Cubic crystal structure 67
FEBIAD	Forced Electron Beam Induced Arc Discharge 26
FLUKA	FLUktuierende KAskade, a Monte Carlo particle physics simulation code 27
FWHM	Full width at half maximum 11
GANIL	The Grand Accélérateur National d'Ions Lourds (Large Heavy Ion National Accelerator) 13
GPS	General Purpose Separator 15
Gr	Graphite 72
HIE-ISOLDE	High Intensity and Energy upgrade for ISOLDE 13
HPGe	High-purity Germanium detectors 58
HRIBF	Holofield Radioactive Ion Beam Facility 12
HRS	High resolution separator 15
IBS	Institute for Basic Science 13
IFS	In-flight separation 9
IGISOL	Jyväskylä Ion Guide Isotope Separator On-Line 12
INFN	Istituto Nazionale di Fisica Nucleare 12
IPA	Isopropanol 70
IPNO	Institut de Physique Nucléaire d'Orsay 12
ISAC	Isotope Separator and ACcelerator 13
ISOL	Isotope Separator OnLine 1

ISOLDE	Isotope Separator OnLine DEvice 1
IT	Isomeric Transition 6
IUPAC	International Union of Pure and Applied Chemistry 51
JYFL	Jyväskylän Yliopiston Fysiikan Laitos (University of Jyväskylä Institute of Physics) 12
KUL	KU (Katholieke Universiteit) Leuven 12
LHC	Large Hadron Collider 14
LIEBE	LIquid Eutetic lead Bismuth loop target for Eurisol 19
LINAC	LINear ACcelerator 13
LISOL	Leuven Isotope Separator On-Line 12
LIST	Laser Ion Source and Trap 25
LNL	Laboratori Nazionali del Sud 12
LTP	Powder Technology Laboratory at EPFL 2
LVDT	Linear variable differential transformer sensor 48
LWH	Langford modified Williamson-Hall plot 56
MAFF	Munich Accelerator for Fission Fragments 12
MEDICIS	MEDical Isotopes Collected from ISolde 16
MIP	Mercury intrusion porosimetry 54
MSC	Master Sintering Curve 109
MWCNT	Multi wall carbon nanotubes 21
MYRRHA	Multi-purpose hYbrid Research Reactor for High-tech Applications 13
NDU	Notre Dame University 12
ORNL	Oak Ridge National Laboratory 12
PID	Proportional–integral–derivative (controller) 46
ppp	Protons per pulse 15
PSB	Proton synchrotron booster 14
PSD	Particle size distribution 50
PVP	Polyvinilpyrrolidone 70
QMS	Quadrupole mass spectrometer 47
RBS	Radioactive Beam Sources section at CERN 3
RED	Radiation enhanced diffusion 21
REX	Radioactive ion beam EXperiment 15
RF	Radio Frequency 23
RFQ	Radio frequency quadrupole 15
RGA	Residual gas analysis 47
RIB	Radioactive ion beam 1

RIBO	Radioactive Ion Beam Optimizer - Monte Carlo code 156
RIBRAS	Radioactive Ion Beam in BRASil 12
RIKEN	RIkagaku KENkyusho, Institute of Physical and Chemical Research 12
RILIS	Resonant ionization laser ion source 25
RISP	Rare Isotope Science Project 13
RNB	Radioactive nuclear beams 8
SC	Synchrocyclotron 14
SCRIT	Self-Confining RI Ion Target 12
SE	Secondary electrons 53
SEM	Scanning Electron Microscopy 52
sf	Spontaneous fission 6
SPES	Selective Production of Exotic Species 13
SPIRAL	Système de Production d'Ions Radioactifs en Ligne (System for Producing Online Accelerated Radioactive Ions) 13
SPS	Spark plasma sintering 112
SSA	Specfic Surface Area 51
STAGISO	Proton beam staggered mode 19
STP	Standard temperature and pressure 51
TiCm	Milled TiC 72
TISS	Target and ion source system 16
ToF-LIS	Time-of-Flight Laser Ion Source 25
TRIUMF	TRI University Meon Facility: Canada's national laboratory for particle and nuclear physics and accelerator-based science 13
VADIS	Versatile Arc Discharge Ion Source 26
VADLIS	Versatile Arc Discharge Laser Ion Source 26
XPS	X-ray photoelectron spectroscopy 94
XRPD	X-rays used in X-ray powder diffraction 55
YSZ	Yttria-stabilized-zirconia 70

Introduction

Alchemists have tried for millennia to unsuccessfully transmute lead into gold, a dream fulfilled by modern physics in the last century. Using particle accelerators, gold can now be produced from lead through nuclear reactions, although not in quantities alchemists once imagined. The study of nuclear reactions is one of the many subjects of nuclear physics, which is the specialty of physics that studies the nucleus. The great majority of all the mass in the universe (99.9 %) is contained within the nucleus of the atom. Even though the smallest nucleus is known to have just one proton, the limit of the number of protons and neutrons, nucleons, in the nucleus hasn't been discovered yet. So far, the largest nucleus discovered has 294 nucleons (Og294 - Oganesson), which only lives for a fraction of a millisecond [1, 2].

While the stars are the source of virtually all energy in our universe, they are as well the factories of elements - transforming hydrogen and helium into heavier elements up to iron during millions of years, and heavier elements in a few seconds in the explosion of a supernova. Nuclear physics seeks to answer fundamental questions about the nucleus, its properties and its boundaries and has as well everyday lives applications such as in electrical power generation (fission and fusion power plants), manufacturing (food preservation) and medicine (radiation therapy) [3].

Radioactive ion beams (RIB) are often used by nuclear physicists to study the nucleus where the former are produced by accelerating particles to hit a fixed target, inducing nuclear reactions which transmute the elements, producing isotopes. In order to build the machines that are capable of producing RIBs, experts with many different expertise's (such as materials science, engineering, physics, chemistry, electronics, informatics, etc.) are needed. One such machine that produces RIBs through a technique called Isotope Separator OnLine (ISOL), is located in Geneva at CERN[1], ISOLDE[2], serving a community of more than 450 scientists with more than 50 experiments every year [6].

At ISOLDE, highly energetic protons are accelerated towards a thick target in order to induce nuclear reactions, which produce the isotopes in the bulk of the target material. These targets are kept at high temperatures while being irradiated in order to promote the release of the isotopes (thus the OnLine word) through solid diffusion and diffusion through the vacuum,

[1] European Organization for Nuclear Research [4]
[2] Isotope Separator OnLine DEvice [5]

called effusion, into an ion source in order to create a beam.

The heart of ISOLDE and any other ISOL facility is the target material, which is the first ISOL step and ultimately the one that limits the facility beam diversity and intensity. The target material, on a materials science point of view, is also one of the least developed technology of the > 60 years old ISOL technique. As in the majority of the existing technologies, they are limited by their composing materials and the ISOL technique is no exception to this rule. ISOL target materials must have: (i) high production cross sections of isotopes of interest, (ii) efficient release of the produced isotopes and (iii) be able to survive the extreme conditions of irradiation and high temperature without ageing. While the production cross section mainly depends on the chemical elements, the release efficiency and stability depend mainly on the target microstructure.

The material stability will directly affect the beam intensities delivered, where decaying target materials will have a direct effect on the beam intensities which will also decay over time. The isotope release efficiency has a direct impact on the physics outcome where a material that is 10 times more efficient will deliver a beam which is 10 times more intense, thus, physics experiments will be able to be conducted in a tenth of the time to acquire the same statistics. Apart from that, target materials development can also provide new elements, as beams, at ISOLDE and also access to shorter lived isotopes which are normally produced in small quantities and thus require highly efficient materials.

Efficient materials are highly porous, have high surface areas and are of nanometric nature, which overall shorten the diffusion and effusion times allowing to extract faster, the decaying isotopes. This also means that efficient materials, are less dense and also reduce the nuclear waste generated by ISOL facilities. Developed target nanomaterials, are more reactive and unstable so under the ISOL operation conditions, microstructure stabilization mechanisms need to be implemented and the limitations of these materials have to be well known.

Ti-based materials are of interest for ISOLDE to produce radioactive ion beams, since the currently used material, Ti-rolled foils, either sinters or melts during operation, bringing decaying beam intensities over time. As such, in this thesis, Ti-based refractory materials are studied, where TiC is selected as the target material to be developed due to its highly refractory properties. As a result, a processing route was developed in order to produce different TiC-carbon nanocomposites and stabilize nanometric TiC at high temperatures. The obtained composites stability was investigated up to 1800 °C, where they were fully characterized. They were after tested for isotope release properties to the select the most promising material before the selected nanocomposite production was scaled up and tested as a prototype target material for isotope production at ISOLDE.

The experimental research work in materials presented in this thesis was done primarily at the Powder Technology Laboratory (LTP) at EPFL in Lausanne, which had the necessary infrastructure and expertise to investigate, develop the TiC processing route, and characterize the obtained materials. To complement the characterizations done at LTP-EPFL, part of the

work was done in the Department of Materials and Ceramics Engineering of the University of Aveiro, in Portugal. The isotope release studies and target protype assembly and testing was done at CERN in the RBS section (Radioactive Beam Sources section, part of the EN-STI group[3]).

This thesis includes four manuscripts which will be submitted to peer reviewed journals, and are integrated into its chapters, where:

- **Chapter 1 - Literature review** where the context of the work is introduced, the important scientific concepts are described and the state of the art in target material development is described in detail;
- **Chapter 2 - Experimental methods** where the relevant methods and characterization techniques are described;
- **Chapter 3 - TiC-carbon nanocomposite development**, describes the preliminary sintering and release studies done on TiO_2 and TiC refractory materials, followed by a manuscript - *Development of a processing route for carbon allotrope-based TiC porous nanocomposites* - where different volumes of MWCNT, graphite and carbon black were mixed with TiC and thermally treated to assess how they affect the sinterability of TiC up to 1500 °C. Another manuscript is included - *Stability of nanometric TiC-carbon composites: effects of carbon allotropes and Zr milling impurities* - where selected TiC nanocomposites were tested up to 1800 °C and their phase composition evolution with temperature and lattice parameters were studied in detail.
- **Chapter 4 - TiC and TiC-carbon black sintering kinetics** describes in the manuscript included - *Master sintering curve determination of nanometric TiC and a TiC-carbon black nanocomposite* - the construction of the master sintering curve to study the sintering kinetics of TiC and a TiC-C nanocomposite.
- **Chapter 5 - Isotope release properties from TiC-carbon nanocomposites** which includes a manuscript - *Constant isotope release properties measured for an online prototype TiC-carbon nanocomposite target material* - where selected TiC-C nanocomposites are tested for isotope release in order to select the best one to be used as a target material prototype. The chosen nanocomposite processing is upscaled to match the mass required for a full ISOLDE target and the prototype target is irradiated online and isotope release efficiency is assessed.
- **Chapter 6 - Conclusions and outlook** where the main conclusions are presented and perspectives for further research work are given, which include a second iteration of an improved TiC-C nanocomposite to be tested at ISOLDE and isotope release modeling review, discussion and suggestions.

[3] ENgineering department - Sources, Targets and Interactions group

1 Literature review

Contents

1.1 Introduction to radioactive ion beams 6

1.1.1 Isotope Separator OnLine (ISOL) 8

1.2 ISOLDE target and ion source system 16

1.2.1 Target materials 18

1.2.2 Transfer line 21

1.2.3 Ion sources 23

1.3 Engineered microstructure ISOLDE target materials 26

1.3.1 Release efficiency: diffusion and effusion 27

1.3.2 (Sub)micrometric microstructure target materials 29

1.3.3 Nanostructured target materials development 30

1.4 Sintering 34

1.4.1 Sintering stages 36

1.4.2 Sintering of porous ceramics 37

1.4.3 Constrained sintering 38

1.4.4 Irradiation influence on sintering 40

This chapter will frame the work making a general overview of the state of the art of the thesis subject and theoretical concepts used. Since the state of the art of TiC-C composites materials is already done on the article included on section 3.2 (page 65), radioactive ion beams and its production will be reviewed as well as engineered microstructure target materials developed at ISOLDE (Isotope Separator OnLine DEvice) at CERN (European Organization for Nuclear Research). Sintering will be introduced where the main aspects relevant for this work will be detailed.

1.1 Introduction to radioactive ion beams

In 1896, Antoine-Henri Becquerel was the first to accidentally report on radioactivity. By studying an uranium compound (uranyl double sulfate, a fluorescent material), he noticed that even when covering it with paper, glass and other substances it emitted a penetrating radiation which darkened a photographic plate. It was probably the fact that the emission of this radiation did not depend on fluorescent uranyl double sulfate but on any uranium compound, that attracted the curiosity of other scientists. Later, Pierre and Marie Skłodowska Curie, studied this phenomenon and showed it to be related to the atom and coined this new discovery "radioactivity" [7].

Except for hydrogen, all nuclei are constituted by protons and neutrons and can be represented by ${}^{A}_{Z}X$ where X is the element, Z is the number of protons or atomic number and A is the number of protons and neutrons or atomic mass number. An element X has a defined Z and can adopt different number of neutrons (N). These nuclides (same Z but different A or N) are also called isotopes and they can either be stable, e.g. carbon is constituted by ${}^{12}_{6}C$ (98.93 %) and ${}^{13}_{6}C$ (1.07 %) [1], or unstable (radioactive), such as ${}^{11}_{6}C$ which has a limited life time of 20.38 min. The isotope life times related to the decay constant (λ_i [s^{-1}]) and/or half-life ($t_{1/2}$ [s]) which is the time by which a certain quantity is reduced by half of its initial value ($N_{i,0}$ [dim][1]). As such, through radioactive decay, the number of isotopes ($N_i(t)$ [dim]) follows an exponential decrease with time (t [s]) [3]:

$$n(t) = n_0 e^{-\lambda t} \quad \text{where} \quad \lambda = \frac{\ln 2}{t_{1/2}} \tag{1.1}$$

Radioactivity was divided into three types of radiation by Ernest Rutherford: alpha (α), beta (β) and gamma (γ) radiations, at the end of the XIX century [3]. The radiation types have remained until today, and were classified according to electric charge and matter penetration. The α decay is the emission of a positively charged alpha particle (${}^{4}_{2}He^{2+}$) by large nuclides (generally $Z > 83$) [8] reducing A by 4 and Z by 2. α radiation can't penetrate more than a sheet of paper [3]. For β decay processes, Z is reduced by 1, but without change in A. β decay can be divided in three main subtypes: electron emission (β^-) , emitting an electron and an antineutrino), positron emission (β^+) , emitting a positron and a neutrino) and electron capture (ϵ) , where the nucleus captures an inner shell electron and emits an X-ray and a neutrino) [3, 7]. β radiation can be stopped by a few millimeters of aluminum. Often, after α or β decay, the nucleus is left in an excited energy state where a highly energetic photon (γ-ray) is usually emitted in order to bring the nucleus to the ground state [3]. γ-rays can penetrate several centimeters of lead and can be used to identify isotopes by using spectrometry [8]. Other less common decay modes exist such as spontaneous fission (sf) , proton decay, beta delayed alfa, isomeric transition (IT) , neutron and proton emissions and cluster emission (CE) , but they won't be detailed here any further [1, 8].

[1] To avoid confusion with references dimensionless units will be represented as [dim] where they are normally represented as [1]

A high repulsive electrostatic force, Coulomb force, exists between the positively charged protons in the nucleus, which would fall apart if not for the even stronger short ranged nuclear force. For light elements, $N = Z$, as seen in the nuclide chart of figure 1.1, but as we move to higher masses, in order to overcome the Coulomb force caused by the high number of protons in the nucleus, $N > Z$ [3]. This is only possible up to $N = 83$, where the addition of neutrons can't compensate anymore for the Coulomb force, so from there on all nuclides are unstable. In physics the most stable system are those with minimum Gibbs free energy. For nuclides also, the energy tends to its minimum, where the energy of the nucleus is lower than the sum of its separated components (nucleons). The difference between these energies is called the binding energy, also defined as the energy necessary to break the nucleus.

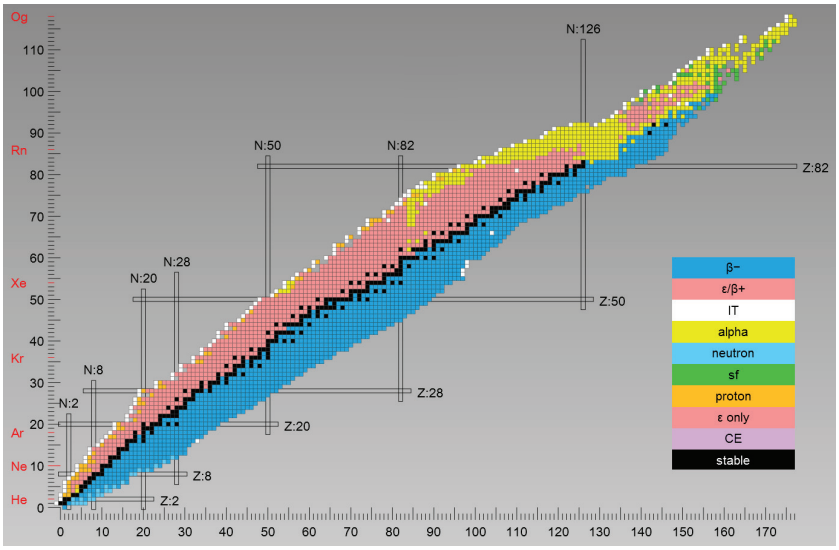

Figure 1.1 – Karlsruhe Chart of Nuclides with the stable (black) and radioactive isotopes (color) represented. The lines correspond to the nuclear magic numbers. Reproduced from [1]. For more information on the radioactive isotope decay modes, see the text on page 6.

Since Becquerel, Curie and Rutherford nuclear physics has advanced much thanks to new techniques, experimental investigations and increase in computational power [9]. Even though very significant progress has been made in nuclear physics in the past years, still basic questions remain: How many nuclides exist? What are the limits of their existence? Why are there certain configurations of protons and neutrons more stable (magic numbers) than others? Just this year, 4 new elements have been added to the periodic table: Nihonium (Nh, $Z = 113$), Moscovium (Mc, $Z = 115$), Tenessine (Ts, $Z = 117$) and Oganesson (Og, $Z = 118$) [2]. The chart of nuclides represents all the nuclides discovered so far in an A vs N configuration, including their modes of decay, as can be seen in figure 1.1. So far 3992 isotopes have been discovered (including 260 stable and 744 isomers) [1], however there are more than 6000 predicted to exist [9].

Nuclear physics has numerous applications in everyday life in areas such as electrical power generation (fission and fusion power plants), warfare, manufacturing (food preservation),

medicine (radiation therapy) and applied and fundamental research [3]. Nuclear physics (and others) uses isotopes as radioactive ion beams (RIB), also referred as radioactive nuclear beams (RNB) or rare isotope beams [9], for research. RIBs can be made from isotopes from microseconds of $t_{1/2}$ to very long half-lives (such as days or many years), with different energies, from a few keV to a couple of GeV [10] where they can be either singly or multiply negatively or positively ionized.

RIBs have a vast field of applications [11] in nuclear, atomic, solid state and astrophysics and also in life sciences, which will be detailed here, however not extensively. In nuclear physics RIBs are used to understand the nucleus and its properties such as the nuclear masses, radii, moments, shape and exotic radioactive decay modes. In fundamental interactions RIBs are used to better understand and validate the Standard Model at low energies [9]. Astrophysics seeks to understand how the elements are created in core of the stars during billions of years and sometimes in a matter of seconds in supernovas [9]. Solid state physics and materials science employ radionuclides as probes in advanced techniques, in order to probe the local environment, either on surface or in the bulk, diffusion dynamics and studying semiconductors [12, 11]. RIBs can be used in life sciences as well, finding new radioisotopes for medical diagnostic and therapy, and to understand how some organic components in the human body interact with the presence of trace chemical elements such as mercury [12, 11].

1.1.1 Isotope Separator OnLine (ISOL)

Nuclear reactions

In order to produce RIBs, nuclear reactions (transmutation) have to be induced by colliding photons, electrons, protons, neutrons, light or heavy ions with a target [9, 7]. The isotopes are produced through different nuclear reactions which depend on the target, projectile and its energy: spallation, fragmentation, fission and fusion-evaporation [9]. Each of these reactions has an independent probability to occur - cross section - and together determine which and how much of each isotope is produced per incident particle [3]. Some of these reactions are represented on figure 1.2, where 1.4 GeV protons are colliding with a uranium target.

Spallation happens when a high energy proton (above 100 MeV) hits a target nucleus. When the proton hits the nucleus it causes an intranuclear cascade which ejects high energy nucleons leaving it in an excited state. While reaching thermal equilibrium, the nucleus evaporates several other nucleons forming the isotope [7]. This reaction channel produces isotopes of $10-20A$ below the A of the target. Spallation reactions are used in spallation neutron source facilities producing neutrons by bombarding thick high-density targets with intense proton beams for research in material, medicine, protein, biology, condensed-matter, geology (and others) studies [13, 14].

Fragmentation can be induced by light projectiles in the GeV range in heavy targets [7]. However, fragmentation usually refers to the fragmentation of an heavy ion beam ($>$ 50 MeV) into

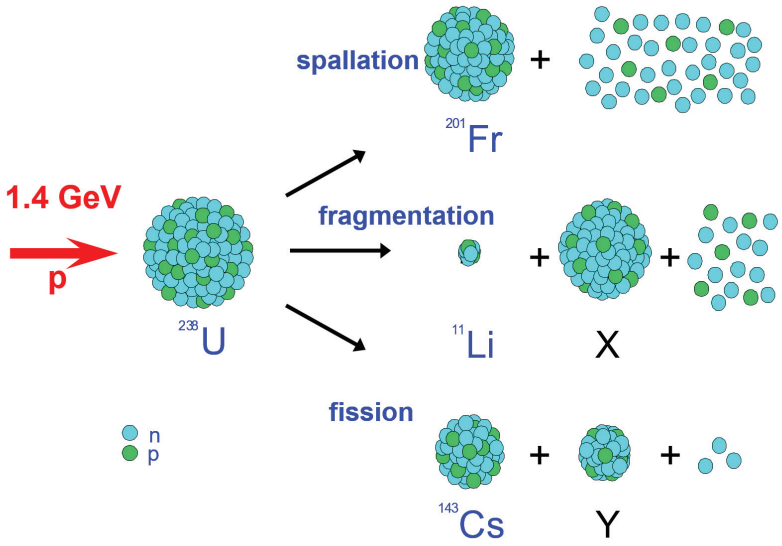

Figure 1.2 – Schematic representation of spallation, fragmentation and fission reactions.

a light target [15]. Fragmentation produces a vast variety of nuclide masses, particularly light nuclides.

Fission usually happens in heavy nuclides where the incident particle is absorbed by the nucleus. The nucleus gets into an unstable excited state and fissions in two nuclides of different masses (usually around 1/3 and 2/3 of the original) emitting neutrons and other light particles [7]. Fission of 235 uranium by thermal neutrons (0.025 eV) is one of the most studied reactions and is responsible for electricity generation in nuclear power plants.

Fusion-evaporation happens when two nuclides are brought together with sufficient energy to overcome the Coulomb barrier and fuse into one [16]. The resulting nuclide gets into and highly excited state and emits more neutrons than protons before undergoing γ decay. This reaction mechanism produces neutron-deficient nuclides [16].

RIB production methods and ISOL

There are two methods to produce a RIB: in-flight separation (IFS) and Isotope Separator On-Line (ISOL) which are both schematically represented on figure 1.3. Both techniques strive to produce exotic isotopes, far from stability with very short $t_{1/2}$. For that, they need [10]: (i) high production rates having the best cross sections which are determined by the target-primary beam[2] (nature and energy) combination; (ii) to be efficient where whatever manipulation (release, transport, ionization, etc.) done to the isotopes must be as efficient as possible; (iii) fast due to the limited and sometimes very short $t_{1/2}$ of the isotopes; and (iv) selective so

[2]The terminology of primary and secondary beam is used, where the primary beam is the beam used to induce the nuclear reactions and the secondary beam is the beam of isotopes produced.

the beams can be successfully separated from unwanted contaminants also produced in the target.

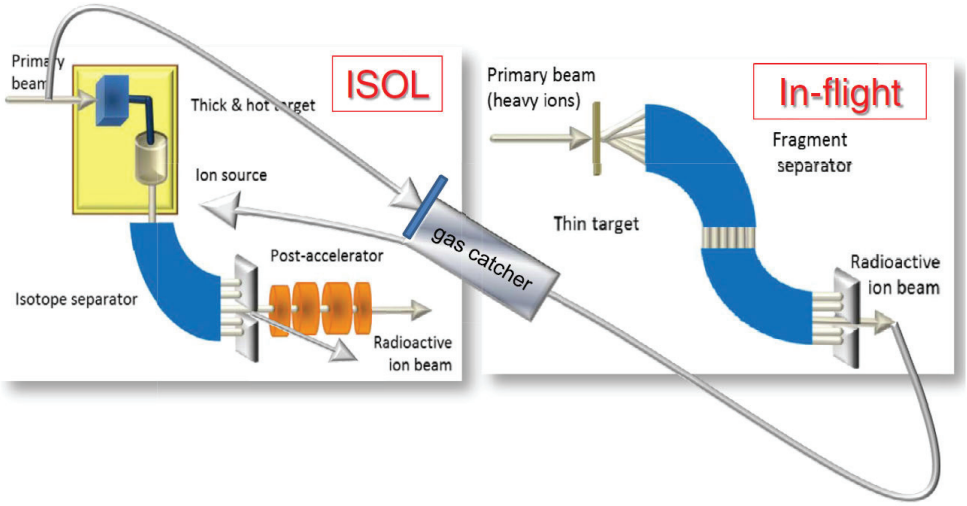

Figure 1.3 – Radioactive ion beam production methods: ISOL vs in flight separation. Reproduced from [10].

In the IFS technique a primary beam of energetic heavy ions (from 100 MeV u^{-1} to 2 GeV u^{-1} [10]) is made to collide with a thin low Z target made of graphite or beryllium. The heavy ions collide with the target, fragmentation and fusion-evaporation reactions take place and the products recoil out of the target with charge, the same momentum and little difference in energy from the original beam [9]. Since the technique doesn't require any other steps, apart from the fragment separation which is done in-flight, it can be applicable to produce very short lived, down to µs isotopes [9].

The ISOL method was born in 1951 when O. Kofoed-Hansen and K.O. Nielsen bombarded an uranium target with neutrons to induce nuclear reactions and extracted krypton isotopes for physics research [17]. Radioactive isotopes from this method are produced by spallation, fragmentation, fission and fusion-evaporation, when bombarding a thick target with a primary beam of energetic particles (photons, electrons, heavy ions, protons, neutrons, etc.). The difference of ISOL to the IFS technique is that the produced isotopes are thermalized in the thick target and need to be extracted, ionized and re-accelerated to be mass separated and delivered for physics experiments. All these extra steps cause delays which only allow for isotopes beams of $t_{1/2} >$ ms, but on the other hand the beams are of ion-optically better quality than the in-flight method [9]. The OnLine word in ISOL name comes from the fact that the extraction and production are made simultaneously and in a continuous way.

On figure 1.4 the ISOL process in terms of isotope release is schematized. When the energetic particles hit the target they induce nuclear reactions which produce isotopes which are thermalized in the bulk of the target material. During the irradiation, the target (which is maintained under vacuum) is kept at high temperatures in order to promote the diffusion

of the produced isotopes to the surface of the material. When reaching the surface, the isotopes have to desorb and evaporate and effuse through the material porosity and through the target container geometry until they reach the ion source and are ionized, mass separated, and this, ready to be delivered for physics experiments. The diffusion and effusion processes can represent high losses where efficiencies can be as low as for e.g. 10^{-6} so in order to keep characteristic diffusion and effusion times lower than the $t_{1/2}$ the choice of material and microstructure is an essential feature for ISOL systems.

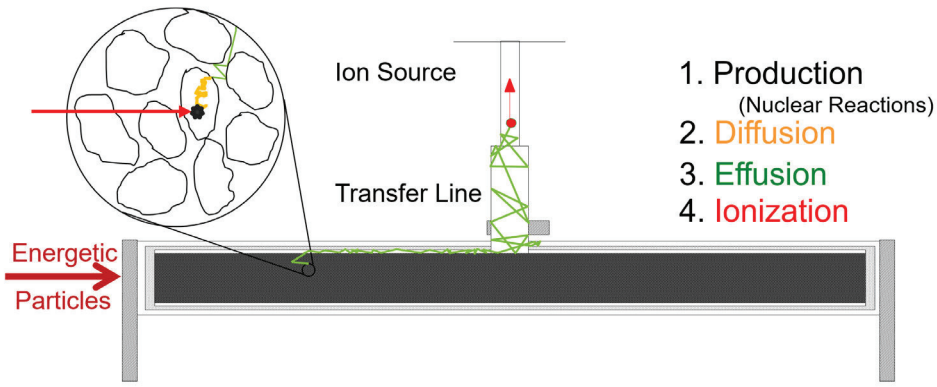

Figure 1.4 – Schematic representation of the ISOL method production, diffusion, effusion and ionization steps.

A very important step in any ISOL method is the mass separation which is done by an analyzing magnet or also called mass separator. This device uses a dipole magnetic field, and through the Lorentzian principle it separates isotopes accordingly to the mass number A - isobars (atoms with the same A but different Z). The quality of a mass separator is expressed by the mass resolving power, R_m [dim]:

$$R_m = \frac{M}{\Delta M} \tag{1.2}$$

where M [ue^{-1}] is the mass of the ions at the focal plane of the separator and ΔM [ue^{-1}] is the full width at half maximum (FWHM) of the same ion beam. Some mass separators have resolutions high enough to separate isobars. The beam can also be ion-optionally treated (cooled and charge bred) and post accelerated from the standard few tens of keV to a few MeV to be used for physics experiments.

ISOL facilities

For any radioactive ion beam production facility the main figures of merit are [18]:

- beam diversity available (number of isotope elements produced and short lived-isotopes);
- beam intensity;
- beam quality in terms of purity (presence of other isotopes) and ion-optical quality

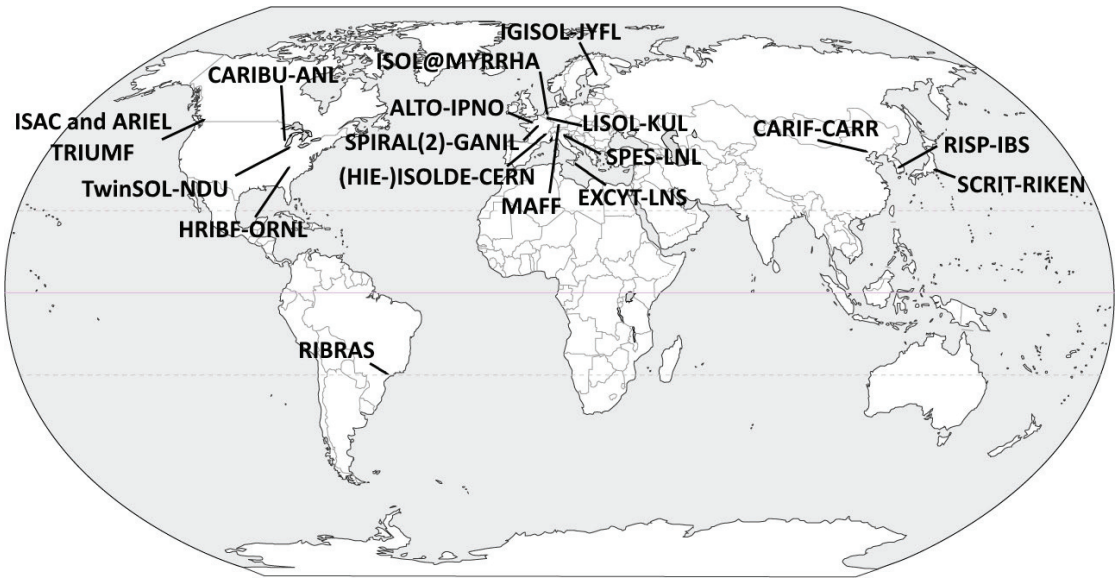

Figure 1.5 – World Map representing the currently existing or under construction ISOL facilities.

(beam emittance);

- facility yearly availability to deliver beams for physics experiments;
- non degradation of beam intensity over time (for ISOL facilities), due to target and ion source ageing.

The main existing ISOL facilities in the world[3], with the largest variety of beams are ISOLDE-CERN in Europe and ISAC-TRIUMF in North America (SPIRAL-GANIL, in Europe, will be part of this group after its ongoing upgrade [19]). Other smaller facilities exist all over the world such as SCRIT-RIKEN[4], IGISOL-JYFL[5], HRIBF-ORNL[6], TwinSOL-NDU[7], CARIBU-ANL[8], RIBRAS[9], ALTO-IPNO [10], MAFF[11], EXCYT-INFN-LNS[12], LISOL-KUL[13] and they are described on [10] and their locations represented on figure 1.5.

GANIL which stands for *The Grand Accélérateur National d'Ions Lourds* (Large Heavy Ion

[3]Since the IFS technique is out of the scope of this work, from here on, only ISOL facilities will be referred. Existent in flight separation facilities can be found on [10].

[4]SCRIT - Self-Confining RI Ion Target ; RIKEN - RIkagaku KENkyusho, Institute of Physical and Chemical Research

[5]IGISOL - Jyväskylä Ion Guide Isotope Separator On-Line ; JYFL - Jyväskylän Yliopiston Fysiikan Laitos (University of Jyväskylä Institute of Physics)

[6]HRIBF - Holofield Radioactive Ion Beam Facility ; ORNL - Oak Ridge National Laboratory

[7]NDU - Notre Dame University

[8]CARIBU - CAlifornium Rare Isotope Breeder Upgrade ; ANL - Argonne National Laboratory

[9]RIBRAS - Radioactive Ion Beam in BRASil

[10]ALTO - Accélérateur Linéaire et Tandem à Orsay ; IPNO - Institut de Physique Nucléaire d'Orsay

[11]MAFF - Munich Accelerator for Fission Fragments

[12]EXCYT - EXotics with CYclotron and Tandem ; INFN - Istituto Nazionale di Fisica Nucleare; LNL - Laboratori Nazionali del Sud

[13]LISOL - Leuven Isotope Separator On-Line ; KUL - KU (Katholieke Universiteit) Leuven

National Accelerator) is a nuclear physics research center in Caen, France which contains the SPIRAL (*Système de Production d'Ions Radioactifs en Ligne* - System for Producing Online Accelerated Radioactive Ions) RIB facility. In this facility a cyclotron accelerated heavy ion beam is made to collide with a thick graphite target causing fragmentation nuclear reactions to produce isotopes [10]. This facility has currently a relatively limited catalog of isotopes, but target and ion source development program called *SPIRAL1 upgrade* is on going in order to expand it [19]. SPIRAL uses a cyclotron to accelerate their beams up to 25 MeV u^{-1}, being currently the highest energy available of all ISOL facilities [10].

TRIUMF stands for TRI University Meon Facility: Canada's national laboratory for particle and nuclear physics and accelerator-based science. It is located in Vancouver, Canada. TRIUMF 500 MeV proton cyclotron provides up to 100 μA protons to one of the two ISAC (Isotope Separator and ACcelerator) target stations [10]. After ISOLDE at CERN, ISAC is the facility with the highest number of beams available for physics thanks to their target and ion source systems, which includes an uranium carbide target and different ionization techniques. TRIUMF has the capability of accelerating their isotopes up to 11 MeV u^{-1} using a superconducting LINAC[14].

As the physics goals get more ambitions and more exotic isotopes with higher intensities are demanded, upgrades to the current facilities and ultimately new ones are necessary. The financial effort to build such facility is to larger to be accomplished on a national level and collaborations on multinational/continental level arise. In Europe this includes the upgrade of facilities like SPIRAL in GANIL (SPIRAL2) and HIE-ISOLDE[15] where both will not only increase the intensity of the primary beam power but also bring more intense and higher energy secondary beams [10]. The construction of SPES at INFN [16] in Italy, ISOL@MYRRHA [17] in Belgium together with SPIRAL2 and HIE-ISOLDE upgrades can be considered as steps towards EURISOL (European ISOL facility) , the ultimate ISOL facility for Europe which will bring together many new developments in ISOL-type facilities [10]. In North America, Canada, TRIUMF is building ARIEL[18], an electron-driven photo-fission ISOL system [20, 10]. In Asia, once called KoRIA, the RISP in IBS[19] facility will be a new ISOL facility to produce RIBs in Korea and China is advancing with plans for CARIF at CARR[20] [21, 10]. All of these facilities are pushing the boundaries of target developments with several hundreds kW (and even a few MW for EURISOL) of primary beam power deposition.

[14] LINear ACcelerator
[15] HIgh Intensity and Energy upgrade for ISOLDE
[16] SPES - Selective Production of Exotic Species
[17] MYRRHA - Multi-purpose hYbrid Research Reactor for High-tech Applications
[18] ARIEL - Advanced Rare IsotopE Laboratory
[19] RISP - Rare Isotope Science Project ; IBS - Institute for Basic Science
[20] CARIF - China Advanced Rare Ion beam Facility ; CARR - Chinese Atomic Energy Commission

ISOLDE at CERN

Originally called *Conseil Européen pour la Recherche Nucléaire* (European Council for Nuclear Research) - CERN, was later changed to the European Organization for Nuclear Research [4] keeping CERN acronym. CERN was founded in 1954 at the Franco-Swiss border close to Geneva, to bring the countries together to study the fundamental structure of the universe for non military purposes. The organization started with only 12 European countries and now counts with 22, where in 2014 CERN expanded beyond the European borders including Israel as its member state and Romania just this summer [4]. CERN houses the largest particle accelerator in the world, the Large Hadron Collider (LHC) with 27 km in circumference and is home to many other accelerators and experiments, as can be seen in figure 1.6.

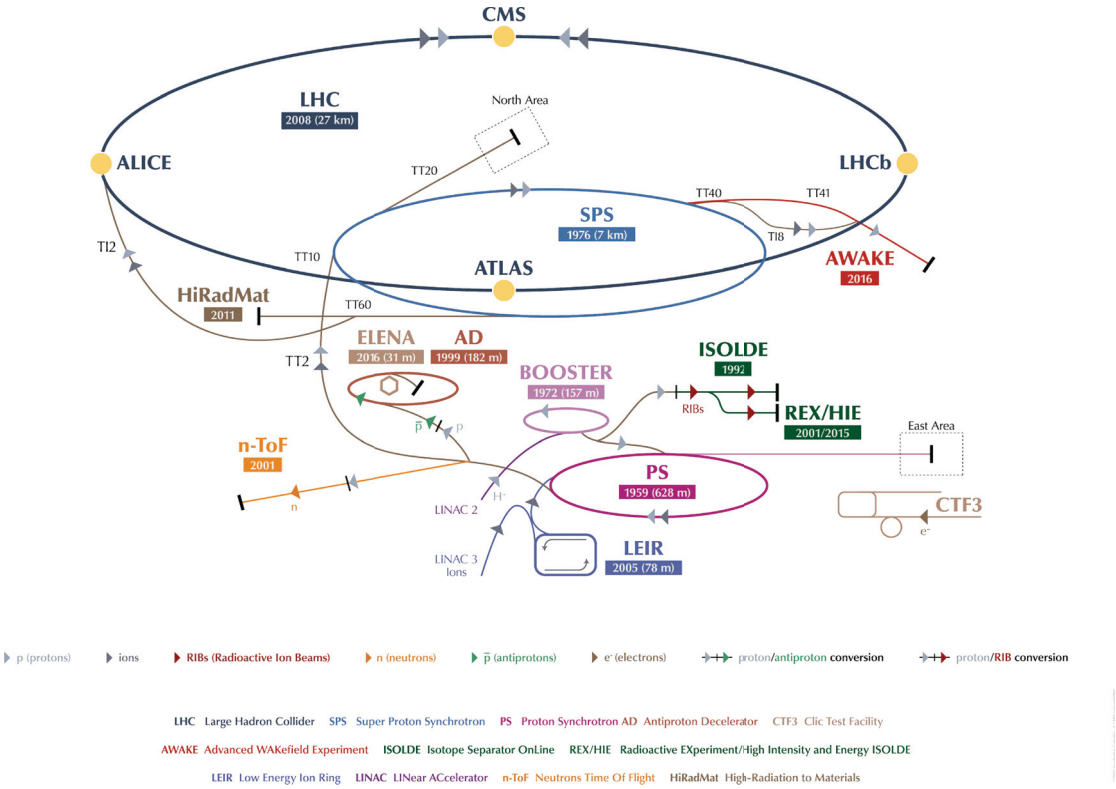

Figure 1.6 – Schematic of the CERN accelerator complex, showing the types of beams provided by CERN as well as the size of its current circular accelerators. Reproduced from [4].

ISOLDE has been part of the CERN accelerator complex for more than 50 years. Its construction was approved by the CERN council in 1964 and had it's first experiment back in 1967 [6, 10]. At the time ISOLDE was served by 600 MeV protons from the synchrocyclotron (SC) for 23 years - the first accelerator built at CERN in 1957 [6]. ISOLDE was in 1992 changed into the proton synchrotron booster (PSB) which served ISOLDE with 1 GeV and after in 1999 [22] upgraded to 1.4 GeV protons with 2 µA of intensity [5]. Currently the ISOLDE facility serves more than 450 scientific users in more than 90 experiments, with a rate of around 50 experiments per year [6]. The facility runs about 8 months (24/7) each year, with around

400 8 h physics shifts per year and technical stops during winter for upgrades and maintenance. The physics very often result in very high quality scientific output as was, for example, the case of 2013 where 3 nature journals articles were published [23, 24, 25].

ISOLDE is currently using 40-50 % of all CERN protons and is able to supply more than 1000 radioactive ion beams from 74 elements ($2 < Z < 92$) with intensities ranging from 10^{-2} to 10^{11} ions /μC from $t_{1/2}$ as low as in the millisecond range.[21]

The PSB sends protons of 1.4 GeV - 2.4 μs length pulses up to 3.3×10^{13} ppp [22] every 1.2 seconds up to an average intensity of 2 μA, into two possible ISOLDE targets stations [22], inducing nuclear reactions of spallation, fragmentation and fission. The target stations are named according to the subsequent mass separators: GPS, general purpose separator and the HRS, high resolution separator . The beams are extracted from the target units at up to 60 keV and both target stations after mass separation connect to a central beamline that serves the full experimental hall (see figure 1.7). While the GPS has a mass resolving power (R_m) of 2200, but is a flexible machine allowing extraction of up to 3 different masses, the HRS can reach theoretically 15000 allowing the separation of some isobars. Following the HRS magnets there is a Radio Frequency Quadrupole (RFQ) Cooler which allows to ion-optically treat the beam by cooling and bunching it to increase the signal to background ratio as required by some experiments [15].

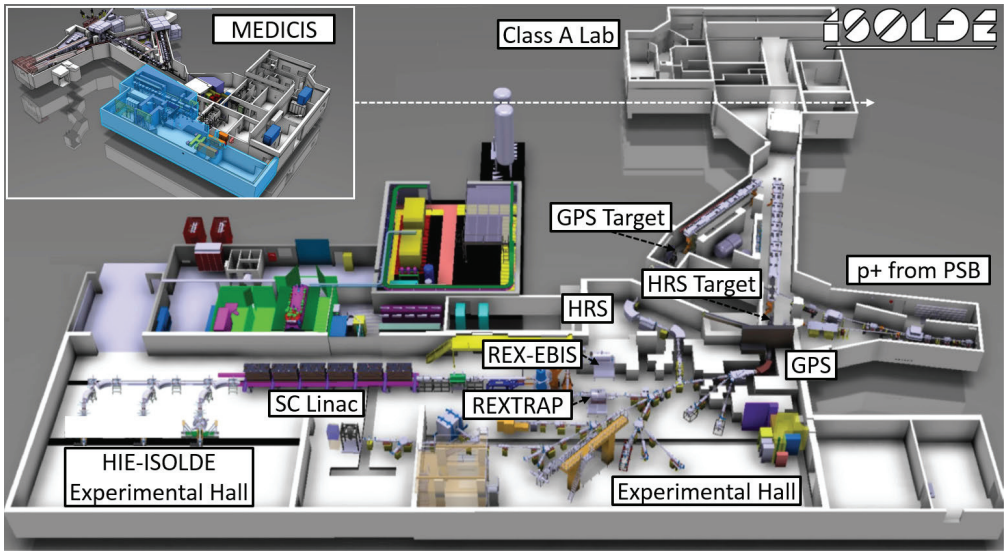

Figure 1.7 – ISOLDE-CERN Facility Layout, including MEDICIS and HIE-ISOLDE.

In the post acceleration chain of ISOLDE (REX[23]-ISOLDE) , there is also a cooler (see figure 1.7) which has the same purpose but uses a different cooling mechanism, the penning trap

[21] The unit [ions /μC] or simply [μC^{-1}] is the normalized unit used for beam intensities at ISOLDE where 1 μC = 6.2×10^{12} protons. If the maximum proton intensity is used, 2.2 μA (2.2 $\mu C s^{-1}$) then the normalized intensities can be converted into [s^{-1}] multiplying by 2.2.

[22] protons per pulse

[23] Radioactive ion beam EXperiment

(REX-Trap) [15]. After cooling and bunching the beams need to be charge state bred in an electron beam ion source (REX-EBIS) which will multiply charge of the singly charge ISOLDE ions coming from the target unit, making the beam ready for post acceleration. REX is made of a normal conducting LINAC and is currently being extended with a superconducting LINAC from HIE-ISOLDE.

The HIE-ISOLDE consists in the upgrade of the old normal conducting post accelerator (REX) as well as the preparation of the facility for the higher intensity and energy primary beams from the PSB. The upgrade for the PSB will ultimately consist in increasing the energy from 1.4 to 2 GeV, the pulses from 3.3×10^{13} to 6.6×10^{13} ppp with a cycle from 1.2 s and the maximum intensity from 2.2 to 8.9 µA [26]. This will directly impact the facility in terms of target station design, where the target deposited power will increase by almost a factor of 6 (from the current 3.1 to 17.8 kW [26]). The post acceleration upgrade, with the installation of high-beta superconducting cavities will allow for secondary beam energies up to $10\,\mathrm{MeV\,u^{-1}}$ (with a mass to charge ratio, $A/q = 4.5\,\mathrm{u}\,e^{-1}$) (from the old $2\,\mathrm{MeV\,u^{-1}}$) [26]. The high-beta cavities are being installed in sets, called cryomodules, and the first set has been commissioned last year to provide the first $4.3\,\mathrm{MeV\,u^{-1}}$ RIB at ISOLDE. This year the second set is already installed and is being commissioned to bring $5.5\,\mathrm{MeV\,u^{-1}}$ RIBs this year [26]. The HIE-ISOLDE project also includes developments in target materials, beam extraction and beam diagnostics [26].

Due to the high energy of the primary beam used at ISOLDE, almost 85 % of the protons traverse the ISOLDE target unit without any interaction. In order to use these protons a new facility coupled to the class A laboratory of ISOLDE, MEDICIS (MEDical Isotopes Collected from ISolde), figure 1.7 inset) was built [27]. In this facility a second target will be transported in a rail conveyor system, irradiated between the HRS unit and the beam dump and brought back to extract the isotopes in an offline separator, for medical research studies. This facility is being commissioned and is expected to separate the first beams for medical isotopes towards the mid of 2017.

1.2 ISOLDE target and ion source system

The target and ion source system (TISS) shown in figure 1.8, is considered the heart of ISOLDE ultimately limits the facility beam intensities and isotopes available. The TISS is made of a target, an ion source and a transfer line which connects the former to the ion source. The TISS or simply called the target unit consists of a water cooled aluminum base plate with a vacuum vessel in order to have high vacuum [24].

The target container (see figure 1.8a) is a 20 cm hollow cylinder with 2 cm internal diameter, made of tantalum which can be resistively heated up to 2400 °C by applying a current up to 1000 A. In this container several different target materials can be inserted accordingly to the isotope to be produced (see subsection 1.2.1, on page 18). The target container is connected

[24] High vacuum normally refers to pressure levels between 10^{-3} and 10^{-7} Pa.

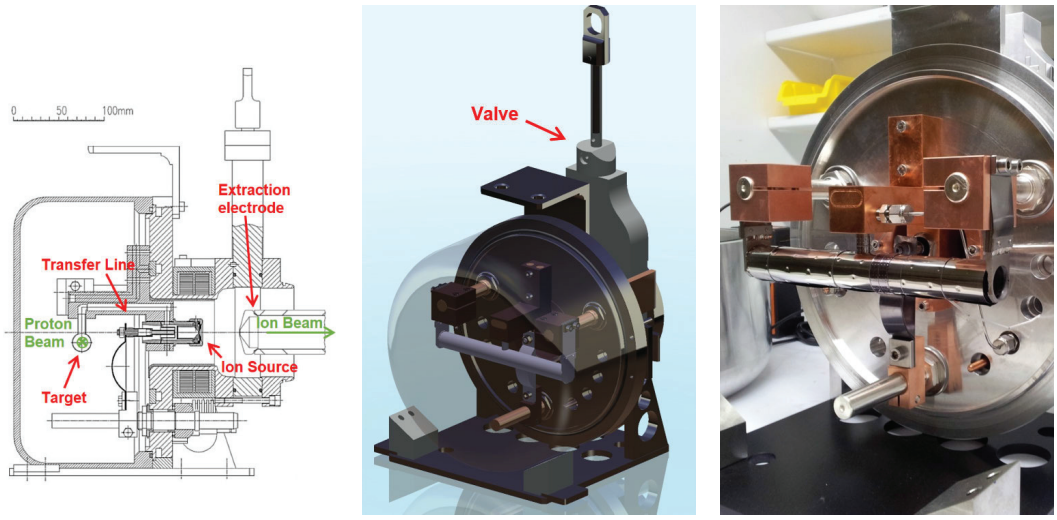

(a) Schematic representation of the ISOLDE TISS.

(b) 3D representation of the ISOLDE TISS.

(c) Photo of an ISOLDE TISS.

Figure 1.8 – Target and ion source system (TISS) of ISOLDE: schematical, 3D representations of the ISOLDE TISS.

to the ion source by a transfer line which can be used to chemically select the isotopes, as will be discussed on subsection 1.2.2, on page 21.

Different ion sources can be coupled to the transfer line which connects to the target container. They can be surface ion, electron impact or laser ion sources. The ion source selection will depend on the isotope of interest and purity intended for the beam as will be discussed on the subsection 1.2.3, on page 23. After the target is mounted in the target station, an extraction electrode (see figure 1.8) is moved close to the ion source in order to extract and accelerate the beam up to to 60 keV.

The TISS can also include a neutron converter where instead of directing the beam of protons into the target, it is directed into a heavy material cylindrical bar (such as tungsten), just below the target [28]. With this process MeV spallation neutrons are produced which irradiate isotropically from the converter bombarding the target and only inducing nuclear fission reactions, reducing by orders of magnitude the contaminants in the beam. However, some protons are scattered when hitting the converter bar and hit the target still producing some contaminants. Another advantage of using the neutron converter is to avoid the stress of irradiating the target with high energy protons reducing target aging [28]. Studies are currently on-going in order to optimize the geometry of such converter in order to avoid/reduce the production of such contaminants [29, 30].

The currently used 23 target materials, the neutron converter, 5 transfer lines and 5 ion sources make room for hundreds of different combinations to deliver the beams required by the ISOLDE physicists which makes the TISS a very complex system.

1.2.1 Target materials

In order to qualify for an ISOL material, the following criteria must be fulfilled [31]: (i) high production cross sections of the isotope(s) of interest, which depends on the material chemical elements, primary beam energy and intensity; (ii) stability at high temperatures, since the target materials are often operated very close to melting point (T_m) to increase effusion and diffusion rates which is highly dependent on temperature (iii) resistance to radiation damage, which can induce physical and chemical changes in the material (iv) and fast diffusion and effusion of the element(s) of interest. The temperature is limited by the material sinterability which will cause grain growth and densification increasing the diffusion distances and effusion times. The material and respective contaminants vapor pressures also limit the target operation temperature, which can create stable beam contaminants or quench the ion source operation.

For the last 50 years of the ISOLDE operation many target materials have been tested and studied as ISOL target materials. A non extensive list of the materials studied at ISOLDE can be seen on figure 1.9. In this figure, the materials are divided into 6 categories (5 of them proposed in [20]) where the last includes the first trials at ISOLDE before 1970 [32]. The "Others" category are mostly experimental/highly specialized materials [20]. The materials in light squares are the ones currently used at ISOLDE while the underlined and bold are the ones which had some kind of recent materials development (including micro or nanostructure developments, which are discussed on subsection 1.3.2, on page 29 and subsection 1.3.3, on page 30). The ISOLDE materials are normally in the form of molten (metals or salts), powder or porous pellets (oxides and carbides) or thin foils (metals). On table 1.1 are the details regarding maximum operation temperatures ($T_{op,max}$), T_m, target thickness (X), and beams produced from the target materials usually operated at the ISOLDE facility.

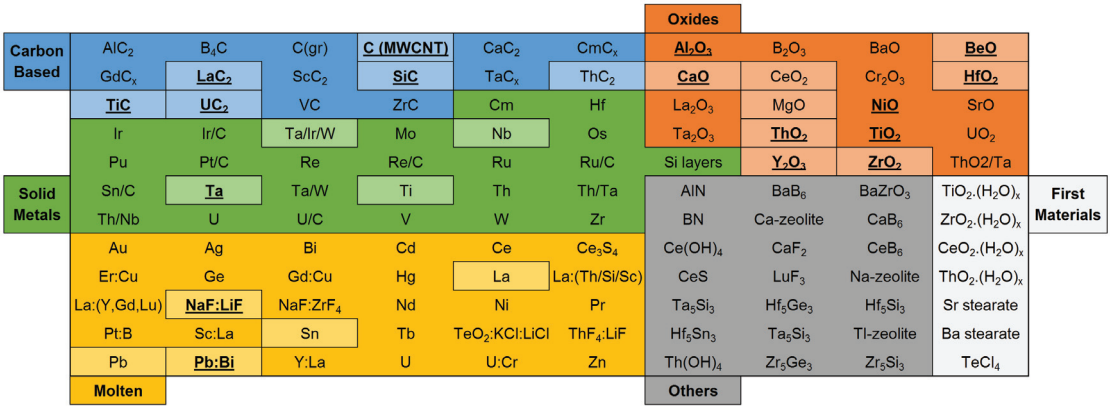

Figure 1.9 – Overview of ISOL studied materials for target application (not extensive). The materials are divided in 6 categories: molten, carbon-based, oxides, solid metals, others and the first trial materials at ISOLDE. The squares represent currently used materials at ISOLDE while the underlined and bold represent materials which had some kind of recent materials development (including microstructure). Data extracted from [20] and [32].

Table 1.1 – List of the materials currently used and available at ISOLDE and respective fraction of targets built, melting point(T_m), maximum operation temperature ($T_{op,max}$), target thickness (X) and beams produced (not extensive). Data extracted from [33, 34, 35, 20] and from ISOLDE target archives.

Type	Material	T_m (°C)	$T_{op,max}$ (°C)	X (g cm^{-2})	Beams produced	No. produced [a] (%)		Ref.
Molten	La	920	1400	124	n-def Cs and Ba	0	6.1	[36, 37]
	NaF:LiF	649	720-740	24.5[b]	^{18}Ne, ^{11}C	0.6		[38]
	Sn	232	1200	128	n-def and n-rich Cd	2.6		[37]
	Pb	328	800	153[b]	Hg	2.6		[36, 37]
	Pb:Bi	398	500	174[b]	Hg, At	0.3		[39]
Solid Metal	Ir/Ta/W	2447	1950	38.7[b]	n-rich Lu, many [c]	1.5	22.7	
	Nb	2470	2050	24[b]	n-def Br, Kr, Rb and Cu	4.7		[40]
	Ta	2996	2200	110[b]	n-rich Li, Be, Hf, lanthanides, many [c]	14.1		[41, 42]
	Ti	1675	1600	16.3	n-def Ca, Sc, K, Mg	2.4		[41, 40]
Carbon-based	C (MWCNT) [d]	3600	1500	4.8[b]	^{8}B	0.6	54.5	[43, 44]
	LaC_2 + 2C [d]	1705 [e]	1900	13[b]	n-def Cs and Ba, Cd, In, Sn	2.1		[45, 46, 47]
	SiC [d]	1650 [e]	1600	21	n-def Na, Mg, F, Al	3.5		[48, 49, 50]
	ThC_2 + 2	2450	2200	50	many [c]	0.9		[48]
	TiC-CB [d]	3067	2000	7	Li, n-def Ca, Na and K	0.3		[this work]
	UC_2 + 2C [d]	2450	2200	50	many [c]	47.1		[51, 20]
Oxides	BeO [d]	2578	1450	30.7	^{6}He	0.6	15.7	[52]
	CaO [d]	2898	800	7.3	He, C, N, n-def Ne and Ar	3.8		[53, 54, 55, 56, 57]
	CeO_2	2600	1300	21.4[b]	n-def Xe, Sb	0.9		[58]
	HfO_2 [d]	2800	1560	14.0	n-rich C	0.6		[58]
	MgO	2800	1500	2.3	n-def Ne	0.6		[53]
	ThO_2 [d]	3050	2100	30	many [c]	0.6		[58]
	Y_2O_3 [d]	2439	1380	28.3[b]	Fe, Cr, Cu, Mn, Co	2.4		[50], page 30
	ZrO_2 [d]	2700	1850	15.1[b]	Mn, Zn, Se, Kr, Cu	6.2		[58]

[a] Estimated from 340 targets that were produced and installed in the ISOLDE frontends since the year 2000. The remaining 1 % are other target materials.
[b] Estimated from the mass of the target assuming a standard ISOLDE container (2 cm diameter).
[c] For more consult the ISOLDE yield database in ref [34].
[d] Submicron or nanomaterial, microstructure engineering for ISOL target application.
[e] Material starts to sublime (vapor pressure 1×10^{-4} Pa).

Liquid targets are very advantageous as ISOL materials due to the very high densities combined with high diffusion coefficients, when compared to solid materials and can be either low melting point metals or salts [37, 38] (see table 1.1). These materials are usually static liquid baths, operated at temperatures slightly higher than their melting point, to keep them liquid. Due to their high vapor pressures the target has usually a *chimney* before the transfer line. This device acts as a condensation point to avoid metal/salt vapors to go into the ion source and ISOLDE beam lines and hinder operation. These targets are operated with a specially designed proton pulse time structure, called staggered mode (STAGISO) . STAGISO protons are distributed in 3 packets in time with intervals of 16-20 µs, less intense than normal pulses (up to 2.2×10^{13} ppp), in order to decrease the shock waves in the target [59]. These shock waves have been known to cause accidents at ISOLDE, splashing liquid metal into the ion source and beam lines [36]. In order to have reduced diffusion distances, to extract exotic isotopes in a liquid target, a novel TISS concept - LIEBE (LIquid Eutetic lead Bismuth loop target for Eurisol) - has been developed [60] and will be tested in 2017. In this concept, a closed circuit of Pb-Bi eutetic is irradiated and forced through a grid to create a shower of 0.4 µm droplets, from which short-lived isotopes will be more easily released [60].

In order to release low vapor pressure element isotopes, solid materials are used since they allow for higher operation temperatures (see figure 1.10). Even though the diffusion constants of solids are much lower than those of liquids, the diffusion distances are reduced from centimeters down to tens of micrometers, or even tens of nanometers. In metals foils, 2 to 30 µm foils can be used while in carbides and oxides reductions down to a few tens of nanometers can be used [54, 55, 49, 61, 51, 20]. Metal powder targets were used before but due to their high sinterability, under pulsed beam irradiation, they were discarded [48]. Oxides are mainly used for noble gas production [20]. Since carbides are one the most refractory materials, they are very suitable to the extreme conditions that ISOL targets require. Uranium carbide (UC_x) is one of the most used target materials at ISOLDE (> 60 % of beam time) and other ISOL facilities. This is due to its refractory properties and to the high isotope production cross-section along the full nuclide chart. Nonetheless, this material after irradiation, presents the highest dose rates of all target materials, which stay active for many decades or even centuries, causing problems for waste management [20].

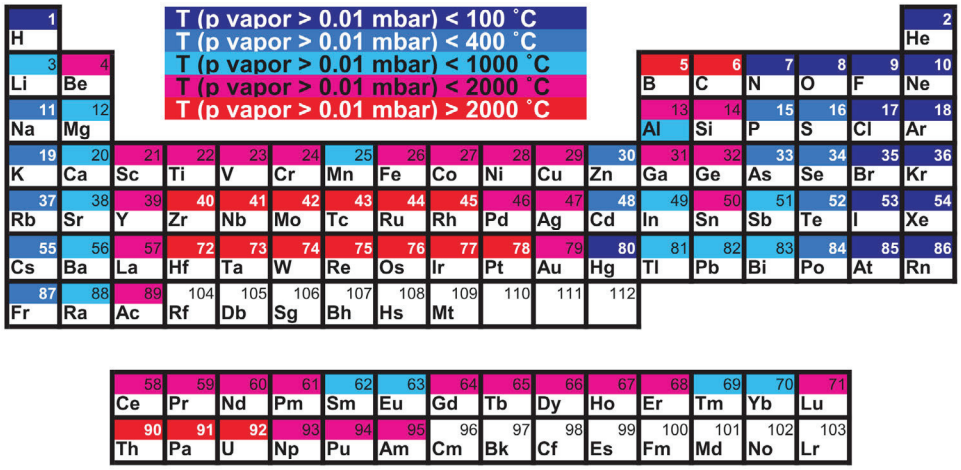

Figure 1.10 – Periodic table representing the temperature at which each element has a vapor pressure of 0.01 mbar. Reproduced from [33].

When designing a target material, chemical reactions with the structural materials of the target (like the Ta from the target container) or with the isotopes themselves must be taken into consideration. For example, oxide targets oxidize the tantalum container so the target material is inserted into a rhenium boat, while carbide/graphite targets are inserted in graphite boats to avoid direct contact and degradation of the Ta container [33, 20]. Some metalic isotopes often react with the target material and form refractory compounds which are not released. An example of that is the release of Sc from Ti metal foils and not from TiC material, since it forms scandium carbide with carbon present in the TiC [34, 62].

In some cases the chemical reactions are welcome and needed to extract isotopes with higher adsorption enthalpies and low vapor pressures, even at high temperatures (see figure 1.10). The reactant can be supplied from the target material itself, which is the case of release of C

isotopes as CO beams from calcium oxide targets: the carbon isotopes react with the oxygen supplied by the target material [43, 54]. A more common way to supply the reactant is through a controlled gas leak in the target, as is done, for example, with boron beams as BF_2 from a multi wall carbon nanotubes (MWCNT) target with a CF_4 leak [43, 44]. Even when the element can be released in its elemental form, this technique can also serve as a beam purification method, creating what is called molecular side bands. This is the case of Ba isotopes which usually come with a very high contamination of Cs. By introducing CF_4 the Ba isotopes form BaF_x which will be separated at higher masses ($A_{Ba} + A_F \cdot x$, where x comes from BaF_x). The Cs, which will not form F molecules, has lower production cross sections at higher masses (shorter lived isotopes) so the intensity of the contamination beam will effectively be reduced.

The primary beam can either be pulsed or in continuous wave (cw) which has a direct impact on the target design. The beams are usually characterized by the type of particle, their energy and integrated intensity which will determine the isotope production cross sections and power deposited. At ISOLDE the beam power is 2.8 kW however if one considers that the proton pulse length at ISOLDE has 2.4 µs, the instantaneous beam power deposition is in the order of 1.2 GW [20]. A pulsed beam brings thermal spikes, shock waves and stresses that need to be taken into account during the target design where passive and/or active cooling solutions have to be found. In general for low energy primary beams (100 MeV or less) the target interaction is higher but so is the deposited power since the targets have a higher stopping power. This brings issues which are usually solved by having thinner and thermally conductive targets with optimized passive or active cooling solutions [20].

Radiation has also an effect on diffusion, which is called radiation enhanced diffusion (RED), which can directly impact the isotope release. Radiation-induced defects such as Frenkel pairs (vacancies and interstitial) are created during irradiation of solids [63]. This is known to significantly increase the diffusion coefficients at low temperatures, where the difference can reach orders of magnitude, when comparing with thermal diffusion coefficients. Although RED was never reported at ISOLDE it was reported at ISAC-TRIUMF where the secondary beam intensity follows a law with the primary beam intensity (I [µA]) between $I^{3/2}$ and I^2 while keeping the temperature constant [64, 65].

1.2.2 Transfer line

As can be seen on figure 1.8, between the target and the ion source there is a tube designated as transfer line that connects both. Apart from the basic function of transferring the newly produced isotopes from the target container to the ion source it can also serve as a beam purification step. In order to achieve purification the transfer line temperature can be changed, for example, by reducing it to trap less volatile elements. The material of the transfer line can also be changed to one that has higher enthalpy of adsorption with certain elements in order to delay them and make them decay before they reach the ion source. The types of transfer lines currently used at ISOLDE can be seen on figure 1.11.

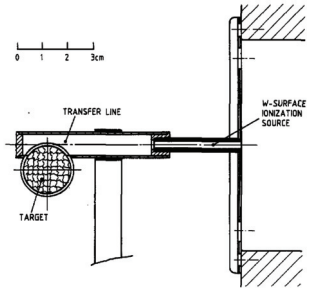

(a) Hot transfer line connected to a surface ion source.

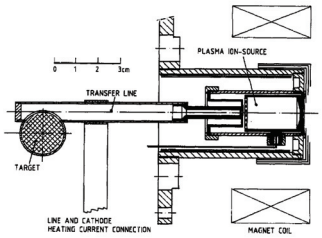

(b) Hot transfer line connected to a electron impact ion source.

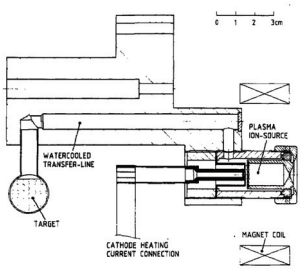

(c) Cold (30 °C) transfer line connected to a electron impact ion source.

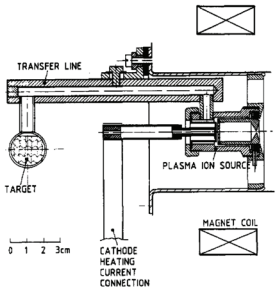

(d) Cold (200-400 °C) transfer line connected to a electron impact ion source.

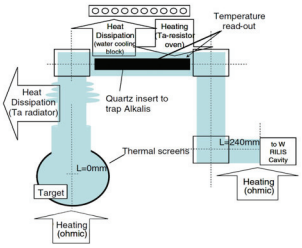

(e) Cold (380-790 °C) quartz transfer line used at ISOLDE.

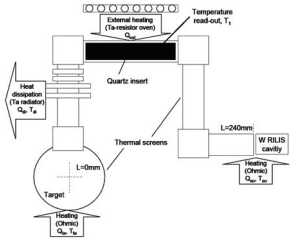

(f) Warm (680-1150 °C) quartz transfer line used at ISOLDE.

Figure 1.11 – Types of transfer line used at ISOLDE. Reproduced from [48], [66] and [67].

The most simple and commonly used transfer lines are the ones represented on figures 1.11a and b, also called the hot lines. They are high temperature transfer lines used for non volatile elements, meaning that they are operated at the same temperature of the target/ion source. The only difference between the transfer lines of figure 1.11a and b is the ion source, which will be introduced later, in the subsection 1.2.3.

Cold transfer lines condense less volatile elements where they are surrounded by water cooled copper blocks, as seen on figures 1.11c and d. In the case where only noble or other volatile molecule beams (such as CO, NO, O_2) are requested, the 30 °C transfer line, on figure 1.11c is used [48]. Where relatively volatile elements are needed but still condensation is mandatory (for high vapor pressure target materials, for example) the 200-400 °C transfer line, figure 1.11d is used [48]. Beams of volatile metals, such as Zn, Cd and Hg can be delivered with this type of transfer line [48]. Cold transfer lines were already used with the first ISOL beam, in 1951, in order to trap non-volatile elements [17].

Transfer lines can also be used to chemically interact with the isotopes coming from the target. Chemical selectivity can be achieved by using materials with which the contaminants have higher adsorption enthalpies, delaying and trapping unwanted elements. At ISOLDE a quartz transfer line, with temperature regulation (see figures 1.11e and f), can be used to

trap alkali contaminants. When comparing with the standard hot transfer line, this line is able to suppress, for example, Rb up to 5 orders of magnitude, Cs by 3 orders of magnitude and Li and K by roughly 2 orders of magnitude [66]. The suppression factors often come with some reduction of the beam of interest, but the obtained beam are of much higher purity. The quartz transfer line at ISOLDE has two versions, the warm transfer line which operates from 680-1150 °C [67] (figure 1.11f) and the cold quartz transfer line operating from 380-790 °C [66] (figure 1.11e). Their selection will depend on the contaminant/beam element of interest.

1.2.3 Ion sources

After passing through the transfer line the isotopes need to be ionized in order to be extracted as a beam and mass separated. Ion sources at ISOLDE produce singly-charged positive ($^{A}_{Z}X^{+}$) or, occasionally, negative ions ($^{A}_{Z}X^{-}$). At ISOLDE, in total three different ionization mechanisms are used: surface ionization, laser ionization and electron impact ionization. The figure 1.12 contains a periodic table, extracted from the ISOLDE yield database [34], with the all the ionization mechanisms used at ISOLDE for each element. The ionization efficiency, to positively charge an element, will depend mainly on the ionization potential (W) of the element which is the total energy necessary to remove one electron from an outer shell. In ISOL type facilities the main requirements for an ion source are efficiency, selectivity and rapidity, all in order to minimize losses [68].

Apart from the three main mechanisms, radio frequency discharge (RF), plasma ion sources also exist. A prototype Helicon ion source which ionizes volatile elements and molecules through this mechanism in a magnetized plasma was successfully tested at ISOLDE [69]. These sources have the advantage of operating cold (no hot surfaces) which increases the survivability of volatile molecules.

Group	1	2		3	4	5	6	7	8	9	10	11	12	13	14	15	16	17	18
	1A	2A		3B	4B	5B	6B	7B	8B			1B	2B	3A	4A	5A	6A	7A	8A
Period									Ion source:										
1	1 H								+	Surface	-								2 He
2	3 Li	4 Be							hot	Plasma	cool			5 B	6 C	7 N	8 O	9 F	10 Ne
3	11 Na	12 Mg								Laser				13 Al	14 Si	15 P	16 S	17 Cl	18 Ar
4	19 K	20 Ca		21 Sc	22 Ti	23 V	24 Cr	25 Mn	26 Fe	27 Co	28 Ni	29 Cu	30 Zn	31 Ga	32 Ge	33 As	34 Se	35 Br	36 Kr
5	37 Rb	38 Sr		39 Y	40 Zr	41 Nb	42 Mo	43 Tc	44 Ru	45 Rh	46 Pd	47 Ag	48 Cd	49 In	50 Sn	51 Sb	52 Te	53 I	54 Xe
6	55 Cs	56 Ba	*	71 Lu	72 Hf	73 Ta	74 W	75 Re	76 Os	77 Ir	78 Pt	79 Au	80 Hg	81 Tl	82 Pb	83 Bi	84 Po	85 At	86 Rn
7	87 Fr	88 Ra	**	103 Lr	104 Rf	105 Db	106 Sg	107 Bh	108 Hs	109 Mt	110 Ds	111 Rg							

* Lanthanides	*	57 La	58 Ce	59 Pr	60 Nd	61 Pm	62 Sm	63 Eu	64 Gd	65 Tb	66 Dy	67 Ho	68 Er	69 Tm	70 Yb
** Actinides	**	89 Ac	90 Th	91 Pa	92 U	93 Np	94 Pu	95 Am	96 Cm	97 Bk	98 Cf	99 Es	100 Fm	101 Md	102 No

Figure 1.12 – Periodic table representing the currently available elements at ISOLDE and respective ionization mechanisms. Reproduced from [34].

Surface ion source

Surface ionization is an efficient technique to ionize elements with low ionization potential ($W < 7$ eV) such as the alkali, alkaline-earth, rare earths (which include the lanthanides), some molecules and others, as seen on figure 1.12. As schematized on figure 1.13, when a low W element atom collides with a hot metal surface of a high work function (Φ) it loses one electron. The surface is at high temperatures to reduce desorption of the ions/atoms. The ionization efficiency (ϵ_{is} [%]) is given by the Saha-Langmuir formula [48, 50]:

$$\epsilon_{is} = \frac{n_+}{n_+ + n_0} = \left(1 + Ce^{\frac{W-\Phi}{kT}}\right)^{-1} \tag{1.3}$$

where n_+ [cm^{-2}] is flux of ions leaving the surface and n_0 [cm^{-2}] the flux of neutrals leaving the surface, C_g [dim] is a statistical constant regarding the ions and atoms quantum states, k [J K^{-1}] is the Boltzman's constant and T is the absolute temperature. As seen on figure 1.11a the geometry of a surface ion source is rather simple: a tube. Using a Ta ionizer, with Φ = 4.0 – 4.8 eV [35] K, Rb, Cs and Fr are ionized with about 90 % efficiency, while with a Re which has a higher work function (Φ = 4.7 eV [35]) can ionize Ba (ϵ_{is} = 10 %) and Ra (ϵ_{is} = 50 %) [48]. With W ion sources (Φ = 4.3 – 5.2 eV [35]), heated to very high temperatures (2400 °C) using the "hot-cavity-effect" [70]), Li, Na, Al, Ca, Sc, Ga, Sr, Y, Tl and the lanthanides can be ionized with 5 % < ϵ_{is} < 50 % [48]. This effect happens in surface ion source with a tube geometry (used at ISOL facilities) where the equation 1.3 needs to be complemented for the number of wall collisions before ionization (which multiplies the ϵ_{is} by a few times and also for the trapping probability of the ion inside of the plasma potential well. [70, 68].

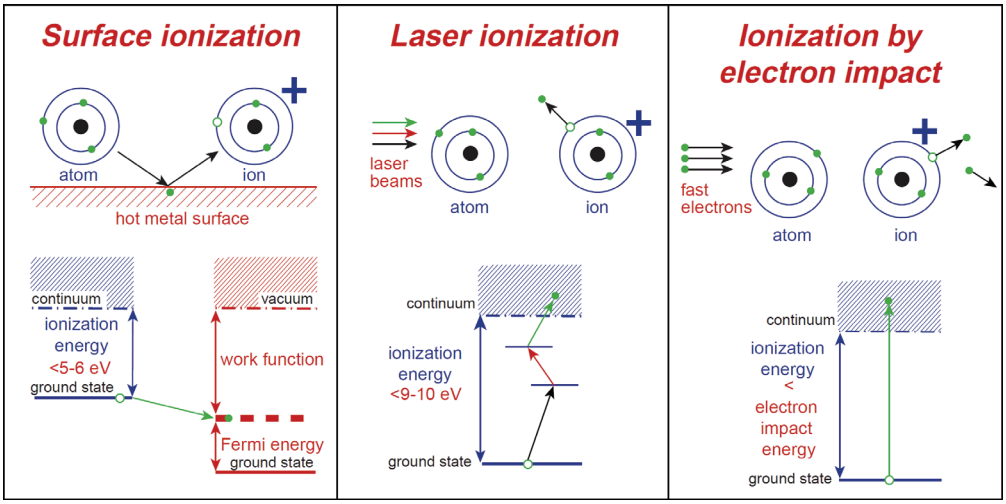

Figure 1.13 – Ionization mechanisms used at ISOLDE: surface, laser and electron impact ionization. Reproduced from [71].

When the work function of the ionizing material is lower than the element electron affinity (E_A) then the material gives an electron, negatively ionizing the element. This type of ionization is suited for elements with high electron affinity, such as the halogens, as can be seen

on figure 1.12 [48]. Ion sources with a pellet of LaB_6 have been successfully used at ISOLDE to deliver beams of Cl, Br, I and At with $\epsilon_{is} = 10$ %. Other negative ion source materials have been proposed such as GdB_6, Ir_5Ce and W(BaOSrO) [72]. The GdB_6 tube geometry ion source has been tested in 2014 and 2015 at ISOLDE.

Laser ion source

The resonant ionization laser ion source (RILIS) at ISOLDE, is used when ionization of elements up to $W < 9-10$ eV with high selectivity is needed. More than 50 % of the beam time at ISOLDE is conducted using RILIS, with more than 35 chemical elements which are possible to ionize by laser [73] (see figure 1.12). As schematized in figure 1.13, the atoms are ionized by interaction with a set of lasers that stepwise excite the outer shell electron to the continuum. Since these steps (also called laser scheme) are specific for each element, high selectivity is possible. RILIS is normally coupled with the Ta surface ion source operated at lower temperatures to reduce surface ionized isobaric contaminants. Since the residence time of the atoms is in the order of a few hundred μs to achieve good ionization, high repetition rate (> 10 kHz) lasers are necessary [15]. Efficiencies for laser ion sources are generally around 10 %.

Even though the laser ion sources are very selective surface ionized contaminants are always present. In order to deal with such contaminants two techniques have been proposed: the LIST [74, 75] (Laser Ion Source and Trap) and the ToF-LIS [76] (Time-of-Flight Laser Ion Source) . In the LIST technique, right after the Ta ion source a device which contains a repeller electrode followed by an RFQ ion guide is installed [74, 75]. As schematized on figure 1.14, this allows to separate the laser ionizing and surface ionizing regions. The surface ionized isotopes will be repelled by the positively charged electrode while the neutral atoms will continue and be laser ionized inside the LIST and guided through the RFQ to the extraction. Using this source, surface contaminants were suppressed by up to a factor 1×10^4 [74, 75]. Knowing that the ionization of surface contaminants is continuous in time, the ToF-LIS aims at making use of the very short laser ionized isotope pulses created by the pulse lasers. Since the time-of-flight of the laser ions is highly affected by the potential created in the ion source by the heating current, using higher resistance materials results in shorter pulses as shown in figure 1.14b for laser ionized Ga from two different ion source materials, for example [76]. Using a fast beam gate, a window could be open just enough to catch these pulses and closed when there is no laser ions formed, suppressing the contaminants.

Electron impact ion source

The electron impact or plasma discharge ion sources are very efficient but have very little selectivity, since they can ionize basically any element this brings many isobaric contaminants. They are well suited to ionize noble gases which can't be ionized by any of the other ion sources, due to the very high ionization potentials. They are very often used for volatile beams, for which they are suited with a cold transfer line (as schematized on figure 1.11c)

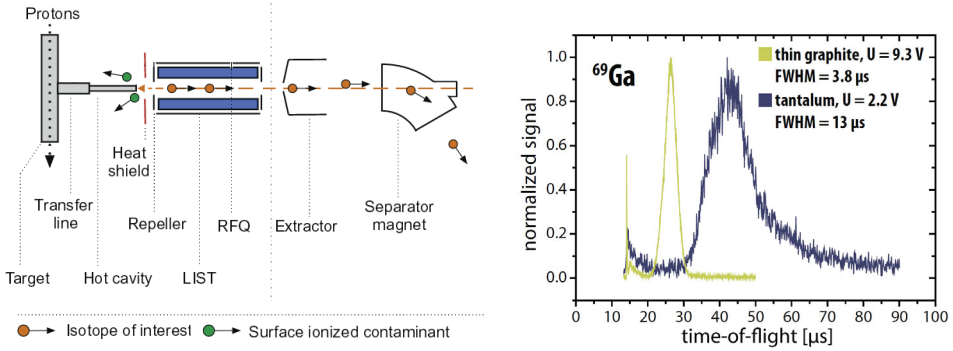

(a) LIST (Laser Ion Source and Trap) principle.

(b) ToF-LIS (Time of Flight Laser Ion Source) pulse length comparing with standard ion sources.

Figure 1.14 – Contaminant suppression techniques for laser ionized element beams: LIST and ToF-LIS. Reproduced from [75] and [76].

which enhances the TISS selectivity. The electron impact source used at ISOLDE is called FEBIAD, acronym of Forced Electron Beam Induced Arc Discharge, and was developed in the 70s [77]. Using the thermionic principle a metallic cathode is heated to emit electrons which are accelerated towards an anode, up to a couple of hundreds of Volt in a small chamber. The electrons are further deflected in this few cm chamber through the use of an axial magnetic field [48]. The ionization then happens by electron impact where the electrons collide with the neutral isotopes coming from the transfer line, ionizing them.

An improved version of the FEBIAD ion source was developed at ISOLDE in the 2000s and was called VADIS - Versatile Arc Discharge Ion Source [78]. In this source the ionization geometry was optimized and the graphite materials present in the first were replaced by metallic ones [78], reducing the CO outgas. With the changes this source has shown 5 to 20 times higher ionization efficiencies [78] and is currently the version used at ISOLDE. Tests have been done and are currently ongoing to use laser ionization inside of a VADIS. This combination is called Versatile Arc Discharge Laser Ion Source (VADLIS) and has the objective of improving the ionization efficiency and selectivity of metals in the VADIS as well as providing in-source spectroscopy tools for the ISOLDE physicists [79].

1.3 Engineered microstructure ISOLDE target materials

ISOL is a complex method which involve many steps, from the moment the isotopes are produced until they are delivered for physics studies. These induce losses, where the delivered beam intensity, also referred to as yield (Y [μC^{-1}]) depends on:

$$Y = Y_{Prod} \cdot \varepsilon_{rel} \cdot \varepsilon_{is} \cdot \varepsilon_{sep} \cdot \varepsilon_{transp} \text{ with } Y_{Prod} = \sigma \cdot j \cdot N_t \cdot n_C \tag{1.4}$$

where Y_{Prod} [μC^{-1}] is the total number of isotopes produced normalized to the primary beam, also known as in-target production and depends on:

- σ [mb], the isotope production cross section , which depends on the type of particle (neutron or proton for ISOLDE), its energy and the target material nucleus and can be simulated at the GeV primary beam energy level, quite accurately with codes such as FLUKA[25] or ABRABLA[26];
- j [cm^{-2}], the primary beam flux which is directly proportional to the Y_{Prod} and is usually the way taken by most ISOL facilities in order to increase their secondary beam intensities, which becomes very challenging due to heat deposition issues;
- N_t [dim], number of atoms exposed to the beam , equivalent to the material density, which can be increased but a certain porosity must be kept to allow for isotope effusion;
- n_C [μC^{-1}], number of protons per μC ($6.242 \times 10^{12}\ \mu C^{-1}$)

The other parameters from equation 1.4 are efficiency parameters which account for losses during the release process and beam manipulation and they are:

- ϵ_{rel} [%], the release efficiency which depends on diffusion and effusion times which are unique for each combination of isotope element-target material-microstructure where both processes are thermally activated. Diffusion refers to isotope release from the bulk of the material while effusion is the diffusion of the atoms through the vacuum: target porosity, transfer line up to the ion source. Re-diffusion into the target material or reaction with any surface of the TISS components is possible. It is in the ϵ_{rel} that, by far, the highest losses exist, as will be discussed below.
- ϵ_{is} [%], the ion source efficiency, already discussed in the subsection 1.2.3, on page 23.
- ϵ_{sep} [%] and ϵ_{tranp} [%] are respectively the mass separation and transport efficiencies , normally close to 100 % and not limiting Y.

While other components for the TISS are well developed, during the past 50 years of ISOLDE, little to no regards were taken on influence of the microstructure on the isotope release as well as it's stability (sinterability) over time. It was only around 10 years ago that more attention was given to the target microstructure influence on the release of isotopes [49, 61].

1.3.1 Release efficiency: diffusion and effusion

Diffusion

The diffusion is a thermally activated process, where the diffusion coefficient (D [$m^2\,s^{-1}$]) has an Arrhenius relation with temperature (T [K]):

$$D = D_0 e^{-\frac{Q}{RT}} \tag{1.5}$$

[25] FLUKA stands for FLUktuierende KAskade and is a very versatile particle physics Monte Carlo simualtion code [80, 81].

[26] Code to calculate nuclear reaction cross-sections using the ABLAsion-ABRAsion model [82, 83].

where D_0 [$m^2\,s^{-1}$], Q [$J\,mol^{-1}$] and R [$J\,K^{-1}\,mol^{-1}$] are respectively the diffusion pre-exponential factor, activation energy and the ideal gas constant.

Unless we are in presence of a highly reactive element or one with high adsorption enthalpies with the TISS materials, the release is usually diffusion limited where by correcting for the other efficiency factors of equation 1.4, the ϵ_{rel} can be approximated by:

$$\epsilon_{rel} = \frac{Y}{Y_{Prod}} = \frac{3}{\pi}\sqrt{\frac{\mu}{\lambda_i}} \text{ with } \mu = \frac{\pi^2 D}{r^2} \text{ and } 2\mu \lesssim \lambda. \tag{1.6}$$

where μ [s^{-1}]is the diffusion time constant [s^{-1}] and r [m] is the target material grain radius.

There are two ways to essentially decrease μ, either increase of the temperature (to increase D, see equation 1.5) or decrease of the particle r. The temperature increase is the approach taken in the last 50 years in ISOL facilities where the target is operated with the highest possible temperature. This brings melting/sintering and target degradation which rapidly decreases the beam intensities over time. The decrease of the particle/grain size was never considered in the past, at ISOLDE. Powders with particle sizes below 1-5 µm were discarded since it could bring fast sintering and so closing of the porous structure of the target materials [84].

Even though recent results have shown that decreasing the particle size results in better Y in most of the cases [49, 54, 50, 20, 51, 57], researchers in the 70s had a valid point with the fast sintering of the small grained materials. In order to have fine particle/grain target materials either the targets have to be operated at lower temperatures or suitable sintering hindering mechanisms have to be employed. Such mechanisms can be, for example, doping the material which will form precipitates that will slow down the grain boundary advancement or hinder self diffusion coefficients. Or the inclusion of a second non-sinterable inert phase can reduce the coordination number of the particles hindering or even stopping sintering.

It has been tried before to increase N in equation 1.4, to increase Y_{Prod}, by using high density uranium carbide ($\rho = 13.2\,g\,cm^{-3}$) instead of the porous and tens of micron UC_x ($\rho = 3.5\,g\,cm^{-3}$) normally used at ISOLDE [20]. Even though Y_{Prod} is almost 4 times higher, the Y extracted for all the isotopes was more than a factor of 2 lower than the standard UC_x intensities. The almost non-existent porosity makes release only possible by diffusion in the solid where even though the Y_{Prod} is large the ϵ_{rel} is much smaller resulting in lower yields.

According to equation 1.6 by keeping the temperature constant and decreasing the particle size by a factor of 10, a factor of 10 should be gained in Y (if effusion doesn't change drastically). It was with this concept in mind that, over the last years, many sub(micron) and nanometric material developments were carried out [49, 54, 50, 20, 51, 46, 57]. Apart from higher release efficiencies nanomaterials have as well the advantage of smaller densities, which directly translate in less radioactive waste. In the next subsections the studies done on a microstructural/sintering point of view on (sub)micrometric and nanometric ISOLDE target materials will be reviewed.

Effusion

Effusion happens right after diffusion, where the isotope species desorb from the material surface and diffuse through material porosity and TISS geometry (transfer line) until the ion source is reached. The effusion mean delay time (τ_v [s]) can be approximated by [85]:

$$\tau_v = \frac{1}{\nu} = n_{wc}\left(\tau_a + \tau_f\right) \tag{1.7}$$

where ν [s^{-1}] is the effusion time constant, n_{wc} [dim] the number of wall collisions, τ_f [s] is the mean flight time between 2 wall collisions and τ_a [s] is the mean sticking time for a wall collision which depends on:

$$\tau_a = \tau_0 e^{-\frac{\Delta H_a}{RT}} \tag{1.8}$$

where τ_0 [s] is a pre-exponential factor , ΔH_a [$J\,mol^{-1}$] is the adsorption enthalpy which depends on the element-surface combination number of collisions.

As can be seen, similarly to diffusion, effusion has also an Arrhenius dependence on the temperature and it becomes the controlling mechanism for reactive elements (high ΔH_a). For effusion it is also important to consider all the surrounding TISS materials which with the isotopes may interact, such as transfer line and ion source materials where an interesting review is made in [43].

1.3.2 (Sub)micrometric microstructure target materials

In order to reduce sintering, instead of powders, fibers can be used reducing the number of contact points. Commercially available CeO_2, ZrO_2, TiO_2 and ThO_2 fibers of micrometric thickness have been reviewed by U. Köster, et al. [58]. All fibers were of similar microstructure and an example, ThO_2 fibers, is represented in the microstructure of figure 1.15a. From these the ZrO_2, ThO_2 and CeO_2 are still used at ISOLDE as target materials, however no long term temperature stability tests in respect to microstructure were done.

Foam microstructures (similar to the one presented in figure 1.15b) have been developed at the HRIBF-ORNL facility by nitride, carbide and/or oxide infiltration coating of carbon foams [86]. At ISOLDE, S. Fernandes studied several microstructures of SiC, from foam samples (pores of few hundred µm, see figure 1.15b) to fully dense, and from submicron average particle size (0.6 µm) to a few micrometer [49]. The release studies have shown that the release of Na, Mg and Be was higher in the case of the 60 % porous submicrometric SiC particle samples than in the case of fully dense ones and even from the foam SiC [49]. These results led to the test of a prototype target material, with a full batch of pressed 0.6 µm particle size SiC pellets (microstructure represented on figure 1.24 on page 41) which were pre-sintered in an argon atmosphere at 1650 °C for 1 h. This prototype delivered Mg and Na yields which were a factor of 4-9 higher than previously operated 10 µm SiC targets [49, 50]. This unit also

allowed for the extraction of the very short lived, never seen before ^{21}Mg with $t_{1/2}$ = 122 ms.

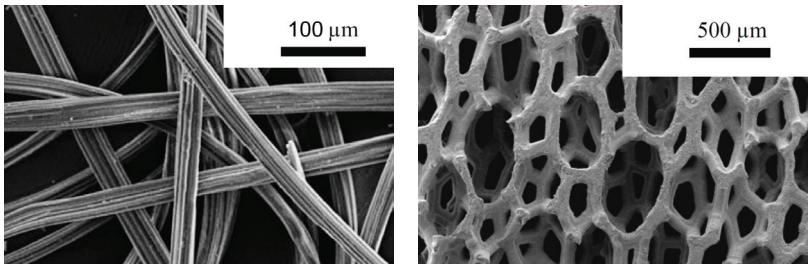

(a) ThO_2 micrometric fibers tested at ISOLDE [58].

(b) SiC foam microstructure tested for release at ISOLDE [49].

Figure 1.15 – Different microstructured materials tested at ISOLDE: ThO_2 fibers and SiC foam. Reproduced from [58] and [49].

Alumina fabricated with different microstructures made by different processes and from different powders (tape casting, anodizing, slip casting, cold pressing and others) was studied for release by S. Fernandes [49]. It was found that for release of Na and Mg, the samples with the highest porosity and lowest grain size were the ones with the highest release efficiency [49].

Using a novel technique named ice-templating, M. Czapski created SiC and Al_2O_3 samples with tailored porosities which ranged between 1.1 to 86 µm in size as spherical and/or elongated shape [87]. An example of such porous structures is represented on figure 1.16a for SiC. These samples were submitted to irradiation in order to study if the pore structure can mechanically sustain the irradiation damage, however the results haven't been published yet. These microstructures are to be used as spallation targets in the future for HIE-ISOLDE beam energy and intensity upgrade [87].

BeO, with around 1-2 µm, was another micrometric material tested at ISOLDE, to provide very intense beams of ^{6}He through the use of a neutron converter [61]. Before being used as a target prototype the microstructure was tested at the maximum operation temperature for 24 h in order to check for sintering, where the final BeO microstructure can be seen on figure 1.16b.

1.3.3 Nanostructured target materials development

Y_2O_3 targets were also tested at ISOLDE, for the first time [50]. Nanometric yttria was commercially acquired and heat treated to 1380 °C in order to assess the stability of the nanostructure [56]. These particles were agglomerated in a plate like structure, as shown on figure 1.17a, which after heat the agglomerates turns into a micrometric/submicron target as shown of figure 1.17b. During the heat treatment the surface area changes from 17.8 to 0.6 $m^2 g^{-1}$, changing the nanostructure into a micrometric one [56]. Nonetheless, this target provided higher intensities on Co and Cu beams than other targets and also many isotopes of Cr and Fe which haven't been seen before at ISOLDE [50]. This material revealed decreasing yields over

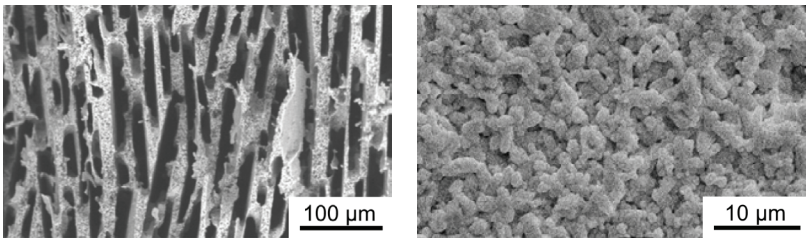

(a) SiC microstructure obtained by ice templating [87].

(b) BeO microstructure used as target material at ISOLDE [52].

Figure 1.16 – Different microstructured materials developed at ISOLDE: SiC ice templating structure and micrometric BeO. Reproduced from [87] and [52].

time, down to 20 % of the initial value over 120 h of operation, likely due to the microstructure degradation [50].

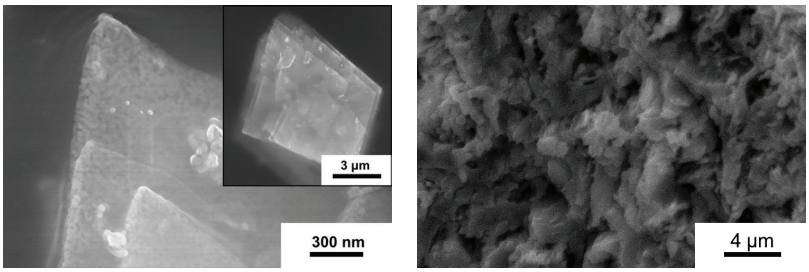

(a) Yttria as supplied.

(b) Yttria heat treated at 1380 °C.

Figure 1.17 – Yttria nanomaterial tested at ISOLDE before and after heat treatment. Reproduced from [56].

Calcium oxide has been used at ISOLDE as a powder target, since 1985 to produce beams of C (as CO), N (as N_2), Ar, Ne and He [54]. However, even though the beam intensities provided from these targets were good, they were known to either reduce over time or even be low from the beginning. Since this was a problem suspected to come from the microstructure (sintering), either during its production and/or operation, material investigations were done [55]. The new mesoporous nanometric CaO material produced, shown on figure 1.18a was developed from the decomposition of $CaCO_3$ in vacuum ($CaCO_3 \rightarrow CaO + CO_2$) and has with about 30 nm particle size and 12 nm pore size [55] [54, 55]. Sintering studies were done following the specific surface area evolution (see figure 1.18b for an example), in order to assess the right operation temperature for the ISOLDE target in order to keep a stable nanometric CaO structure [55]. It was reported that surface diffusion controlled the sintering kinetics at low temperatures while at higher temperatures volume diffusion was the dominating mechanism for CaO sintering [55]. A conservative operation temperature was defined to maximum of 800 °C in order to keep the nanostructure stable over time and to account for irradiation effects, contrarily to before where there was no temperature limit [54]. This was the first target nanomaterial operated at ISOLDE. Even though a lower temperature was used, high yields

of Ar, Ne, He and CO beams were extracted from this target and is now a standard unit at ISOLDE [54].

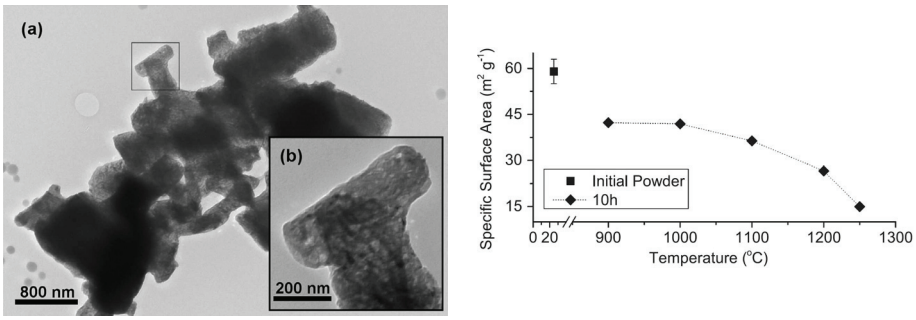

(a) Mesoporous nanometric CaO material developed for ISOLDE.

(b) Sintering behaviour, in terms of specific surface area of the nanometric CaO.

Figure 1.18 – Mesoporous nanometric CaO material developed for ISOLDE and its sintering behaviour. Reproduced from [54].

An interesting fact was noticed in the isotope release time structure of nanometric CaO, which was also seen in all the following nanomaterials at ISOLDE. As exemplified, on figure 1.19c and d, the isotope release is apparently longer from nanometric form (figure 1.19b) than micrometric form (figure 1.19a) of the same solid compound [57]. The term apparently longer is used since the yields obtained are usually much higher than those of micrometric materials with "fast release": in the example of figures 1.19c and d, while a yield of $2.0 \times 10^6\,\mu C^{-1}$ was obtained for the micrometric target, one of $3.7 \times 10^7\,\mu C^{-1}$ was obtained for the nanometric one. This is likely due to the fact that the release is not any longer only limited by diffusion, due to the small particle sizes of the target material. In fact, the release is likely limited by both diffusion and effusion due to the complex nanometric pore network which will multiply by orders of magnitude the number of atom collisions before they are extracted. This effect has also been reported for UC_x materials [20].

Nanometric CaO has also been used to unexpectedly produce radioactive argon while cold, meaning without any temperature supplied by the target oven [57]. The beams provided by this cold target were only a factor 2 to 3 lower than the ones with the target at 800 °C, which doesn't follow classical diffusion laws predicting that the fall should be orders of magnitude in beam intensity [57]. In this report the release was attributed to the spallation recoil momentum from the nuclear reaction, during production, which could eject the isotopes from their production positions. The recoil energy was estimated to be 9.2 ± 1.8 keV which would make a projected ion range of 10.9 nm, more than enough to escape the nanometric CaO particles [57].

Uranium carbide is usually developed by mixing micrometric forms of UO_2 and graphite, pressing them into pellets and heat treat them up to 2000 °C to promote the carbothermal reduction of the UO_2 into UC_x ($UO_2 + 6C \rightarrow UC_{2-x} + (2+x)C + 2CO$, where $0 \leq x \leq 1$). By milling down the UO_2 to a median size of 160 nm and replacing the graphite by multiwall carbon

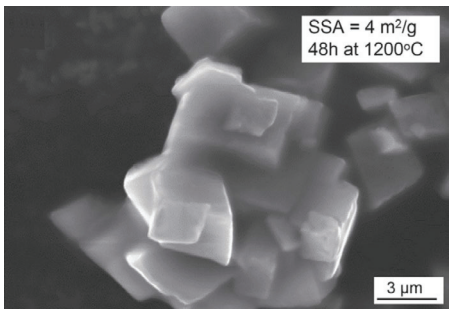

(a) Old CaO micrometric material used at ISOLDE.

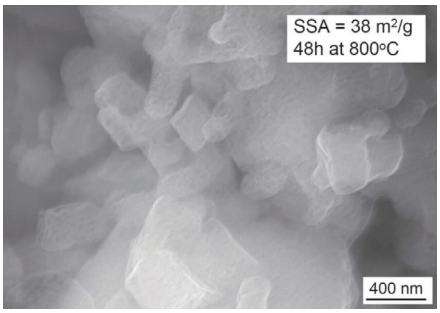

(b) Newly developed nanometric CaO for ISOLDE.

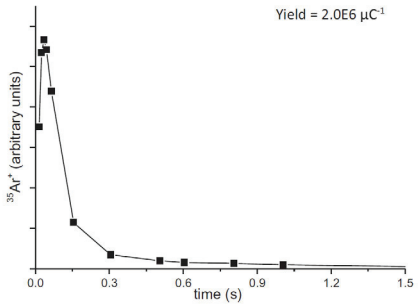

(c) Release profile of ^{35}Ar from micrometric CaO targets.

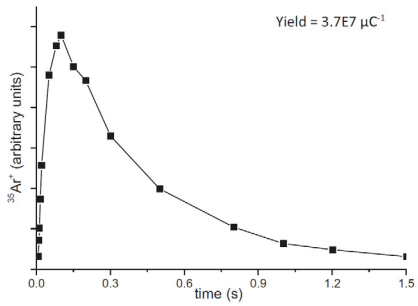

(d) Release profile of ^{35}Ar from nanometric CaO targets.

Figure 1.19 – Calcium oxide microstructure used before at ISOLDE and the newly developed nanometric CaO in [55] and respective release profiles. Reproduced from [57].

nanotubes (MWCNT) and following the same thermal treatment procedure, a nanocomposite was obtained [51, 20]. This yielded an extremely stable structure at high temperatures, which was able to deliver short lived isotope intensities (^{30}Na - $t_{1/2}$ = 48 ms) over more than 12 days without any decrease. Such isotope in standard UC_x targets would reduce by almost two orders of magnitude [20, 51] in the same period of time. The beams delivered by this target were all of higher intensity than the standard uranium carbide and stable over time [51]. A similar composite, but developed through a different process was developed by SPES and tested at the HRIBF-ORNL [88]. The isotope release results were inferior to those of standard (micrometric grains) target (tested in the same conditions), contrarily to what was obtained at ISOLDE. Comparison is difficult between the two nanometric UC_x targets since the material processing, TISS and also primary beam energy were all different. The low yield results were attributed to possibly low efficiency ion source due to target outgassing or possibly high effusion times [88].

A LaC_2-MWCNT nanocomposite was also developed at ISOLDE, following the studies of Biasetto et al. [89] at INFN where an LaC_2-carbon nanotubes (CNT) nanocomposite was developed by mixing La_2O_3 with different volume ratios of graphite and CNT. Using a similar process to the UC_x nanocomposite and $La(OH)_3$ and MWCNT as starting materials, a LaC_2-

MWCNT was produced [45], and tested online [46] to produce beams of Cs and Ba. The same apparently long release profiles were seen with high release efficiencies, however this prototype was not able to deliver as high intensities as the molten La target [46]. This is thought to be due to the very low densities (when comparing to La molten targets) and mainly the limitation in operation temperature at which the LaC_2 starts to sublime.

The last nanometric target to be tested at ISOLDE was developed to extract boron beams, a highly refractory and reactive element which was never before extracted in ISOL-type facilities. Due to the very low vapor pressure and high reactivity of this element, its extraction as $^{A}BF_2$ was seen as a very efficient mechanism [43]. After release studies and in order to have a low as possible diffusion times, pressed pellets of MWCNT were used as target material. The huge surface area of MWCNT also helps to promote the reaction of the CF_4 with the B and extract it [43, 44].

1.4 Sintering

Sintering is "a processing technique used to produce density-controlled materials and components from metal or/and ceramic powders by applying thermal energy", as simply defined in S.-J. Kang's book [90]. In sintering usually a powder compact is turned into a monolith, and particles into grains by the action of temperature, reducing the internal interface area. The main driving forces for sintering are: the curvature radius of the particle surfaces or/and an external applied pressure or/and a chemical reaction [91]. In the absence of the latter two, the surface free energy (E_s [J]) which depends on the system surface area, will drive the sintering process [91]:

$$E_s = \gamma S_A = \gamma \frac{3V_m}{r} \tag{1.9}$$

where γ [$J\,m^{-2}$] is the specific surface energy, S_A [m^2] is the total surface area of the system, V_m [m^3] is the molar volume and r [m] is the particle radius. From equation 1.9 in can be seen that the reduction of the particle size will bring a higher surface energy and so a higher sintering driving force.

The sintering driving force is the reduction of the E_s which depends on the γ and on S_A. As schematized on figure 1.20a, while the change in interfacial energy ($\Delta\gamma$) is due to densification, the change in surface area (ΔS_A) is because of coarsening (particle growth) [90].

For sintering to occur, atoms have to change positions and they do so according to the chemical potential of the zone they are in: they will move from zones with higher chemical potentials (sources: such as concave curvature) to zones with lower chemical potential (sinks: like convex surfaces). This movement can happen accordingly to at least 6 different mechanisms which lead to bonding and neck growth between the particles (see figure 1.20b) [91, 90]. These mechanisms can either be nondensifying mechanisms, bringing coarsening, such as surface diffusion, lattice diffusion from the particle surfaces and vapor transport (in figure

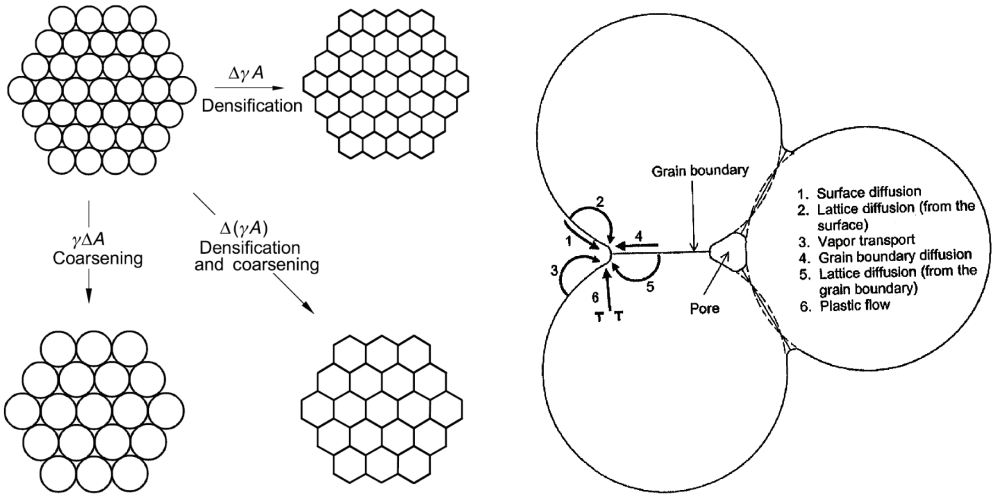

(a) Sintering basic phenomena of densification and coarsening under the sintering driving force.

(b) Basic sintering mechanisms.

Figure 1.20 – Sintering basic phenomena (sintering and densification) due to driving force and main sintering mechanisms. Reproduced from [90, 91].

1.20b, mechanisms 1, 2 and 3) or densifying such as grain boundary, lattice diffusions from the grain boundary and plastic flow (mechanisms 4,5 and 6).

Sintering involves solid state diffusion, where the flux of atoms (J_x [$J^{-1}\,s^{-1}$]) depends on the concentration (C [m^{-3}]) gradient:

$$J_x = -D\nabla C \tag{1.10}$$

where D [$m^2\,s^{-1}$] is the diffusion coefficient, a material property and dependent on element and host matrix combination. Imperfections in crystalline structures, also called defects, also influence diffusion. Since the type (vacancies, interstitials, respective pairs, etc.) and quantity of such defects controls matter transport they control the processes such as sintering and grain growth [91].

There are many variables affecting sintering, making it a complex phenomena to model and even though in many studies the same chemical compound is used, totally different sintering results can be obtained [90]. Sintering depends on the raw material powder characteristics as well as on its chemistry. The powder size (and size distribution), agglomeration degree, shape as well as its composition, stoichiometry, homogeneity and impurities all play a very important role in the sintering process. During sintering the temperature and respective heating and cooling ramps, time, pressure and atmosphere influence the sintering rates and mechanisms.

There are two main categories of sintering: solid state sintering and liquid phase sintering. Solid state sintering has been described so far while liquid phase sintering happens when a liquid phase is present in between the powder particles during the sintering process. Liquid

phase sintering allows for a fast densification at lower temperatures and easy control of the microstructure at the cost of, for example, mechanical properties [90].

In the next subsection the different stages of sintering will be detailed. This will be followed by a literature review of important sintering aspects for this work: sintering of porous ceramics, constrained sintering and irradiation influence on sintering. A review of the literature TiC sintering studies is done on the article included in section 4.1 (page 109) where the master sintering curve concept is also introduced.

1.4.1 Sintering stages

Sintering is usually divided into three sequential stages for simplicity: initial, intermediate and final stages. In each stage, for polycrystalline materials and for modeling purposes, the microstructure is well defined in terms of geometrical structures (see figure 1.21) and each one represents a defined range of relative densities.

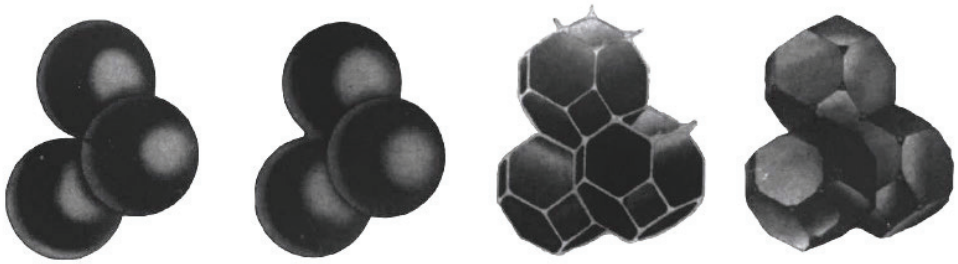

(a) Before sintering. (b) Initial stage sintering. (c) Intermediate stage sintering. (d) Final stage sintering.

Figure 1.21 – Geometrical models representing the beginning, initial, intermediate and final stages of sintering. Reproduced from [92].

Initial stage

In the initial stage the major differences in surface curvature are eliminated by neck formation (from figure 1.21a to b). The neck formation is generally accompanied by densification and shrinkage of the structure with densifying mechanisms (see above). The initial sintering kinetics can be modeled by two spheres of radius a, representing the particles, where [91]:

$$\left(\frac{x}{r}\right)^m = \frac{H}{r^n}t \quad \text{or} \quad \left(\frac{\Delta l}{l_0}\right)^{m/2} = -\frac{H}{2^m r^n}t \tag{1.11}$$

where x [m] is the neck radius, $\Delta l/l_0$ [%] is the linear shrinkage, t [s] is time, m and n are exponents depending on the sintering mechanism and H [s^{-1}] contains the geometrical and material parameters of the powder which also depends on the sintering diffusion mechanism.

The initial stage sintering lasts until the neck is about 0.4 - 0.5 of the particle radius and it is characterized for systems with $0.5-0.6\rho_t$ (theoretical density) and linear shrinkage from 3 to 5 % [91]. It is also limited to specific surface area reductions of down to 50 % [93].

Intermediate stage

The geometrical model to describe intermediate stage sintering kinetics was proposed by Coble [92] and describes particles as being tetrakaidecahedra, where 3 particles are represented on figure 1.21c. This geometrical model assumes that pores are continuous, cylindrical and contained along the edges of the tetrakaidecahedron. It is assumed that the pore geometry is uniform and only densifying mechanisms operate, since the chemical potential is the same on every pore surface [91]. It is assumed that densification can only occur by pore shrinkage in cross section, until they become unstable and isolated. This stage characterizes systems up to $0.9-0.95\rho_t$. Since plastic flow is not expected to be present in a ceramic systems, only lattice and grain boundary diffusion mechanisms are expected. In this model the densification rate is predicted to depend on the inverse to the cube of the grain size for lattice diffusion and on the inverse to the fourth power for grain boundary diffusion [91].

Final stage

The final stage sintering is characterized by densities higher than $0.95-0.98\rho_t$. The pore isolation in the grain corners, referred in the intermediate stage, marks the beginning of the final stage, as represented on figure 1.21 [91]. In this stage, it is assumed that the pores will shrink and disappear and ideally, densities of 100 % are reached.

1.4.2 Sintering of porous ceramics

In early stage sintering of porous ceramics there is some coarsening through surface diffusion or vapor transport which is followed by heavy densification with limited grain growth. These which greatly influences the subsequent microstructure evolution and rest of the sintering process [91]. Usually grain growth (coarsening) only becomes more dominant towards intermediate and final stage sintering, whereas densification and loss of surface area is dominant in the early stage sintering, due to the high surface energies associated with the high porosity.

The open porosity is expected to slowly convert into closed porosity, which process only depends on the packing uniformity. For heterogeneus packed powders the closed porosity may even increase and then only finally decrease as the sintering time and density increases [91]. This is mainly related with the sintering of agglomerates. The thermodynamics of pore evolution states that in order for the pore to shrink, there must be a decrease of the free energy (decrease of surface area) larger than the increase of the free energy due to more grain boundary area creation [91]. This energy equilibrium is intrinsically related with the number of grains surrounding the pore, where for large number of grains around a pore will dictate that

the pore grows while a low number will make the pore shrink. As a result, poorly compacted powders, with larger pores than its particles will be difficult to densify.

The kinetics of grain growth in porous ceramics is complex but it can be discussed in a qualitative way. After neck formation in two isolated spherical particles, the boundary is very stable since for it to move changes in interfacial energy would be needed [94], however coalescence still happens in porous ceramics. Greskovich and Lay [94] have proposed a simple two sphere model, assuming surface diffusion where they explain qualitatively this phenomena, which is schematically represented on figure 1.22a. The two particles, which differ in size, will create a curved grain boundary which curvature radius is inversely proportional to the size ratio between the large and the small particles. The larger the curvature is, the greater the driving force is for it to move towards the center of its curvature [94] which in the end will result in an elongated grain. The mechanism is further demonstrated on figure 1.22b, where 6 particles form 2 elongated grains.

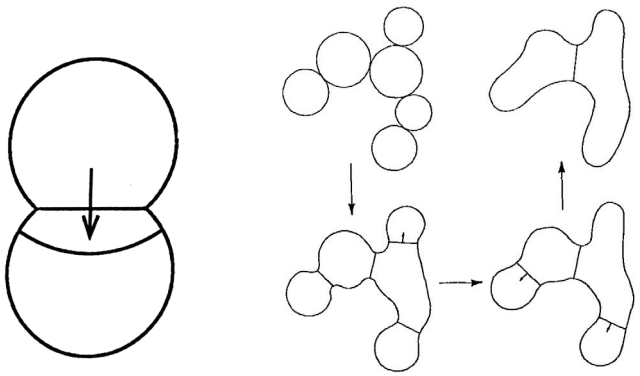

(a) Two sphere model for coarsening of porous ceramics.

(b) Sintering of 6 particles by the Grescovich and Lay mechanism.

Figure 1.22 – Sintering mechanisms proposed by Grecovich and Lay for coarsening of porous ceramics. Adapted and reproduced from [94] and[91].

1.4.3 Constrained sintering

Every sintering system is under some kind of constrained sintering where, for example, inhomogeneities such as agglomerates, cause stresses which will directly affect the sintering behaviour [91]. However in the literature, constrained sintering refers to when a sintering matrix is constrained by a second non-soluble phase that reduces densification rates. The second phase can either be a dispersion of a second phase or a rigid substrate. In extreme cases the stresses created can either induce cracks or film delamination, but normally takes place as localized porosity [95].

Dispersion of a second phase powder can be either be done by mixing it homogeneously or

by coating powders (sintering particles are surrounded uniformly by a second phase). A composite densification rate has much lower densification rates than predicted from a simple rule of mixtures, accounting for the respective volumes and densification rates of the two phases [91, 96]. In some cases, for high volume fractions of the second phase (> 20 %) densification is even completely halted [91]. This is mainly due to the presence of transient stresses between the two phases due to differential sintering or due to the percolation of one of the phases that will form a network and inhibit sintering.

Transient stresses happen with solid inclusions in the sintering matrix, since shrinkage will happen at different rates. Hydrostatic (compressive) and tangential stresses will be generated on the inclusion surfaces and will be relieved by viscous flow or creep. Models such as Scherer's can calculate the stresses generated up to additions of 15 vol.% inclusions [91].

For higher fractions of the second phase, percolation is likely to happen, which means there will be enough particle-particle contacts of the second phase to form a continuous second phase network. In order to have percolation, assuming equiaxial particles in a random arrangement, a volume ratio of 16 % is necessary, which is known as the percolation threshold [91]. After this threshold, if the second phase particles bond an form a rigid skeleton it won't be possible to densify the composite [91]. The exception lies on systems which form liquid phase and/or where the inclusions do not form bonds to have a rigid network. If this is the case, higher second phase volumes can be accommodated before the sintering rates are affected, where the coordination number of the first phase particles will likely control the sintering rate.

Apart from densification, grain growth can also be severely hindered by the presence of a second phase in high volumes [97]. In a study done by French et al. [97] a 50 vol.% Al_2O_3 - ZrO_2 composite, which have limited mutual solubility, was produced and the sintering mechanism was hypothesized to be grain boundary and interphase-boundary diffusion which limits sintering in percolated structures. In this study grain growth was up to 20x less than in the independently sintered phases.

There are some examples (not extensive) in the literature of constrained sintering due to addition of high volumes of second phases [96, 97, 98, 99, 100]. In a study done by Jonghe et a. [96] addition of 27 vol.% 12 µm SiC in 0.4 µm ZnO hindered its densification rates by almost 2 orders of magnitude, due to tensile hydrostatic stresses which opposed sintering stresses and reduced densification rates. Numerical simulations have also been attempted in this field where the size ratio between the second and primary phase particles, as well as agglomeration state of the second phase, influences were studied in terms of densification rates [98]. Yan et al [98] found that the smallest second phase particles added (1/3 or the particle size of the primary phase), in a deagglomerated state and with the largest volume ratio had the strongest effect. Here, it was seen that highest number of second phase-primary phase contacts created by the homogeneously dispersed second phase particles, was the main reason for sintering hindering.

1.4.4 Irradiation influence on sintering

Even though the effect of radiation on sintering will not be studied in this work, it is important to review what has been done in the field. Sintering is in fact controlled by diffusion and it is known that radiation affects the crystalline structure increasing the defect concentration through which diffusion processes are governed. In 1961, Aitken proposed the following mechanisms of radiation interaction with sintering [101]: (i) radiation enhanced diffusion (RED) (production of vacancy-interstitial pairs) (ii) alteration of the number and locations of sinks for vacancies to migrate, (iii) vaporization and re-condensation of non-volatile atoms by recoil processes (iv) enhanced surface mobility. Aitken estimated that in the order for RED to be seen in linear shrinkage during sintering (bulk diffusion controlling mechanism) fine particle sizes (at least smaller than tens of microns) have to be used [101]. In this process the type of radiation used will also have a great effect since the number of displacements, after the primary knock-on, will greatly determine the type of defects and respective concentration [101].

As discussed in the subsection 1.2.1 on page 18, while a material is being irradiated vacancies and interstitial are created at constant rates which can cause RED [63]. If the temperature is high enough these defects anneal by direct recombination or migrate to sinks [63]. In steady state, since the temperature will affect the mobility of such defects it will also affect the thermodynamic balance between these two processes (defect creation and annealing). This will determine the defect concentration which is directly proportional to the diffusion coefficients [63]. RED is only valid at temperatures where the defects are mobile. Under irradiation, at low temperatures, the radiation induced defects concentration will exceed that of the thermal vacancy concentration and diffusion will be temperature independent. This is schematized on figure 1.23. A study done by Dienes and Damask [63] shows experimental proof of this phenomena on irradiated brass, where the defects are mobile at −30 °C.

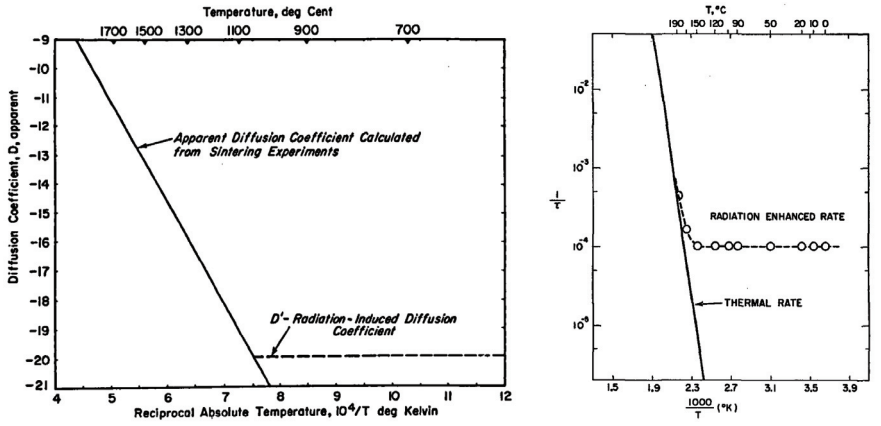

(a) Radiation enhanced diffusion concept.

(b) Experimental proof of radiation enhanced diffusion.

Figure 1.23 – Radiation enhanced diffusion. Reproduced from [101] and [63].

Sintering under irradiation conditions has been reported for 80 µm diamond dust at 50 °C with

1 MeV neutrons at a flux of 10^{20} cm^{-2} [102, 103]. Grains of Al_2O_3 with 40 µm are also reported to sinter at the same temperature with 6×10^{18} cm^{-2} [102, 103]. However, no references are made regarding sintering rates or final densities obtained. In another study [104] Al_2O_3 has been reported to sinter at $T > 150$ °C, where 20 % specific surface area (SSA) reductions have been reported, whereas the non-irradiated sample could only achieve the same SSA reduction at 1100 °C.

A SiC target has been used online and post-irradiation studies were made on the material [49]. Figure 1.24a shows the SiC fracture microstructure submitted to 1600 °C for 1.5 h (material before irradiation) while in figures 1.24b and c shows the fracture microstructures after irradiation in the center and in the rim of the pellet [49]. In this study the particle growth from 0.6 µm (average) on figure 1.24a to 2 to 5 µm in the microstructure of figure 1.24 was attributed to enhanced sintering due to RED. The microstructure of the pellet rim (figure 1.24c) which was exposed to less protons (due to the beam Gaussian profile) has more angular grains which are reported to be due to radiation grain breakage [49]. The difference between the microstructures in figures 1.24b and c is likely due to presence of RED sintering in the microstructure of figure 1.24b, which was exposed to a higher flux of protons than the microstrucure of figure 1.24c.

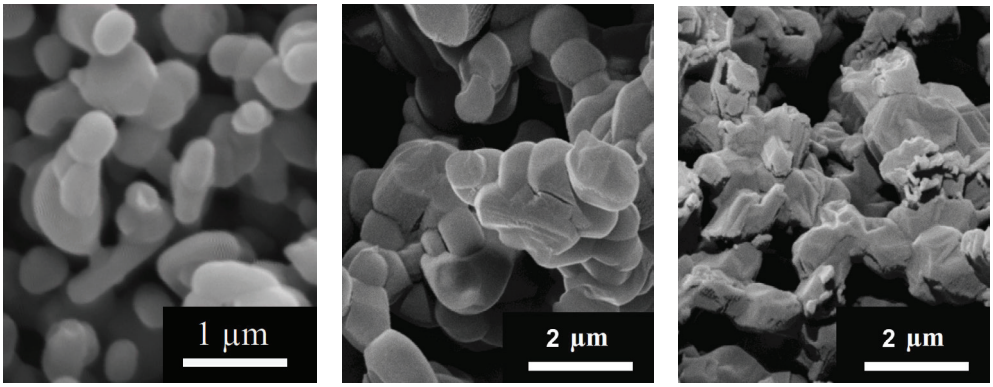

(a) SiC before irradiation.

(b) SiC after irradiation - center of the pellet.

(c) SiC after irradiation - rim of the pellet.

Figure 1.24 – SiC target microstructure post irradiation analysis after being operated at ISOLDE. Adapted and reproduced from [49].

S. Fernandes [105] submitted Al_2O_3 and Y_2O_3 to proton irradiation at 72 MeV with an integrated intensity of 824 µA h and a SiC-Carbon nanotube composite for 3546 µA h. Practically all samples have shown signs of RED assisted sintering and other radiation induced changes. It was found that Al_2O_3 contrarily to the studies shown before, that there was no noticeable RED, likely due to the high temperatures used, 1272 °C, where thermal diffusion dominates. However at lower temperatures (783 °C) there was a noticeable RED assisted sintering when compared to non-irradiated samples at the same temperatures. Furthermore depending on the sintering mechanism the activation energy for sintering during irradiation was found to be 5 to 10 times lower than for non-irradiated Al_2O_3 [105].

As curiosity, a Science article from 1965 [102], reports sintering of lunar particles into rigid porous structures by solar radiation. The author points out that due to the high levels of radiation coming from the sun and the temperatures on the surface of the moon (150 to 350 K or from -123 to and 77 °C), over long times would cause RED and so sintering of the particles. Another study [103] confirms *radiation sintering* to be the mechanism responsible for the rigid adhesion of the moon particles. A threshold of 6×10^{14} cm^{-2} flux of fast neutrons for the mechanism to occur is established, which is equivalent to 60 days of solar wind in the temperature conditions of the moon.

As discussed above there are not many studies on sintering under irradiation conditions. Additionally, no studies regarding nanomaterials sintering under irradiation conditions were found. Nonetheless the material ability to resist radiation damage is defined by how effectively it can remove vacancies and interstitials in similar quantities [106]. Nanomaterials have shown very good radiation damage resistance due to their high proportion of grain boundaries to bulk. In standard materials the interstitials defects created by the irradiation move to the surface causing swelling while the vacancies group into voids causing embrittlement [106]. In nanomaterials, the many grain boundaries can capture interstitials and "release" them back to heal a vacancy as schematized on figure 1.25 [106, 107]. Due to this fact, nanomaterials are being considered for application in high radiation environment such as future nuclear fusion power plants [106].

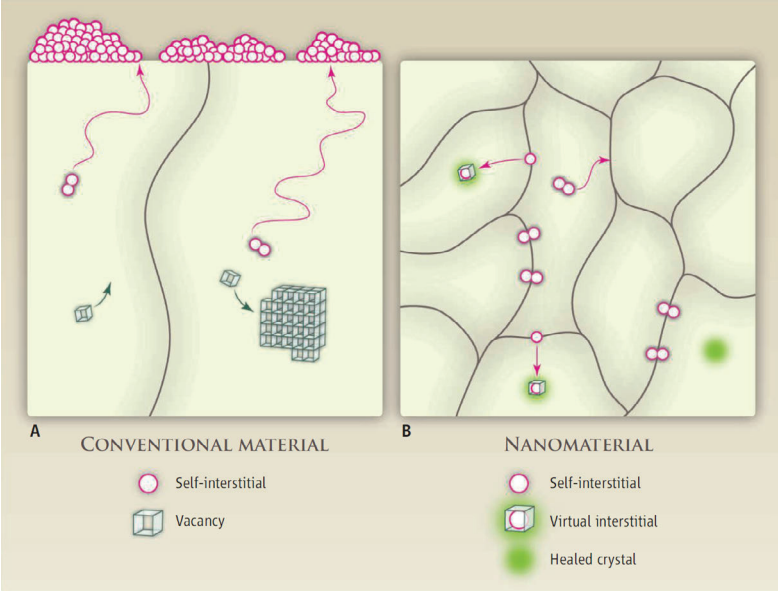

Figure 1.25 – Radiation damage in nanomaterials (self-healing) vs in normal materials (swelling and embrittlement). Reproduced from [106].

2 Experimental Methods

Contents

2.1 Methods 44

2.1.1 Attrition milling 44

2.1.2 Thermal treatments 45

2.1.3 Residual gas analysis 47

2.1.4 Dilatometry 48

2.2 Material characterization techniques 50

2.2.1 Particle size distribution by laser diffraction 50

2.2.2 Nitrogen physisorption isotherms 51

2.2.3 Scanning electron microscopy 52

2.2.4 Mercury Intrusion Porosimetry 54

2.2.5 X-ray powder diffraction 55

2.3 Isotope release studies 57

2.3.1 Offline methods: gamma spectroscopy 58

2.3.2 Online methods: tape station 58

In this section the experimental methods used during this work will be described. However, the raw materials used and the full production method for the nanocomposites will not be described here since it is described in detail in the Materials and Methods section of the article included in section 3.2 on page 69. Furthermore, since this thesis chapters are composed of separate articles, the specific relevant experimental methods are just briefly described. Here, we introduce the methods, which were used during the production and characterization of the TiC-C nanocomposites as well as respective prototype testing isotope release characterization methods in more depth.

2.1 Methods

2.1.1 Attrition milling

Attrition milling was used to co-mill the carbon allotropes with the TiC. Since all the materials were already nanometric in primary particle size, with the exception of graphite, the main function of the co-milling was to break the primary particle agglomerates and mix them homogeneously. A study of the effect of attrition milling on the raw materials can be found in the Discussion and Results of the article included in section 3.2 on page 65.

The attrition mill, also called attritor [108] is an equipment used to reduce the primary particle size and/or agglomerate size of powders. It was developed by the US Bureau of Mines in the 60's [109] and is considered to be one of the most efficient milling methods among the grinding media-based compression-shear type mills [110]. As schematically represented in figure 2.1, they normally consist of an immobile chamber with a vertical centrally positioned stirring rod which has horizontal arms spaced vertically and with angles of 90° between them [108, 110]. The grinding jar is usually inserted in a water cooled bath in order to control the temperature and the mill usually has around 80 % of its volume filled with griding balls.

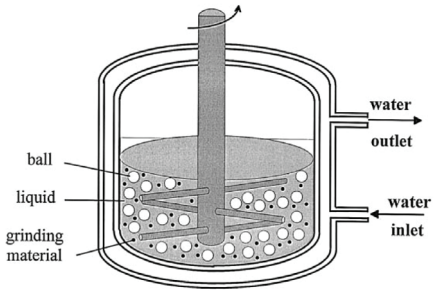

Figure 2.1 – Scheme of an attrition mill. Reproduced from [110].

The arms, normally made of the same material of the grinding balls, stirs the balls which makes them lift and fall back, causing a difference in motion between the material to be ground and the balls, providing an higher surface of contact [108]. The milling mechanisms present are: impact, shear forces (attrition or friction) and compression forces [110, 108]. In a kinetics study the milling rate was found to increase with the mills rotational speed and smaller ball sizes (if friction is the main mechanism in place) [110]. When milling very hard materials, the main mechanism is usually impact rather than friction, since their surfaces are difficult to abrade. The kinetics of particle breakage in attrition mill are normally described by first-order equations [109, 110].

High impact energy allows for use of smaller diameter milling media resulting in smaller particle sizes, which can get down to tens of nanometer, depending on the mill geometry and grinding media material [109]. The mill walls, balls and stirring rods can be designed in steel, tungsten carbide, aluminum oxide, zirconium oxide and polyamide. [108].

The main advantages of attrition milling are high energy utilization, fast and efficient and fine grinding, temperature control, simple operation [110, 109] and possibility to use in semi continuous way since the mill does not rotate [108]. However the attritors present some disadvantages such as the relatively low product output and high power consumption which both together can make it difficult to run and maintain cost effectively [108].

In the literature, milling volumes ranging from 0.25 to 8L with rotation speeds up to 2500 rpm were found [108]. Attrition mills are used in production of metallic and ceramic ultrafine powders [108], alloying of immiscible elements, powder metallurgy alloy blending and dispersion strengthening.

In this work, two different attritors were used depending on the charge (quantity of powder intended to be milled) size intended. For small charge a Union Process 01HD mill was used which can reach 800 rpm with an 80 ml grinding bowl. For higher charges (production of a full target) a Netzsch PR075 with a milling capacity of 500 ml which could reach 2000 rpm was used.

2.1.2 Thermal treatments

Two different ovens were used to treat and evaluate the TiC composites. They cover temperatures between 25-1800 °C. Here we describe details of the two ovens as they were specially adapted for the production of the TiC and composite materials.

Oven A

High temperature thermal treatments (> 1500 °C) were all conducted in vacuum in order to avoid burning of the carbon ($C + O_2 \rightarrow CO_2$) and oxidation of the TiC. To further protect the samples from residual oxygen graphite boats and crucibles were also used (where an example is shown on figure A.1.2 of the appendix A.1 - page 161). This resulted in a very reductive oven atmosphere with partial pressures of CO, P_{CO}, which were estimated to be between 10^{-11} to 10^{-3} and P_{O_2} between 10^{-28} to 10^{-20}, as was determined in the article included on section 3.3, as shown on figure 3.b5, on page 98.

In order to test the effect of the carbons on the sinterability of nanometric TiC the samples were submitted to thermal treatments of 2 and 10 h at 1500 °C in a vacuum atmosphere with heating/cooling ramps of 8 °Cmin^{-1}. This was accomplished using a *Carbolite STF 15/450* horizontal recrystallized alumina tube furnace which was adapted for vacuum as represented on figure 2.4 and schematized on figure 2.2.

In-house designed and built vacuum flanges were fitted to the alumina tube and coupled to an *Agilent TPS-mobile TV301* pumping station which in this configuration could reach a pressure of 10^{-4} - 10^{-3} Pa at 1500 °C in the gauge zone (see figure 2.2a). Specially designed thermal shields (see figure 2.2a and b) were built in order to maximize the oven temperature

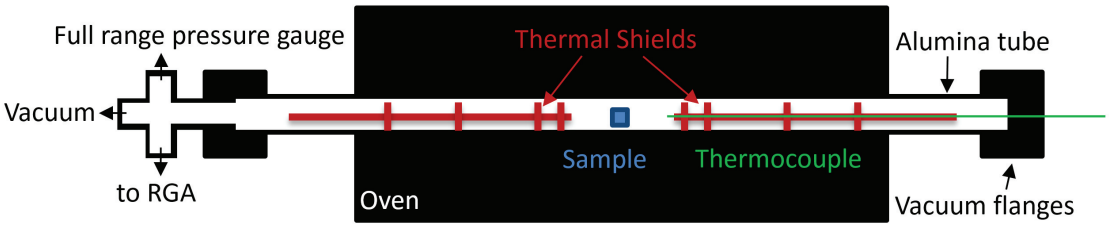

(a) Oven A: Schematic of *Carbolite STF 15/450* adapted oven for vacuum.

(b) Specially designed thermal shields for oven A.

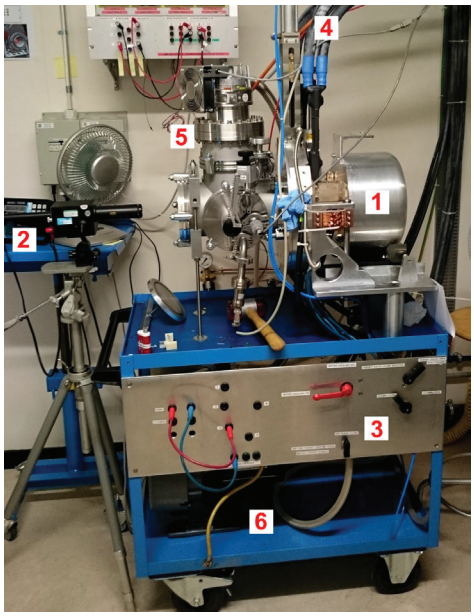

(c) Oven B: used for $T > 1500\,^{\circ}\mathrm{C}$.

Figure 2.2 – Details of the ovens used for thermal treatments of TiC and respective composites, where in (c) 1 is the oven itself (similar to a target unit), 2 is the pyrometer to measure temperature, 3 is a panel to control water cooling valves and other electrical connections, 4 are the power cables to ohmically heat the oven, 5 is turbo pump and 6 is scroll pump.

uniformity in the sample zone, as well as allow efficient pumping. Through these thermal shields a type R thermocouple was brought to the sample zone which was connected to an Eurotherm proportional–integral–derivative (PID) controller to regulate the oven temperature. This oven also had an extra port to connect to a residual gas analysis setup which will be described in the next subsection.

Oven B

The samples which exhibited the best behavior from the tests in oven A were selected to be heat treated in oven B at 1650 and 1800 °C and also 1500 °C for comparison with oven A (where the comparison study can be found on section 3.3, 86). For that, oven B (figure 2.2c) was made

in-house from the same components as the target units detailed on subsection 1.2 (page 16). However this "target unit" had no ion source, using only the target container as an oven. These target containers can be ohmically heated up to 2400 °C under a 10^{-4} - 10^{-5} Pa vacuum.

In oven B the temperature was measured and controlled through the use of a pyrometer. A pyrometer is a non-contact thermometer, which based on the emitted thermal radiation to estimate the temperature of a certain body [111]. The material where the temperature was measured was Ta and an emissivity of 0.49 was considered.

2.1.3 Residual gas analysis

Residual gas analysis (RGA) using mass spectrometry is an analytical technique able to ionize the atoms present in a gas phase, which can come from any sample, and then separating them according to their mass to charge ratio (A/q), in order to identify them. It has applications in biochemistry, pollution control, food control, forensic science, as well as in fields such as atomic physics, reaction physics, geochronology and many others [112].

RGA always comprises of three steps: ionization followed by mass separation and detection. Even though there are several types of ion sources for RGA in our case, electron impact ionization was used (as described in subsection 1.2.3 on page 25). As for the second step, several mass analysers exist which can be divided into two categories: scanning analysers (allowing only a specific A/q at a given time) or those which allow simultaneous transmission of all the ions (time-of-flight analyser and ion traps). In the instrument used, the scanning type analyser was present: a quadrupole. This instrument is made of 4 parallel rods, as schematically represented on figure 2.3), grouped 2 by 2 with opposing charges, connected to a radio frequency voltage power supply. By varying the voltage, a certain A/q can be selected to be allowed to be able to go through the rods while all the others will have unstable trajectories and be neutralized in the walls [112]. This way, by varying the voltage a continuous scan of A/q can be done and a mass spectrum can be obtained. Detection is usually done by means of a Faraday cup, which is a metal cup with a small hole all connected to ground through a resistor [112]. When the ions reach the interior and collide with the Faraday cup walls, they either accept or donate electrons causing a current through the resistor which will be amplified and detected.

In this work residual gas analysis was used to determine at which temperatures and which volatile molecules are formed during the thermal treatments which cause the mass losses observed. A *Pfeiffer PrimaPlus QMA200* was used which contained an electron impact ion source, a quadrupole mass spetrometer (QMS) and a faraday cup detector. This RGA had a mass resolution from $A = 1$ to $A = 100$. The RGA unit had its own vacuum system which had to be baked out at 80 °C for 3 days, to desorb volatile elements from the vacuum chamber walls, improving the signal to noise ratio during use. The system was connected to the oven A described above (schematized on figure 2.2a) through a small valve, as seen on figure 2.4. This was done to limit the conductance in order to be able to operate the RGA in the required

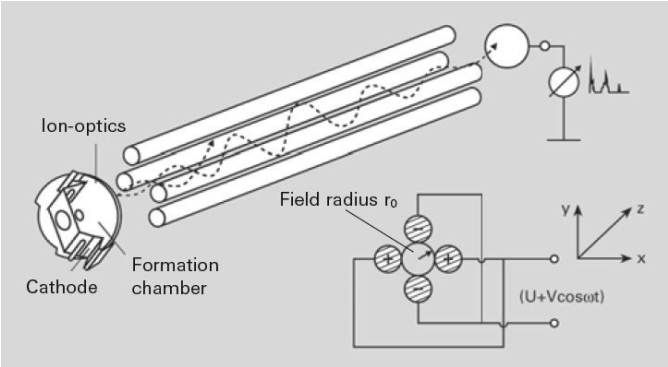

Figure 2.3 – Schematic of a quadrupole mass separator. Reproduced from [113].

pressure conditions ($< 1 \times 10^{-2}$ Pa), avoiding the pressure spikes of the oven cycle.

2.1.4 Dilatometry

Dilatometry is a thermoanalytical method used to study materials dimensional behaviour under a certain temperature cycle and atmosphere. Dilatometry can be used for example to study thermal expansion, phase changes, sintering and reaction kinetics. In this work, dilatometry was used to study the sintering behaviour of TiC and the effect of the addition of different volumes to the carbon allotropes.

The dilatometer used, previously made in-house in the Department of Materials and Ceramics Engineering at the University of Aveiro (Portugal) is briefly described here. The dilatometer is divided into 4 parts: the oven (see figure 2.5a), the dilatometer cell (figure 2.5b, electronics/software and the vacuum pump/water cooling circuit. The oven was made of graphite, in a water-cooled vacuum tight vessel which could be pumped down to 10^{-1} - 1 Pa by an oil rotary pump. The oven temperature was controlled with a Eurotherm PID controller where a maximum temperature of 1500 °C could be reached with heating/cooling rates up to 50 °C min^{-1}. The temperatures were measured with a conveniently placed type R thermocouple in the dilatometer cell (see figure 2.5b). The cell, entirely made of graphite, was of "push rod" type where a graphite bar made the connection between the sample and a linear variable differential transformer sensor (LVDT). The LVDT was water cooled, had a measuring range from -5000 to +5000 µm and a precision of about 0.1 µm. To control the oven and register the LVDT signal over time and temperature a *DasyLab v9* routine was used.

In order to obtain the shrinkage, $\Delta l/l_0(T)$, the dilatometer data was treated in the following way:

$$\frac{\Delta l}{l_0}(T) = \frac{\left(l_{LVDT}(T) - l_{LVDT,i} - \Delta l_{blank}(T) - \Delta l_{exp}(T)\right)}{l_0} \tag{2.1}$$

where $l_{LVDT}(T)$ [µm] is the LVDT position as a function of temperature, during a dilatome-

Figure 2.4 – Setup used for the residual gas analysis which consisted of oven A (1), the RGA unit (2), the valve connecting the oven and the RGA unit vacuum systems (3) the heating elements to bake out the vacuum system of the RGA unit (4), the oven and RGA unit pumping groups (5 and 6 respectively), the computer with the software to analyze the signal coming from the RGA unit (7).

try temperature cycle, $l_{LVDT,i}$ [µm] is the initial LVDT position, $\Delta l_{blank}(T)$ [µm] is the LVDT position variation due to expansion of the dilatometer cell, $\Delta l_{exp}(T)$ [µm] accounts for the LVDT sample differential thermal expansion relatively to the blank and l_0 [µm] is the initial size of the sample. The $\Delta l_{blank}(T)$ is extracted from a thermal cycle by replacing the sample with a sample made from the same material as the dilatometer cell. $\Delta l_{exp}(T)$ is extracted from the cooling ramp of the thermal cycle after blank corrections, where any change in the LVDT signal can only be due to the differential thermal expansion.

The samples had rectangular cuboid shape with a size of about $15 \times 2 \times 5$ mm. In order to extract relative densities (ρ_r), $\Delta l/l_0(T)$ was assumed to be isotropic, and the relative density as a function of temperature ($\rho_r(T)$) could be calculated:

$$\rho(T) = \frac{V_0 \cdot [\Delta l/l_0(T) + 1]^3}{m_0\,[1 - \Delta m/m_0 \cdot \Delta m/m_0(T)]} \frac{1}{\rho_t} \tag{2.2}$$

where, V_0 [cm^3] and m_0 [g] are respectively, the initial volume and mass of the sample, $\Delta m/m_0$ [%] is the total sample mass losses during the dilatometry cycle, $\Delta m/m_0(T)$ [%] is the mass loss as a function of temperature extracted from the RGA and ρ_t is the theoretical density of the TiC or composite.

(a) Dilatometer oven.

(b) Dilatometer cell with a sample mounted.

Figure 2.5 – Dilatometer oven and cell used in the TiC/TiC-C composites.

2.2 Material characterization techniques

2.2.1 Particle size distribution by laser diffraction

Laser diffraction also referred to static laser diffraction is a technique where particle sizes from 0.01 µm, in special cases, or normally from 0.1 to 3000 µm [114] can be measured. The technique is based on the detection of a scattering pattern generated by a monochromatic laser when interacting with particles in a suspension. The scattering pattern depends on the size of those particles and refraction indexes of the medium and of the particles material [114]. When light interacts with a particle, diffraction, reflection, refraction and adsorption can happen, which are represented by complex mathematical models. There are several models used for laser diffraction, which convert a model-based matrix into a particle size distribution (PSD). In this case, the Mie theory was used [114], which accounts for all types of interactions referred before and uses the optical properties of the materials divided in a real part, which accounts for the refractive properties of the material and an imaginary one which takes into account the absorption phenomena [114]. The refractive indexes used can be found on on page 71, in the article included in subsection 3.2.

The laser scattering PSD was measured with a *Master Malvern Mastersizer S* which can measure sizes from 50 nm to 880 µm using a red (633 nm) 2 mW He-Ne laser. The Malvern was coupled with a small volume wet dispersion unit which recirculated the sample suspension through the optical cell. Before measuring, all samples (100 ml) were sonicated (100 W,20 kHz for 15 min under constant agitation. The median particle sizes ($D_{v,50}$ or P_S [nm]) were extracted from the PSD.

2.2.2 Nitrogen physisorption isotherms

Adsorption is the adhesion of an atom to a surface at a pressure (P [Pa]) lower than it's vapor pressure or saturation pressure (P_0 [Pa]). Adsorption can be divided in two different types: physisorption, characterized by weak bonding to the surface (van der Waal forces) and chemisorption, forming ionic or covalent bonds. Adsorption will depend on the molecule (adsorbate) and the surface (adsorbent) and each element/surface combination will produce an unique isotherm [115]. An isotherm is the amount of adsorbate on a surface, at a constant temperature, as a function of the absorbate pressure, up to its P_0. The isotherms can also be done for desorption, the inverse process of adsorption [115]. They can have hysteresis between adsorption and desorption, which can give much information about a material, including its surface area, pore size and shape. A well established technique uses nitrogen as adsorbent at liquid nitrogen temperature (−195.8 °C - 77.2 K [35]) to determine the full adsorption-desorption isotherm of a given material, assuming only physisorption is taking place. From these isotherms information about specific surface area, mesopore size and respective distribution and micro porosity[1] can be obtained.

A *Quantachrome ANOVA2200* equipment was used which possesses 2 vacuum outgassing stations (up to 400 °C) and 2 measuring cells. Samples were outgassed in vacuum at 300 °C for 24 h in the outgas system before analysis, to remove any unwanted sorbants (such as water) from the surface. The isotherms were built with 34 points for adsorption and 26 points for desorption, down to $P/P_0 = 0.35$, and high precision mode was used in the machine (0.05 torr of pressure tolerance and 180 s of equilibration time [117]). P_0 was measured simultaneously every 3 points of the isotherm for higher precision in a separate cell. The specific surface area (SSA) from the Brunaeur, Emmett and Teller model (BET), PSD and volumes from the Barrett, Joyner and Hallenda model (BJH) were extracted using the software *Quantachrome NovaWin v11* and the median pore size in volume, $D_{Pv,50}$ [nm], was extracted from the cumulative pore size distributions. Both BET and BJH models are briefly described below.

BET - specific surface area determination

When a monolayer of physisorbed adsorbate is formed on the surface of a material, then the specific surface area (S [$m^2 g^{-1}$], acronym SSA) can be determined knowing the adsorbate molecule cross section (σ_{mol} [m^2]):

$$S = \frac{N_A \sigma_{mol} V_{ml}}{V_{m,STP}} \tag{2.3}$$

where N_A [mol^{-1}] is the Avogadro number, V_{ml} [m^3] is the adsorbate monolayer volume and $V_{m,STP}$ [$m^3 mol^{-1}$] is the molar volume of 1 mol of N_2 at STP (standard temperature and pressure) conditions. V_{ml} can be extracted from the linear zone of the isotherm ($0.05 < P/P_0 <$

[1] IUPAC (International Union of Pure and Applied Chemistry) recommendation: micropores are smaller than 2 nm, mesopores are between 2 and 50 nm and macropores are higher than 50 nm [116]

0.35) using the model of Brunaeur, Emmett and Teller (BET) [118]:

$$\frac{P}{V_a(P_0-P)} = \frac{1}{V_{ml}C_b} + \frac{C_b-1}{V_{ml}C_b}\frac{P}{P_0} \tag{2.4}$$

where C_b [dim] is a constant and V_a [m^3] is the volume of adsorbate adsorbed. By plotting $P/V_a(P_0-P)$ vs P/P_0, the intercept becomes $1/(V_{ml}C_b)$ and the slope $(C_b-1)/(V_{ml}C_b)$.

BJH - mesopore size and distribution

After creating the monolayer, if more gas keeps being added into the system, multilayers start to form and pores start to be filled with liquid separated by a meniscus from the gas phase. In the pores, the gas condenses at P below the P_0, due to capillary condensation, which allows the assessment of the pore volume distributions (size if pores are assumed to have a certain shape) since different pore sizes will lead to condensation at different pressures [115].

The Barrett, Joyner and Hallenda (BJH) model allow us to extract the pore size distributions from the desorption branch of the isotherm, assuming cylindrical pores and non-connecting pore geometry [119]. In this model the P/P_0 can be related with the capillary radius (r_c [nm]) using the Kelvin Equation [119, 115]:

$$RT\ln\frac{P}{P_0} = -\frac{2\gamma_L V_m}{r_c} \tag{2.5}$$

where the R [$J\,K^{-1}\,mol^{-1}$] is the universal gas constant, T [K] is the absolute temperature, γ_L [$N\,m^{-1}$] is the liquid surface tension and V_m [$m^3\,mol^{-1}$] is the molar volume of liquid nitrogen. Since capillary condensation only takes place after monolayer formation, one must consider that the pore radius (r_p [nm]), $r_p = r_c + t_{ml}$, where t_{ml} [nm] is the monolayer thickness [115]. The thickness of this layer t_{ml} [nm] is lower in small pores than larger pores due to solid/liquid interactions [119]. Applying the Kelvin equation (equation 2.5) and accounting for the t_{ml} change the BJH model can compute the pore size distribution. This technique is limited to pore sizes between 4 nm and around 200 nm, working very well for mesopore sizes. The lower bound is due to the non applicability of the equation 2.5 while the upper limit is due to the experimental difficulty in determining P/P_0 higher than 0.99 with high enough precision, due to equipment sensitivity constrains.

2.2.3 Scanning electron microscopy

In scanning electron microscopy (SEM) electrons with a few to tens of keV are swept (scanning) over the surface of a material which builds a 3D-like image of the topography of the sample [120]. These electrons interact with the matter from the sample which can be used to probe many different material characteristics: the material surface topography, crystallography, phase composition contrast, chemical composition and others [120].

Secondary electrons (SE) are produced when the electrons from the beam collide inelastically with outer shell electrons of the sample, ejecting them. These electrons have very low energies (< 50 eV) and thus don't travel much in the material, however those close the surface escape and can be detected by a SE detector. Due to their short travel distance they give information on the surface and are used to describe topography. SE detectors, also referred as Everhardt-Thornley detectors, usually located by the side relatively to the sample. These detectors have an electrode which attract only the low energy SE to be detected on scintillator with a photomultiplier (described in detail in this chapter in subsection 2.3.2 on page 58). Due to their positioning and low solid angle the generated images are often of low signal and suffer from shadow effect. A new type of detectors, referred to as in-lens detector due to their location inside the SEM accelerator column which collect SE with much higher efficiency and with much less noise and without shadowing, producing images of much higher quality.

Back scattered electrons (BSE) are electrons from the beam which trajectory gets very close to the nucleus and so gets altered by elastic Coulomb interaction with the nucleus [120]. Their energy is very close to the one of the incident beam and they give information about the chemical composition of the phases (through different contrasts). These electrons are usually detected by semiconductor detectors.

SEM can work with energies from a few hundreds of eV to few to tens of keV this will result in bigger or smaller interaction volumes (normally pear shaped) [120]. This is due to the higher penetration depth of the electrons which will excite a larger zone. This will directly affect the resolution of the image obtained since the larger excited volume will produce more electrons from an area neighbor to the beam spot, blurring the image. However very low energies are also difficult to focus and to work with. In order to estimate the excited volume and determine the best energy to work with a software such as the CASINO (monte CArlo SImulation of electroN trajectory in sOlids) software [121] was used.

When the beam of electrons interacts with the material, characteristic X-rays are produced. These X-rays can be used to infer the chemical composition of the sample being analysed. This technique is called EDS (Energy-dispersive X-ray spectroscopy) and can be used to qualitatively and quantitatively identify the chemical composition of a sample. Higher energies allow the excitation of higher electron shell energy levels, facilitating the identification of the elements present. However, this results in a larger excited volume bringing a lower resolution which is detrimental if elemental mapping is desired.

The SEM used was mainly a *Carl Zeiss SMT Σigma*, located at CERN, which has a field emission Schottky ZrO/W cathode electron gun able to operate up to 30 keV. This SEM can produce images of up to 500000 ×, with a maximum resolution of 1.5 nm at 20 kV and is equipped with an SE, BSE and an in-lens detector. It can also be coupled with an Electron BackScatter Diffraction (EBSD) detector for crystallography and possesses EDS - *Oxford INCA Synergy 350 X-Max 50 / HKL ADV* - for chemical composition quantification. A second SEM was also used, located in the University of Aveiro: an *Hitachi SU-70* which operates up to 30 kV and has a

point to point resolution of 1 nm at 15 kV.

For SEM analysis, the samples have to be electrically conductive otherwise the sample will charge up and deflect the electrons causing aberrations in the image. Since, in the case of this work, the TiC and the carbon the samples are conductive, there was no need for any special sample treatment which is normally done through carbon or gold coating, to make samples conductive. The samples were simply fractured and mounted in a SEM support with a conductive carbon sticker. The plasma cleaning step, normally used to remove hydrocarbons from the samples was avoided due to the carbon which is present in the samples.

2.2.4 Mercury Intrusion Porosimetry

Mercury intrusion porosimetry (MIP) is one of the most complete porosity characterisation techniques, it allows us to scan a vast pore size range (3 nm to 500 µm) determining its pore size distribution, total pore volume and determine the apparent density. The technique has some limitations such as the assumption that all pores are accessible through larger pores or from the surfaces. This will make big pores with small entrances be identified as having the size of the entrance. Another limitation is the impossibility to analyse closed porosity since mercury has no way to access these types of pores [122].

Similarly to the BJH method (see page 52, on subsection 2.2.2) the MIP assumes cylindrical pores. Since Hg shows a non-wetting behaviour towards most substances, it won't enter the pores while the sample is immersed in it (even under vacuum) unless pressure is applied. By applying pressure, the mercury is forced into the pores of the sample, where pore size (r_p [m] is inversely proportional to the pressure applied on the Hg, as given by the Washburn equation [122]:

$$P = \frac{2\gamma_L \cos\theta_{Hg}}{r_p} \tag{2.6}$$

where the P [Pa] is the pressure necessary for the Hg (with a surface tension γ_L [N m^{-1}]), with a contact angle (θ_{Hg} [°]), to penetrate into a pore capillary.

For MIP two machines were used, the first one, *Thermo Scientifc Pascal 140 Series*, is used to evacuate and fill the sample dilatometer cell with Hg and can reach pressures up to 400 kPa evaluating mostly µm size pores. The second, was used to analyze smaller pore sizes, *Thermo Scientifc Pascal 440 Series* which can reach 400 MPa (down to 4 nm), however only 200 MPa were used due to the fragile nature of the samples. Due to the size of the samples only very small masses were used which were between 0.1 and 0.3 g (approximately the same volume) whereas normally, it is recommended for 1 g to be used. MIP results are consistent as long as the same mass (or volume) is used [123]. However for density and total pore volume determinations this mass is not high enough since the total quantities of mercury intruded are not high enough to be regarded as valid due to precision limitation of the porosimeter. As such, only the pore size distribution curves obtained were used from the MIP. A contact angle (θ_{Hg})

of 140° was assumed between Hg and the samples, since no data exists for TiC and TiC-C composites.

2.2.5 X-ray powder diffraction

The wavelength of X-rays used in X-ray powder diffraction (XRPD) crystallography, 0.5 to 2.5 Å, makes them perfect probes to study atomic structures since their size is in the same order of magnitude as the inter atomic distances [124]. These X-rays are normally generated in an X-ray tube, by bombarding a certain metal with electrons which are produced from an hot tungsten filament [124]. The metal bombarded will determine the X-ray energies produced, called characteristic X-rays, which result from outer shell electron transitions. When these X-rays interact with crystalline structure they will interact with the electrons, producing waves (elastic scattering) which have mostly a destructive interference but also constructive interference with a high signal. This constructive interference has to respect the Bragg's law [124]:

$$2d\sin\theta = n_R\lambda \tag{2.7}$$

where d [Å] is the spacing between the crystallographic planes, θ [°] is the incident angle of the beam, n_R [dim] is the order of the reflection and λ [Å] is the wavelength of the incident beam.

Depending on the crystal system and lattice parameters each crystallographic phase will produce distinct peaks, by scanning over different angles. In XRPD, a powder is assumed to have randomly oriented crystallites where a statistically representable signal for each crystallographic direction can be obtained. These powders produce a X-ray diffraction pattern which will look like many concentric rings in 2D, however by using the Bragg-Brentano, a simpler data arrangement can be obtained. Here, a flat sample is scanned in reflection (2θ) basically along a line which connects the center of the concentric rings to the last ring using a goniometer, obtaining a 1D diffractogram expressed in intensity over 2θ.

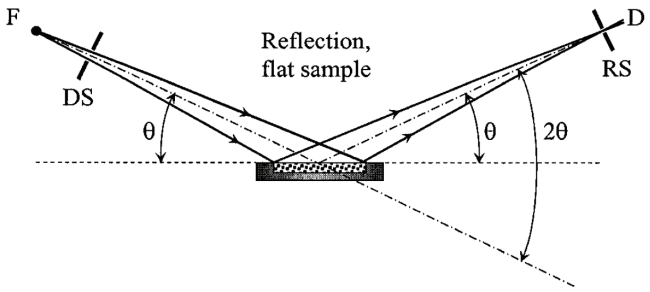

Figure 2.6 – Bragg-Brentano geometry used normally in X-ray powder diffraction. Reproduced from [124].

The diffractometer used was a *PANalytical X'PERT PRO* in Bragg-Brentano geometry, located

in the Department of Materials and Ceramics Engineering in University of Aveiro, Portugal. This equipment has a Cu X-Ray source ($K_\alpha, \lambda = 1.54$ Å) operated at 45 kV and 40 mA. The measurements were done from 20 to 125 °2θ with a step size of 0.013 °2θ and 97.92 s per step, without monochromator. For a good resolution a fixed divergence slit of 0.218° was used and spinning of the sample holder was done in order to have better statistics. The samples preparation is very important in XRPD. The powders were deagglomerated in an agate mortar and uniformly put into the sample holder to avoid texture or preferred orientation. Before each measurement the diffractometer was fine aligned.

Crystallite size analysis

In XRPD, peak broadening can be due to small crystallite sizes, which was proposed by Scherrer [125] in 1918 and used throughout the literature as a standard method to determine cyrstallite size (h) from XRPD:

$$h = \frac{K_h \lambda}{B \cos\theta} \tag{2.8}$$

where K_h [dim] is a constant which depends on the crystallite shape [126], λ [Å] is the wavelength of the X-ray and B [Å] is the peak broadening, in radians, which can be expressed either through the full width at half maximum (FWHM) or the integral breadth which is the area under the diffraction peak divided by its intensity [127].

However peak broadening can also be caused by non-uniform lattice stress, from crystallite structure defects. In order to deconvolute these, Williamson and Hall have proposed a formula using all reflections and using the Bragg's law [128]:

$$B = 2s\tan\theta + \frac{\lambda}{h\cos\theta} \iff B^* = d^* s + \frac{1}{h} \tag{2.9}$$

where s is the lattice stress, d^* is the reciprocal lattice ($d^* = 2\sin\theta/\lambda$) and B^* is the reciprocal broadening ($B^* = 2\sin\theta/\lambda$). This relationship can be plotted in $B\cos\theta$ vs $\sin\theta$ (or B^* vs d^*) where h can be extracted from the slope and s from the intercept or the inverse in reciprocal space. This relationship has the assumption that the peak has a Lorentzian shape which is in most cases not true [127]. The peaks are usually a convolution of Lorentz and Gaussian shapes which is described by the pseudo Voigt function [127]. To account for that, Langford modified the Williamson-Hall (LWH) plot method, where [127]:

$$\left(\frac{B}{d^*}\right)^2 = \frac{B}{h(d^*)^2} + \left(\frac{s}{2}\right)^2 \tag{2.10}$$

where in a plot of $(B/d^*)^2$ vs $B/(d^*)^2$, s can be obtained from the intercept and h from the slope. These methods also allow us to verify if the crystallite sizes are the same along all the planes. If the shapes are close to spheres then these methods give an average size for the crystallites.

Since most instruments produce an instrumental broadening of the XRPD peaks, a standard sample should be analysed to deconvolute instrumental broadening from the size-stress broadening. The standard sample must have no lattice stress, usually tens of micron grains/particles and as many peaks as possible along 2θ to well characterize the instrumental broadening. In the case of this work LaB_6 was used.

Rietveld refinement

In the Rietveld method, the entire diffractogram obtained is fitted to a calculated profile using the least-squares minimization of the residuals. The method was invented by Rietveld in the late 60's for neutron diffraction and it can be applied as well for X-ray diffraction [129]. For Rietveld refinement, the unit-cell parameters and the space group of the present phases need to be known. This method can deconvolvolute and determine many different parameters where a calculated profile for a given phase, is generally expressed by the following equation [130]:

$$Y_{i,calc} = y_{b,i} + S_{ph} \sum_{k} L_k |\, F_k \,|^2 \phi\,(2\theta_i - 2\theta_k)\, P_k A_b \tag{2.11}$$

where $Y_{i,calc}$ is the XRPD intensity at an arbitrarily chosen point i and the k in the summation represents the Miller indices hkl for a certain Brag reflection and:

- $y_{b,i}$ is the background at the i^{th} step, normally defined by a polynomial function;
- S_{ph} is a scale factor which will determine the fraction of a certain phase;
- L_k is a parameter containing the Lorentz, polarization and multiplicity factors;
- ϕ is the peak-shape function, where it is normally Gaussian, Lorentzian, Pseudo-Voigt or Pearson VII;
- $(2\theta_i - 2\theta_k)$ is related with line broadening due to small crystallite size or lattice stress;
- P_k is the preferred orientation function;
- A_b is the absorption factor;
- F_k is the structure factor for the k^{th} Bragg reflection and contains the unit cell parameters.

As can be seen, Rietveld refinement can easily reach many tens of variables to fit, which during the fit, can easily destabilize it and giving it no direction to converge. Because of that, the fit variables should be grouped accordingly to the parameters defined above, fitted in an isolated way and sequentially [124, 130]. In this work the Rietveld refinement was done using the software *ANalytical HighScore Plus v4.1* [131].

2.3 Isotope release studies

The isotope release studies can be divided in two types: offline and online. Offline studies are those characterized by separating the isotope production and isotope extraction phases, meaning that they happen at different times. While for the online studies refers to the test of

a target prototype mounted in the ISOLDE target station.

2.3.1 Offline methods: gamma spectroscopy

Since the offline methods procedure is explained in detail on page 133, in the article included in subsection 5.1 while here we will only describe the gamma spectrometry which was used during the offline studies.

γ-rays can be detected through the use of a semiconductor material, such as germanium. When a γ-ray passes through the germanium it generates a certain number of electron-hole pairs which are proportional to the γ-ray energy [132]. The semiconductor is usually between two electrode plates which generate an electric field where the electrons and holes travel in opposite directions before being detected.

Germanium detectors are normally high-purity Germanium detectors (HPGe) and have to be operated at cryogenic temperatures. This is due to the small bandgap of the Ge semiconductor (0.7 eV) where at room temperature, electrons easily jump cross the band gap to the conduction band, causing an electrical background [132].

These detectors have to be energy and efficiency calibrated with radioactive sources which have well known gamma intensities and energies, close to the energies to be measured. Many isotopes have unique signatures in terms of γ-ray energies and intensities which can be used to identify and quantify the isotopes present in a specific implantation.

At ISOLDE a *Canberra Cryo-Pulse 5 HPGe Detector* was used and the results were analyzed with the *Genie 2000: Gamma Acquisition & Analysis v.3.2.1* software. This detector has a built-in refrigerator which presents a big advantage towards other HPGe detectors where no periodic liquid nitrogen refillings are necessary.

2.3.2 Online methods: tape station

After proton impact, due to the release delays described in subsection 1.3.1 on 27 (diffusion and effusion), the isotope release time-structure has a pulse shape, as schematized on figure 2.7c. The pulse shape length can sum up to milliseconds, tens of seconds or even hours depending on the TISS, isotope element released and its $t_{1/2}$. The release time-structure is very important to document since it can give an idea of the TISS condition, can be used to compare different TISS and even to extract effusion and diffusion time constants (as described in this thesis outlook in subsection 6.2.2 on 153). However, for simplicity, this pulse shape is normally fitted to a 3 exponential formula, which is given on page 137 in the article included on section 5.1.

Due to the limitations of ion-counting techniques, such as Faraday cups, which can't detect low quantities ($< 1 \times 10^6\,s^{-1}$), radiation detection techniques are necessary. With radiation

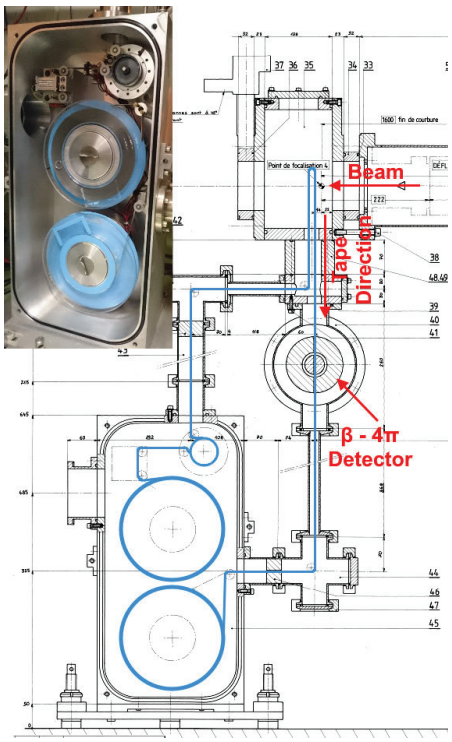

(a) ISOLDE Tape Station with tape represented in blue.

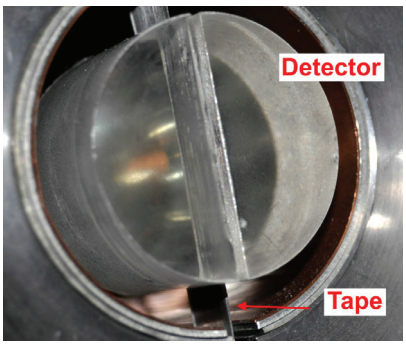

(b) ISOLDE Tape Station Beta detector.

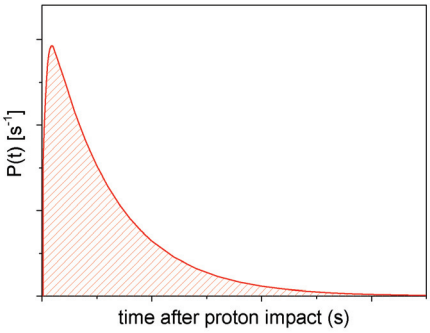

(c) Representation of the pulse shape of a radioactive ion beam after proton impact.

Figure 2.7 – ISOLDE tape station and its beta detector and representation of the pulse shape of a radioactive ion beam after proton impact.

detection techniques one normally needs to implant the isotopes so they can be measured. If several measurements are needed in a short times, the same implantation spot can't be used or it would have a contribution to the next measurement. For that, a tape station can be used, like the ISOLDE tape station represented on figure 2.7a. This device uses a tape which is made to go through different bearings and rolls, passing through the beam spot and detection spot and rolled onto two tape reels at its ends which are used to move the tape. The advantage of this system is to move the implanted isotopes from the collection point into the detection zone so they can be measured and at the same time clear the implantation zone for a new collection. The tape is long such that so many measurements can be made, rolling the tape between the tape reels where the implanted isotopes decay, making the tape reusable.

The tape station also allows great control of its timings, where one can control the:

- t_d, delay time, the time at which the beam gate opens after proton impact, allowing to scan the full release profile;
- t_c, collection time, the amount of time the beam gate will remain open after t_d, which is normally set to the minimum possible value, to avoid isotope decay losses and increase the release curve resolution;
- t_t, transport time, the time it takes for the tape to move, after the beam gate closes

($t_d + t_c$), from the implantation spot to the measurement spot where the detector is located (see figure 2.7), which is 900 ms at the ISOLDE tape station;
- t_m, measurement time, the time that the detector measures the radioisotopes activity implanted on the tape.

After data recording, the activities need to be corrected for t_c, t_t and t_m and also isotope daughter corrected.

The tape station uses a beta detector and a gamma detector (described above). When an electron passes through the plastic of a scintillator, it emits visible light in a process called fluorescence [132]. In this process, an electron from an atom or molecule gets excited (by means of electromagnetic radiation or particles) and emits a photon when relaxing to its ground state [132, 3]. The light generated in the scintillator is very weak so, they are generally associated with a photomultiplier tube. In this device the photons are initially converted into low energy electrons through a photocathode (using the photoelectric effect) and this electron signal is amplified many orders of magnitude in order to be detected[132]. The beta detector used at the ISOLDE tape station is a plastic scintillator type with a 4π steradians solid angle, as seen on figure 2.7b, where detection efficiencies close to 100 % can be reached. This detector is also fully shielded to reduce background and ambient radiation. Background levels at ISOLDE are usually around 5 - 10 counts/s while the detector saturates at around 27000 counts/s.

3 TiC-carbon nanocomposite development

Contents

3.1 TiO_2 and TiC preliminary studies 62

3.1.1 Sintering studies 62

3.1.2 Release studies 64

3.2 Article: Development of a processing route for carbon allotrope-based TiC porous nanocomposites 65

1. Introduction 67

2. Materials and Methods 69

3. Results and Discussions 72

4. Conclusions 82

3.3 Article: Stability of nanometric TiC-carbon composites: effects of carbon allotropes and Zr milling impurities 86

1. Introduction 89

2. Materials and Methods 92

3. Results and Discussions 93

4. Conclusions 104

3.4 Summary of the TiC-carbon nanocomposite development 107

This chapter is divided into four main sections which correspond to the three phases while developing the TiC-C nanocomposites. Section 3.1 describes the first tests and the reason why TiC was chosen for this work from the Ti-based materials. In section 3.2, a manuscript is included which describes the synthesis method developed to produce TiC-C nanocomposites in order to stabilize TiC up to 1500 °C. In the section 3.3 selected nanocomposites from section 3.2, in another manuscript, are tested up to 1800 °C and in-depth crystalline phase analysis is performed. Finally, in section 3.4 the main chapter conclusions will be summarized.

3.1 TiO_2 and TiC preliminary studies

The titanium element has good production cross sections of Ca, Sc and K which are requested for physics studies at ISOLDE[1]. There are 3 refractory materials which are good ISOL material candidates: TiC, TiO_2 and Ti metal. TiO_2 has been used in form of micrometric fibers as mentioned in subsection 1.3.2 (page 29) but was discarded. A Ti metal foils target is used at ISOLDE (see table 1.1, page 19), however it shows reduced beam intensities over time due to foil melting/sintering. Finally, TiC has been studied for its release properties but never implemented as a target material, attributed to very slow release [84, 62]. A literature review is done for the Ti-based material at ISOL facilities is included in the introduction of the article on section 5.1 (page 127).

Due to the potential of the sub micron or nanometric materials (section 1.3, page 26), commercial nanometric TiO_2 and TiC were acquired and evaluated. The Ti metal is excluded since, metallic foils thicknesses are limited to a few tens of µm and metallic powders sinter too fast [48]. The sinterability of nanometric TiC and TiO_2 was assessed in terms of specific surface area, relative density and morphology and selected microstructures were studied in terms of isotope release properties at the ISOLDE facility.

3.1.1 Sintering studies

Nanometric TiO_2 (< 100 nm), 99.5 % pure nanometric, composed majorly by anatase and also by rutile [2], was obtained from Sigma Aldrich (ref. 534662). TiC in nanometric form (80 to 130 nm) was obtained from Goodfellow (ref. LS 396999/1) with 99 % purity.

The powders were pressed into compacts of 14 mm and 1-2 mm of thickness in a manual hydraulic press with 57 MPa and heat treated in the *Carbolite STF 15/450* vacuum adapted alumina tube oven (oven A) at different temperatures for 2 h. Different thermal treatments for 2 h, from 800 to 1300 °C every 100 °C were conducted for TiO_2, and at 1200, 1300, 1400 and 1450 °C for TiC. The samples were characterized according to their geometrical density (obtained from weight and size) which was used to calculate the relative density[3]. SSA, morphology through SEM, EDS and XRPD were conducted as well.

The microstructures of the starting materials which can be seen in figure 3.1a for TiO_2 and below in figure 1a of the following article (page 71) for TiC, show that both powders are heavily agglomerated. EDS analysis has shown a 1 at.% of Si for the TiO_2 material, which, as reported by the supplier, comes from the production procedure. SSA of 33.7 $m^2 g^{-1}$ and 18.6 $m^2 g^{-1}$ were obtained for TiO_2 and TiC, respectively. From the SSA, the particle sizes calculated were

[1] For cross section simulation results with ABRABLA see figure A.4.2 in appendix, page 173

[2] Anatase is a low temperature TiO_2 phase (up to 1200 °C [133]), which transforms into rutile. They both have a tetragonal crystal structure but have different lattice parameters and space groups, which bring sightly different properties [133].

[3] Relative densities were calculated assuming theoretical densities of 4.93 $g cm^{-3}$ for TiC and 4.23 $g cm^{-3}$ for TiO_2 [35].

42 and 65 nm, for TiO_2 and TiC, respectively, which agree relatively well with those observed on the microstructures of figures 3.1a and 3.a1a (page 71).

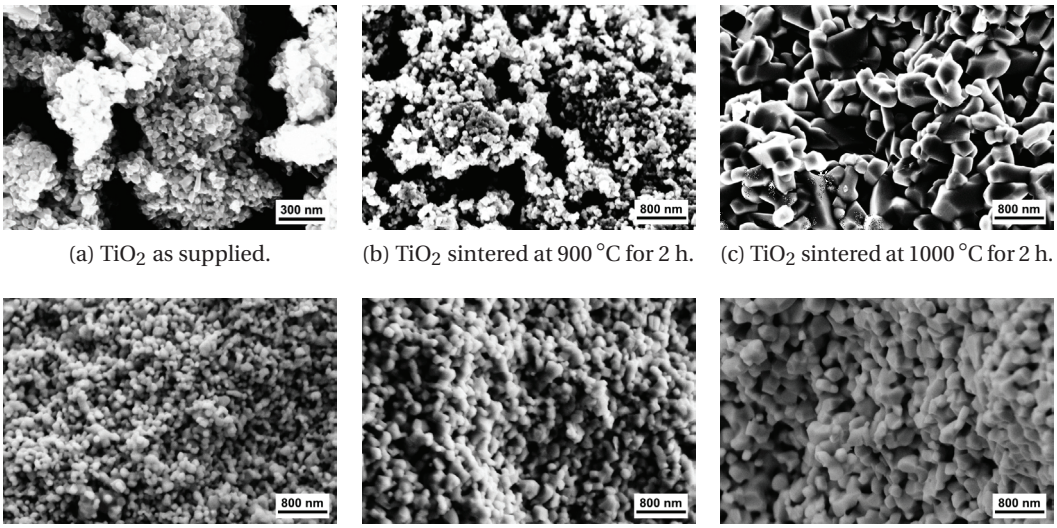

(a) TiO_2 as supplied. (b) TiO_2 sintered at 900 °C for 2 h. (c) TiO_2 sintered at 1000 °C for 2 h.

(d) TiC sintered at 1200 °C for 2 h. (e) TiC sintered at 1300 °C for 2 h. (f) TiC sintered at 1450 °C for 2 h.

Figure 3.1 – SEM microstructures obtained for the TiO_2 and TiC sintering studies.

The results SSA and density results for TiO_2, as a function of the sintering temperature, can be seen on figure 3.2a. In this figure, TiO_2 shows net sintering effects, specially at 1000 °C, where there is a drastic increase in density and decrease in SSA. This is also confirmed from the microstructures of figure 3.1b which shows the TiO_2 sintering at 900 °C and figure 3.1c showing the same material but sintered at 1000 °C, where a large difference in grain size is seen. XRPD results revealed that the anatase/rutile phase ratio remains unchanged until 1000 °C, where after, the anatase completely transforms into rutile.

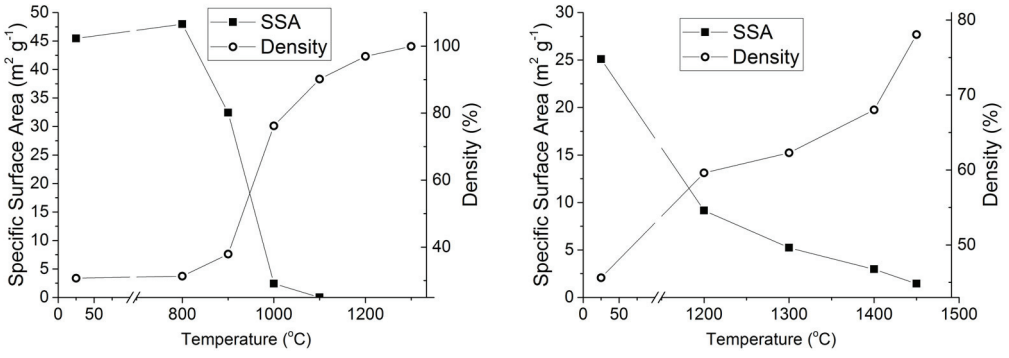

(a) TiO_2. (b) TiC.

Figure 3.2 – TiO_2 and TiC specific surface area and relative density evolution as a function of the 2 h heat treatment temperatures.

The phase transformation of rutile to anatase is known to accelerate sintering due to the higher atom mobility [134], which is observed here, from 900 to 1000 °C. Furthermore, the Si doping of TiO_2 is known to significantly shift the anatase/rutile transformation to higher temperatures and to arrest grain growth [135]. Even though the Si impurity acts in favor of delaying sintering, after 1100 °C the surface area is almost zero and relative densities are close to 1.

The TiC microstructures after 1200, 1300 and 1450 °C can be seen on figure 3.1d, e and f, respectively. In here, the sintering of TiC is much lower than TiO_2 case but, nonetheless, the nanometric structure is lost at 1300 °C, where at this temperature and above, a submicrometric structure is seen (figures 3.1e and f). The increase in particle size is accompanied by SSA reduction down to 1.0 $m^2 g^{-1}$ and density increase up to 78 % at 1450 °C. The samples sintered at 1400 and 1450 °C showed a light brown color in the surfaces exposed to the vacuum (where TiC is normally black). The sample at 1450 °C revealed the presence of the element O, which shows that the TiC samples are oxidizing in the current conditions. In this case, even though the oven was under vacuum the samples were just deposited on an alumina surface, which was likely the reason for such oxidation. (In this case graphite crucibles should have been used.)

3.1.2 Release studies

For isotope release studies only samples produced at a temperature > 1000 °C, with acceptable densities (< 80 %) and with at least a submicrometric structure were selected. In the TiC case, all samples were selected, whereas for TiO_2, only the one sintering at 1000 °C was selected. From 1 to 3 samples of each temperature were used for in release studies, to increase the statistical validity of the experiment.

The experimental method to study isotope release properties is explained in detail in section materials and methods of the article included in section 5.1 (page 133), where here, only a short description will be made: (i) the samples are first irradiated with protons at ISOLDE to produce the radioisotopes in the bulk of the material; (ii) the activity of each isotope is measured through gamma spectroscopy for each sample; (iii) a heat treatment is done for a short time (5 min), for each sample, with fast heating/cooling rates to promote release of the isotopes; (iv) the sample is measured again for radioisotope activity. The temperature for the isotope release is the same at which the sample was thermally treated, in order to limit microstructure evolution. The obtained activities are corrected for decay losses and compared before and after the thermal treatment. The corrected difference between the two activity measurements will dictate if a certain isotope was released and in which quantity.

The final results obtained for the release studies can be seen on figure 3.3, where the percentages of Be, Na, Mg, K or Sc released (released fraction, F) from each sample are shown. Ca was also monitored, but due to the very low activities the uncertainty in the results was too high to draw any conclusions. As observed from TiO_2 on figure 3.3, there is practically no release

of any elements at 1000 °C. Peräjärvi et al. [136] reports similar results for TiO_2 (for Mg) where, even when going up to 1380 °C there was no release (even though they saw very good release of sulfur at temperatures higher than 1000 °C, an element not studied here).

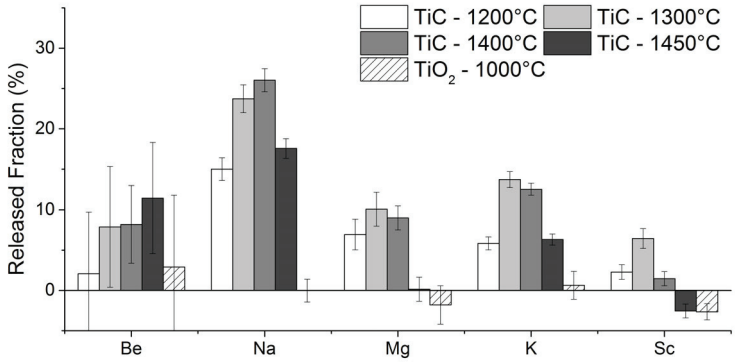

Figure 3.3 – Released fraction for Be, Na, Mg, k, Sc for TiO_2 at 1000 °C and for TiC from 1200 to 1450 °C.

TiC showed more promising results where even at temperatures as low as 1200 °C, which corresponds to the structure with the highest porosity and smallest grain size, there was some release. Sc is not released at any temperature likely due to the formation of scandium carbide with carbon from the TiC lattice. The release of TiC increases for all elements except Sc, with increasing temperature up to 1300 °C. Whereafter the release barely increases, within the error bars, compared with the increase from 1200 to 1300 °C. We believe that the TiC surface oxidation and/or the higher density (78 %) may be hindering the release.

When comparing the results obtained here, with those obtained in the literature for micrometric TiC (1-50 µm) at 2300 °C [84], indicates a big potential for our fine TiC. Release fractions of 30 % were obtained from K at 2300 °C [84] after 5 min, where in here release fractions up to 14 % were measured. Since diffusion has an Arrhenius dependence with temperature (equation 1.5, page 27), the result obtained shows great potential if the TiC particle size can be stabilized at higher temperatures. It was also the first time that Mg and Na release was reported for a Ti-based ceramic material [84, 62, 136].

3.2 Article: Development of a processing route for carbon allotrope-based TiC porous nanocomposites

Due to difficulties in stabilizing TiO_2, high sinterability and low release profile, this material was discarded from this work. TiC nonetheless, shows great potential and if a way is found to successfully stabilize the TiC particle sizes at higher temperatures this can make it a suitable and promising material for ISOLDE.

In the article draft presented in this section, a synthesis route is developed where the TiC

used so far is mixed with graphite, carbon black and multi-wall carbon nanotubes (MWCNT) in order hinder the TiC sintering and obtain smaller particles sizes than those obtained at 1500 °C. Precautions were also took in order to avoid oxidation of the TiC.

The article below, included in this thesis, is a draft to be submitted for publication in the Journal of the European Ceramic Society. The author of the thesis (first author) has written the manuscript (which was reviewed by the co-authors), did the great majority of the experimental work and analysis of the results. The figures and tables from this article are present in the list of figures and list of tables of the thesis with the numbering form of 3.ax, where x is the number of table/figure in the article. The supplementary materials of this article can be found starting on page 160 on the appendix section A.1.

Development of a processing route for carbon allotrope-based TiC porous nanocomposites

J.P. Ramos[a,b,*], A.M.R. Senos[c], T. Stora[b], C.M. Fernandes[c], P. Bowen[a,*]

[a] *Laboratory of Powder Technology, École Polytechnique Fédérale de Lausanne (EPFL), CH-1015 Lausanne, Switzerland*
[b] *European Organization for Nuclear Research (CERN), CH-1211 Genève 23, Switzerland*
[c] *Department of Materials and Ceramics Engineering, Universidade de Aveiro, CICECO, 3810-193 Aveiro, Portugal*

Abstract

Due to the enhanced release rates, porous nanomaterials are being studied as spallation target materials for radioactive ion beam production at CERN. These materials are operated under extreme conditions which include very high temperatures (up to 2300 °C) and high energy proton bombardment. Titanium carbide is a material with a very high melting point and thermal shock resistance making it an interesting material to replace the Ti foils currently used. The latter are usually operated very close to their melting point bringing sintering and/or melting which decreases the radioisotope production rates over time.

Because of sintering, porous nanometric TiC can't be maintained at very high temperatures. To overcome this, a new processing route was developed where TiC was co-milled with graphite, carbon black or multi-wall carbon nanotubes in different volume ratios in order to hinder the sintering of TiC. The influence of milling on the particle size distribution was studied for all materials using laser diffraction analysis and the best conditions were chosen to prepare the composites. The obtained nanocomposite particle sizes, density, specific surface area and porosity were characterized and compared using ANOVA - analysis of variance. All carbon allotropes mixed with the TiC, were able to successfully stabilize the nanometric TiC (primary particle size of 48 nm), hindering its sintering up to 1500 °C. At this temperature, the best composite was TiC-MWCNT with TiC grain sizes of 62 ± 26 nm and 37 % density followed by TiC-carbon black and TiC-graphite which were roughly 50 % dense and had grain sizes of 58 ± 29 nm and 85 ± 42 nm, respectively.

Keywords: nanocomposites, titanium carbide, spallation target, porous ceramics, high temperature applications

1. Introduction

Titanium carbide (TiC) is a well known FCC interstitial carbide and had its properties studied mainly during the 50s and the 60s [1]. Due to its high melting point (3067 °C), high hardness

*joao.pedro.ramos@cern.ch, paul.bowen@epfl.ch
URL: http://www.joaopedroramos.com (J.P. Ramos)

and strength, good thermal and electrical conductivities, thermal shock resistance, and low evaporation rate it is mainly used as a refractory ceramic. It is used in the aerospace industry (rocket and aircraft materials) and in super-hard and wear-resistant tools (as a cermet and as a coating material) [1, 2].

For nuclear applications, TiC has been studied as a coating material [3] or as a reinforcement in carbon for plasma facing materials [4] for future fusion plants. TiC has also been subject to numerous irradiation studies as a potential material for nuclear fuel coatings in fission power plants [5]. In the past, at the ISOLDE (Isotope Separator OnLine DEvice) facility at CERN [6], TiC was studied as a potential spallation target material for production of radioactive ion beams [7, 8].

ISOLDE relies on the on-line isotope separation method (Isotope Separator OnLine, ISOL) [6] to produce radioactive ion beams for nuclear, atomic, solid state and bio-physics studies. In this method, a target material kept at high temperatures in vacuum, is irradiated with energetic particles which will induce nuclear reactions in the material, producing isotopes. These isotopes have then to diffuse out of the material bulk to the surface where they evaporate and effuse through the material porosity. They then effuse through a transfer line into an ion source. The ion-source finally transforms the released isotopes into ions and shape a beam for physics experiments [9].

The target materials used for ISOL vary from liquids (low melting point metals or salts) to solids in powder, pellet or fiber form (carbides or oxides) or metallic foils [10]. The materials should be as pure as possible, since impurities can produce unwanted isotope contaminants, either through nuclear reactions or vaporization as radiologically stable contaminants. High target material operation temperatures are needed to accelerate diffusion and effusion processes while being limited by the material melting point, vapor pressure and sintering rates. A highly porous microstructure with the smallest particle size is desired, so the diffusion distances are shortened but it has to be stable at the highest operation temperature. Reducing the particle size of the target material either to submicrometric [11, 12] or nanometric [10, 12–14] has shown in the past, enhanced isotope release and, consequently, higher beam intensities. However nanometric materials tend to sinter readily so a particle size which allows for high diffusion/effusion and at the same time poor sinterability has to be found [13, 14].

In the past, micrometric TiC (1-50 μm) was discarded as a target material due to slow release of isotopes even at 2300 °C [7, 8]. Micrometric SiC (1-50 μm) was discarded as well for the same reasons [8], and in recent developments, by reducing SiC particle size to the sub-micron level (0.6 μm) the release of isotopes was shown to be improved [11, 12]. We believe that the same methodology can be used on TiC by reducing its particle size down to the submicron or nanometric level. Additionally, particle size stabilization mechanisms can be employed, so higher operation temperatures can be reached. Such mechanisms can be achieved by doping the TiC or by introducing a second highly-refractory inert phase, such as carbon, to reduce the coordination number of TiC particles and hinder its sintering.

Dual-phase sintering or constrained sintering is used in ceramics to prevent grain growth by having two homogeneously mixed and interpenetrating phases which have limited or no solid solubility with each other [15, 16]. There are examples in the literature where grain growth and densification was successfully hindered in ZnO-SiC [17] systems, Al_2O_3-ZrO_2 [16], and Al_2O_3-Cu [18]. For the TiC-C system a study done by B. Manley et al. [19] shows that additions up to 14 at.% (3.2 wt.%) of C, hinder the sintering of submicrometric TiC by reducing the relative volume changes by more than a factor of 2. Furthermore, in SiC, it has been shown that the addition of very small quantities of carbon (up to 3 wt.%) promote sintering (with 0.5 wt.% B) while further additions, studied up to 16 wt.%, successfully hinder its grain growth [20].

2

TiC-C (nano)composites can be found in the literature in a wide range of sizes (4 nm to tens of micron), shapes (fibers or particles) and different TiC volumes (5 vol.% to almost 100% TiC) [4, 21–32]. A considerable amount of the TiC-C studies are found for fiber shape where normally the carbon is a by-product from the TiO_2 carbothermal reduction with C. Such fibers are used in reinforced polymers (with 300 nm fiber diameter [21]), semiconductor films (tens of micron diameter fiber [22]), filtration membranes (120 nm mesoporous fibers with 19 nm TiC crystallites [23]), solar cells (200-400 nm fiber diameter with 20 nm TiC crystallite size, 70wt.% TiC [24]) and for supercapacitors (280 nm diameter fibers, TiC crystallite size 20-50 nm, 40 wt.% TiC [25]). In the rest of the studies found, TiC-C composites include application in electrodes and catalysis (4 nm TiC, 30 wt.% Ti as membranes [26] or 35 nm TiC-C core-shell particles [27]), fuel cells (25-75 wt.% of micrometric TiC in C as coating [28]), as high temperature structural material (tens of micron TiC with 2-40% of C, 15% porous to fully dense [29–31] or with 100 nm TiC crystallite size, 30% porous with 9/1 - Ti/C molar ratio [32]) and for nuclear applications (5 vol.% ≈100 nm TiC inclusions in graphite [4]).

The sintering driving force is provided by the decrease of the free energy of the system which depends on the total free surface and particle radius and curvature. As such, the sintering kinetics of nanomaterials are enhanced when compared to conventional materials, because of their intrinsic high surface areas. While conventional powders are expected to sinter at about 0.5-0.8 T_m (T_m being the material melting point), in nanomaterials this can happen at 0.2-0.4 T_m [33]. In the literature, TiC powders with 140-170 nm primary particle size, reached 91 % density at 1627 °C while 5 µm TIC powders needed 2797 °C for the same density [34]. Furthermore, nanopowders are often found in an agglomerated form, having a bimodal pore size distribution: small intra-agglomerate and large inter-agglomerate pores [35]. While the small pores from the intra-agglomerate porosity are easily eliminated during sintering, the large inter-agglomerate pores require significantly higher temperatures to be removed. The sintering temperature of nanomaterials often scales up with the agglomerate size, rather than with the primary particle size [33].

Although, TiC-C composites already exist in the literature their processing is either too complex or not suitable for the application described here. Moreover, the structure required is one which should be stable at high temperatures (at least 1500 °C) while keeping nanometric TiC, which wasn't found in the literature. Additionally, the simplest processing route should be used to reduce and control the possible sources of contamination to the target material. Since the titanium is the element of interest (selected due to the high isotope production cross-sections), one wants the highest concentration as possible while keeping acceptable levels of open porosity. Also, the processing route must be easy to scale up, since TiC targets are expected to have up to 100 g of material depending on the TiC % present. As a result, in order to stabilize nanometric TiC (≈100 nm) a new processing route is developed here where different carbon allotropes (graphite, carbon black and carbon nanotubes) with different volume ratios were added to the TiC. The TiC-C composites obtained were characterized before and after heat treatments in order to assess the degree of stabilization of nanometric TiC.

2. Materials and methods

2.1. Materials

Commercially available nanometric TiC powder was acquired from *Goodfellow*, 99.9% pure, with nominal particle sizes between 80-130 nm (Ref. LS396999/1). The carbon allotropes used

were: graphite (*Alfa Aesar*, Ref. 40798, 325 mesh - <44 μm), carbon black (*Orion Engineered Carbons*, *Printex A Pulver*, 40 $m^2\ g^{-1}$ - 40 nm primary particle size) and multi-wall carbon nanotubes, MWCNT, (*Nanocyl*, Ref. NC3100, >95% purity, 10 nm diameter, 1.5 μm length). The mixtures were done in isopropanol, IPA, (from *Reactolab SA*, Ref. 99295, 99 % pure) using polyvinylpyrrolidone, PVP, (*Fluka*, K-30 mol.wt 40k) as a dispersant for the TiC and the allotropic carbon materials [36]. The characteristics of the raw materials can be found in table 1 and scanning electron microscope microscopy (SEM) microstructures on figure 1.

Table 1: Characteristics of the raw materials used in this study, where SSA is the specific surface area, P_S is the median pore size, $v_{P,BJH}$ is the pore volume (both determined by BJH) and $D_{v,50}$ is the average particle size.

Characteristic	TiC	Graphite	Carbon Black	MWCNT
Density ($g\ cm^{-3}$)	4.93 [37]	2.16 [37]	1.85 [a]	2.16 [b] (0.15 [a] - bulk)
Dimensions	80-120 nm[a]	<44 μm [a]	≈40 nm [a]	9.5 nm×1.5 μm [a]
SSA ($m^2\ g^{-1}$)	25.1	2.1	36.9	293.1
G_{BET} - k_S [c]	48 nm - 6	5.3 μm - 24	88 nm - 6	-
P_S (nm)	41	62	70	38
$v_{P,BJH}$ ($cm^3\ g^{-1}$)	0.07	0.02	0.43	2.70
$D_{v,50}$ (μm)	1.70	33.17	0.46	42.79
A_F [d]	35.4	6.3	5.2	n.a.

[a] Given by supplier.
[b] Graphite density assumed for MWCNT theoretical density.
[c] $G_{BET} = k_S/(SSA*\rho_t)$, where G_{BET} is the particle size and k_S is a parameter depending on the shape; $k_S = 6$ - for spheres; $k_S = 24$ - for 1:10 flakes [38].
[d] $A_F = D_{v,50}/G_{BET}$ and represents the agglomeration factor [38].

2.2. Methods

2.2.1. Processing

The TiC-C composites were co-milled using an attrition mill (*Union Process, 01HD*) at 800 rpm in a small volume grinding bowl (70 ml) using 1.5 mm yttrium-stabilized-zirconia (YSZ) milling balls. The milling suspension was added to the grinding bowl with 2.6 vol. % of solids in IPA containing 0.5 wt. % PVP and 130 g of YSZ balls were added to fill the grinding bowl up to 90 %. Preliminary studies on the milling of the raw materials were done interrupting the milling process at defined times to take small samples. After these studies and optimizations, 2 h was defined as milling time to produce the TiC-C composites. In the case of the MWCNT, the bulk density (see table 1) was used to calculate the MWCNT solid volume, because they dominate the mixing behavior. The carbon volumes tested were 25, 50 and 75 vol. %.

In the case of the MWCNT composites an additional composite was produced where the MWCNT were not co-milled with the TiC. This composite, was produced by milling the TiC for 2 h separately and later mixed with MWCNT which were treated by ultrasonication for 15 min beforehand. The TiC milled suspension was added to the MWCNT suspension and sonicated for a further 30 min.

After the milling/mixing process, the suspensions were dried using a rotary evaporator (*Buchi Rotovapor R-114*), at 80 °C in vacuum with constant agitation to avoid segregation of the TiC from the carbon. The obtained powder was deagglomerated manually using an agate mortar and pestle, and pressed into 12 mm cylindrical compacts with 1-2 mm thickness, in a hydraulic press at 62 MPa.

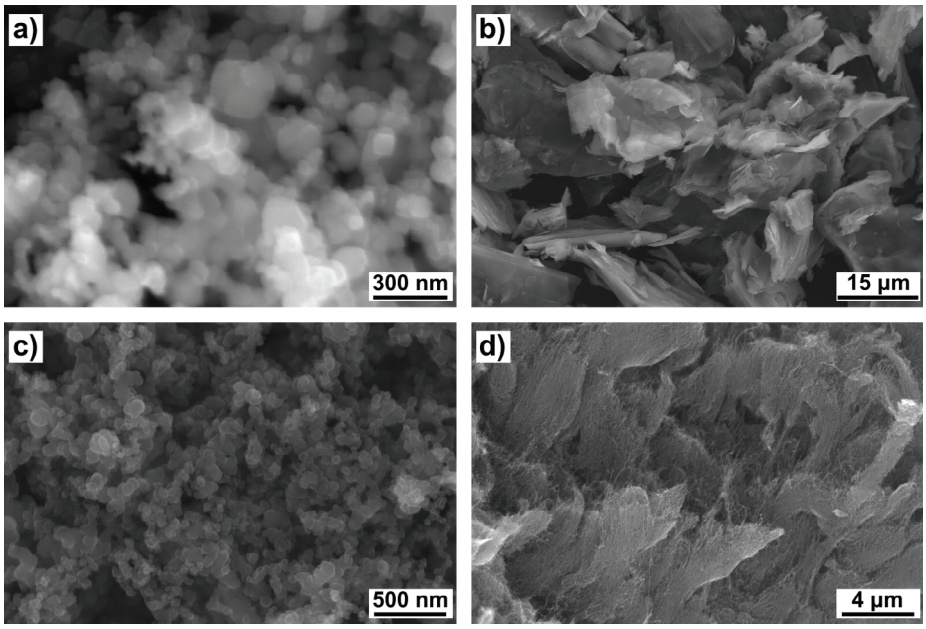

Figure 1: SEM microstructures of the raw materials used in this study: TiC (a), graphite (b), carbon black (c) and MWCNT (d).

In order to remove the PVP, the powder compacts were pre-heat treated under a flowing argon atmosphere at 450 °C for 3 hours (3 °C min^{-1}, heating and cooling) in a quartz tube which was inserted in an horizontal alumina *Heraeus* oven [36]. The samples were then heat treated at 1500 °C in vacuum with holding times of 2 and 10 h with 8 °C min^{-1} heating/cooling ramps. The oven used was a *Carbolite STF 15/450* horizontal alumina tube oven, adapted with in-house made flanges to allow vacuum, which was connected to an *Agilent TPS-mobile TV301* pumping station. Overall, the pressure reached at 1500 °C was around 10^{-3} - 10^{-4} Pa. To protect the samples from oxidation and minimize carbon losses (due to residual presence of oxygen), in addition to the vacuum atmosphere, a specially built double layer graphite crucible was designed to introduce the samples (see figure A.1.2 in supplementary material).

2.2.2. Characterizations and data handling

The particle size distributions (PSD) and median volume diameter ($D_{v,50}$) during the milling tests, were measured using laser scattering in a *Malvern Mastersizer S*. Before the measurements, the suspensions were ultrasonicated for 15 min. For the laser scattering PSD measurements, the refractive indexes used were 1.38 for the IPA [37], 3.05+2.67i for TiC [39], 1.84+0.46i for carbon black [40], 2.13+1.11i for graphite [40] which was also used for the MWCNT. The cylindrical powder compacts were measured and weighed in all steps to check for geometrical density (ρ) changes ($\Delta\rho/\rho_0$) and mass losses. Nitrogen adsorption-desorption isotherms were done in a *Quantachrome eNOVA2200*, using the BET (Brunauer-Emmett-Teller) model [41] for specific surface area (SSA) and the BJH (Barrett-Joyner-Halenda) model [42] to determine the pore size distributions and pore volumes ($v_{P,BJH}$) limited up to 200 nm from the desorption branch of the isotherm. The pores were assumed to have a cylindrical shape and the average median volume

diameter ($D_{Pv,50}$ or simply pore size, P_S) was determined from the cumulative size distribution obtained from the BJH model. The sample microstructures were obtained using an in-lens detector on a *Carl Zeiss SMT* Σ*igma* scanning electron microscope (SEM). In selected samples the particle size was measured directly from the SEM images (G_{SEM}), measuring 400 particles per sample, using *ImageJ* v1.50 [43]. The samples were also studied by dilatometry in an homemade vertical graphite dilatometer, that could reach 1500 °C and was equipped with an LVDT sensor (linear variable differential transformer) to measure sample linear variation with temperature - shrinkage ($\Delta l/l_0$). The oven was connected to a primary oil rotary vacuum pump that could reach 1 - 10^{-1} Pa. The heating rate was 8 °C min^{-1}.

Since all the composites have different initial characteristics, only a comparison in terms of relative evolution of the initial characteristics is possible. $\Delta\rho/\rho_0$, the pore size variation below 200 nm ($\Delta P_S/P_{S,0}$) and SSA (S) variation ($\Delta S/S_0$) before and after the 2 and 10 h thermal treatments at 1500 °C were calculated in the following way:

$$\Delta X/X_0 = (X - X_0)/X_0 \tag{1}$$

where X is replaced by either ρ, S or P_S, the measured value after heat treatment and X_0 can be replaced by ρ_0, S_0 or $P_{S,0}$, the same characteristic before the heat treatment.

The experiments were organized in a statistical design with 2 samples for each thermal treatment (1500 °C - 2 and 10 h) for each composite. A schematic with the statistical design can be found on figure A.1.1 on supplementary materials. The results were analysed by factorial ANOVA, statistical analysis of variance [44] in order to study the evolution of the described characteristics with the carbon allotrope and volume ratio added to the TiC.

Samples were named X{carbon} where X is vol. % of carbon added and {carbon} is the carbon allotrope added: CB, Gr, CNT and TiCm standing for the carbon black, graphite, MWCNT and TiC milled without carbon, respectively. So, for example, 50Gr corresponds to the 50 vol. % graphite mixed with TiC. For the case where the MWCNT were not co-milled with the TiC this sample will have a {Carbon} name as CNTb.

3. Results and discussion

The carbon allotropes were chosen in order to have as different a size and morphology as possible. This was done in order to be able to assess the TiC sinterability when mixed with the carbons. The G_{BET} value obtained for TiC (48 nm) and carbon black (88 nm), on table 1, confirm the nanometric nature given by the suppliers. As expected, MWCNT present the highest pore volume below 200 nm - $v_{P,BJH}$ - (2.70 cm^3 g^{-1} on table 1) followed by carbon black (0.43 cm^3 g^{-1}) and titanium carbide (0.07 cm^3 g^{-1}) where P_S, in all values don't differ too much. Graphite was obtained in micrometric form so it presents very little $v_{P,BJH}$ (0.02 cm^3 g^{-1} and high G_{BET} (5.3 µm).

In total, during this study, 11 materials were produced and heat treated (sintered) at 1500 °C for 2 and 10 h: TiC, TiCm, 25Gr, 50Gr, 25CB, 50CB, 75CB, 25CNT, 50CNT, 75CNT, 75CNTb. Only 5 of the produced materials were selected to be discussed in this article: TiC, TiCm, 50Gr, 50CB and 75CNTb (and partially 75CNT). The results of the other composites, which don't add value to the discussion, can be found in supplementary material, A.1.2.

In the following subsections the milling optimization will be firstly discussed, as well as its influence on the agglomerate size of TiC, which affects its sinterability. Then, in order to serve as a comparison for the nanocomposites, the sintering behavior of TiC at high temperatures will

be discussed. Finally, the influence of each carbon allotrope (Graphite, CB and MWCNT) on the sintering of TiC will be discussed independently and compared with the other composites. This will be done by following the evolution of the composite characteristics, ρ, SSA and $P_{S,0}$ as well as microstructure morphology together with dilatometry. Relative density (ρ_r) and porosity were also used to characterize the nanocomposites. The porosity ($P_r = 1 - \rho_r$) was divided in porosity below 200 nm ($P_{r,<200\,nm}$), determined from $v_{P,BJH}$, and porosity above 200 nm ($P_{r,>200\,nm}$), determined from the later and the relative density. The calculation of ρ_r, $P_{r,<200\,nm}$, $P_{r,>200\,nm}$ can be found in supplementary material A.1.1.

3.1. Milling influence on the raw materials

The lowest possible degree of agglomeration is desired to have homogeneous mixtures for the synthesis of the nanocomposites. Laser scattering is able to detect agglomerates (assemblies of primary particles) giving an agglomerate size distribution, represented by $D_{v,50}$. G_{BET} is more indicative of primary particle size since it is not very dependent on the degree of agglomeration as it is determined from the total SSA. The ratio of these two parameters, $D_{v,50}$ and G_{BET}, can be used to determine the agglomerate factor, A_F, as shown on table 1.

As seen in figure 1, all powders look to be in an agglomerated form, especially those with higher surface areas (and of nanometric nature - namely TiC, CB and MWCNT, see table 1). While both CB and TiC look to be heavily agglomerated in the SEM figures (figure 1a and c respectively) their A_F is quite different, 6.3 and 35.4 respectively as seen on table 1. This is likely related with the nature of those agglomerates, where in TiC case they are more difficult to break during the sample preparation for laser scattering by agitation and sonication.

The particle size distribution was used to follow the milling of the raw materials in order to find the best parameters. The powders were individually milled up to 4 h and particle size distributions were taken at the beginning and at 0.5, 1, 2, 3 and 4 h of milling, to assess the agglomerate distribution. The results of these tests can be seen in figure 2.

During attrition milling, titanium carbide $D_{v,50}$ changes from 1.70 µm to 300 nm in the first hour of milling, stabilizing in the 300 to 400 nm range for longer milling times, as seen in figure 2a. For graphite, $D_{v,50}$ keeps reducing for longer milling times, from 33.17 µm to 14.05 µm for 4 h (figure 2b). In the case of CB, the milling is very efficient in destroying the CB agglomerates, where, after 4 h of milling, the $D_{v,50}$ (110 nm on figure 2c) almost matches the primary particle size value on table 1 - G_{BET}=88 nm.

There is a very significant impact of the milling on the MWCNT where, on figure 2d, the $D_{v,50}$ is changing from 42.79 µm (an highly agglomerated state - as seen by SEM on figure 1d) to 0.06 µm only after 2 h of milling. At 2 h of milling of MWCNT, the cumulative size distribution shows that around 50 % of the particles is below 50 nm, meaning that it can't be detected. Although this technique is not ideal to measure the MWCNT sizes, due to their shape, figure 2d seems to indicate that the MWCNT are being destroyed ("chopped") during the milling process, as has been seen in other studies [45].

When co-milled with TiC (75CNT) and heat treated at 1500 °C for 10 h, the MWCNT are barely visible, in the SEM microstructures of figure 3a and b) before and after the heat treatment. In order to overcome this, another mixing method for the TiC-MWCNT composite was tried: mill TiC first and then add a suspension of MWCNT after without milling, just after agitation and ultrasound. The resulting SEM microstructures are on figures 3c and d, which correspond to as produced material (75CNTb) and heat treated at 1500 °C for 10 h. In both cases, before

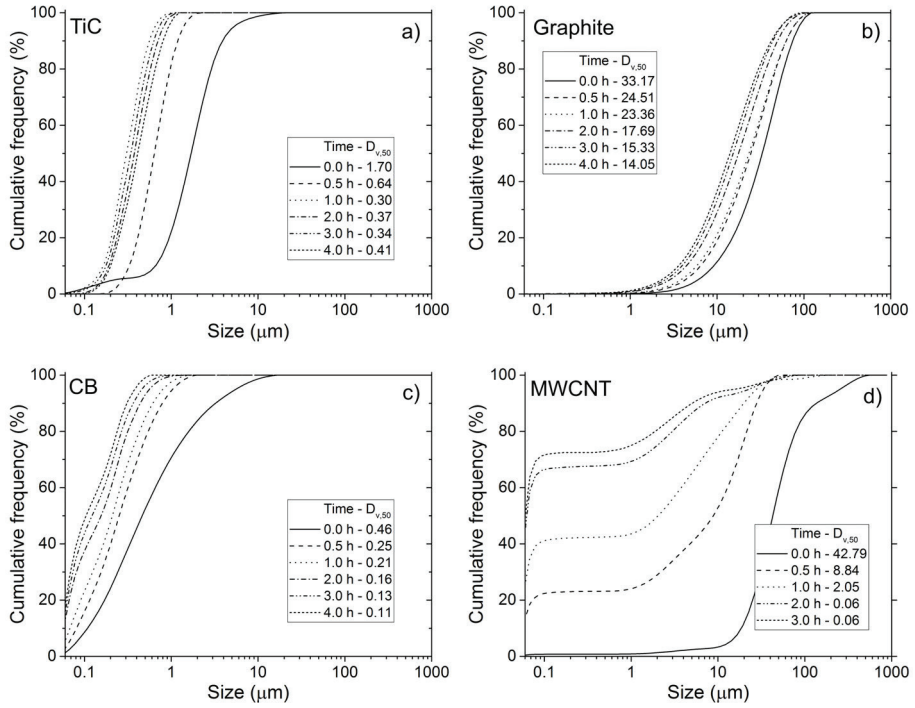

Figure 2: Particle size distributions for different milling times and respective $D_{v,50}$ values in μm for (a) TiC, (b) graphite, (c) carbon black (CB) and (d) MWCNT.

and after the heat treatment, there are more MWCNT visible on 75CNTb than on 75CNT[1]. The MWCNT milling ("chopping") has a detrimental effect on the TiC sintering hindering as well, as will be briefly discussed later on. Thus, only 75CNTb nanocomposites were chosen to be discussed further in this article.

A contamination of 3 to 6 % of ZrO_2, determined by XRPD (X-ray powder diffraction), was found in all as produced nanocomposites, coming from the wear of the milling media due to the hard nature of TiC. After the thermal treatments at 1500 °C the ZrO_2 was reduced to ZrC, as expected due in the presence of carbon[2]. Although not in the scope of this paper, this reduction is the cause of the somewhat high mass losses - 11,12 and 13 % for graphite, CB and MWCNT nanocomposites, respectively, obtained after heat treatments, when comparing to TiC only, ≈6 % mass losses.

The milling was seen to have an effect on the TiC sintering with no carbon addition. A TiC sample was milled for 2 h (named TiCm), heat treated at 1500 °C for 10 h, together with a non-milled sample. The results of the heat treatment can be seen on figure 4a) for TiC and b) for TiCm. Although TiC and TiCm had the same thermal cycle, they have distinct morphologies. TiC have G_{SEM} of about 738±254 nm and TiCm around 314±108 nm which are close to their

[1]More information on the properties of 75CNT can be seen on figures A.1.8 and A.1.4 and table A.1.1 on supplementary material A.1 and can be compared with 75CNTb presented throughout this article.

[2]Refer to figure A.1.3 in the supplementary materials A.1.2 for an XRPD characterization

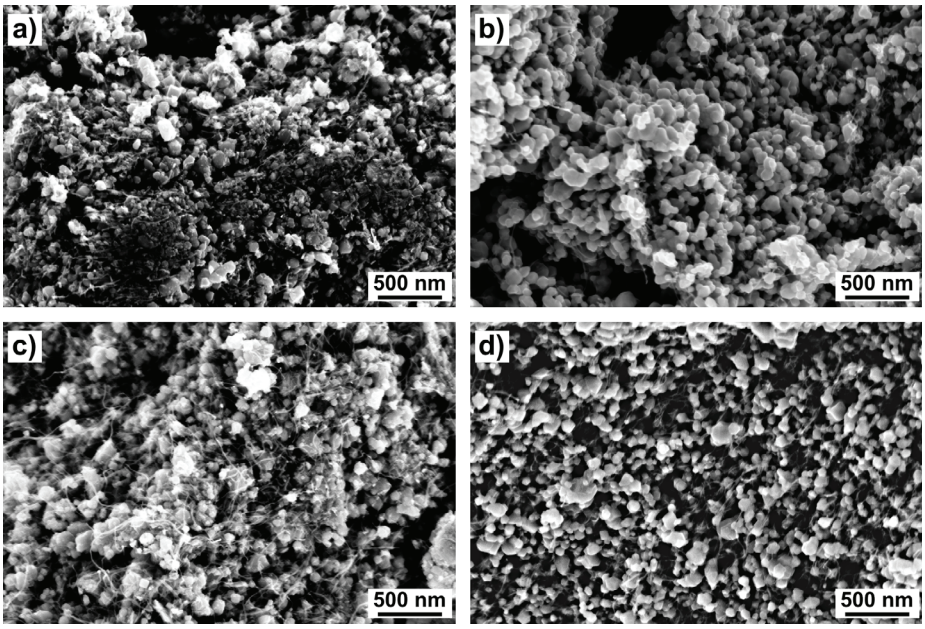

Figure 3: SEM microstructures of 75CNT as produced (a) heat treated at 1500 °C for 10 h (b) and of 75CNTb (MWCNT not milled) as produced (c) and heat treated at 1500 °C for 10 h (d). For the latter, G_{SEM} is 62±26 nm.

$D_{v,50}$ values as measured by laser scattering: 1.70 µm for TiC and 0.37 µm for TiC milled for 2 h (figure 2a - milling times of 0 h and 2 h). The discussion of this phenomena will be done in the next subsection.

In the case of TiC milled for 2 h (hereinafter TiCm), the SSA was determined (29.4 $m^2\ g^{-1}$), from which the G_{BET} is calculated to be 41 nm. This gives an A_F for TiCm of 9.0 showing a significant reduction of the TiC agglomeration (A_F of 35.4 for TiC) through attrition milling. Since little influence on TiC $D_{v,50}$ was seen at longer milling times, these milling settings were chosen for the nanocomposites production.

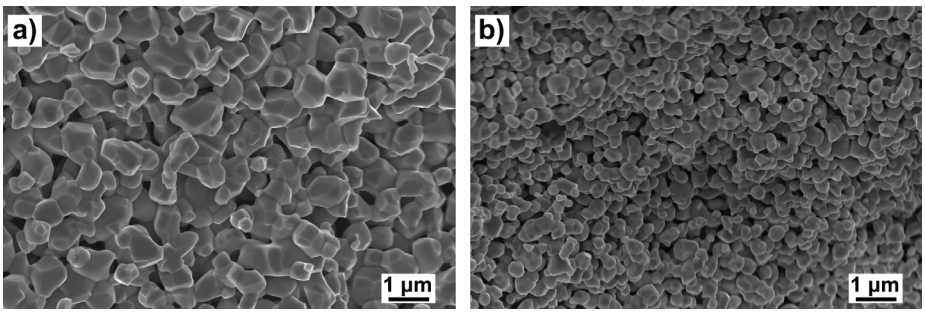

Figure 4: SEM microstructures of TiC heat treated at 1500 °C for 10 h (a) and of TiC milled, TiCm, for 2 h and with the same heat treatment (b). G_{SEM} is 738±254 nm for TiC and 314±108 nm for TiCm.

3.2. Titanium carbide sintering behaviour

Milled and non-milled TiC was subjected to the same heat treatments as the produced nanocomposites, as control samples. In figure 4 the milling seems to have an hindering effect on the grain growth of TiC at 1500 °C. Both show grain sizes similar to the agglomerates size measured by laser diffraction, indicating that the primary particles in the agglomerates sinter and then sintering between, the non dense agglomerates starts.

The control chart of figure 5a was built using analysis of variance (ANOVA), in order to assess statistical significant differences on the characteristics studied. $\Delta\rho/\rho_0$ is shown for TiC and TiCm for the heat treatments at 1500 °C for 2 and 10 h and the rest will be discussed later. In this figure the average values (triangle), the adjusted values from ANOVA (column) and respective 95 % confidence intervals (column error bars) are represented. In figure 6, the obtained ρ_r and P_r, for TiC and TiCm can be found (the nanocomposites will be discussed later). In this figure, the P_r was divided accordingly to pore size: porosity below ($P_{r,<200\,\mathrm{nm}}$) and above 200 nm ($P_{r,>200\,\mathrm{nm}}$)[3] (also presented on table 2).

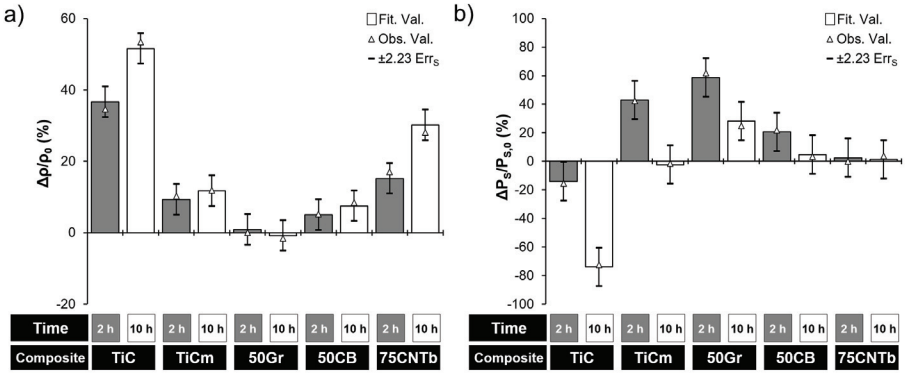

Figure 5: TiC, TiCm, 50Gr, 50CB and 75CNTb $\Delta\rho/\rho_0$ (a) and $\Delta P_s/P_{s,0}$ (b) for heat treatments at 1500 °C for 2 and 10 h. The error bars correspond to the standard error of the mean ($\mathrm{Err_S}$) - 95 % confidence intervals - for the adjusted values (columns) obtained by ANOVA - analysis of variance.

In the control chart of figure 5a there is a significant difference between the TiC and TiCm density variations ($\Delta\rho/\rho_0$), being about 4 times smaller in the case of TiCm. This is seen as well in the values of the relative density, ρ_r in figure 6: while TiC ρ_r goes from 48 to 73 % for 10 h, TiCm densifies much less, from 46 to 53 % (absolute densities are found in table 2). In the dilatometry of figure 7 both TiC and TiCm seem to start sintering at the same temperatures, ≈1100 °C. While TiC reaches linear shrinkage values of 12 %, TiCm shrinks much less, up to ≈4 %. TiC sinters continuously with no rate decrease while TiCm shows some shrinkage before 1100 °C and rate changes around 1200 and 1400 °C which is likely due to mass losses due to the presence of ZrO_2 milling contaminants (to be addressed in another publication [46]).

In order to discuss the porosity evolution, a simple phenomenological 3 stage model is proposed:

1. as known for nanomaterials, sintering starts predominantly within the agglomerates, due to the high free energy and particle coordination number, reducing and eliminating the small

[3]For details about the calculations of $P_{r,<200\,\mathrm{nm}}$ and $P_{r,>200\,\mathrm{nm}}$ please refer to the supplementary material A.1.1

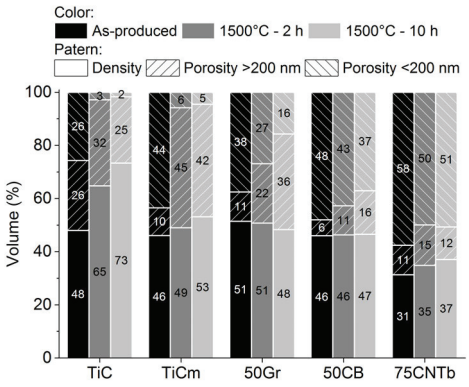

Figure 6: Relative density and porosity ratios (below and above 200 nm) for the TiC, TiCm, 50Gr, 50CB and 75CNTb as produced and heat treated for 2 and 10h.

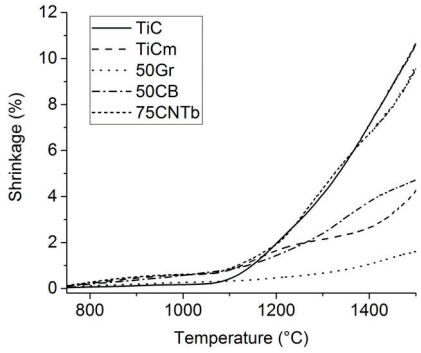

Figure 7: Dilatometry of TiC, TiCm, 50Gr, 50CB and 75CNTb up to 1500 °C.

intra-agglomerate porosity ($P_{r,<200\,\mathrm{nm}}$); this will likely happen with small changes to ρ_r (coalescence - surface diffusion) [33, 35, 47, 48];

2. when the intra-agglomerate porosity is reduced or gone, and a network of big pores is formed (once inter-agglomerate porosity, here $P_{r,>200\,\mathrm{nm}}$), stabilizing the structure, sintering will progress at a slower rate; an increase in the BJH pore size (P_S) may be seen because large pores shrink into sub 200 nm pores and thus they can be detected by the technique;
3. the microstructure densification will continue, bringing further reduction of relative pore volumes ($P_{r,>200\,\mathrm{nm}}$ and $P_{r,<200\,\mathrm{nm}}$) and size (P_S); if the temperature is high enough, sintering will continue until full densification is achieved.

For 2 and 10 h at 1500 °C for both TiC and TiCm cases, almost all of $P_{r,<200\,\mathrm{nm}}$ is disappearing, which points to the stage 1 of the model proposed. However, in the case of TiC for both 2 and 10 h there is significant densification (as seen in figure 6) which point to the stage 2 of the model already. In both cases, from the as produced sample to the heat treated for 2 h $P_{r,>200\,\mathrm{nm}}$

Table 2: Density (ρ), SSA, median pore size (P_S), BJH pore volumes ($v_{P,BJH}$), SEM particle sizes determined with *ImageJ* (G_{SEM}) and mass losses ($\Delta m/m_0$) of TiC, TiCm, 50Gr, 50CB and 75CNTb as produced and after heat treatments at 1500 °C for 2 and 10 h.

		TiC	TiCm	50Gr	50CB	75CNTb
ρ (g cm^{-3})	As produced	2.37	2.27	1.87	1.60	1.41
	1500 °C - 2 h	3.19	2.44	1.89	1.69	1.65
	1500 °C - 10 h	3.61	2.64	1.81	1.70	1.79
SSA (m^2 g^{-1})	As produced	25.1	29.4	32.6	37.5	49.8
	1500 °C - 2 h	1.5	3.2	13.1	21.2	27.0
	1500 °C - 10 h	0.5	2.1	11.9	21.1	23.6
P_S (nm)	As produced	41	27	27	33	27
	1500 °C - 2 h	35	39	44	40	27
	1500 °C - 10 h	11	27	34	37	28
$v_{P,BJH}$ (cm^3 g^{-1})	As produced	0.07	0.16	0.17	0.27	0.30
	1500 °C - 2 h	0.01	0.01	0.10	0.20	0.21
	1500 °C - 10 h	0.00	0.01	0.05	0.16	0.21
$\Delta m/m_0$ (%)	1500 °C - 2 h	6.2	6.6	9.4	10.9	10.6
	1500 °C - 10 h	6.9	7.2	10.5	11.3	12.8
G_{SEM} (nm)	1500 °C - 10 h	738±254	314±108	85±42	58±29	62±26

increases (especially for TiCm), which seems to indicate that at some point, there is coarsening of the microstructure with little densification. This phenomena is common during the initial stage sintering of nanometric particles, due to the large surface areas, through surface diffusion [33, 35, 47, 48].

On figure 5b the pore size evolution ($\Delta P_S/P_{S,0}$) treated by ANOVA is also shown. For TiC and TiCm the $\Delta P_S/P_{S,0}$ is distinct: while in TiC it reduces for 2 h at 1500 °C and further reduces for 10 h, for TiCm it first increases for 2 h and is zero for 10 h (showing a decrease relatively to 2 h value). The absolute P_S can be seen in table 2. For the TiCm heat treated for 2 h, this seems to indicate that we just passed the 1st stage (pore size increase) and for 10 h we are going towards the 3rd stage. In contrast, since the inter-agglomerate pores of TiCm are expected to be smaller (smaller agglomerates), once agglomerates sinter, they shrink to sizes below 200 nm and can be detected BJH. This could give an idea of an increase in pore size as seen in figure 5b, for TiCm 2 h. In the case of TiC, for both heat treatments, where constant reduction of pore size is seen on figure 5b, the 3rd stage is dominant, confirmed by the large relative density values on figure 6.

Although in the literature reducing the agglomerate size of nanometric powders is known to increase their densification [35] (and so sintering kinetics), such is not seen in the data presented here. In our case TiC densifies more than TiCm, even though it has a larger agglomerate sizes. When the agglomerates sinter, this will create a network of large pores (once inter-agglomerate pores) which reduce the sintering rate. As in the TiCm case this is likely to happen faster (at lower temperatures), since the agglomerates are smaller and the rate is reduced sooner, because a network of large pores is created. If higher temperatures would be used, very likely the TiCm would densify sooner than TiC, because of the smaller grain sizes. Furthermore, the introduction of Zr in the case of TiCm, could act as a dopant that hinders the sintering, thus explaining the lower densities obtained, however no studies in the literature can be found in this subject.

The SSA evolution ($\Delta S/S_0$) with heat treatment for 2 and 10 h can be seen on figure 8, and the absolute SSA values are in table 2. For both TiC and TiCm the $\Delta S/S_0$ are negative (SSA reduction) and very high (>90 %), especially for TiC. In the case of TiCm heat treated for 2 h at 1500 °C, SSA reduction of ≈90 % is accompanied by small densification - from 46 to 49 %

(figure 6). Large SSA reductions and small densifications are a sign of prevalent coarsening of the structure, which shows that a non-densifiying sintering mechanism, such as surface diffusion, is dominant in the sintering. As referred before, this is very common in initial stage sintering of nanomaterials [33, 35, 47, 48].

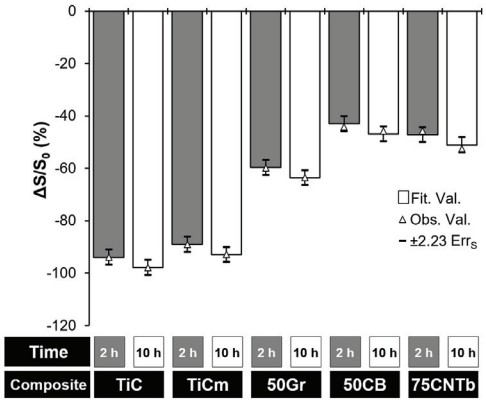

Figure 8: TiC, TiCm, 50Gr, 50CB and 75CNTb $\Delta S/S_0$ for heat treatments at 1500 °C for 2 and 10 h. The error bars correspond to the standard error of the mean (Err_S) - 95 % confidence intervals - for the adjusted values (columns) obtained by ANOVA - analysis of variance.

3.3. TiC-graphite composites

The 50 vol.% graphite-TiC composite (50Gr) SEM microstructures as produced and heat treated at 1500 °C for 10 h can be seen in figure 9a and b respectively. Comparing these microstructures, it can be seen that the TiC has grown in particle size, but not even near to the TiC or TiCm cases (figures 4a and b). Furthermore, G_{SEM} was determined to be be 85±42 nm. Consequently, already with the SEM microstructures it is clear that TiC sintering is hindered by a large extent by graphite.

Since the graphite SSA is small when compared to TiC (table 1) and graphite particle size isn't drastically affected during milling, the main contribution to the SSA of 50Gr (32.6 $m^2\,g^{-1}$ - table 2) comes from the TiC. When heat treating the 50Gr (2 and 10 h), the $\Delta S/S_0$ values (figure 8) are both around −60 %. This SSA reduction can only be due to the TiC sintering, since graphite particles are not expected to sinter. Although reduced, the percolation of the TiC particles in 50Gr is still present in between the graphite particles, as can be seen in the SEM microstructure of figure 9a. As a result TiC-TiC contacts will have a constrained sintering, which results in a reduction of the SSA ($\Delta S/S_0$). Furthermore the $\Delta S/S_0$, from 2 to 10 h at 1500 °C, is not changing much which indicates that the TiC is not sintering anymore. As a result, TiC particle size of G_{SEM} = 85±42 nm seems to be stabilized at this temperature.

Regarding the composite densification behavior, there is no appreciable densification of the 50Gr composites as seen from the $\Delta\rho/\rho_0$ values (figure 5a) which are close to zero. The dilatometry of the 50Gr also confirms the very low shrinkage, below 2 % in this case. The almost non existent densification of 50Gr is very likely due to the size of the graphite particles which are around 2 orders of magnitude larger than the TiC, creating a very stable, non-sinterable skeleton for the microstructure.

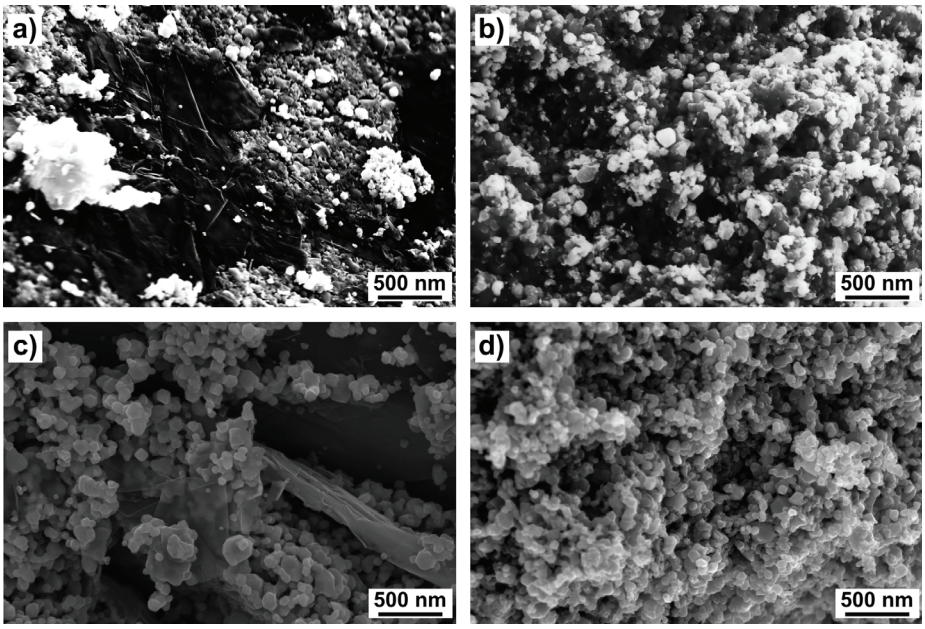

Figure 9: SEM microstructures of 50Gr before (a) and after (c) heat treatment at 1500 °C and of 50CB before (b) and after (d) the same heat treatment. For 50Gr and 50CB after 1500 °C, G_{SEM} is 85±42 nm and 58±29 nm, respectively.

The small $P_{r,>200\,\mathrm{nm}}$ of 50Gr before heat treatment is low (figure 6) which shows that the mixing was successful since there is a good filling by TiC of the big pores created by the graphite particles. Otherwise, one would expect large pores from the graphite micrometric size. The relative surface area $\Delta S/S_0$ values don't change from 2 to 10 h (figure 8), whereas the $P_{r,>200\,\mathrm{nm}}$ and $P_{r,<200\,\mathrm{nm}}$, increase and decrease respectively (figure 6). This shows that there is still sintering happening among the TiC particles which can only progress where TiC-TiC contacts exist but progresses slowly due to the reduced TiC coordination number. In addition, on figure 5b, both 50Gr $\Delta P_S/P_{S,0}$ are seen to be positive, where the 10 h value is smaller. The increase in the pore size for 50Gr sintered for 2 h, shows that we are on the 1st stage of the model proposed, where the agglomerates are sintering, but slower than in the case of TiCm, due to a lower TiC coordination number. A reduction in the pore size is seen for 50Gr at 10 h (when comparing to 50Gr 2 h) showing that sintering is now on the 2nd stage of the model (network of big pores formed). Here the sintered TiC agglomerates are sintering with each other, which, once again, is hindered by the presence of graphite.

3.4. TiC-carbon black composites

Figures 9c and 9d show, the microstructures of the 50CB before and after 1500 °C - 10 h, respectively. It is difficult to identify the TiC from the carbon black particles, due to their similar particle size. Furthermore, little to no changes are seen before and after heat treatment, showing that CB is very effective hindering the TiC sintering. Even though CB could not easily be distinguished from the TiC, the G_{SEM} was still determined - 58±29 nm. Although the later value is affected by the carbon black particle size, observing figures 9d no considerable big particles are seen, so the determined value can work as an estimate for the TiC. Since both TiC and CB are

similar in particle size, if homogeneously mixed CB should reduce the TiC coordination number significantly which, as seen, hinders its sintering.

Similarly to the 50Gr, the density variations, $\Delta\rho/\rho_0$, are quite small (up to 8.5 % in the case of 50CB for 10 h). Curiously, the dilatometry of 50CB on figure 7 shows small shrinkage but close to the ones of TiCm. Both, at around 1400 °C, present changes in the shrinkage rate: in the case of TiCm the shrinkage rate is increasing while for 50CB it is decreasing (effect of the carbon black addition).

High values of $P_{r,<200\,\mathrm{nm}}$ are kept at 1500 °C for 2 and 10 h for the 50CB composites, as seen on figure 6. Also, the BJH pore size of 50CB is not changing much with the heat treatments (figure 5b). As both materials are nanometric and the mixture homogeneous, one does not expect big changes either in pore volume or pore size since the structure is sintering little. Nonetheless, in figure 6, there is a small increase of the $P_{r,>200\,\mathrm{nm}}$ towards higher heat treatment times, showing that TiC-TiC contacts still exist.

As seen before, SSA is a very sensitive parameter to assess the sintering of TiC in the composites since the SSA reductions are mainly due to the TiC sintering. SSA variations, $\Delta S/S_0$, of the 50CB composites are presented on figure 8, while the absolute SSA values are on table 2. 50CB presents the lowest $\Delta S/S_0$ of all composites (≈-45 %) and quite high absolute SSA after 2 h of heat treatment, (21.2 $\mathrm{m^2\,g^{-1}}$), which is not changing for 10 h, showing the stability of the structure at 1500 °C.

50CB is more effective than 50Gr hindering the sintering of TiC, where the TiC coordination number reduction is expected to be higher. After 1500 °C - 10 h, 50CB presents a surface area 2 times higher than 50Gr (21.1 vs 11.9 $\mathrm{m^2\,g^{-1}}$ - table 2 - likely coming from the carbon black higher SSA (table 1)). SEM microstructures (figure 9) clearly show that TiC particle size is smaller in the case of 50CB. The G_{SEM} obtained for 50CB , 58±29 nm, is considerably lower than the one determined for the TiC on 50Gr, 85±42 nm (see table 2). In terms of porosity after 1500 °C - 10 h, 50Gr presents larger $P_{r,>200\,\mathrm{nm}}$ than $P_{r,<200\,\mathrm{nm}}$ where in the 50CB it is the inverse, as seen in figure 6. This is due to the nature of the carbons added and how well they are expected to reduce the TiC coordination number.

3.5. TiC-MWCNT composites

From the MWCNT composites, only 75CNTb will be discussed here - where the TiC was milled independently and added later to the MWCNT in a suspension (see more in the sub-section 2.2.1 of the Materials and Methods and figures 3b and 3d). In the other MWCNT composites, the milling had a detrimental effect on the MWCNT. The 25CNT, 50CNT and 75CNT characterizations can be found on supplementary materials on A.1.2.

When comparing the $\Delta\rho/\rho_0$ of 75CNTb on figure 5 with the other nanocomposites it is noticeable that 75CNTb presents the highest density variation (17 and 28 % for 2 and 10 h respectively). Although these density differences are high, they are likely to be related with mass losses of carbon which can easily collapse the very porous structure of the composite (ρ_r = 31 % for 75CNTb, figure 6). Furthermore, although these density differences are quite high in absolute terms (figure 5a), ρ_r values at 10 h of heat treatment are still the lowest of all the composites. In the dilatometry of 75CNTb on figure 7 its shrinkage is as high as TiC. By looking at the TiC microstructures after 1500 °C - 10 h (figure 4a) and 75CNTb (figure 3d), the shrinkage in the case of 75CNTb is not due to sintering of TiC, since nanometric TiC is present on 75CNTb and not on TiC, so it must be related to the mass losses (see table 2) and rearrangement.

Regarding the $\Delta P_S/P_{S,0}$ (figure 5b) there are virtually no changes, probably due to the nanometric porous nature of the nanotubes which dominates the pore sizes before and after the thermal

treatments (75CNTb, see table 2). Also, the successfully hindered TiC sintering will contribute as seen in figure 6 where $P_{r,<200\,\mathrm{nm}}$ is higher than in any other composite.

The 75CNTb composites before and after heat treatments have the highest SSA: 49.8 $m^2\,g^{-1}$, before and 23.6 $m^2\,g^{-1}$ after - table 2. Furthermore, in the 75CNTb case, $\Delta S/S_0$ on figure 8, is on the same level as 50CB after thermal treatments. However, the contribution from the huge MWCNT SSA (293.1 $m^2\,g^{-1}$) makes SSA a poor metric to evaluate TiC sintering. In the SEM microstructures obtained (figure 3d) nanometric TiC can be seen, where the TiC particles are G_{SEM} = 62±29 nm. It can be concluded that MWCNT also successfully hinders the sintering of TiC. It is also relevant to mention that in the case of 75CNT volume calculations, a much lower density was used for the MWCNT than for graphite and carbon black. If calculated in mass, for 50Gr and 50CB the TiC/Carbon ratios initially added are respectively, 2.3 and 2.7 while for 75CNTb it was 10.9. Thus, with small quantities of MWCNT when not co-milled, is very efficient in hindering the sintering of TiC.

The statistical analysis employed in this work for the evolution of parameters like density, pore size and specific surface area, allowed us to have great confidence in the results obtained, with minimum experiments conducted.

4. Conclusions

Even though TiC-C composites are present in the literature, their characteristics are not suited for the application as ISOL target materials. A new processing route had to be developed in order to stabilize nanometric TiC under high temperatures.

TiC as supplied (48 nm sinters at 1500 °C to grain sizes of 738±254 nm. When milled for 2 h TiC sintering was hindered, where with the same heat treatment as TiC the grain sizes were about 314±108 nm. Even with milling nanometric TiC could not be maintained at 1500 °C, so carbon addition was investigated to keep the nanometric structure at high temperatures.

A successful processing route was created to produce three different TiC - Carbon nanocomposites: TiC - Carbon Black, TiC - Graphite and TiC - multi wall carbon nanotubes (MWCNT). Attrition milling was used to co-mill the nanocomposites in isopropanol, except for the TiC-MWCNT composite where MWCNT were added later to the TiC (to avoid destruction of the MWCNT). The obtained composites were heat treated at 1500 °C for 2 and 10 h to assess TiC sintering hindering.

All 3 different carbon allotropes used were successful hindering the sintering of nanometric TiC where the most successful was the TiC-MWCNT, followed by TiC-carbon black and finally TiC-graphite. At 1500 °C for 10 h TiC-MWCNT showed TiC particles of 62±26 nm, and 37 % density, with only 8.4 wt.% C addition to TiC. Where in the others around 30 wt% of C addition to TiC, after the same heat treatment conditions, gave grain sizes of 58±29 nm and 85±42 nm with densities around 50 %, for TiC-carbon black and TiC-graphite composites, respectively.

In the current tests we aimed for stability of nanometric TiC at 1500 °C. Since for the application in sight can benefit from higher temperatures (such as 1800 °C) to bring faster isotope releases, these nanocomposites will be tested at higher temperatures and presented in another article [46]. Furthermore, the zirconium oxide (and carbide) and respective mass losses need to be studied in detail to know its impact on the nanocomposites and phase stability, a key factor for production of stable and high intensity radioactive ion beams.

Acknowledgments

The authors would like to acknowledge Carlos Morais for the technical expertise with the attrition milling and during experimental work, Filipe Oliveira for lending the dilatometer equipment and Prof. Jacques Lemaître for the ANOVA - analysis of variance - calculation tools and interesting discussions. We would like to acknowledge as well Orion Engineered Carbons, S.A. for supplying the carbon black for this study. The author J.P. Ramos gratefully acknowledge CERN and EPFL for the doctoral studentship funding.

References

[1] T. Y. Kosolapova, Carbides - Properties, Production and applications, Plenum Press, New York and London, 1971.
[2] H. O. Pierson, Handbook of Refractory Carbides and Nitrides: Properties, Characteristics, Processing, and Applications, Noyes Publications, Bracknell, 1996.
[3] A. Mullendore, J. Whitley, D. Mattox, The development and laboratory testing of low refractory coatings for fusion reactor limiters, Journal of Nuclear Materials 93-94 (9) (1980) 486–492. doi:10.1016/0022-3115(80)90162-2.
[4] J. M. Ramos-Fernández, M. Martínez-Escandell, F. Rodríguez-Reinoso, Production of nanoTiC-graphite composites using Ti-doped self-sintering carbon mesophase powder, Journal of the European Ceramic Society 33 (3) (2013) 583–591. doi:10.1016/j.jeurceramsoc.2012.09.019.
[5] C. Dickerson, Y. Yang, T. R. Allen, Defects and microstructural evolution of proton irradiated titanium carbide, Journal of Nuclear Materials 424 (1-3) (2012) 62–68. doi:10.1016/j.jnucmat.2012.02.005.
[6] E. Kugler, The ISOLDE facility, Hyperfine Interactions 129 (2000) 23–42. doi:10.1023/A:1012603025802.
[7] L. Carraz, I. Haldorsen, H. Ravn, M. Skarestad, L. Westgaard, Fast release of nuclear reaction products from refractory matrices, Nuclear Instruments and Methods 148 (2) (1978) 217–230. doi:10.1016/0029-554X(70)90171-0.
[8] P. Hoff, O. Jonsson, E. Kugler, H. Ravn, Release of nuclear reaction products from refractory compounds, Nuclear Instruments and Methods in Physics Research 221 (2) (1984) 313–329. doi:10.1016/0167-5087(84)90002-4.
[9] U. Köster, Intense radioactive-ion beams produced with the ISOL method, The European Physical Journal A - Hadrons and Nuclei 15 (1-2) (2002) 255–263. doi:10.1140/epja/i2001-10264-2.
[10] A. Gottberg, Target materials for exotic ISOL beams, Nuclear Instruments and Methods in Physics Research Section B: Beam Interactions with Materials and Atoms , In the press. doi:10.1016/j.nimb.2016.01.020.
[11] S. Fernandes, Submicro- and Nano-Structured Porous Materials for Production of High-Intensity Exotic Radioactive Ion Beams, Phd thesis, École polytechnique fédérale de Lausanne (2010). doi:10.5075/epfl-thesis-4813.
[12] T. Stora, Recent developments of target and ion sources to produce ISOL beams, Nuclear Instruments and Methods in Physics Research, Section B: Beam Interactions with Materials and Atoms 317 (PART B) (2013) 402–410. doi:10.1016/j.nimb.2013.07.024.
[13] J. Ramos, A. Gottberg, R. Augusto, T. Mendonca, K. Riisager, C. Seiffert, P. Bowen, A. Senos, T. Stora, Target nanomaterials at CERN-ISOLDE: synthesis and release data, Nuclear Instruments and Methods in Physics Research Section B: Beam Interactions with Materials and Atoms 376 (2016) 81–85. doi:10.1016/j.nimb.2016.03.003.
[14] J. Ramos, A. Gottberg, T. Mendonça, C. Seiffert, A. Senos, H. Fynbo, O. Tengblad, J. Briz, M. Lund, G. Koldste, M. Carmona-Gallardo, V. Pesudo, T. Stora, Intense $^{31-35}$Ar beams produced with a nanostructured CaO target at ISOLDE, Nuclear Instruments and Methods in Physics Research Section B: Beam Interactions with Materials and Atoms 320 (2014) 83–88. doi:10.1016/j.nimb.2013.12.009.
[15] L. C. D. Jonghe, M. N. Rahaman, Sintering of Ceramics, in: S. Somiya, F. Aldinger, N. Claussen, R. M. Spriggs, K. Uchino, K. Koumoto, M. Kaneno (Eds.), Handbook of Advanced Ceramics, Volume I: Materials Science, Elsevier, Academic Press, 2003, Ch. Chapter 4, pp. 187–264. doi:10.1016/B978-012654640-8/50006-7.
[16] J. D. French, M. P. Harmer, H. M. Chan, G. A. Miller, Coarsening-Resistant Dual-Phase Interprenetrating Microstructures, Journal of the American Ceramic Society 73 (8) (1990) 2508–2510. doi:10.1111/j.1151-2916.1990.tb07621.x.
[17] M. W. Weiser, L. C. De Jonghe, Inclusion Size and Sintering of Composite Powders, Journal of the American Ceramic Society 71 (3) (1988) C–125–C–127. doi:10.1111/j.1151-2916.1988.tb05030.x.
[18] L. Olmos, C. L. Martin, D. Bouvard, Sintering of mixtures of powders: Experiments and modelling, Powder Technology 190 (1-2) (2009) 134–140. doi:10.1016/j.powtec.2008.04.057.
[19] B. Manley, J. B. Holt, Z. A. Munir, Sintering of Combustion-Synthesized Titanium Carbide, in: Materials Science Research, Springer US, Boston, MA, 1984, pp. 303–316. doi:10.1007/978-1-4613-2761-5_22.
[20] L. Stobierski, A. Gubernat, Sintering of silicon carbideI. Effect of carbon, Ceramics International 29 (3) (2003) 287–292. doi:10.1016/S0272-8842(02)00117-7.

[21] D. Cho, J. Hoon Park, Y. Jeong, Y. Lak Joo, Synthesis of titanium carbide-carbon nanofibers via carbothermal reduction of titania with carbon, Ceramics International 41 (9) (2014) 10974–10979. doi:10.1016/j.ceramint.2015.05.041.
[22] K. Thorne, S. J. Ting, C. J. Chu, J. D. Mackenzie, T. D. Getman, M. F. Hawthorne, Synthesis of TiC via polymeric titanates: the preparation of fibres and thin films, Journal of Materials Science 27 (16) (1992) 4406–4414. doi:10.1007/BF00541573.
[23] J. R. Martin, L. Borchardt, M. Oschatz, G. Mondin, S. Kaskel, Titanium carbide and carbide-derived carbon composite nanofibers by electrospinning of Ti-resin precursor, Chemie-Ingenieur-Technik 85 (11) (2013) 1742–1748. doi:10.1002/cite.201300057.
[24] Y. Zhao, A. Thapa, Q. Feng, M. Xi, Q. Qiao, H. Fong, Electrospun TiC/C nano-felt surface-decorated with Pt nanoparticles as highly efficient and cost-effective counter electrode for dye-sensitized solar cells., Nanoscale 5 (23) (2013) 11742–7. doi:10.1039/c3nr04170k.
[25] G. Zhou, T. Xiong, S. Jiang, S. Jian, Z. Zhou, H. Hou, Flexible titanium carbide–carbon nanofibers with high modulus and high conductivity by electrospinning, Materials Letters 165 (2016) 91–94. doi:10.1016/j.matlet.2015.11.119.
[26] T. Yu, Y. Deng, L. Wang, R. Liu, L. Zhang, B. Tu, D. Zhao, Ordered mesoporous nanocrystalline titanium-carbide/carbon composites from in situ carbothermal reduction, Advanced Materials 19 (17) (2007) 2301–2306. doi:10.1002/adma.200700667.
[27] Z. Abdullaeva, E. Omurzak, C. Iwamoto, H. Okudera, M. Koinuma, S. Takebe, S. Sulaimankulova, T. Mashimo, High temperature stable WC1-x@C and TiC@C core–shell nanoparticles by pulsed plasma in liquid, RSC Advances 3 (2) (2013) 513. doi:10.1039/c2ra22028h.
[28] V. Kiran, K. L. Nagashree, S. Sampath, Synergistic electrochemical activity of titanium carbide and carbon towards fuel cell reactions, Rsc Advances 4 (24) (2014) 12057–12064. doi:10.1039/c3ra46281a.
[29] J. L. Li, L. J. Wang, G. Z. Bai, W. Jiang, Microstructure and mechanical properties of in situ produced TiC/C nanocomposite by spark plasma sintering, Scripta Materialia 52 (9) (2005) 867–871. doi:10.1016/j.scriptamat.2005.01.006.
[30] W. Yang, L. Zhang, Y. Liu, L. Cheng, W. Zhang, Preparation and Mechanical Properties of Carbon Fiber Reinforced (BC x –SiC) n Multilayered Matrix Composites, Applied Composite Materials 14 (4) (2007) 277–286. doi:10.1007/s10443-007-9046-y.
[31] I. L. Shabalin, D. M. Tomkinson, L. I. Shabalin, High-temperature hot-pressing of titanium carbide-graphite hetero-modulus ceramics, Journal of the European Ceramic Society 27 (5) (2007) 2171–2181. doi:10.1016/j.jeurceramsoc.2006.07.008.
[32] X. Wang, M. Lu, L. Qiu, H. Huang, D. Li, H. Wang, Y. B. Cheng, Graphene/titanium carbide composites prepared by sol-gel infiltration and spark plasma sintering, Ceramics International 42 (1) (2015) 122–131. doi:10.1016/j.ceramint.2015.08.017.
[33] C. C. Koch (Ed.), Nanostructured Materials: Processing, Properties and Potential Applications, 2nd Edition, Noyes Publications, New York, 2002.
[34] S. Panfilov, O. Padalko, N. Mitrenko, Behavior of Ultrafine Titanium Carbide Powders During Annealing and Sintering, Soviet Powder Metallurgy and Metal Ceramics 24 (11) (1985) 824–828. doi:10.1007/BF00802551.
[35] P. Bowen, C. Carry, From powders to sintered pieces: forming, transformations and sintering of nanostructured ceramic oxides, Powder Technology 128 (2-3) (2002) 248–255. doi:10.1016/S0032-5910(02)00183-3.
[36] P. Bowen, R. Mulone, P. Streit, T. A. Ring, Slip Casting of TiCxN1-x - Mo2C-Ni Cermets., in: P. Duran, J. Fernandez (Eds.), Third Euro-Ceramics - Volume 1, Vol. 1, Faenza Editrice Iberica, 1993, pp. 549–554.
[37] D. R. Lide (Ed.), CRC Handbook of Chemistry and Physics, 90th Edition, CRC Press, 2010.
[38] R. M. German, A measure of the number of particles in agglomerates, International journal of powder metallurgy 32 (4) (1996) 365–373.
[39] E. D. Palik (Ed.), Handbook of Optical Constants of Solids, Elsevier, 1998.
[40] J. Janzen, The refractive index of colloidal carbon, Journal of Colloid and Interface Science 69 (3) (1979) 436–447. doi:10.1016/0021-9797(79)90133-4.
[41] S. Brunauer, P. Emmett, E. Teller, Adsorption of Gases in Multimolecular Layers, Journal of the American Chemical Society 60 (2) (1938) 309–319. doi:10.1021/ja01269a023.
[42] E. P. Barrett, L. G. Joyner, P. P. Halenda, The Determination of Pore Volume and Area Distributions in Porous Substances. I. Computations from Nitrogen Isotherms, Journal of the American Chemical Society 73 (1) (1951) 373–380. doi:10.1021/ja01145a126.
[43] C. A. Schneider, W. S. Rasband, K. W. Eliceiri, NIH Image to ImageJ: 25 years of image analysis, Nature Methods 9 (7) (2012) 671–675. doi:10.1038/nmeth.2089.
[44] D. C. Montgomery, Design and Analysis of Experiements, 8th Edition, John Wiley & Sons, Inc., 2012.
[45] B. Munkhbayar, M. J. Nine, J. Jeoun, M. Bat-Erdene, H. Chung, H. Jeong, Influence of dry and wet ball milling on dispersion characteristics of the multi-walled carbon nanotubes in aqueous solution with and without surfactant,

Powder Technology 234 (2013) 132–140. doi:10.1016/j.powtec.2012.09.045.
[46] J. P. Ramos, A. M. R. Senos, T. Stora, P. Bowen, Stability of nanometric TiC-carbon composites: effects of carbon allotropes and Zr milling impurities, to be published.
[47] J. Ramos, C. Fernandes, T. Stora, A. Senos, Sintering kinetics of nanometric calcium oxide in vacuum atmosphere, Ceramics International 41 (6) (2015) 8093–8099. doi:10.1016/j.ceramint.2015.03.007.
[48] A. Senos, J. Vieira, Processing Effects on Morphological Evolution of ZnO during Sintering, in: P. Vincenzini (Ed.), Proceedings of the World Ceramics Congress, part of the 6th CIMTEC, Advances in Science and Technology, 3C, Ceramics - Charting the Future, Techna Srl, Florence, Italy, 1995, pp. 1777–1784.

3.3 Article: Stability of nanometric TiC-carbon composites: effects of carbon allotropes and Zr milling impurities

As shown in section 1.3 (equation 1.5, page 27) the diffusion has an Arrhenius relation with temperature, which means that if the same particle size is kept, big gains on diffusivity can be obtained by increasing the temperature. This will have a direct impact on the beam intensities in the ISOL method. Due to the successful nanometric TiC stabilization by all the carbons at 1500 °C obtained in the section above, it was decided to test them at even higher temperatures.

Since oven A could only reach up to 1500 °C, oven B was used[4]. The main difference between the two ovens is the global geometry which influences the conductance making pumping more or less efficient and the oven materials. Oven B could reach slightly lower pressure than oven A, and the surrounding materials were tantalum instead of alumina. This may bring differences in the local oven atmosphere which may or may not influence the nanocomposites.

In order to find out if the ovens produced samples that were not statistically different (95 % confidence interval), an experimental design with a $2^{2\times4}$ factorial ANOVA was done [137]. The experimental design had three factors - oven, repetition and composite - with 2 levels for the first 2 factors - oven: A or B; repetition: sample 1 or sample 2 - and 4 levels for the later one - composite: TiCm, 50Gr, 50CB, 75CNTb. Thermal treatments of 1500 °C for 10 h were done in both ovens for the samples and the system response was evaluated on mass evolution ($\Delta m/m_0$ [%]), SSA evolution ($\Delta S/S_0$ [%]) and density evolution ($\Delta\rho/\rho_0$ [%]) results can be seen in figure 3.4.

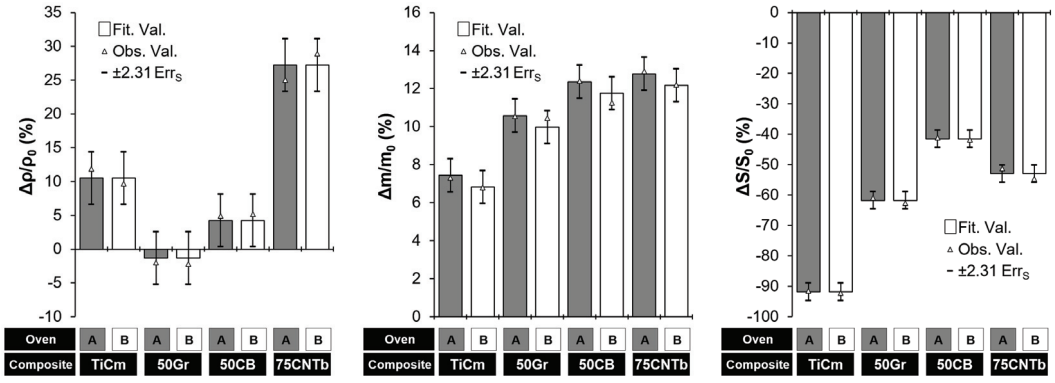

(a) $\Delta\rho/\rho_0$ (b) $\Delta m/m_0$ (c) $\Delta S/S_0$

Figure 3.4 – TiCm, 50Gr, 50CB and 75CNTb results for heat treatments at 1500 °C for 10 h in two different ovens. The error bars correspond to the standard error of the mean (Err_S) - 95 % confidence intervals - for the adjusted values (columns) obtained by ANOVA - analysis of variance.

As can be observed from figure 3.4a and c, there is no statistically relevant difference between

[4] Both ovens are described in detail in subsection 2.1.2, page 45.

the ovens in terms of obtained sample $\Delta\rho/\rho_0$ and $\Delta S/S_0$ but there is a small difference on $\Delta m/m_0$, as seen from figure 3.4b. The $\Delta m/m_0$ values show a slight difference, where in oven B there is less mass losses than in oven A. This is likely due to the oven atmosphere where in oven B the optimized geometry for conductance and the hot Ta tube will act as an oxygen getter. This, all together, will reduce the partial pressure of oxygen in oven B where less carbon will be burnt. Even though this slightly affects the mass losses, it doesn't seem to affect the $\Delta\rho/\rho_0$ and $\Delta S/S_0$, the important sintering parameters. It can then be concluded that the two ovens are similar enough, since the hypothesis of the ovens being different was rejected. Therefore, oven B was used in the article following to test the nanocomposites at higher temperatures.

Even though stable nanometric TiC up to 1500 °C was obtained, the mass losses measured in the TiC and composites still remain unexplained and to be characterized. In the following article that will be done together with the study of the ZrO_2 impurities and their influence in the nanocomposites phase composition and evolution as a function of the temperature. These are important features as impurities or secondary phases can significantly influence isotope release and their intensities.

The article ahead, included in this thesis, is a draft to be submitted for publication in the Journal of the European Ceramic Society. The author of the thesis (first author) has written the manuscript (which was reviewed by the co-authors), did all the experimental work and result analysis. The figures and tables from this article are present in the list of figures and list of tables of the thesis with the numbering form of 3.bx, where x is the number of table/figure in the article. The supplementary materials of this article can be found starting on page 165 on the appendix section A.2.

Stability of nanometric TiC-carbon composites: effects of carbon allotropes and Zr milling impurities

J.P. Ramos[a,b,*], T. Stora[b], A.M.R. Senos[c], P. Bowen[a,*]

[a] *Laboratory of Powder Technology, École polytechnique fédérale de Lausanne (EPFL), CH-1015 Lausanne, Switzerland*
[b] *European Organization for Nuclear Research (CERN), CH-1211 Genève 23, Switzerland*
[c] *Department of Materials and Ceramics Engineering, Universidade de Aveiro, CICECO, 3810-193 Aveiro, Portugal*

Abstract

In the ISOL (Isotope Separator OnLine) method a target is bombarded with high energy protons in order to produce isotopes through nuclear reactions. The isotope extraction happens simultaneously with irradiation (OnLine) where the target is kept hot enough (up to 2300 °C to promote isotope diffusion and effusion from the material grains into an ion source to form a radioactive ion beam. Due to the enhanced isotope release properties of nanosized materials, titanium carbide-carbon porous nanocomposites have been developed at CERN and tested up to 1500 °C. The carbon was in the form of graphite, carbon black or multi-wall carbon nanotubes (MWCNT).

In the interest of the ISOL application, in this study we extended the range of temperatures up to 1800 °C, to test the sintering hindering capabilities of the nanocomposite carbons. Carbon black was the most effective carbon hindering the sintering of TiC, where the smallest TiC crystallite size was found: < 80 nm at 1800 °C. Nonetheless TiC-graphite and TiC-MWCNT also had a great effect on the TiC sintering hindering with crystallite sizes smaller than 140 nm at the same temperatures. This finding makes the stability of some of the composites against sintering sufficient for eventual use as a target material.

Additionally, using thermodynamic modelling, ex-situ X-ray powder diffraction and in-situ gas phase analysis, we show that there are interesting phase and lattice parameter changes due to the ZrO_2 impurities from the attrition milling. In all nanocomposites the ZrO_2 was reduced to ZrC and gradually solubilized into the TiC lattice, where at 1800 °C there is no more ZrC phase. This was accompanied by lattice unit cell increase, which is also influenced by the TiC_x stoichiometry and oxygen and nitrogen impurities.

Keywords: porous nanocomposites, high temperature applications, lattice parameters, solid solution, zirconium carbide-titanium carbide

1. Introduction

Radioactive ion beams are used all over the world for nuclear, atomic, solid state and biophysics studies. ISOLDE (Isotope Separator OnLine DEvice) at the European Organization for

*joao.pedro.ramos@cern.ch, paul.bowen@epfl.ch
URL: http://www.joaopedroramos.com (J.P. Ramos)

Nuclear Research - CERN has developed beam technologies since its start in 1967, with almost 1000 isotope beams available of 74 chemical elements (from Z=2 to 92) [1]. ISOLDE uses the ISOL (Isotope Separator OnLine) method to produce radioactive isotopes where high energy particles (in this case protons) are used to bombard a target to induce nuclear reactions which transmute a fraction of the target material atoms into different isotopes of lower mass number [2]. Such isotopes are then trapped in the bulk of the target material and have to diffuse to the surface, evaporate and effuse through the material porosity and to a transfer line connected to an ion source. Here the isotopes are ionized and made into a beam which is then conducted to a mass separator where the they are separated according to their mass with a magnetic field thanks to the Lorentz Force. The separated beam is then finally conducted to the experimental setup where it will be used for physics research.

As in the ISOL acronym the process is online, that is to say, by bombarding the target which is kept at high temperatures, in vacuum, to promote diffusion and effusion of the isotopes, which are continuously being released, ionized and mass separated. In such an extreme environment the target materials are required to have high resistance to radiation damage, high production cross-section of the isotope of interest, being inert in respect to the isotope to be produced and have low diffusion and effusion times. Commonly, target materials at ISOLDE are made of metals, oxides or carbides. While the metals are usually in the form of thin foils, the oxides and carbides are in powder (or pressed powder) form.

Usually, in order to have the highest release efficiency, target operation temperatures are brought close to the material melting point. The material microstructure degradation, due to the proximity to the melting point, is given as the main reason for beam intensity reduction over time. Such degradation is assumed to happen through sintering of the target material, bringing changes in porosity and increase in grain size, which increases diffusion distances. Besides temperature increase, diffusion times can be reduced by reducing the material grain size. However, if no microstructure stabilization mechanisms are employed, reduced operation temperatures have to be used since nano and submicrometric particle materials sinter faster than conventional ones. Furthermore, in order to produce beams of exotic isotopes (with very short half-lives - down to a few tens of milliseconds), the isotope release times (diffusion and effusion times included) must be below or in the same order of magnitude of the isotope half-life. The achievement of such operation parameters is not trivial, requiring investigation and engineering of stable and ultra fine microstructures.

1.1. ISOL target nanomaterials state of the art

It was only during the last decade that special attention has been given to the target material microstructure and its influence in the isotope release efficiency and stability over time [3–8]. Before, large particles were favored with the justification that smaller particles (below 5 μm) would sinter too fast and would not provide a stable structure for the target material [9].

It was found that by reducing the material particle size of silicon carbide (SiC) from ≈10 to ≈0.6 μm and having high porosity, generally an increase by a factor of 5 to 10 was seen for magnesium beam intensities [3, 4]. Consequently, this material is currently operated at ISOLDE even though after having been incorrectly discarded in the past because of its very poor release properties, in its micrometric form (≈10 μm) [10].

Calcium oxide (CaO) targets were also known to have unreliable beam intensities and often decreasing over time. By synthesizing a nanometric CaO and studying its sintering characteristics [6], stable argon beam intensities over time, and about five fold higher in intensity could be produced despite the low operation temperature needed to avoid material sintering [5].

Uranium carbide targets are usually produced through carbothermal reduction of uranium oxide with excess graphite. By replacing the graphite as the carbon source with multi-wall carbon nanotubes (MWCNT) and milling the uranium oxide down to ≈180 nm a very porous MWCNT and uranium carbide nanocomposite was obtained [11]. This target material has shown improved release rates up to a factor of 10 higher without any decrease during operation time. Furthermore the MWCNT hinder sintering so the material can be operated at higher temperatures.

1.2. TiC as a target material

TiC has also been evaluated as an unsuitable target material when it was studied in micrometric powder form (1-50 μm) for isotope release at 2300 °C [9] and at 1900 °C when mixed with graphite [10]. TiC composite targets are used at ISAC-TRIUMF (TRI University Meon Facility – Isotope Separator and Accelerator in Canada's National Laboratory for Particle and Nuclear Physics - an ISOL facility in Canada) to produce radioactive isotopes [12–14]. The targets are produced by mixing 1 and 7 μm TiC particle sizes (1:1) by milling, followed by slip casting on a graphite foil and sintered up to 1900 °C. The final material is said to be in between 1-10 μm and the TiC layer to be 50 % dense [12].

Currently at ISOLDE for targets, the element Ti is used in the form of metallic titanium. Rolled foils loaded in a 2 cm internal diameter, 20 cm long cylinder, are used as a target, however the beam intensities produced from such configuration, often decay over time due to sintering of the foils, when the operation temperatures is often higher than 1200 °C. Titanium oxide (TiO_2) has also been studied and used at ISOLDE to produce radioactive ion beams, in the form of micrometric fibers, however they are outperformed by other oxides (such as CaO) [1, 15, 16].

1.3. Previous work

We have made preliminary studies on the processing and sintering to 1500 °C of nanosized TiC powders and TiC carbon composites [17]. The results showed that when nano-TiC powders were mixed and/or milled with different carbon allotropes - graphite, carbon black and MWCNT - stable porous nanocomposites could be formed at 1500 °C even after 10 h at these elevated temperatures. Without the carbon allotropes the nanosized TiC powders sintered to higher densities with significant grain growth. Interestingly, attrition milled nano TiC showed lower sinterability than the as-received powder. This was hypothesised as being due to ZrO_2 impurities introduced from the milling media during the attrition milling. For the TiC-carbon nanocomposites, the carbon is assumed to act as an inert second phase that reduces the coordination number of TiC and thus hindering the sintering. To test the suitability of these nanocomposites for application at ISOLDE, higher temperatures, up to 1800 °C, are investigated here. These higher temperatures can only be beneficial for isotope release as long as the target microstructure is stable at the defined operation temperature. To this end we study in detail the phase composition and mass losses at these elevated temperatures, not previously reported. Using thermodynamic modelling, ex-situ X-ray powder diffraction, in-situ gas phase analysis, and scanning electron microscopy we show that there are interesting phase changes (including interaction with the ZrO_2 impurities from the attrition milling) and the stability of some of the composites against sintering is sufficient for eventual use as a target material.

2. Materials and Methods

2.1. Processing

The processing used for the composites was developed in a previous study [17] and will be only briefly described here. Nanometric TiC was mixed with graphite, carbon black and MWCNT[1], in an attrition mill in isopropanol with 0.5 wt.% polyvinylpyrrolidone, PVP, as a dispersant. The mixtures where then dried, manually deagglomerated, pressed into cylindrical compacts and heat treated at 450 °C in argon, to remove the PVP. An in-house built vacuum-oven was used, consisting of a thermally shielded tantalum tube ohmically heated. The oven was operated in vacuum (10^{-3} - 10^{-4} Pa) and heat treatments of 10 h at 1500, 1650 and 1800 °C were conducted with ramps of 8 °C min^{-1}. The samples selected for the higher temperature studies were the ones with the best results obtained in our previous investigation [17]. These were 50 vol.% graphite-TiC (50Gr), 50 vol.% carbon black-TiC (50CB), 75 vol.% MWCNT-TiC (75CNTb, bulk density, given by the supplier) and TiC milled with no carbon (TiCm) for comparison. Other samples with different carbon volumes were also developed but not used in this study. The starting powders characteristics can be found on table A.2.1 in supplementary materials.

2.2. Characterization and data handling

Samples dimensions and weight were determined before and after thermal treatment in order to check for mass losses and follow any evolution of the geometrical density (ρ). Specific surface area (SSA) and pore size volume and distribution below 200 nm, assuming cylindrical pore shape, were determined by nitrogen adsorption isotherms in a *Quantachrome eNOVA2200*. The average median pore size, P_S, was determined from the cumulative size distribution. Microstructures were observed in a *Carl Zeiss SMT* Σ*igma* scanning electron microscope (SEM) with an in-lens secondary electron detector. Considering that the composites had different initial values of ρ, SSA and P_S, the respective variation for each sample and sintering condition was determined through the formula:

$$\Delta X/X_0 = (X - X_0)/X_0 \quad (1)$$

where X corresponds to the characteristic after heat treatment (ρ, S or P_S) and X_0 is the characteristic before the heat treatment (ρ_0, S_0 or $P_{S,0}$). The influence of the thermal treatment temperature and carbon allotrope added to TiC were analysed on the variation of SSA - $\Delta S/S_0$, density - $\Delta\rho/\rho_0$ and pore size below 200 nm - $\Delta P_S/P_{S,0}$. A repetition for each test (2 samples) was done and statistical analysis of variance (factorial ANOVA) [18] was done - the statistical design schematic can be found on figure A.2.1 in supplementary materials).

X-ray powder diffraction (XRPD) was made using a *PANalytical X'PERT PRO* diffractometer with a X-ray Cu source, from 20 to 125° of 2θ with 0.013 step size (measurement 98 $s/°2\theta$) for good statistics. The *PANalytical HighScore Plus v4.1* software [19] was used for Rietveld refinement in order to extract lattice parameters and quantify phase ratios. The Williamson-Hall method (W.H.) is used to evaluate both crystallite size and microstrain in the TiC [20]. However, the peaks did not present either a Lorentz shape (linear W.H.) neither a Gaussian shape (quadratic W.H.), they had a contribution from both (Voigt function). Hence, a variation to the

[1] TiC - *Goodfellow* (Ref. LS396999/1), 99.9 % pure, 80-130 nm; Graphite - *Alfa Aesar*, Ref. 40798, 325 mesh, <44 μm; Carbon black - *Orion Engineered Carbons*, *Printex A Pulver*, 40 m^2 g^{-1}, 40 nm primary particle size; MWCNT - *Nanocyl*, Ref. NC3100, >95 % purity, 10 nm diameter, 1.5 μm length

W.H. method to account for this proposed by J. Langford [21] was used (hence forward called LWH). The instrumental broadening was determined with a LaB_6 standard material.

Residual gas analysis (RGA) was used in order to study the mass losses of the composite over temperature. A *Pfeiffer Prisma Plus QMA200* quadrupole mass spectrometer (QMS) connected to a *Agilent TPS-mobile TV81* pumping station was used. The samples were heated in a *Carbolite STF 15/450* horizontal alumina tube oven, adapted with in-house made flanges to allow vacuum, which was connected to an *Agilent TPS-mobile TV301* pumping station. The QMS was connected to the oven through a small chicane with reduced conductance to reduce the gas supply rate. This was done in order to keep the pressure in the QMS as low as possible as required for its proper function. The oven was heated to 1500 °C, where the QMS was recording a mass spectrum ($1 \leqslant A \leqslant 100$) every 2 minutes during the 8 °C min^{-1} heating ramp. Additionally to the mass spectrum, the pressure was also recorded during the heating ramp, which can be directly correlated with the mass losses ($\Delta m/m_0$). All the results obtained were corrected for the system and crucibles outgas without any sample.

3. Results and Discussion

3.1. Phase evolution

Mass losses ($\Delta m/m_0$) at the end of each thermal cycle for each sample were followed using ANOVA which results can be seen on figure 1. In this figure, $\Delta m/m_0$ is represented with triangles (Obs. Val.) while the columns represent the ANOVA adjusted values (Fit. Val.) and the error bars, the standard error of the mean for a 95 % confidence interval. The analysis show a clear increase of -$\Delta m/m_0$ with temperature for all cases which is related with favorable thermodynamics to carbon burning (Boudouard reaction, C + CO_2(g) $\rightleftharpoons$ 2CO(g)). In the case of TiCm, the free carbon comes from the raw material and the carbonaceous deposit from the PVP burning during processing. Overall, the TiC-carbon nanocomposites have generally higher mass losses related to the higher amounts of carbon. The nanocomposites produced from higher SSA carbons (see table A.2.1 on supplementary materials), present higher mass losses, due to higher amount of adsorbed oxygen or water on the carbons.

In order to clarify the mass losses and check for phase evolution, XRPD and evolved gas phase analysis were conducted to the materials as produced and thermally treated. ZrO_2 is found in all milled materials, typical example, for 50Gr on figure 2, with quantities from the XRPD, that vary from from 2.6 to 5.7 wt.%, (table 1). This contamination arises from the milling media and, during the thermal treatments, reacts with carbon producing ZrC, as detected in the 1500 °C diffractogram. At 1650 °C, the ZrC peaks are still present but reduced in intensity and at 1800 °C they disappear completely.

The residual gas analysis (RGA) was made as a function of temperature up to 1500 °C. All of the carbon composites showed similar behaviour (A.2.2 SM) and a typical result is illustrated for the 50 CB in figure 3. In figure 3, the ion current in [A] is shown a function of mass, A=1 to 100 and temperature. The pressure, proportional to the mass losses, in function of temperature can also be seen. The RGA allows the identification of the temperatures at which certain volatile compounds are released from the samples. Mass 44 - CO_2, 32 - O_2, 28 - CO (or N_2 - not really expected) and 18 - H_2O were followed, where the other masses below $A = 50$ are either isotope combinations of the referred molecules (such as ^{12}CO and ^{13}CO), fragments due to molecular breakup during ionization or minor leaks in the system. Above $A = 50$ the fragments found are likely due to decomposed PVP which wasn't fully removed from the sample at 450 °C. At temperatures >600 °C, CO represents most of the gases released from the sample when comparing

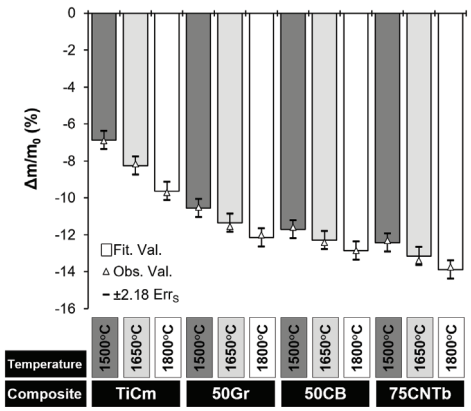

Figure 1: Mass losses ($\Delta m/m_0$) of TiCm, 50Gr, 50CB and 75CNTb for heat treatments at 1500, 1650 and 1800 °C for 10 h. The error bars are the standard error of the mean (Err_S) - 95 % confidence intervals - for the adjusted values (columns) obtained by ANOVA - analysis of variance.

with the intensities obtained for other masses. CO_2 is not expected in large quantities, even if it is produced, since the Boudouard reaction is spontaneous at T>700 °C.

The pressure for TiC, TiCm and 50CB obtained during the RGA are plotted as function of temperature, in figure 4. Only 50CB is shown as a representation of all the composites since they all show the same trend with only a slight shift in the highest temperature peak position. Figure 4 shows 3 peaks, the first at 870 °C, the second at 1100 °C and a third at 1400 °C, not present for TiC and TiCm.

The first peak is attributed to the reaction of carbon burning either from the free carbon present in the TiC and/or that resulting from the PVP burnout - which leaves a carbonaceous deposit on the TiC when carried out in an inert atmosphere. X-ray photoelectron spectroscopy (XPS), which allows for element identification at surfaces (0 - 10 nm) identified 17.4 wt.% of oxygen, in the TiC as supplied, likely in the form of TiO_2, probably from the powder production process. Since no TiO_2 was identified in XRPD it can be concluded that TiO_2 must be present in very low quantities and at the surface of the particles. The second peak at 1100 °C, which was seen in all cases, is likely to due to the conversion of the titanium oxide into titanium carbide releasing CO (as seen in figure 3), through the reaction $TiO_2 + 3C \rightarrow TiC + 2CO(g)$. The third peak at 1400 °C is attributed to the reaction of ZrO_2 with the carbon in the composites forming zirconium carbide (ZrC), again with release of CO (as seen on figure 3), through the reaction $ZrO_2 + 3C \rightarrow ZrC + 2CO(g)$.

Thermodynamic phase stability diagrams were computed using *HSC 7.11 Chemistry Software* [22] for Ti-C-O and Zr-C-O at 1200 °C and are shown on figure 5 (and also for other temperatures on figure A.2.3 in supplementary materials), showing where TiC and ZrC are stable in terms of P_{CO} and P_{O_2}. From the conversion of ZrO_2 into ZrC which only starts after about 1200 °C (main peak of gas release curve), the approximate oven atmosphere conditions can be pin pointed in terms of O_2 and CO partial pressures, as marked on figure 5: $P_{CO} = 10^{-11}$ to 10^{-3} atm and $P_{O_2} = 10^{-28}$ to 10^{-20} atm. The upper limit for $P_{CO} = 10^{-3}$, 10^{-3} atm, is an approximation and is limited by the vacuum system. In another study [23], an XRPD done to two 50CB samples thermally treated only until 1400 and 1200 °C, respectively, and immediately

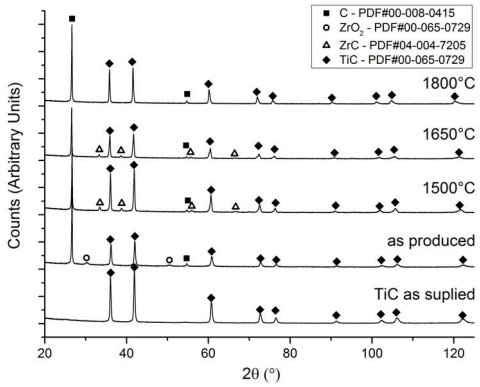

Figure 2: Diffractograms obtained through XRPD for the TiC as supplied and 50Gr as-produced and heat treated for 1500, 1650 and 1800 °C.

cooled down, revealed the presence of ZrO_2 and no ZrC in the 1200 °C sample and ZrC and no ZrO_2 at 1400 °C, confirming the observations of this study.

3.2. TiC lattice parameters

Due to the possible TiC_x broad range of composition where $0.5 \leqslant x \leqslant 1$, there is a considerable variation in the lattice parameter which is a function of x [24–26]. In the literature [24, 25] the TiC_x lattice (a) is minimum for $TiC_{0.5}$ where $a = 4.299$ Å, increases up to $TiC_{0.85}$ where $a = 4.331$ Å and decreases slightly in stoichiometric TiC, down to $a = 4.326$ Å. It is also known that O and N contamination, down to tens of a percent decreases the TiC lattice considerably [25]. In order to determine C, N and O concentrations in TiC, combustion with infrared adsorption spectrometry [27] was used for C, and carrier gas hot extraction analysis [28] for N and O. The results of these analysis can be seen on table 2, where Ti quantity was deducted from C, N and O concentration and no other contamination were assumed to be present.

A lattice reduction from 4.315 to 4.310 Å is seen on table 1, matching the oxygen at.% decrease in table 2, from the as-supplied to the thermally treated sample. The decrease of the C/Ti ratio seen on table 2 confirms the free carbon present in the sample which burns at low temperatures, seen at 870 °C in the mass losses. The real C/Ti ratio is the one of the TiC sample thermally treated at 1500 °C, 0.68 from table 2. The TiC lattice determined in this work, $a =$ 4.310 Å, is slightly lower from the lattice predicted by Storms et al. [25] for $TiC_{0.68}$ of 4.324 Å. This can be due to the O and N contamination in the sample.

The ZrO_2 milling contamination reacts with the carbon present in the nanocomposites and forms ZrC at 1400 °C. As the heat treatments temperature increases, the newly formed ZrC quantity is reduced at 1650 °C and vanishes after 1800 °C for all cases, as seen in table 1. The TiC-ZrC phase diagram shown in figure 6 (reproduced from [29]), shows that ZrC forms a continuous solid solution with TiC ($Ti_{(1-x)}Zr_xC$). At low temperatures this solid solution presents an immiscibility asymmetric dome, where the solid solution segregates into 2 phases. Since our ZrC mol.% is generally quite low (up to 5 mol.%, ca. from table 1), phase segregation is not expected. It should be noted that the wt.% determined by Rietveld has some error since except for 50Gr, the carbon peaks were often too low or not visible. In any case, it is clear that the ZrC is

Table 1: Crystallite sizes and stress determined by XRPD using the LWH method and lattice parameter and phase ratios determined from Rietveld refinement of the XRPD diffractograms.

Composite	Temperature (°C)	Crystallite size (nm)	Stress (%)	Unit Cell (Å)	ZrO_2 (wt.%)	ZrC (wt.%)	TiC (wt.%)	C (wt.%)
TiC	As supplied	51	0.25	4.315	-	-	100	-
	1500	252	0.01	4.310	-	-	100	-
TiCm	As produced	48	0.26	4.316	4.3[b]	- [b]	95.7	-
	1500	107	0.02	4.323	- [b]	- [b]	100	-
	1650	122	0.03	4.324	- [b]	- [b]	100	-
	1800	277	0.02	4.322	- [b]	- [b]	100	-
50Gr	As produced	43	0.20	4.316	5.7	-	66.8	27.4
	1500	59	0.16	4.323	-	3.4	72.4	24.2
	1650	64	0.30	4.326	-	1.1	49.5	49.4
	1800	134	0.23	4.355	-	-	64.8	35.1
50CB	As produced	43	0.20	4.313	5.7	-	68.5	25.8
	1500	52	0.10	4.322	-	4.1	80.3	15.6
	1650	58	0.12	4.325	-	1.1	61.2	37.7
	1800	76/68[a]	0.22/0.11	4.361/4.330	-	-	48.3/44.3	7.8
75CNTb	As produced	46	0.26	4.316	2.6	-	87.1	10.3
	1500	52	0.10	4.321	-	1.3	89.8	-
	1650	47	0.20	4.336	-	-	100	-
	1800	138	0.07	4.340	-	-	100	-

[a] Sample presented phase demixing with two TiC phases. More information in the text.
[b] Energy-dispersive X-ray spectroscopy (EDS) reveals the presence of Zr in 4.4±0.4 wt.% in all samples.

Table 2: C, N and O concentrations in TiC and TiC thermally treated at 1500 °C determined by combustion with infrared adsorption spectrometry and carrier gas hot extraction analysis.

	As supplied	1500 °C
C (at. %)	40.55	40.46
O (at. %)	4.54	0.04
N (at. %)	0.06	0.07
Ti (at. %)	54.77	59.33
C/Ti	0.74	0.68

gradually dissolving in the TiC lattice which seems to be diffusion limited since only at 1800 °C it is totally integrated.

XRPD made on the composites revealed a small gradual shift (see figure 7) in the TiC peak position which was inversely proportional to the ZrC phase quantity present in the XRPD. 50Gr was used to show the shift on figure 7 since it presents an intense carbon peak which conveniently serves as an internal standard. Rietveld refinement was conducted to all samples in order to quantify the lattice parameter change, as can be seen on table 1. Looking at this table it is clear that for all cases there is an increase of the lattice from around 4.315 Å (as supplied TiC) to a maximum of 4.361 Å for 50CB, 4.355 Å for 50Gr and 4.340 Å for 75CNTb. In solid solutions the host species is distorted, especially where there is a significant difference between the solid solution atoms radii: in our case Ti, 1.40 Å, and Zr, 1.55 Å [30]. It is also seen that in the samples, like 75CNTb, where lower amounts ZrO_2 was present, lower lattice distortions were observed.

The Vegard's law [31] is an empirical law used to predict the lattice of a solid solution, $A_{1-x}B_x$ of phases A and B, originally in ionic salts:

$$a_{A_{1-x}B_x} = (1-x)a_A + xa_B \tag{2}$$

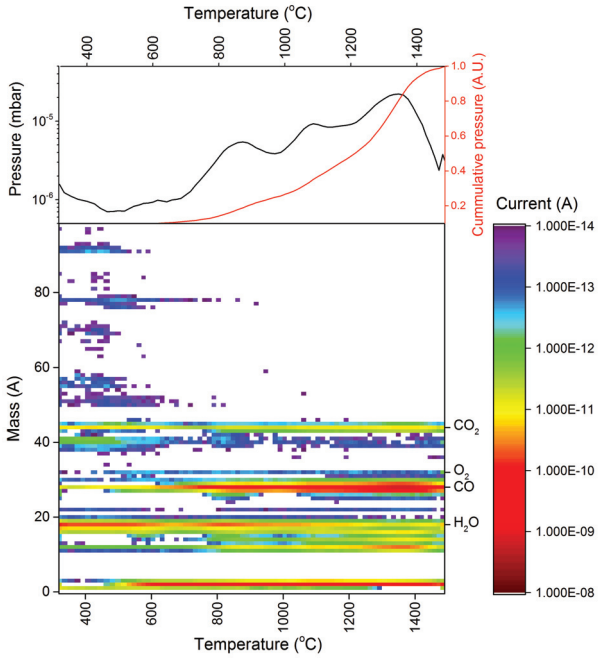

Figure 3: Mass spectrum shown in mass ($1 \leqslant A \leqslant 100$) vs ion current, obtained by residual gas analysis of 50CB from 350 to 1500 °C (a - bottom) and respective pressure evolution over temperature (a - top).

where a_A and a_B are the lattice parameter of the component A and B respectively, x is the mol.% of B in A and $a_{A_{1-x}B_x}$ is lattice parameter for the solid solution. Using the lattice obtained in this work for TiC (a = 4.310 Å, table 1) and 4.698 Å for ZrC [24], the Vegard's law predicts a lattice of 4.329 Å for $Ti_{0.96}Zr_{0.04}C$ (which is the case of 50Gr) where in our case a value of 4.355 Å was obtained (table 1). Even though the Vegard's law is normally used for alloys, Li et al [29] obtained a lattice parameter for $Ti_{0.80}Zr_{0.20}C$ which was relatively close to the one predicted by the law. In our study, this difference might be due to the possible error in determining the absolute ZrC phase ratio from XRPD or more likely to the increase of the TiC lattice which can be dissolving carbon from the allotropes, which increases its lattice [25]. In any scenario the values present the right tendency - increase of the lattice with addition of ZrC - shown by the Vegard's law.

In the case of TiCm the ZrC disappears after 1500 °C, contrarily to what has been seen for the carbon composites, as seen on figure 7. Additionally, no clear RGA signal for ZrO_2 transformation into ZrC was seen on figure 4. Energy-dispersive X-ray spectroscopy (EDS) revealed the same quantity of Zr element in all TiCm samples (as produced and thermally treated), 4.4±0.4 wt.%, showing that Zr is still present in the samples. The XRPD systematic peak shift for higher temperatures on the composites is not seen for TiCm (figure 7). Instead, an increase of the TiC lattice parameter (from 4.310 to 4.323 Å) already at 1500 °C is seen which doesn't change at higher temperatures. With the current evidence, we believe that the Zr from the ZrO_2 is being introduced into the TiC lattice, increasing the lattice parameter from the as produced sample to the 1500 °C one, which wasn't seen for TiC as supplied to the heat treated one at 1500 °C (table

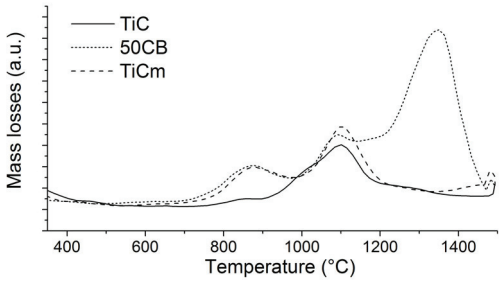

Figure 4: Mass losses evolution with temperature extracted the RGA pressure evolution for TiC, TiCm and 50CB for comparison.

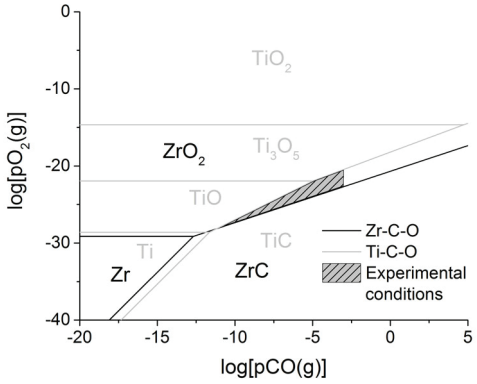

Figure 5: Thermodynamical Ti-C-O (black) and Zr-C-O (grey) overlapped phase stability diagrams at 1200 °C, showing the calculated range of CO and O_2 partial pressures in the experimental setup: $P_{CO} = 10^{-3} = 10^{-3}$ to 10^{-11} atm and $P_{O_2} = 10^{-28}$ to 10^{-20} atm.

1). ZrO_2 reduction to ZrC is not seen in RGA and is likely happening slower and during the 10 h dwell time, after the cooling ramp. This delay is caused by the lower carbon contents available in TiCm.

Using the Vegard's law for the TiCm case, which is $Ti_{0.976}Zr_{0.024}C$ (c.a. from TiCm as produced, table 1) a lattice parameter of 4.319 Å is found very close to the one obtained experimentally, $a = 4.323$ Å. The applicability of the law in this case, further supports the hypothesis that the TiC must be increasing its lattice also from feeding from the C of the carbon allotropes.

Even though it is unlikely that our TiC-ZrC composition is in the immiscibility dome in the phase diagram of figure 6, in one sample - 50CB heat treated at 1800 °C - we had phase segregation with two different lattice parameters obtained as seen on table 1 (the XRPD diffractogram obtained can be found on supplementary materials figure A.2.4. Phase segregation in the TiC-ZrC system was seen in the study of Li et al. [29] for $Ti_{0.80}Zr_{0.20}C$ where a higher lattice ZrC-rich phase (a=4.68 Å) and a lower lattice TiC-rich phase (a=4.35 Å) were formed. The same seems to be happening here where a lattice of 4.361 Å was found, likely the one with higher ZrC content and a 4.330 Å, the one with less ZrC. Since we didn't follow ZrO_2 quantities sample by sample, we believe that in this sample the initial ZrO_2 quantity was higher due to a possible wear of the

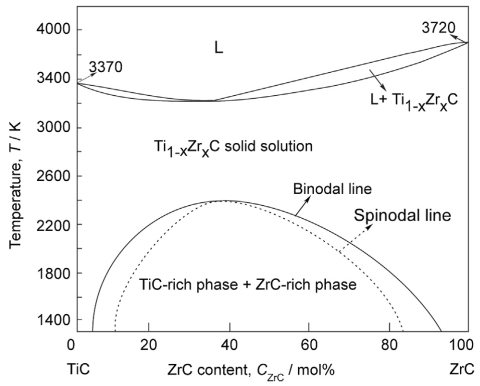

Figure 6: Phase diagram of TiC-ZrC. Adapted from [29]

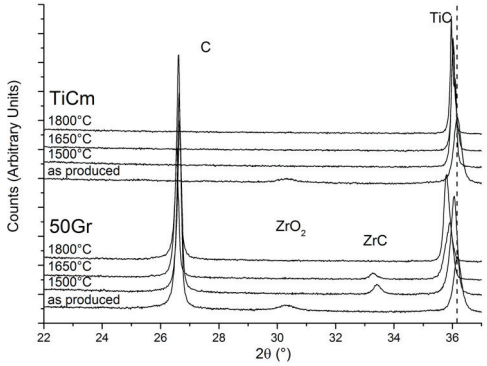

Figure 7: Diffractograms obtained through XRPD for the TiCm and 50Gr as-produced and heat treated for 1500, 1650 and 1800 °C revealing TiC peak shift for higher temperatures.

milling elements, which would increase the ZrC content and cause phase segregation at 1800 °C.

On table 1 the lattice stress values are also presented. Lattice strain can be divided in two categories: uniform strain and nonuniform strain [32]. Uniform strain is caused by uniform changes in d spacing, causing a shift in the peak position, such as in solid solutions, as seen before. The nonuniform strain is usually due to imperfections in the lattice such as defects, which broaden the peaks and reduce the intensities. By looking at table 1, the initial TiC material has already some degree of strain (0.25 %) likely from the production methods used (which usually involve milling). As expected for the TiC without any additive, the strain on table 1, is reduced during heat treatments, since the defects are annealed. Such does not happen for any of the composites when heat treated at high temperatures. Both types of strain are present in the TiC-C nanocomposites: uniform strain due to the incorporation of Zr in the TiC lattice and nonuniform strain which likely arises from the sintering stresses [32] due to the TiC constrained sintering.

3.3. Microstructure studies

In order to use these materials for ISOL targets, their microstructure is of high importance since the smallest particle size stable at the highest possible temperature is of interest. Important sintering parameters such as $\Delta\rho/\rho_0$, $\Delta S/S_0$ and pore size and volume evolutions were followed for all samples as function of the heat treatments temperature. To have a reference, TiC without any carbon (TiCm) to stabilize its particle size, was submitted to the same heat treatments.

TiCm microstructures thermally treated at 1500, 1650 and 1800 °C for 10 h, can be seen in figure 8. When comparing them, grain growth is clear in the sintered samples where grain sizes go from 48 to more than 500 nm at 1800 °C. As can be seen on figure 9, $\Delta\rho/\rho_0$ values increase for increasing temperature and reach around 67 % for 1800 °C. The absolute ρ values can be found on table 3 where TiCm is seen to reach a density of 3.85 g cm^{-3}, approaching the theoretical one[2] - 4.93 g cm^{-3}, showing a non-desired high degree of sintering.

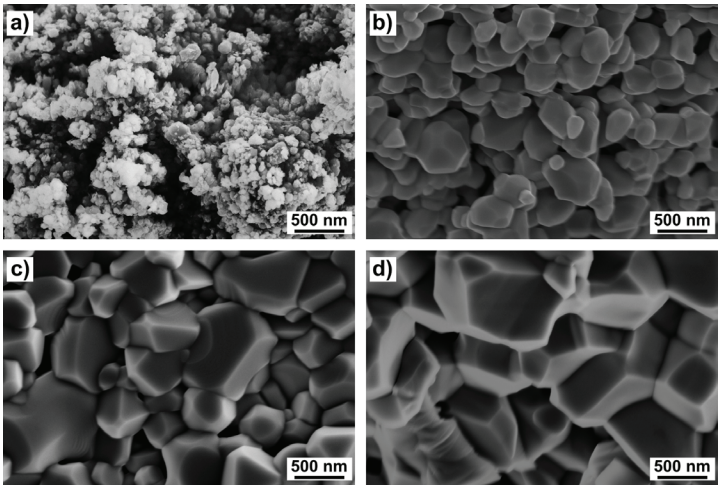

Figure 8: SEM microstructures of TiC milled, TiCm (a) and heat treated for 10 h at 1500 (b), 1650 (c) 1800 °C (d).

The high values of $\Delta\rho/\rho_0$ are accompanied by SSA reductions ($\Delta S/S_0$), which can be found on figure 9. $\Delta S/S_0$ values for TiCm on this figure vary from more than 90 to almost 100 %, where in the extreme case of 1800 °C SSA varies from 29.1 to 0.1 m^2 g^{-1}, as seen on table 3. In the particular case of TiCm heat treated at 1500 °C, on figures 9a and b, small $\Delta\rho/\rho_0$, ≈ 9.7 % (from 2.35 to 2.55 g cm^{-3} - table 3) are accompanied by large $\Delta S/S_0$ values, ≈-91 % (from 29.1 to 2.1 m^2 g^{-1} - table 3). In this case it is likely that a non-densifying mechanism, such as surface diffusion is controlling sintering, as seen before for TiC [17]. Surface diffusion is usually a very important transport mechanism in the early stage sintering, namely for nanomaterials [33, 34], bringing increase in grain size and, from the contribution of secondary densifying mechanisms, reduced densification .

The relative pore volumes were calculated from the relative density (ρ_r=ρ/ρ_t) using the $v_{P,BJH}$ (represented on table 3). The porosity fraction below 200 nm - $P_{r,<200\,nm}$ - and above - $P_{r,>200\,nm}$ - were calculated as well [3]. These are represented on figure 10, where TiCm as produced has

[2]For simplicity the ρ_t was assumed not to vary with the TiC stoichiometry.

[3]The calculation method, also used as in [17], is reproduced in supplementary materials A.2.1 of this publication

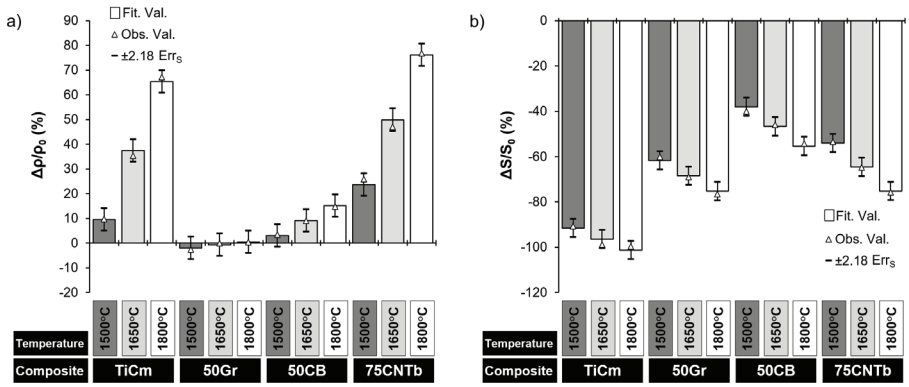

Figure 9: TiCm, 50Gr, 50CB and 75CNTb $\Delta\rho/\rho_0$ (a) and $\Delta S/S_0$ (b) for heat treatments at 1500, 1650 and 1800 °C for 10 h. The error bars are the standard error of the mean (Err_S) - 95 % confidence intervals - for the adjusted values (columns) obtained by ANOVA - analysis of variance.

53 % of porosity, the majority with a size below 200 nm ($P_{r,<200\,nm}$=48 %). On the contrary, after thermal treatment at 1500 °C, the TiCm density is slightly increased (from 48 to 52 %) but accompanied by an enlargement of the pore size ($P_{r,>200\,nm}$ = 44 %). This transformation is explained by the sintering of the nanometric TiC aggregates which, as referred before, is likely controlled by surface diffusion, bringing coarsening of the particles with reduced densification. After 1500 °C, the approximate ratio between $P_{r,>200\,nm}$ and $P_{r,<200\,nm}$ is kept while the total porosity keeps reducing as expected for densification processes. Pore size (P_S) and its relative evolution ($\Delta P_S/P_{S,0}$) can be seen on table 3 and figure 11, respectively. $\Delta P_S/P_{S,0}$ is positive for 1500 °C, doubles for 1650 °C and gets negative for 1800 °C. As discussed before, for 1500 and 1650 °C, there is mainly sintering of agglomerates eliminating the small intra-agglomerate pores ($P_{r,<200\,nm}$). Since coarsening is in place, an increase of the porosity between the aggregates is expected, so the global pore size increases, whereas for the highest temperature of 1800 °C densification of the microstructure among the agglomerates occurs, bringing simultaneously reduction of porosity and pore size.

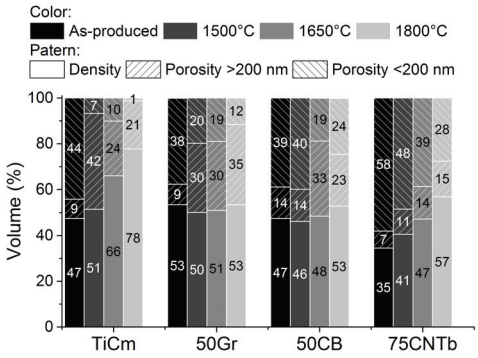

Figure 10: Relative density and porosity (below and above 200 nm) for the TiCm, 50Gr, 50CB and 75CNTb as produced and heat treated for 10 h at 1500, 1650 and 1800 °C.

Table 3: Density (ρ), SSA, median pore size (P_S) and BJH pore volumes ($v_{P,BJH}$) of TiCm, 50Gr, 50CB and 75CNTb as produced and after heat treatments for 10 h at 1500, 1650 and 1800 °C.

		TiCm	50Gr	50CB	75CNTb
ρ (g cm^{-3})	As produced	2.35	1.94	1.64	1.54
	1500 °C	2.55	1.88	1.69	1.95
	1650 °C	3.27	1.91	1.77	2.27
	1800 °C	3.85	1.99	1.91	2.70
SSA (m^2 g^{-1})	As produced	29.1	32.8	36.6	49.4
	1500 °C	2.3	13.0	22.1	23.0
	1650 °C	0.3	10.2	19.7	17.4
	1800 °C	0.1	7.7	16.7	12.0
P_S (nm)	As produced	27	28	30	28
	1500 °C	42	35	35	28
	1650 °C	55	39	28	24
	1800 °C	13	33	32	24
$v_{P,BJH}$ (cm^3 g^{-1})	As produced	0.16	0.17	0.19	0.31
	1500 °C	0.01	0.07	0.18	0.20
	1650 °C	0.02	0.06	0.06	0.13
	1800 °C	0.00	0.04	0.09	0.08

The microstructures of the TiC nanocomposites based on graphite (50Gr), carbon black (50CB) and MWCNT (75CNTb), as produced and heat treated, can be seen on figure 12. While for 50Gr (figures 12a, d, g and j) and 75CNTb (figures 12b, e, h, k) there is a clear increase of the grain size, there is no such evidence for 50CB, even after 1800 °C (figures 12c, f, i and l). Relatively to densities, (table 3, ρ and figure 10, ρ_r), the 75CNTb had the lowest green density (1.54 g^3 cm^{-1} - ρ_r=35 %) and the highest of the composites after 1800 °C (2.70 g^3 cm^{-1} - ρ_r=57 %) - which results in the $\Delta\rho/\rho_0$ values (up to 77 %), on figure 9a. On figure 9, $\Delta\rho/\rho_0$ was close to zero for 50Gr and for 50 CB is up to 15 %. In 50Gr, the graphite which has large micrometric particles, form a stable non-sinterable skeleton where only TiC particles in between the graphite grains can sinter, which has restricted influence on the overall sample density. The small nanometric carbon black primary particles which are close to the sizes of the TiC ones (see table A.2.1 in supplementary materials), blend well with TiC and greatly affect the TiC coordination number, hindering sintering [17]. The large density changes on 75CNTb are likely related with the carbon mass losses, which very likely partially collapse the very porous structure created by the MWCNT.

On figure 9b, 50Gr and 75CNTb present the highest $\Delta S/S_0$ of the composites (at 1800 °C, 77 and 76 %, respectively) while for 50CB, for the same temperature, $\Delta S/S_0$ was only 54 %. As seen on table 3, as produced 75CNTb has the highest SSA, followed by 50CB and 50Gr (49.4, 36.6 and 49.4 m^2 g^{-1}, respectively), which is due to the carbon allotropes added to the TiC (see table A.2.1 in supplementary materials). The final SSA at the highest temperature was 16.7 m^2 g^{-1} for the 50CB followed by the 75CNTb with 12.0 m^2 g^{-1} and 7.7 m^2 g^{-1} for 50Gr. The $\Delta S/S_0$ is a very sensitive sintering parameter, since the growing necks between the TiC particles and grain coarsening come with great SSA reductions. Despite the influence of mass losses (figure 1), the SSA reductions on figure 9 indicate that carbon black is further confirmed to be the most effective hindering the sintering of TiC.

Pore size evolution, $\Delta P_S/P_{S,0}$, in the composites in figure 11 doesn't present any relevant changes within the error (95 % confidence interval). It can be interpreted as no significant pore

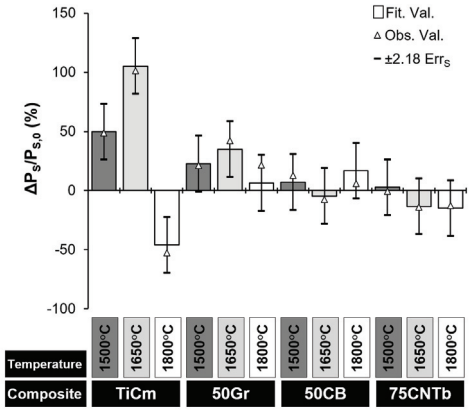

Figure 11: TiCm, 50Gr, 50CB and 75CNTb $\Delta P_S/P_{S,0}$ for heat treatments at 1500, 1650 and 1800 °C for 10 h. The error bars are the standard error of the mean (Err_S) - 95 % confidence intervals - for the adjusted values (columns) obtained by ANOVA - analysis of variance.

size <200 nm changes, which can be attributed to the TiC sintering hindering by the carbons. Relatively to the pore volumes on figure 10, the nanocomposites, with the exception of 50Gr, keep higher $P_{r,<200\,nm}$ than $P_{r,>200\,nm}$ contrarily to TiCm, even at 1800 °C. For 75CNTb the $P_{r,<200\,nm}$ is likely to be dominated by the CNT small porosity, while in the case of 50Gr, since the graphite has a small $v_{P,BJH}$ (table A.2.1 in supplementary materials), the main contribution to the $P_{r,<200\,nm}$ comes from the TiC. Although in all composites there is some evolution of $P_{r,<200\,nm}$ to $P_{r,>200\,nm}$ this is not as high as in the case of TiCm. Together with ρ_r, this evolution is an indication of the TiC sintering. Sintering of TiC will bring densification and/or increase the $P_{r,>200\,nm}$ relatively to $P_{r,<200\,nm}$, since carbon does not sinter (as seen for TiCm, and less in the nanocomposites).

The data presented allows for a quantitative assessment of the TiC sintering in terms of grain/particle size, where conclusions can be drawn regarding the effectiveness of each carbon allotrope in the TiC sintering hindering. In order to have a more qualitative approach and confirm these observations, XRPD was used to isolate and quantify the TiC crystallite sizes through peak broadening using the LWH method, as seen on table 1. In this table, the crystallite sizes calculated for the TiCm, 50Gr, 50CB and 75CNTb for the different thermal treatments can be found. A good level of precision for the XRPD crystallite size is obtained since the 51 nm obtained for TiC are consistent with SEM measured particles (64±29 nm [23]) and also with particle size calculated from SSA (48 nm - table A.2.1 in supplementary materials). Furthermore good reproducibility of the technique is shown through the consistency of the TiC crystallite size measurements, which should be of similar size across all the as produced composites, as seen on table 1. At 1800 °C the smallest TiC crystallite sizes obtained are: 76 nm for the 50CB, followed by 75CNTb and 50Gr with 138 and 134 nm, respectively. The TiCm grains shown on the microstructure of TiCm on figure 8 at 1800 °C are larger than the XRPD crystallite size determined on table 1 - 277 nm, likely due to limitations on the LWH technique which is normally up to 100-200 nm. With the XRPD crystallite size determinations, it is clear that the most effective carbon allotrope hindering the sintering of TiC is carbon black in 50CB followed by CNT in 75CNTb and graphite in 50Gr. 50Gr present a slightly higher porosity, but 75CNTb presents smaller pores, for the same crystallite sizes.

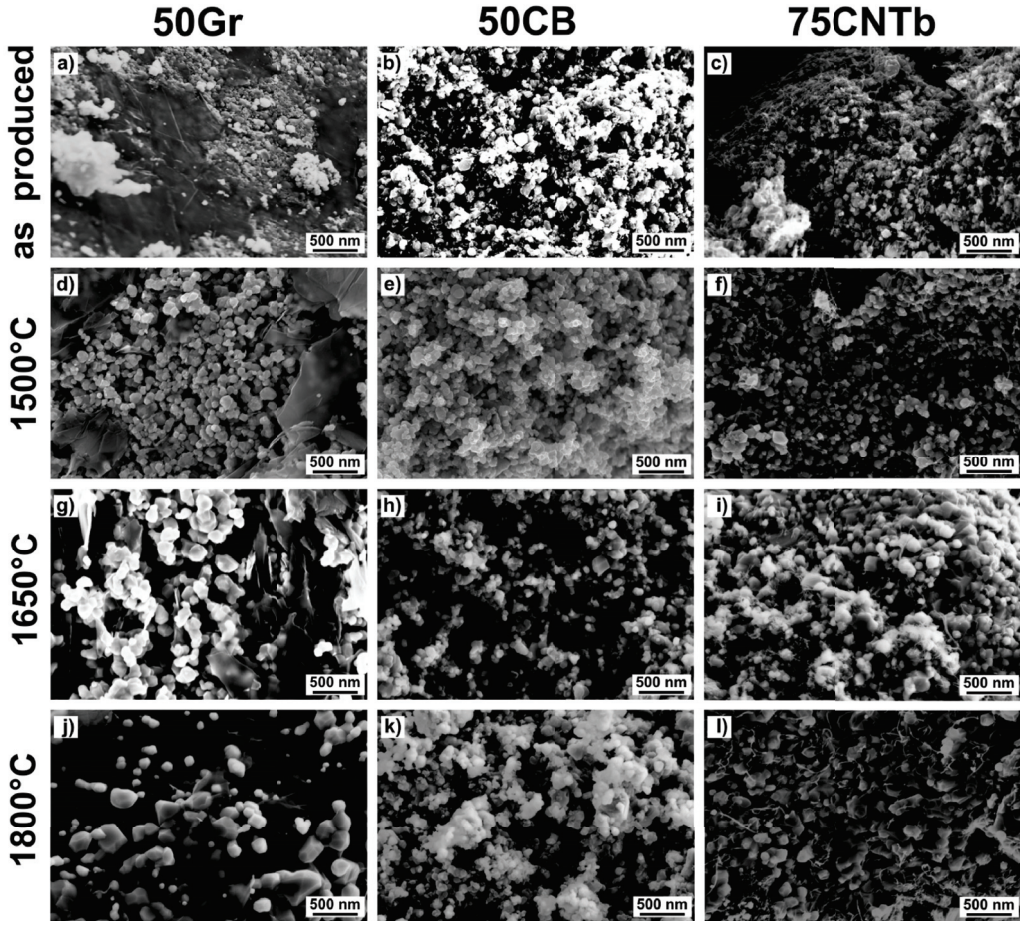

Figure 12: SEM microstructures of 50Gr, 50CB and 75CNTb as produced (a, b and c respectively) and the same composites but heat treated for 10 h at 1500 (d, e and f), 1650 (g,h,i) and 1800 °C (j, k and l).

4. Conclusions

Nanometric titanium carbide was successfully stabilized up to 1800 °C with addition of 3 different carbon allotropes: graphite, carbon black and MWCNT. The most effective carbon allotrope hindering the sintering of TiC was carbon black, followed by MWCNT and graphite. After heat treatment at 1800 °C, the TiC crystallite sizes without any carbon addition were more than 0.5 μm while for 50 vol. % carbon black-TiC (50CB), 50 vol. % graphite-TiC (50Gr) and 75 vol. % MWCNT (bulk density)-TiC (75CNTb) the crystallite sizes were 76, 134 and 138 nm, respectively. A relative density of 78 % was obtained for TiC sintered at 1800 °C while the composites attained significantly lower densities: 55 % for both 50CB and 50Gr and 58 % for 75CNTb.

The processing route for the composites introduces a ZrO_2 contamination (from 2.6 to 5.7 wt.%) that comes from the milling elements. This contamination converts at about 1400 °C, to ZrC consuming carbon of the nanocomposites and releasing CO gas. The ZrC phase gradually

solubilizes in the TiC lattice, where at 1800 °C there are no more ZrC XRPD phase peaks seen. This was followed by XRPD where the lattice parameter of TiC increases, due to solubility of ZrC, from 4.315 nm up to 4.361 nm. Although there seems to be an effect of the element Zr in the sintering of TiC [17, 35], this is not the main mechanism responsible for hindering the sintering of the nanometric TiC. The carbon addition is the controlling factor, reducing the coordination number of TiC, as shown when comparing the sintering behaviour of the TiCm (containing Zr) and the nanocomposites produced.

All of the produced carbon composites fulfill the microstructural requirements for ISOL target application (high porosity and nanometric particle size) to ensure smaller diffusion lengths, which result in shorter diffusion times, while the high porosity makes effusion faster reducing the probability of collision and or/trapping of the isotopes in the bulk of the material.

Acknowledgments

The authors would like to acknowledge Carlos Morais for the technical expertise with the attrition milling and during experimental work, Maria João Bastos and Artur Sarabando for the XRPD tests, Nicolas Xanthopoulos for the XPS tests. We acknowledge Prof. Jacques Lemaître for the ANOVA - analysis of variance - calculation tools and Prof. Heinrich Hofmann for the interesting phase diagrams discussions. We would like to acknowledge as well Orion Engineered Carbons, S.A. for supplying the carbon black for this study. The author J.P. Ramos gratefully acknowledge CERN and EPFL for the doctoral studentship funding.

References

[1] ISOLDE-CERN, ISOLDE Yield Database.
URL `http://test-isolde-yields.web.cern.ch/test-isolde-yields/query_tgt.htm`

[2] E. Kugler, The ISOLDE facility, Hyperfine Interactions 129 (2000) 23–42. doi:10.1023/A:1012603025802.

[3] S. Fernandes, Submicro- and Nano-Structured Porous Materials for Production of High-Intensity Exotic Radioactive Ion Beams, PhD Thesis, École polytechnique fédérale de Lausanne (2010). doi:10.5075/epfl-thesis-4813.

[4] T. Stora, Recent developments of target and ion sources to produce ISOL beams, Nuclear Instruments and Methods in Physics Research, Section B: Beam Interactions with Materials and Atoms 317 (PART B) (2013) 402–410. doi:10.1016/j.nimb.2013.07.024.

[5] J. Ramos, A. Gottberg, T. Mendonça, C. Seiffert, A. Senos, H. Fynbo, O. Tengblad, J. Briz, M. Lund, G. Koldste, M. Carmona-Gallardo, V. Pesudo, T. Stora, Intense $^{31-35}$Ar beams produced with a nanostructured CaO target at ISOLDE, Nuclear Instruments and Methods in Physics Research Section B: Beam Interactions with Materials and Atoms 320 (2014) 83–88. doi:10.1016/j.nimb.2013.12.009.

[6] J. Ramos, C. Fernandes, T. Stora, A. Senos, Sintering kinetics of nanometric calcium oxide in vacuum atmosphere, Ceramics International 41 (6) (2015) 8093–8099. doi:10.1016/j.ceramint.2015.03.007.

[7] J. Ramos, A. Gottberg, R. Augusto, T. Mendonca, K. Riisager, C. Seiffert, P. Bowen, A. Senos, T. Stora, Target nanomaterials at CERN-ISOLDE: synthesis and release data, Nuclear Instruments and Methods in Physics Research Section B: Beam Interactions with Materials and Atoms 376 (2016) 81–85. doi:10.1016/j.nimb.2016.03.003.

[8] A. Gottberg, Target materials for exotic ISOL beams, Nuclear Instruments and Methods in Physics Research Section B: Beam Interactions with Materials and Atomsdoi:10.1016/j.nimb.2016.01.020.

[9] L. Carraz, I. Haldorsen, H. Ravn, M. Skarestad, L. Westgaard, Fast release of nuclear reaction products from refractory matrices, Nuclear Instruments and Methods 148 (2) (1978) 217–230. doi:10.1016/0029-554X(70)90171-0.

[10] P. Hoff, O. Jonsson, E. Kugler, H. Ravn, Release of nuclear reaction products from refractory compounds, Nuclear Instruments and Methods in Physics Research 221 (2) (1984) 313–329. doi:10.1016/0167-5087(84)90002-4.

[11] A. Gottberg, et al., Development and Online Tests of a Nano-Structured Uranium Carbide – MWCNT Composite for the Production of Rare Isotope Beams at ISOLDE-CERN, in preparation.

[12] M. Dombsky, H. V., Method of forming composite ceramic targets, Patent no. US 7682664 B2 (2010).

[13] V. Hanemaayer, P. Bricault, M. Dombsky, Composite ceramic targets for high power proton irradiation, Nuclear Instruments and Methods in Physics Research Section B: Beam Interactions with Materials and Atoms 266 (19-20) (2008) 4334–4337. doi:10.1016/j.nimb.2008.05.094.
[14] TRIUMF-ISAC, TRIUMF-ISAC Yield Database.
URL http://mis.triumf.ca/science/planning/yield/target
[15] K. Peräjärvi, U. Bergmann, V. Fedoseyev, A. Joinet, U. Köster, C. Lau, J. Lettry, H. Ravn, M. Santana-Leitner, Studies of release properties of ISOLDE targets, Nuclear Instruments and Methods in Physics Research Section B: Beam Interactions with Materials and Atoms 204 (2003) 272–277. doi:10.1016/S0168-583X(02)01924-9.
[16] U. Köster, U. Bergmann, D. Carminati, R. Catherall, J. Cederkäll, J. Correia, B. Crepieux, M. Dietrich, K. Elder, V. Fedoseyev, L. Fraile, S. Franchoo, H. Fynbo, U. Georg, T. Giles, A. Joinet, O. Jonsson, R. Kirchner, C. Lau, J. Lettry, H. Maier, V. Mishin, M. Oinonen, K. Peräjärvi, H. Ravn, T. Rinaldi, M. Santana-Leitner, U. Wahl, L. Weissman, Oxide fiber targets at ISOLDE, Nuclear Instruments and Methods in Physics Research Section B: Beam Interactions with Materials and Atoms 204 (2003) 303–313. doi:10.1016/S0168-583X(03)00505-6.
[17] J. P. Ramos, A. M. R. Senos, C. M. Fernandes, T. Stora, P. Bowen, Development of a processing route for carbon allotrope-based TiC porous nanocomposites, to be published.
[18] D. C. Montgomery, Design and Analysis of Experiements, 8th Edition, John Wiley & Sons, Inc., 2012.
[19] T. Degen, M. Sadki, E. Bron, U. König, G. Nénert, The HighScore suite, Powder Diffraction 29 (S2) (2014) S13–S18. doi:10.1017/S0885715614000840.
[20] G. Williamson, W. Hall, X-ray line broadening from filed aluminium and wolfram, Acta Metallurgica 1 (1) (1953) 22–31. doi:10.1016/0001-6160(53)90006-6.
[21] J. Langford, The Use of the Voigt Function in Determining Microstructural Properties from Diffraction Data by means of Pattern Decomposition, in: E. Prince, J. Stalick (Eds.), Proceedings of the international conference Accuracy in Powder Diffraction II, NIST Special Publication 846, NIST, Gaithersburg, MD, 1992, pp. 110–126.
[22] Outotec Research Center, A. Roine, HSC 7.11 Chemistry Software (2011).
URL http://www.hsc-chemistry.net/
[23] J. P. Ramos, A. M. R. Senos, T. Stora, P. Bowen, Master sintering curve determination of nanometric TiC and a TiC-carbon black nanocomposite, to be published.
[24] H. O. Pierson, Handbook of Refractory Carbides & Nitrides, William Andrew, 1996. doi:10.1016/B978-081551392-6.50001-5.
[25] E. K. Storms, The Refractory Metal Carbides, Academic Press, New York, 1967.
[26] B. Predel, C-Ti (Carbon - Titanium), in: B. Predel (Ed.), Landolt-Börnstein - Group IV Physical Chemistry 12B: B - Ba ... Cu - Zr, Springer-Verlag Berlin Heidelberg, 2012, pp. 147 – 149. doi:10.1007/978-3-540-44756-6_102.
[27] S. Terashima, The rapid determination of total carbon and sulfur in geological materials by combustion and infrared absorption photometry, Analytica Chimica Acta 101 (1) (1978) 25–31. doi:10.1016/S0003-2670(01)83836-8.
[28] W. Gruner, Determination of oxygen in oxides by carrier gas hot extraction analysis with simultaneous COx detection, Fresenius' Journal of Analytical Chemistry 365 (7) (1999) 597–603. doi:10.1007/s002160051529.
[29] Y. Li, H. Katsui, T. Goto, Phase decomposition of TiC-ZrC solid solution prepared by spark plasma sintering, Ceramics International 41 (10) (2015) 14258–14262. doi:10.1016/j.ceramint.2015.07.055.
[30] J. C. Slater, Atomic Radii in Crystals, The Journal of Chemical Physics 41 (10) (1964) 3199. doi:10.1063/1.1725697.
[31] L. Vegard, Die Konstitution der Mischkristalle und die Raumfullung der Atome, Zeitschrift fur Physik 5 (1) (1921) 17–26. doi:10.1007/BF01349680.
[32] A. Khorsand Zak, W. Abd. Majid, M. Abrishami, R. Yousefi, X-ray analysis of ZnO nanoparticles by Williamson–Hall and size–strain plot methods, Solid State Sciences 13 (1) (2011) 251–256. doi:10.1016/j.solidstatesciences.2010.11.024.
[33] M. N. Rahaman, Ceramic Processing and Sintering, Marcel Dekker, 2003.
[34] C. C. Koch (Ed.), Nanostructured Materials: Processing, Properties and Potential Applications, 2nd Edition, Noyes Publications, New York, 2002.
[35] Ramos, et al., Constant isotope release properties measured for an online prototype TiC-carbon nanocomposite target material, to be published.
[36] R. M. German, A measure of the number of particles in agglomerates, International journal of powder metallurgy 32 (4) (1996) 365–373.

3.4 Summary of the TiC-carbon nanocomposite development

In this chapter the preliminary studies and development of the processing route for the TiC-C nanocomposites and respective full characterizations were presented.

In the preliminary studies section (3.1, page 62), Ti-based nanometric materials, TiO_2 and TiC, were studied in terms of sinterability and selected samples were studied for release, where the main conclusions were:

- TiO_2 sinters to submicrometric grain sizes, at 1000 °C, where the anatase to rutile transformation accelerates sintering. The, transformation is delayed by Si contamination which is also known to hinder grain growth;
- There was no isotope release at 1000 °C for any of the studied elements from TiO_2, due to the low temperatures used in order to keep its submicrometric structure stable;
- TiC loses the nanometric structure at 1300 °C but keeps submicrometric grains up to 1500 °C, however TiC oxidation is detected on the samples at $T > 1400$ °C;
- The TiC release properties were studied from 1300 to 1450 °C and showed increasing released fractions, F, up to 1400 °C, e.g. $F = 25$ % for Na for 1400 °C, which at 1450 °C, F starts to decrease, probably due to the sample oxidation;
- the TiC results show great potential as target material if the nanostructure can be stabilized. The F was not much lower than those obtained in the literature for micrometric TiC at much higher temperatures (2300 °C).

In the second section (3.2, page 65), to stabilize the nanometric TiC up to 1500 °C, a processing route to produce TiC-C nanocomposites (where C is graphite, carbon black (CB) or MWCNT) is developed, where:

- a processing route using attrition milling to co-mill the TiC and the carbons in IPA with PVP to act as a dispersant was developed by first milling all raw materials individually. In the case of TiC it reduces the agglomerate size by about a factor of 5 and introduces a ZrO_2 contamination in the materials from the milling media;
- three nanocomposites were produced, tested up to 1500 °C and characterized:
  - TiC - to serve as a reference;
  - TiCm - TiC milled for 2 h - to serve as a reference;
  - 50Gr - 1:1 volume TiC-graphite nanocomposite;
  - 50CB - 1:1 volume TiC-carbon black nanocomposite;
  - 75CNTb - 3:1 volume TiC-MWCNT nanocomposite (MWCNT bulk density considered);
  - and others which were not discussed - 25Gr, 25CB, 75CB, 25CNT, 50CNT, 75CNT - their results can be found on appendix section A.1.2, page 162.
- milled TiC (TiCm) shows lower sinterability than the as supplied TiC, where either the lower agglomerate size or the introduction of Zr are affecting the sintering phenomena;
- MWCNT is the most successful carbon hindering the sintering of nano TiC at 1500 °C, where with a TiC/C weight ratio of 10.9 is able to keep low densities (37 %) and TiC grain

sizes of $G_{SEM} = 62 \pm 26$ nm (from primary particle sizes of 41 nm);
- graphite and carbon black are also able to hinder the sintering of nanometric TiC where TiC/C ratios of 2.3 and 2.7, respectively, of the nanocomposites sintered at 1500 °C are roughly 50 % dense and have G_{SEM} values of 85 ± 42 nm and 58 ± 29 nm, respectively.

Finally, on the third section (3.3, page 86), the developed TiC-C nanocomposites were tested at higher temperatures (up to 1800 °C) and the mass losses, phase evolutions and TiC lattice parameters were studied in depth. It can be concluded from this section, that:

- using residual gas analysis, coupled with thermodynamic modeling and XRPD, the mass losses, which were up to 14 % of the nanocomposites were determined to be due to free carbon burning (≈ 870 °C, TiO_2 (present in the TiC raw material, ≈ 1100 °C) reduction into TiC and ZrO_2 reduction into ZrC (≈ 1400 °C);
- through thermodynamic modeling the oven P_{CO} was estimated to be between 10^{-11} and 10^{-3} atm and P_{O_2} to be between 10^{-28} and 10^{-20} atm;
- the ZrC formed solubilizes slowly into the TiC phase, where at 1800 °C is totally solubilized, forming a $Ti_{(1-x)}Zr_xC$ which brings an increase of the TiC crystalline lattice parameter;
- the stoichiometry of TiC_x was determined to be $TiC_{0.68}$ where the results suggest that x may be increasing during the thermal treatments of the nanocomposites, since the increase in lattice parameter can't all be described by the ZrC solubilization, as predicted by the Vegard's law;
- TiC lattice parameter was found to be $a = 4.315$ Å which agrees with those present in the literature;
- the most effective carbon hindering the sintering of the TiC at 1800 °C was the carbon black, followed by MWCNT and graphite, where crystallite sizes were 76, 134 and 138 nm, respectively, and densities between 55 and 58 %; all fulfill the requirements to be considered as ISOL target materials.

4 TiC and TiC-carbon black sintering kinetics

Contents

4.1 Article: Master sintering curve determination of nanometric TiC and a TiC-carbon black nanocomposite . . . 109

1. Introduction . . . 111
1. Materials and Methods . . . 113
3. Results and Discussion . . . 115
4. Conclusions . . . 122

4.2 Further discussion and summary of the TiC and TiC-carbon black sintering kinetics . . . 125

4.1 Article: Master sintering curve determination of nanometric TiC and a TiC-carbon black nanocomposite

In this section the sintering kinetics of TiC and TiC-carbon black are studied through constant heating rate dilatometry in order to determine the Master Sintering Curve (MSC). Through the MSC the apparent activation energy for the TiC sintering can be found and compared with values in the literature, both with and without carbon addition (TiC-carbon black nanocomposite). Another major advantage of the MSC is adding a predictive power to the TiC and TiC-CB sintering systems. An article draft is presented with the sintering studies and in the section after (4.2) the discussion started in the article draft is further extended and the main conclusions are presented for this chapter. For the sintering studies the dilatometer and data analysis described in section 2.1.4 on page 48 was used.

The article below, included in this thesis, is a draft to be submitted for publication in a peer reviewed journal. The author of the thesis (first author) has written the manuscript (which was reviewed by the co-authors), did the experimental work and result analysis. The figures and tables from this article are present in the list of figures and list of tables of the thesis with the numbering form of 4.ax, where x is the number of table/figure in the article. The

supplementary materials of this article can be found starting on page 169 on the appendix section A.3.

Master sintering curve determination of nanometric TiC and a TiC-carbon black nanocomposite

J.P. Ramos[a,b,*], D. Geissbühler[a], A.M.R. Senos[c], T. Stora[b], P. Bowen[a,*]

[a] *Laboratory of Powder Technology, cole Polytechnique Fdrale de Lausanne (EPFL), CH-1015, Switzerland*
[b] *European Organization for Nuclear Research (CERN), CH-1211 Genve 23, Switzerland*
[c] *Department of Materials and Ceramics Engineering, Universidade de Aveiro, CICECO, 3810-193 Aveiro, Portugal*

Abstract

A pragmatic approach to study sintering is through the use of the master sintering curve (MSC) which contrarily to many other sintering models, has real predictive powder. The MSC uses the combined-stage sintering model which can predict the sintering densities independently of the temperature-time path chosen as well as give an apparent activation energy for sintering. Titanium carbide pressureless sintering studies are scarce in the literature. Here we report on the first MSC determined for (nanometric) TiC, using constant heating rate dilatometry under vacuum, up to 1500 °C. An apparent activation energy of 390 kJ mol^{-1} was determined for nanometric TiC sintering using this method, which agrees with those determined in the literature.

The MSC was also determined for a TiC-carbon black nanocomposite, and compared to the pure TiC MSC, with the objective of assessing the sintering hindering of TiC. The sintering hindering was successful where the apparent activation energy was slightly higher for the TiC-CB composite, 555 kJ mol^{-1}. Furthermore, stops were made in both TiC and TiC-carbon black runs in order characterize the density, particle size, specific surface area and pore size of the samples. While in the pure TiC, at 1500 °C, the crystallite size grew up to 192 nm (from 51 nm) and densities up to 66 % (from 45 %), in the TiC-CB, TiC crystallite sizes as low as 61 nm and densities slightly increased up to 44 % (from 40 %).

Keywords: master sintering curve, titanium carbide, sintering, TiC-C nanocomposite, dilatometry

1. Introduction

Titanium carbide (TiC) is mostly known for its very high melting point, high chemical stability and very high hardness. It is used mainly in aerospace industry and in tooling - as a coating or in cermets [1, 2]. TiC has an extensive homogeneity range - TiC_x where x=0.5 to 1, which affects its melting point, being the highest, T_m=3067 °C, for $TiC_{0.86}$ [2]. Besides the referred characteristics, TiC is also a good thermal and electrical conductor. The former make it also an interesting choice for nuclear applications, in fusion and fission reactors [3]. TiC has been studied as well as a spallation target material for the production of radioactive ion beams (RIB) [4–9].

*joao.pedro.ramos@cern.ch, paul.bowen@epfl.ch
URL: `http://www.joaopedroramos.com` (J.P. Ramos)

Pure TiC densification studies by pressureless sintering, seldomly appear in the literature, due to its poor sinterability, where TiC is often found in sintering studies as a component in composite materials. Cermets are such an example, where TiC is mixed with, among others, Co, Ni, Fe, Mo and/or Cr to promote liquid phase sintering, allowing full densification at relatively low temperatures [10]. For other types of composites, which include TiC with Al_2O_3, SiC or graphite, mainly for tooling applications, hot-pressing consolidation is often used [11].

Pressureless sintering of pure TiC can be found in the literature for nanometric (70 - 200 nm) [12–14], submicron [15, 16] and micrometric [17, 18] powders at temperatures in the range of 1200 to 2400 °C [19]. Titanium carbide sintering was also attempted, unsuccessfully, with the aid of ultrasonic vibrations with and without pressure [20]. Micrometric TiC has been sintered by spark plasma sintering (SPS) and full densities were reached at relatively low temperatures, 1450-1600 °C [11].

In the pressurless sintering of nanometric TiC (140-170 nm) densities of ≈ 91 % density at 1627 °C are reached while, to reach the same density with ≈ 5 μm TiC, 2797 °C were needed [12]. Such behaviour is expected for nanomaterials since generally the sintering temperature is around $0.2 - 0.4T_m$, as opposed to 0.5-0.9T_m for micrometric materials [21]. This is also confirmed from another study, where submicron TiC particles reached 95 % density at 1800 °C while particles > 44 μm reached only 72 % at 2300 °C [16]. Additionally, higher sintering rates were observed between 1250 and 1500 °C for the submicrometric TiC. The sintering of TiC is also affected by the TiC_x stoichiometry, where lower carbon contents ($0.58 \leqslant x \leqslant 0.78$) bring higher densification rates at lower temperatures [15, 18].

To the best of our knowledge, very few studies can be found, in the literature, for titanium carbide pressureless sintering kinetics. Chermant et al. [14] computed Ashby sintering diagrams [22] from experimental results for nanometric and micrometric TiC (0.1 and 10 μm). For both, grain boundary diffusion was found to be the predominant sintering mechanism for the final stages of sintering with an activation energy of 192 kJ mol^{-1} between 1900 and 2400 °C. In another study, Ordan'yan et al. [15], has determined that depending on the stoichiometry of TiC_x the activation energy for self-diffusion (determined from sintering studies) varied from 293 kJ mol^{-1}, for x=0.6 to 468 kJ mol^{-1} for x=1. In the literature, sintering activation energies of around 400 kJ mol^{-1} are found throughout the literature for TiC [13–15], independently of the TiC size and sintering temperature. TiC grain growth as an isolated process (at full density) has also been studied and the activation energy found to be around half of the sintering Q, 200 kJ mol^{-1} [14]. All these values are summarized later in this article in table 1.

The master sintering curve (MSC), is a tool used to study sintering and to predict densification independently of the temperature-time path used [23]. We will, in this study, determine the TiC MSC and its respective apparent activation energy where to the best of our knowledge, is non existant in the literature. Furthermore, we will determine the MSC of a 1:1 volume ratio TiC-carbon black nanocomposite (TiC-CB) and compare it to the pure TiC sintering. The TiC-CB composite was developed in previous studies [7, 8] to hinder the sintering of nanometric TiC, in order to keep a nanometric TiC grain size and high porosity which are stable at high temperatures ($\geqslant$ 1500 °C) [9].

1.1. Master Sintering Curve

The classical 3-stage sintering models are good approximations to the sintering phenomena, however, they have many geometrical assumptions. This makes them only useful to interpret sintering in a qualitative way and, in most practical cases, have no predictive power [23]. Sintering is a very complex phenomena, which apart from the material, depends on the pore and particle

sizes and respective size distributions, chemical impurities, particle shape, agglomeration degree and other factors. The MSC was proposed by Su and Johnson [23] to allow for practical prediction of the density independently of the thermal path.

The MSC was derived from the unified stage sintering model final equation [23, 24]:

$$-\frac{d\rho}{3\rho dt} = \frac{\gamma\Omega}{kT}\left(\frac{\Gamma_v D_v}{G^3} + \frac{\Gamma_b \delta D_b}{G^4}\right) \tag{1}$$

where ρ is the sample density, t is the time, γ is the surface energy, Ω is the atomic volume, k is the Boltzmann constant, T is the absolute temperature, G is the mean grain size, δ is the grain boundary width and D_v and D_b are respectively the volume and grain boundary diffusion coefficients. Γ_v and Γ_b are scaling parameters that represent volume and grain boundary diffusion. From equation 1, assuming that only one dominant diffusion mechanism is active and that the microstructure evolution (which G and Γ describe) is a function of density with no regard for thermal history, one can rearrange the terms in the following way [23]:

$$\int_0^t \frac{1}{T} e^{-\frac{Q}{kT}}\, dt = \frac{k}{\gamma\Omega D_0}\int_{\rho_0}^{\rho} \frac{[G(\rho)]^n}{3\rho\Gamma(\rho)}\, d\rho \tag{2}$$

where Q is the apparent activation energy, R is the ideal gas constant, $D_0 = D_{v,0}$ (pre-exponential factor in the Arrhenius formula) and $n = 3$ for volume diffusion and $D_0 = \delta D_{b,0}$ and $n = 4$ for grain boundary diffusion. In equation 2, the left hand can be called the work of sintering, $\Theta[t, T(t)]$, only dependent on Q and the time-temperature profile, such as:

$$\Theta[t, T(t)] \equiv \int_0^t \frac{1}{T} e^{-\frac{Q}{kT}}\, dt \tag{3}$$

The right hand side of equation 2 only depends on the microstructural and material characteristics, and can be called $\Phi(\rho_r)$, where overall $\Theta[t, T(t)] = \Phi(\rho_r)$ and ρ_r is the relative density. The relative density is described from the relation $\rho_r = \rho/\rho_t$, where ρ_t is the theoretical density of the material. The MSC is obtained by the relation of ρ_r with $\Theta[t, T(t)]$.

A simple way to determine the MSC is through the use of a dilatometer which records instantaneous linear shrinkage over temperature. This can be done by recording 4-5 constant heating rate (c) curves which can be converted to density over temperature [23]. For this case, $c = dT/dt$ and equation 3 becomes:

$$\Theta \equiv \frac{1}{c}\int_{T_0}^{T} \frac{1}{T} e^{-\frac{Q}{kT}}\, dT \tag{4}$$

where T_0 is the temperature up to which no sintering happens. The density can then be plotted with the computed $\Theta[t, T(t)]$ curves for each heating rate assuming a Q value. The MSC is finally obtained when all curves converge into one by iterating Q [23]. The MSC has several assumptions in order to be applied: (i) it can only predict sintering of the same green-body (same powder and same green processing); (ii) the microstructural evolution (grain size and geometry) depends only on density - which is true normally below ρ_r=1 and (iii) one diffusion mechanism (volume or grain-boundary diffusion) dominates the sintering [23].

2. Materials and Methods

Nanometric TiC was acquired from *Goodfellow* (Ref. LS396999/1 99.9% pure, 80-130 nm) and pressed into rectangular section bars of about 15×5×2 mm with applied pressure of 62 MPa.

A TiC-carbon black nanocomposite (TiC-CB) was also produced as described elsewhere in detail [7, 9]. Briefly, carbon black was obtained from *Orion Engineered Carbons* (*Printex A Pulver*, 40 $m^2\,g^{-1}$ - 40 nm particle size). The TiC was mixed with carbon black in 1:1 volume ratio[1] in an attrition mill in isopropanol with 0.5 wt.% polyvinilpyrrolidone (PVP) to act as a dispersant. Yttria stabilized zirconia was used for milling elements. The obtained slurry was dried in a rotary evaporator, deagglomerated and pressed in the same way as the pure TiC. The TiC-CB powder compacts were thermally treated to 450 °C in a flowing argon atmosphere in order to remove the PVP.

The samples were then introduced one by one in a dilatometer made in-house. The dilatometer cell and oven were entirely made in graphite and were connected to a rotary oil pump that could maintain a 1 - 10^{-1} Pa vacuum. The sample was in contact with a graphite bar that was connected to a linear variable differential transformer sensor (LVDT), to measure sample shrinkage ($\Delta l/l_0$) at all times. In order to build a MSC, different heating ramps, 4, 8, 16 and 30 °C min^{-1}, were used until 1500 °C (oven maximum temperature).

All dilatometer curves were corrected for the blank, a curve made with a graphite sample. Corrections were also made for thermal expansion difference of TiC and graphite. This was done using the cooling part of the $\Delta l/l_0$ signal which, after blank correction, can only be due to thermal expansion. Usually the corrected $\Delta l/l_0$ can be directly converted into relative density, assuming no mass losses. In our case significant mass losses occurred and thus these were used to correct data as described below.

TiC and TiC-CB mass losses were found to be on average 6.1 % and 8.4 %, respectively. To calculate ρ_r vs T, mass loss curves over temperature were taken from a previous article [8], and can be found reproduced in the supplementary materials. At high temperatures (>800 °C) these mass losses were attributed to burning of free carbon (peak around 900 °C), TiO_2 conversion into TiC (peak around 1100 °C) and ZrO_2 conversion to ZrC (peak around 1350 °C for the case of TiC-CB). TiO_2 is present in the starting TiC at the surface, while the ZrO_2 comes from the milling elements during the processing of the TiC-CB. Densities were calculated using the mass loss curves and assuming isotropic shrinkage, $\Delta l/l_0$ to correct for sample dimensions at all times. While the different phases and respective changes will affect the theoretical density during the dilatometries, their amount is reduced, in the order of a few percent. Consequently, to simplify the data treatment, ρ_t was maintained at 4.93 g cm^{-3} for TiC and for TiC-CB the calculated value of ρ_t = 3.39 g cm^{-3} was used.

The $\Theta\,[t, T(t)]$ - ρ_r curves were computed for each heating rate for a large range of Q values using *Wolfram Mathematica v10.4*. The convergence of the curves - best Q - was found, by minimizing the reduced χ^2 using *Origin Pro 2016* to fit to a sigmoidal function, as proposed by Teng et al. [26]:

$$\rho = \rho_0 + \frac{a}{\left[1 + \exp\left(-\frac{\log(\Phi)-\log(\Phi_0)}{b}\right)\right]^c} \tag{5}$$

where a, b and c are constants, ρ_0 is the initial density and $\log(\Phi_o)$ is the abscissa coordinate in the reflection point of the curve.

To follow the microstructure evolution during sintering, some TiC and TiC-CB samples were obtained by heating up to certain temperatures at 8 °C min^{-1}. Morphology was evaluated on the sample fracture through scanning electron microscopy (SEM) in a *Carl Zeiss SMT* Σ*igma* using an in-lens secondary electron detector. *ImageJ v1.50* software was used to measure the

[1] Theoretical densities considered: TiC - 4.93 g cm^{-3} [25]; carbon black - 1.85 g cm^{-3} (given by the supplier)

particle size/grain distribution, measuring 375 particles in each SEM microstructure [27]. Specific surface area (SSA), through nitrogen adsorption was determined with a *Quantachrome eNOVA2200*. X-ray powder diffraction (XRPD) was made in a *PANalytical X'PERT PRO* diffractometer. Phase ratios were quantified by Rieveld refinement using the *PANalytical HighScore Plus v4.1* software [28]. Using the same software, crystallite size was extracted using the modified Williamson-Hall method proposed by Langford [29]. Mercury intrusion porosimetry (MIP) was done to assess pore size distribution with a *Thermo Scientific Pascal 440 Series* and a mercury contact angle of 140° was assumed for the data treatment of all samples.

3. Results and Discussion

3.1. TiC Master Sintering Curve

The dilatometric curves (ρ_t vs T) of TiC and respective derivatives ($\mathrm{d}\rho/\mathrm{d}T$) for 4, 8, 15 and 30 °C min^{-1}, can be found on figure 1a) and b), respectively. The maximum densification reached for TiC was ≈ 66 % at 4 °C min^{-1}, on figure 1a), while green densities were around 45 %. Furthermore, no plateau on the ρ_r values was reached for TiC, showing that sintering is far from complete at 1500 °C. The derivative curves on figure 1b) show an almost continuous increase of the sintering rate with the temperature, except for 1200-1300 °C. This behavior is likely due to the conversion reaction of the residual TiO_2 with the free carbon present forming TiC, which come with a density reduction as pointed on [8]. Since the dilatometer pressure was around 1 - 10^{-1} Pa and the setup where the mass losses were determined was around 10^{-3} - 10^{-4} Pa [8], this can produce a shift in the reaction thermodynamics to higher temperatures, due to higher partial pressures of CO (TiO_2+3C→ TiC+2CO). A small density decrease around 1100 °C is also noticed on figure 1a), which is likely burning of free carbon before sintering starts, delayed for the same reasons as described before.

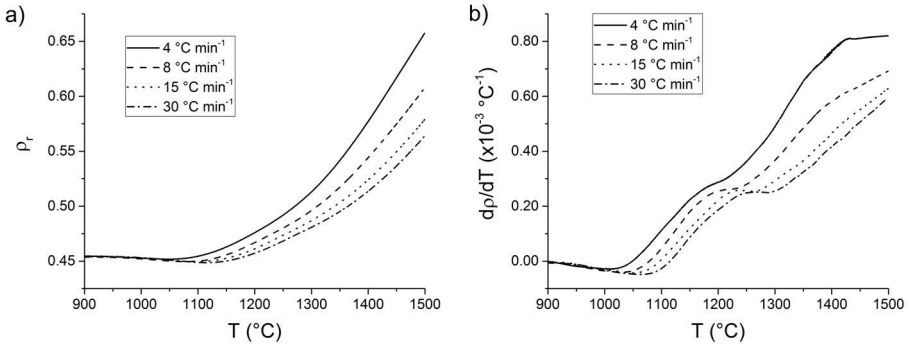

Figure 1: Dilatometric curves for nanometric TiC (a) and respective derivative (b) for different heating rates: 4, 8, 15 and 30 °C min^{-1}.

From the dilatometries of figure 1a) the equation 4 was used to compute Θ vs ρ_r for different Q values. The sigmoid function (equation 5) was used to fit the best Q value, obtaining the MSC seen in figure 2. Due to the fact that the top part of the sigmoid is unknown, the fit did not converge unless ρ_0 from equation 5 was fixed to the minimum value of the curve. The apparent activation energy found for TiC sintering was Q=390 kJ mol^{-1} with a reduced χ^2 of 1.66×10^{-6}, as seen in figure 2 and its inset. Even though ρ_0 was fixed, a good reduced χ^2 was achieved and

as seen on figure 2, the fit function follows the Θ values reasonably well especially for increasing densities - when sintering is occurring.

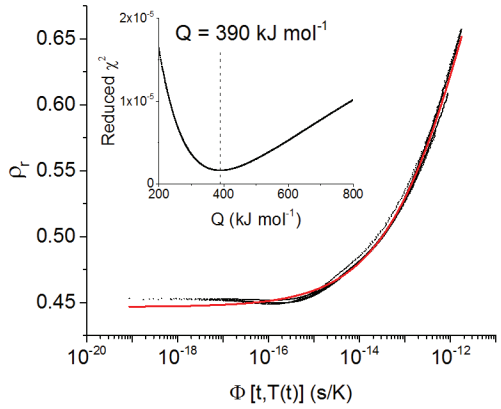

Figure 2: MSC of nanometric TiC and reduced χ^2 minimization (inset). The parameter values for the sigmoid function (equation 5) were ρ_0=0.447, θ_0=3.623 × 10^{-12}, a=0.551, b=2.573, c=1.173.

As no other MSC curves exist for TiC in the literature for comparison, the apparent activation energy found can be compared with those found for pressureless sintering of TiC [13–15], as summarized in table 1. Literature nanometric TiC Q values of 389, 458 [13] and 460 kJ mol^{-1} [14] (position 2, 3 and 4 on table 1), are very close to the one determined in this work, even when, in the later case, the temperatures used were much higher (1900-2100 °C). Although on line 4 of table 1, TiC is submicron, that didn't significantly change its Q, 468 kJ mol^{-1} [15] which was obtained for stoichiometric TiC.

In a previous study, the stoichiometry of the titanium carbide used in this study was determined to be $TiC_{0.68}$ [8]. In the literature the TiC_x stoichiometry affects the sintering behaviour of TiC [15, 18]. Ordan'yan et al. [15] reported increasing Q values with x on TiC_x, where a TiC with exactly the same stoichiometry of the one used in this study ($TiC_{0.68}$) had Q = 297 kJ mol^{-1} (line 6 of table 1). This value was significantly lower than the one obtained in the same study for stoichiometric TiC, Q = 468 kJ mol^{-1} (line 5 of table 1) and also significantly lower than the one obtained in this study for the same stoichiometry. Activation energies for grain growth (lines 7 and 8 of table 1) were found significantly lower [14] than the ones obtained for sintering in this work and others.

In addition to the values of Q for sintering and grain growth, the activation energies of C and Ti self-diffusion on TiC are also presented on lines 9 and 10 in table 1. With respect to single crystal diffusion of Ti in TiC (Q = 740 kJ mol^{-1}), our value is smaller, as would be expected for polycrystalline materials where high concentration defect zones facilitate diffusion though surface and grain boundary diffusion mechanisms. Carbon self-diffusion Q is close to the one of this work, where the high number of carbon vacancies present in TiC [30–32] make it not depending on the sample structure. Nonetheless, Ti is still expected to control the sintering as the largest atom (Ti - 1.40 Å, C - 0.70 Å), and consequently is also the slowest - ≈ 10^4 slower than C [30, 31].

Where noticeable changes in dρ/dT were seen (figure 1b), stops at 1250 and 1400 °C in the 8 °C min^{-1} dilatometric runs were made in order to assess the TiC microstructure. Characteriza-

Table 1: Activation energies for pressureless sintering of TiC, for C and Ti self-diffusion in TiC and for the MSC curves for TiC and TiC-carbon black composites (TiC-CB).

#	Form	Q (kJ mol^{-1})	Technique	Temperature (°C)	Reference
1	Nanometric TiC[a]	390	MSC	1000-1500	this work
2	TiC (12.4 m^2 g^{-1} ca. 98 nm)[b]	389 ± 20	Sintering	1197-1472	[13]
3	TiC (13.6 m^2 g^{-1} ca. 89 nm)[a,b]	458 ± 13	Sintering	1155-1456	[13]
4	Nanometric TiC (75 nm)	460	Sintering	1900-2100	[14]
5	TiC (>4 m^2 g^{-1} ca. 304 nm)[a,b]	468	Sintering	900-1900	[15]
6	$TiC_{0.68}$ (>4 m^2 g^{-1} ca. 304 nm)[a,b]	297	Sintering	900-1900	[15]
7	Nanometric TiC (75 nm)	192	Grain Growth (ρ_r=1)	2250-2400	[14]
8	Micrometric TiC[a]	251	Grain Growth (ρ_r=1)	1900-2400	[14]
9	Single Crystal TiC	740 ± 15	Residual activity (^{44}Ti)	1920-2215	[30]
10	Single and polycristalline TiC	399-447	Residual activity (^{14}C)	1450-2280	[31, 32]
11	TiC-CB nanocomposite	555	MSC	1000-1500	this work

[a] Commercially available.
[b] $G_{BET} = 6/(SSA * \rho_t)$, assuming spherical particles, where G_{BET} is the particle size.

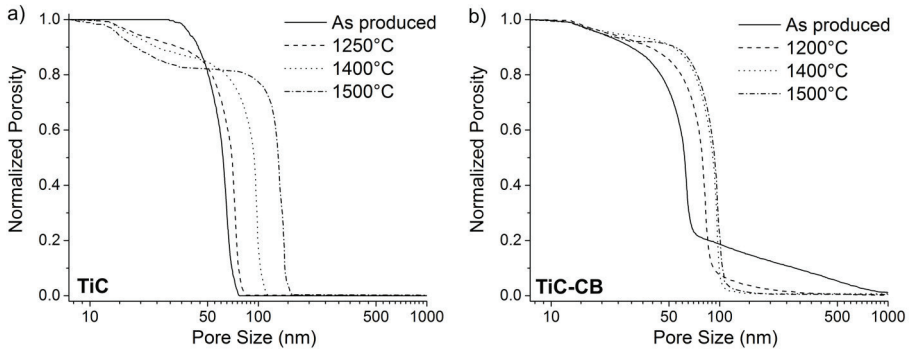

Figure 3: Cumulative pore size distributions for the 8 °C min^{-1} dilatometry curves, as supplied, 1250, 1400 and 1500 °C, for TiC (a) and TiC-CB (b).

tions were also done before sintering and at the end (1500 °C). MIP was done for each sample as represented on figure 3a and SEM microstructures can be seen in figure 4. The mean particle size and standard deviation from the size distribution measured with *ImageJ v1.50* from the SEM pictures, can be found on table 2, together with the results from SSA, calculated G_{BET}, XRPD crystallite size and MIP median pore diameter.

On the microstructures of figure 4 sintering through neck formation can clearly be seen, leading to crystallite size growth. The crystallite size determined by XRPD and the one observed in SEM, on table 2, agree very well with each other. In here TiC crystallite size evolves from ≈ 60 nm to ≈ 200 nm, accompanied by large surface area reductions (≈1/10 of initial SSA) as seen on table 2. From room temperature to 1250 °C large surface area reduction, from 25.1 to 11.7 m^2 g^{-1}, is accompanied by a very small densification (figure 1a). This points to the controlling of early stage sintering by surface diffusion, which leads to coarsening of the structure with reduced densification.

The median pore size, determined by MIP, increases for higher temperatures, from 62 nm as

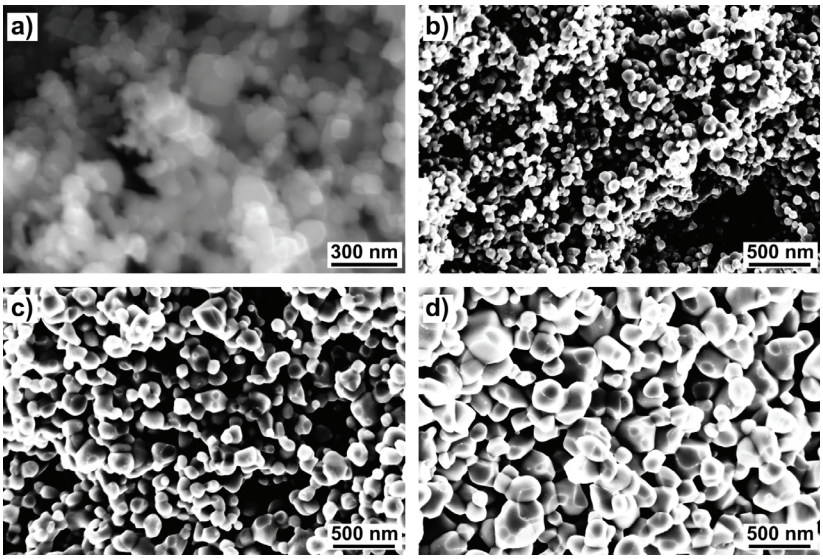

Figure 4: SEM fracture microstructures for the TiC 8 °C min^{-1} dilatometry curves: as-produced (a), 1250 (b), 1400 (c) and 1500 °C (d).

supplied to 131 nm at 1500 °C, as seen on table 2. The respective normalized pore size distributions, on figure 3a, show this tendency together with an increase of small pores fraction (<50 nm). A fraction of around 50 % of the porosity of the as supplied TiC has been reported to be of pores larger than 200 nm (related with intra-agglomerate porosity) [7], contrarily to what is reported by MIP. The large pores are not detected by MIP due to the assumption of the technique that each pore is accessible through larger pores or from the surface, which is obviously not the case here. Nonetheless the observed increase of the small pores fraction is expected from sintering of the TiC particles while the general increase in pore size can be explained by the coalescence of these particles within the agglomerates which increase the overall pore size.

Table 2: SSA, SEM particle size, XRPD crystallite size, for the TiC as supplied and heated at 8 °C min^{-1} up to 1250, 1400 and 1500 °C as well as for the TiC-CB as produced and heat treated at the same rate up to 1200, 1400 and 1500 °C.

Material	Temperature (°C)	ρ_r[a]	SSA ($m^2\,g^{-1}$)	SEM particle size (nm)	XRPD crystallite size (nm)	MIP Median Pore Diameter (nm)
TiC	RT	0.46	25.1	64 ± 29	51	62
	1250	0.51	11.7	71 ± 32	57	70
	1400	0.51[b]	5.4	129 ± 54	120	94
	1500	0.60	2.7	192 ± 72	220	131
TiC-CB	RT	0.41	30.0	54 ± 29	48	62
	1200	0.42	23.2	47 ± 30	45	79
	1400	0.46	20.4	50 ± 24	50	91
	1500	0.44	13.0	58 ± 28	61	93

[a] Determined through the geometrical density.
[b] Sample partially broken.

3.2. TiC-CB nanocomposite Master Sintering Curve

As in the TiC case, the densification curves and respective derivative from the dilatometric experiments of TiC-CB nanocomposite were obtained at the same heating rates as for TiC (4, 8, 15 and 30 °C min^{-1}) and are plotted on figure 5a and b, respectively. The green densities were close to 40 % and densification was very small, reaching at 1500 °C, only ≈ 44 % (figure 5a). Similarly to TiC, there is a negative derivative up to 1100 °C on figure 5b) which is likely linked with losses of carbon reacting with residual oxygen as pointed out on [8]. Additionally, the reaction of TiO_2 to TiC is also seen but in this case at slightly lower temperatures (between 1125 and 1275 °C) than the TiC. The temperature shift is likely due to the reductive environment created by carbon black present in the sample's microstructure.

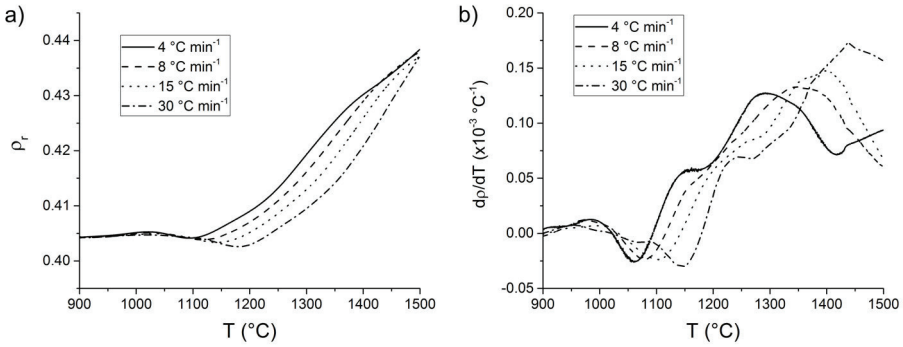

Figure 5: Dilatometric curves for TiC-carbon black nanocomposite (a) and respective derivative (b) for different heating rates: 4, 8, 15 and 30 °C min^{-1}.

Similarly to TiC, stops were made during the dilatometric runs in the 8 °C min^{-1} curves where dρ/dT (figure 5b)) would present significant changes: at 1200 and 1400 °C. Characterization was also conducted on the as-produced TiC-CB material and at the end of the dilatometry (1500 °C). XRPD was done to all the TiC-CB samples to assess the crystalline phases, where ZrO_2 and ZrC were found, as seen on figure 6. Although ZrO_2 is not found in the as-produced TiC-CB, likely due to the low contents and poor crystallinity, it appears at 1200 °C on the XRPD diffractograms. The ZrO_2, coming from the milling elements, reacts with the carbon to form ZrC, as seen on the diffractograms of the 1400 and 1500 °C samples on figure 5, and in other studies done before [8]. ZrC quantities at 1500 °C, calculated by Rietvelt refinement, are ≈ 2.5 wt.%. This reaction is also detected in the dρ/dT curves (figure 5) starting at 1275 °C for 4 °C min^{-1} and 1450 °C for 30 °C min^{-1}, slowing down the apparent sintering rate due to density losses.

The MSC of TiC-CB nanocomposite was computed from the dilatometries of figure 5 and can be found on figure 7. The MSC curve follows very well the computed $\Theta\,[t, T(t)]$ - ρ_r values except for the lowest and highest density parts, both likely due to mass loss shifts in temperature. In the case of TiC-CB, the apparent activation energy found was 555 kJ mol^{-1} with a reduced χ^2 of 1.47×10^{-7}. There are no sintering kinetics studies on TiC-carbon composites for comparison with the Q obtained in this work. However, the TiC-CB Q obtained is higher than the one obtained for TiC (390 kJ mol^{-1}). The carbon in the TiC microstructure, acts as a non-sintering inert phase, reducing the TiC-TiC coordination number, hindering the sintering process, thus increasing Q.

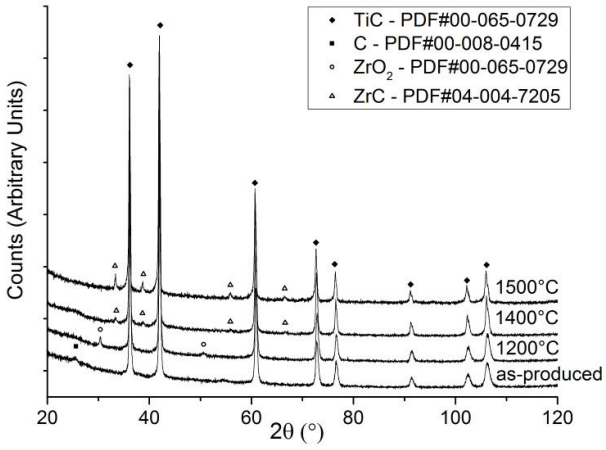

Figure 6: Diffractograms obtained through XRPD for the TiC-CB 8 °C min^{-1} dilatometry curve stops: as-produced (a), 1200 (b), 1400 (c) and 1500 °C (d).

No qualitative size difference between the TiC and CB in the TiC-CB microstructures of figure 8 is observed. But, with careful analysis, particle sizes determined from the TiC-CB SEM microstructures, show very coherent results with those crystallite sizes determined by XRPD on table 2. There is barely any evolution of the TiC-CB particle size values as seen on table 2, which sit around its initial value, 50-60 nm. In the same table, TiC-CB SSA values are reducing to slightly less than to 1/2 of the initial SSA. The SSA losses are likely due to necking, where TiC contact points transform into grain boundaries, pore coarsening (as seen from the MIP values on table 2 and figure 3b) and surface smoothing.

The pore sizes for TiC-CB can be found on table 2 and respective distributions on figure 3b. On table 2 TiC-CB median pore size increases from 62 nm as produced, to 93 nm at 1500 °C, showing an expected smaller variation when comparing to TiC, due to sintering hindering by the CB. The pore size distribution of TiC-CB as produced, contrarily to TiC as supplied, shows around 12.6 vol.% pores higher than 200 nm which agree quite well with the 9.6 vol.% deducted from a nitrogen desorption isotherm in a previous study [7]. The large pore fraction is then reduced significantly at 1200 °C as seen on figure 3b, disappearing at 1400 and 1500 °C, where small increases in the median pore size are seen. In another study of TiC-CB at 1500 °C for 2 h the volume ratio of pores above 200 nm is increasing [7] and not decreasing. Since it is unlikely that such big pores are closing at low temperatures and the MIP basically determines the pore entry size, the large pore size reduction is likely due to TiC sintering.

4. Conclusions

In this work, the master sintering curve, MSC, of nanometric TiC was determined through the use of a graphite vacuum dilatometer, building different relative density vs temperature curves at different heating rates. From green densities of 0.45, relative densities up to 0.66 were reached during the dilatometries. The determined apparent activation energy, Q=390 kJ mol^{-1}, from the MSC analysis describe well the sintering of TiC inside the interval of densities studied. This Q value is close to reported literature values for TiC pressureless sintering.

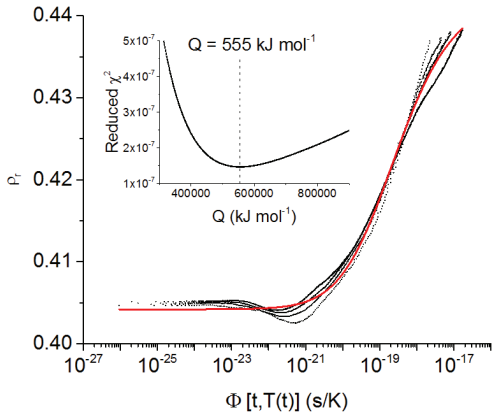

Figure 7: MSC of TiC-CB nanocomposite and reduced χ^2 minimization (inset). The parameter values for the sigmoid function (equation 5) were ρ_0=0.404, θ_0=7.586 × 10^{-20}, a=0.038, b=2.022, c=1.654.

The sintering of a 1:1 volume ratio TiC-carbon black was studied as well using the master sintering curve. The Q in this case was higher (555 kJ mol^{-1}) since the carbon acts as an inert phase, hindering sintering of TiC and reducing its coordination number, where very low densifications are reached during the dilatometries (up to 44 % from 40 %). Furthermore, while in the pure TiC, at 1500 °C, the crystallite size grew from 51 nm to 192 nm, in the TiC-CB, TiC crystallite sizes were up to 61 nm.

The MSC is a very useful tool which can be used to predict the microstructure independently of the time-temperature profile. The MSC obtained here can be of value to predict the sintering behaviour for the use of this TiC in other fields, such as tooling and ultra-high-temperature materials.

Acknowledgments

The authors would like to acknowledge Maria Joao Bastos for the XRPD tests, Filipe Oliveira for lending the dilatometer equipment, Zhangli Hu for the support with the mercury intrusion porosimetry tests and Cristina Fernandes, Manuela Fernandes and Isabel Antunes for the support during the experimental work. We would like to acknowledge as well Orion Engineered Carbons, S.A. for supplying the carbon black for this study. The author J.P. Ramos gratefully acknowledge CERN and EPFL for the doctoral studentship funding.

References

[1] T. Y. Kosolapova, Carbides - Properties, Production and applications, Plenum Press, New York and London, 1971.
[2] H. O. Pierson, Handbook of Refractory Carbides and Nitrides: Properties, Characteristics, Processing, and Applications, Noyes Publications, Bracknell, 1996.
[3] C. Dickerson, Y. Yang, T. R. Allen, Defects and microstructural evolution of proton irradiated titanium carbide, Journal of Nuclear Materials 424 (1-3) (2012) 62–68. doi:10.1016/j.jnucmat.2012.02.005.
[4] P. Hoff, O. Jonsson, E. Kugler, H. Ravn, Release of nuclear reaction products from refractory compounds, Nuclear Instruments and Methods in Physics Research 221 (2) (1984) 313–329. doi:10.1016/0167-5087(84)90002-4.

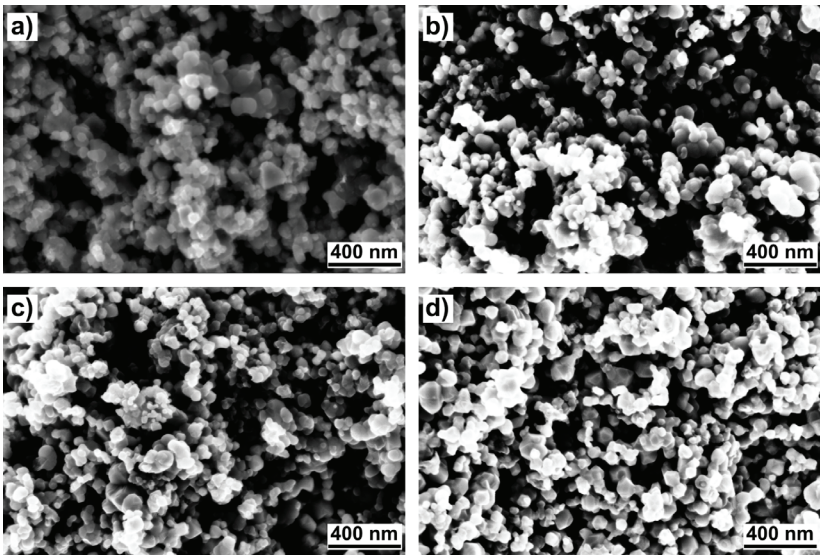

Figure 8: SEM fracture microstructures for the TiC-CB 8 °C min^{-1} dilatometry curves: as-produced (a), 1200 (b), 1400 (c) and 1500 °C (d).

[5] L. Carraz, I. Haldorsen, H. Ravn, M. Skarestad, L. Westgaard, Fast release of nuclear reaction products from refractory matrices, Nuclear Instruments and Methods 148 (2) (1978) 217–230. doi:10.1016/0029-554X(70)90171-0.

[6] V. Hanemaayer, P. Bricault, M. Dombsky, Composite ceramic targets for high power proton irradiation, Nuclear Instruments and Methods in Physics Research Section B: Beam Interactions with Materials and Atoms 266 (19-20) (2008) 4334–4337. doi:10.1016/j.nimb.2008.05.094.

[7] J. P. Ramos, A. M. R. Senos, C. M. Fernandes, T. Stora, P. Bowen, Development of a processing route for carbon allotrope-based TiC porous nanocomposites, to be published.

[8] J. P. Ramos, A. M. R. Senos, T. Stora, P. Bowen, Stability of nanometric TiC-carbon composites: effects of carbon allotropes and Zr milling impurities, to be published.

[9] Ramos, et al., Constant isotope release properties measured for an online prototype TiC-carbon nanocomposite target material, to be published.

[10] A. Rajabi, M. J. Ghazali, J. Syarif, A. R. Daud, Development and application of tool wear: A review of the characterization of TiC-based cermets with different binders, Chemical Engineering Journal 255 (2014) 445–452. doi:10.1016/j.cej.2014.06.078.

[11] L. Cheng, Z. Xie, G. Liu, W. Liu, W. Xue, Densification and mechanical properties of TiC by SPS-effects of holding time, sintering temperature and pressure condition, Journal of the European Ceramic Society 32 (12) (2012) 3399–3406. doi:10.1016/j.jeurceramsoc.2012.04.017.

[12] S. Panfilov, O. Padalko, N. Mitrenko, Behavior of Ultrafine Titanium Carbide Powders During Annealing and Sintering, Soviet Powder Metallurgy and Metal Ceramics 24 (11) (1985) 824–828. doi:10.1007/BF00802551.

[13] B. Manley, J. B. Holt, Z. A. Munir, Sintering of Combustion-Synthesized Titanium Carbide, in: Materials Science Research, Springer US, Boston, MA, 1984, pp. 303–316. doi:10.1007/978-1-4613-2761-5_22.

[14] J. Chermant, M. Coster, B. Mordike, Sintering and grain growth in titanium carbide, Science of Sintering 12 (3) (1980) 171–180.

[15] S. S. Ordan'yan, G. S. Tabatadze, L. V. Kozlovskii, Densification of nonstoichiometric titanium carbide during sintering, Soviet Powder Metallurgy and Metal Ceramics 18 (7) (1979) 458–461. arXiv:arXiv:1011.1669v3, doi:10.1007/BF00797248.

[16] D. Moskowitz, M. Humenik Jr., A Note on Vacuum Sintered Fine-Particle Titanium Carbide, Planseeberichte fur Pulvermetallurgie 9 (1/2) (1961) 60–64.

[17] I. P. Kushtalova, Investigation of the sintering of loosely poured titanium carbide and zirconium carbide powders, Soviet Powder Metallurgy and Metal Ceramics 6 (8) (1967) 604–605. doi:10.1007/BF00774543.

[18] A. Gubernat, Sintering Kinetics of Various Carbides, in: Proceedings of the 10th International Conference of

the European Ceramic Society, Faculty of Materials Science and Ceramics, Department of Advanced Ceramics, Cracow, 2007, pp. 148–153.
[19] A. Gubernat, L. Stobierski, Fractography of Dense Metal-Like Carbides Sintered with Carbon, Key Engineering Materials 409 (2009) 287–290. doi:10.4028/www.scientific.net/KEM.409.287.
[20] P. S. Kislyi, L. S. Golubyak, Sintering of titanium carbide during isothermal heating, Soviet Powder Metallurgy and Metal Ceramics 10 (1) (1971) 19–21. doi:10.1007/BF00798040.
[21] C. C. Koch (Ed.), Nanostructured Materials: Processing, Properties and Potential Applications, 2nd Edition, Noyes Publications, New York, 2002.
[22] M. Ashby, A first report on sintering diagrams, Acta Metallurgica 22 (3) (1974) 275–289. doi:10.1016/0001-6160(74)90167-9.
[23] H. Su, D. L. Johnson, Master Sintering Curve: A Practical Approach to Sintering, Journal of the American Ceramic Society 79 (12) (1996) 3211–3217. doi:10.1111/j.1151-2916.1996.tb08097.x.
[24] J. D. Hansen, R. P. Rusin, M.-H. Teng, D. L. Johnson, Combined-Stage Sintering Model, Journal of the American Ceramic Society 75 (5) (1992) 1129–1135. doi:10.1111/j.1151-2916.1992.tb05549.x.
[25] D. R. Lide (Ed.), CRC Handbook of Chemistry and Physics, 90th Edition, CRC Press, 2010.
[26] M.-H. Teng, Y.-C. Lai, Y.-T. Chen, Computer Program of Master Sintering Modeling to Accurately Predict Sintering Results, Western Pacific Earth Sciences 2 (2) (2002) 171–180.
[27] C. A. Schneider, W. S. Rasband, K. W. Eliceiri, NIH Image to ImageJ: 25 years of image analysis, Nature Methods 9 (7) (2012) 671–675. doi:10.1038/nmeth.2089.
[28] T. Degen, M. Sadki, E. Bron, U. König, G. Nénert, The HighScore suite, Powder Diffraction 29 (S2) (2014) S13–S18. doi:10.1017/S0885715614000840.
[29] J. Langford, The Use of the Voigt Function in Determining Microstructural Properties from Diffraction Data by means of Pattern Decomposition, in: E. Prince, J. Stalick (Eds.), Proceedings of the international conference Accuracy in Powder Diffraction II - NIST Special Publication 846, NIST, Gaithersburg, 1992, pp. 110–126.
[30] S. Sarian, Diffusion of ^{44}Ti in TiC_x, Journal of Applied Physics 40 (9) (1969) 3515. doi:10.1063/1.1658229.
[31] S. Sarian, Diffusion of carbon in TiC, Journal of Applied Physics 39 (7) (1968) 3305–3310. doi:10.1063/1.1656774.
[32] D. L. Kohlstedt, W. S. Williams, J. B. Woodhouse, Chemical diffusion in titanium carbide crystals, Journal of Applied Physics 41 (11) (1970) 4476–4484. doi:10.1063/1.1658485.

4.2 Further discussion and summary of the TiC and TiC-carbon black sintering kinetics

In the figure 4.a7, of the the article just presented, the MSC obtained for the TiC-CB composite and respective Q, reflects more the initial sintering of the TiC-TiC contacts and, to some extent, density variations are affected by the mass losses (reaction of TiO_2 and ZrO_2) rather than the later stabilization of TiC with carbon. On figure 4.a5a, towards $T \gtrsim 1350\,^{\circ}C$ sintering of TiC-CB seems to slow down (reduction of the $d\rho/dT$, figure 4.a5b) and ρ_r vs Θ turns into an approximately straight line, steadily increasing the density. This effect is less and less visible for high heating rates, as expected due to delayed sintering kinetics, where at $30\,^{\circ}C\,min^{-1}$ it is not seen anymore. The TiC-CB MSC determined on figure 4.a7 does not reflect very well this later regime, since the points seem to start to diverge from each other for ρ_r values higher than 43 %.

Isolation of small sections of the MSC has been done before to obtained activation energies for different stages of sintering [138]. Since a different regime is probably in play here, these sections were isolated and a new Q computation was done, as seen in figure 4.1. In this case, since the sections are straight, instead of the sigmoid equation, a simple line ($\rho = m\Theta + y_i$, where m is the slope and y_i is the y-intercept) was used to study the points convergence with different Q values. The result on this computation can be found on the inset of figure 4.1 where the darker points in this figure represent the isolated heating rate sections used for the fit. The best Q was found to be $3.0\,MJ\,mol^{-1}$ with a reduced χ^2 of 6.00×10^{-10}. This Q value is extraordinarily high and, to our knowledge, far from any activation energy in the literature for sintering. Nonetheless an activation energy of 1.3 MJ for a composite of ZrO_2+3 mol % Y_2O_3 was found in the literature using the MSC [138].

Even though, this Q can be outside of the assumptions of this model and is only indicative of the sintering stage where all the TiC-TiC contact points have sintered and very few or no TiC-TiC contacts exist anymore. In this later stage, the majority of contacts are TiC-C where for sintering of TiC to happen (or other microstructural changes), large amounts of energy are necessary, explaining the very high Q obtained.

In a study which is presented later (in section 5.1, page 127), XRPD crytallite sizes of 115 nm at 1800 °C were determined for 10 h and 119 nm at 2000 °C for 14 h using the same TiC-CB composite. These results show how effective CB is in stabilizing nanometric TiC even at such extreme temperatures, which goes in the direction of the high effective Q obtained.

The determined Q in this latter case, could be further investigated using a dilatometer which allows for higher temperatures to add more points and improve its precision. In our case, the dilatomter used only allowed up to 1500 °C, so the Q obtained serves as an indication only. Another approach would be to carry out further sintering modeling and/or simulation, allowing a prediction of the coordination number of TiC and other sintering parameters for the double phase structure.

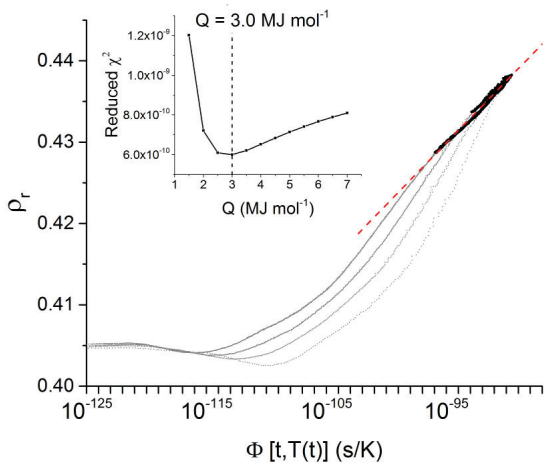

Figure 4.1 – MSC for late stage sintering of TiC-CB nanocomposite and reduced χ^2 minimization (inset). The red line represents the best fit for the dark points which represent the later stage (see text), while the grey points are the remaining points. The parameter values for the linear function fitted in the linear-log plot are m=0.0015 and y_i=0.574.

To summarize the main conclusions of this chapter are:

- dilatometry was successfully used to compute the master sintering curve (MSC) of nanometric TiC and the nanocomposite TiC-carbon black up to 1500 °C, data which was not available in the literature (particularly in the case of TiC);
- TiC green bodies with relative densities of 45 % were sintered up to 66 %, where the microstructure was followed through morphology, grain size, SSA and pore size and an activation energy of 390 kJ mol^{-1} was obtained, which agrees well with literature values for pressureless sintering of TiC;
- TiC-carbon black starting densities were about 40 % which were sintered up to 44 %, where the TiC crystallite size barely grew and MSC was also computed where an activation energy of 555 kJ mol^{-1} was determined.
- even thought it is reported in the literature that sintering of TiC_x with low values of x, such as the one of this work ($TiC_{0.68}$), have higher sintering rates and lower Q values than for those with x close to 1, this was not verified in this work;
- an apparent activation energy of 3.0 MJ mol^{-1} was obtained, isolating the dilatometry sections of TiC-carbon black, above 1300 °C. Even though this value is very likely outside the assumptions of this model it serves as an indication of the hindering effect of the carbon black on the sintering of TiC.

5 Isotope release properties from TiC-carbon nanocomposites

Contents

5.1 Article: Constant isotope release properties measured for an online prototype TiC-carbon nanocomposite target material 127

1. Introduction 129
2. Materials and Methods 133
3. Results and Discussion 137
4. Conclusions 142

5.2 Summary of the isotope release properties from TiC-carbon nanocomposites 147

5.1 Article: Constant isotope release properties measured for an online prototype TiC-carbon nanocomposite target material

This project culminates with the test of the studied nanocomposites for isotope release and ultimately the operation of a prototype target material at the ISOLDE facility at CERN. In this section we present an article with the isotope release studies which allowed the selection of the most promising TiC-C nanocomposite to be used at ISOLDE, as well as its production scale up to build a full target and, the results of the prototype target beam time at ISOLDE. In the next section (5.2) the discussion is further extended and the main conclusions for this chapter are presented.

The article below, included in this thesis, is a draft to be submitted for publication in Nuclear Instruments and Methods in Physics Research Section B: Beam Interactions with Materials and Atoms. The author of the thesis (first author) has written the manuscript, organized the experiment beam time, participated in the shift rotation and did the rest of the experimental work and result analysis. The figures and tables from this article are present in the list of figures and list of tables of the thesis with the numbering form of 5.ax, where x is the number

of table/figure in the article. The supplementary materials of this article can be found starting on page 170 on the appendix section A.4.

Constant isotope release properties measured for an online prototype TiC-carbon nanocomposite target material

J.P. Ramos[a,b,*], A. Gottberg[a,1], T.M. Mendonca[a], R.S. Augusto[a], B. Blank[c], K. Johnston[a,d], P. Bowen[b], A.M.R. Senos[e], J. Lehnert[d], M. Deicher[d], H. Wolf[d], T. Stora[b,*]

[a] *European Organization for Nuclear Research (CERN), CH-1211 Genève 23, Switzerland*
[b] *Laboratory of Powder Technology, École Polytechnique Fédérale de Lausanne (EPFL), CH-1015, Switzerland*
[c] *CEN Bordeaux-Gradignan, Le Haut-Vigneau, F-33175 Gradignan Cedex, France*
[d] *Experimentalphysik, Universität des Saarlandes, 66041 Saarbrücken, Germany*
[e] *Department of Materials and Ceramics Engineering, Universidade de Aveiro, CICECO, 3810-193 Aveiro, Portugal*

Abstract

Through the Isotope Separator OnLine (ISOL) technique, radioactive isotopes are produced by bombarding a target material with highly energetic particles. The isotopes produced in the bulk of the material have to diffuse out, evaporate and effuse through the material porosity to a transfer line into an ion source. Rolled and embossed Ti metal foils of 30 µm have been used at ISOLDE to deliver beams of Sc, Ca and K. However, due to the high operation temperatures, target degradation through foil sintering and melting happens, bringing reduced beam intensities over time.

Highly porous target materials with nanosized grains have been successfully tested at the ISOLDE facility at CERN, throughout the past 10 years, to deliver high and stable intensities of several radioactive ion beams. These materials profit from short diffusion distances and high porosity to enhance isotope release rates. TiC is a highly refractory Ti-based material with potential to become an ISOL nanostructured material. In order to accomplish this, an offline investigation of isotope release properties was done on previously developed TiC microstructures: a submicrometric TiC and two TiC-C nanocomposites, where C is in the form of carbon black or multi wall carbon nanotubes. TiC-carbon black (TiC-CB) nanocomposite has shown the best release properties and it's production procedure was scaled up to produce a full target to be tested at ISOLDE from 1300 to 2000 °C.

The TiC-CB nanocomposite target showed improved yields of Na and Li relatively to the Ti foils target (at operation start), slighly lower yields K yields but low yields on Ca isotopes due to reaction with the target carbon black. Furthermore, this target has shown no signs of degradation during its operation time, which brings generally higher integrated yields over time. Even though the yields are high, this target shows an apparently longer release time-structure for all isotopes, as all nanomaterials operated at ISOLDE so far.

Keywords: titanium carbide, radioactive ion beams, target nanomaterials, CERN-ISOLDE, isotope separator online

[*] joao.pedro.ramos@cern.ch, thierry.stora@cern.ch
URL: `http://www.joaopedroramos.com` (J.P. Ramos)
[1] Present Address: TRIUMF, 4004 Wesbrook Mall, Vancouver, BC V6T 2A3, Canada.

1. Introduction

The ISOL (Isotope Separator OnLine) technique, invented in 1951 [1], allows the production of beams of isotopes which can be used for physics research. The isotopes are produced by transmutation of the atoms of a thick target by bombarding it with a beam of highly energetic particles, also refered to as primary beam. The target material is kept at temperatures high enough to promote the diffusion of the recently produced and thermalized products to the surface of the grains. From here, the isotopes evaporate and effuse through the material porosity and escape the target material. The isotopes then travel through a transfer line which connects the target container to an ion source. Arriving at the ion source, they are singly ionized and extracted to form a beam, also called secondary beam, which is mass separated and ready to be delivered for physics experiments.

There are many ISOL facilities with different primary beams around the world [2], but among the largest is ISOLDE at CERN[2] using a primary proton beam of 1.4 GeV, 2.2 μA and ISAC at TRIUMF[3] using 500 MeV up to 100 μA. Even though all ISOL facilities have quite different target and ion source systems to cope with the different primary beam properties, they need to overcome very similar challenges.

Due to the limited isotope half-lives ($t_{1/2}$), the process of creating a radioactive ion beam has to be as efficient and as fast as possible in order to avoid losses which lead to lower radioactive ion beam intensities or yields (Y [μC^{-1}]):

$$Y = \sigma \cdot I \cdot N \cdot n_C \cdot \varepsilon_{rel} \cdot \varepsilon_{is} \cdot \varepsilon_{sep} \cdot \varepsilon_{transp} \tag{1}$$

where the total number of isotopes produced a.k.a in-target production, $Y_{Prod}[\mu C^{-1}] = \sigma \cdot I \cdot N \cdot n_C$, where σ [mb] is the isotope production cross section, I [μA] is the primary beam intensity, N [dim] is the number of target material atoms exposed to the primary beam and n_C [μC^{-1}] is the number of protons per μC: $6.242 \cdot 10^{12}\,\mu C^{-1}$. The process then depends on the efficiency of release from the target material (diffusion and effusion times), ε_{rel} [%], ionization efficiency, ε_{is} [%], mass separation efficiency, ε_{sep} [%] and beam transport efficiency, ε_{transp} [%]. The ε_{rel} is usually, by far, the most liming factor in the production of radioactive ion beams due to slow diffusion of the element of interest or chemical interaction between the target material and/or the structural materials. By engineering the material microstructure, in the case of solid materials [3–5] and studying the chemistry of the isotope element [6] one can gain orders of magnitude or even introduce new ISOL beams.

ISOL target materials can vary amongst metals, oxides, carbides and others in powder (free or compacted), molten or solid form [7]. Generally, they must have a high production cross section for the isotope of interest, be refractory to be able to operate at the highest possible temperature to promote the release processes, diffusion and effusion, which are thermally activated. The temperature is limited by target degradation through decomposition, vaporization (of itself or impurities) or sintering which can bring reduced beam intensities [8]. From the parameters of equation 1, when developing a target material, one can only vary σ, by choosing the appropriate element with the highest production cross section for the isotope of interest, N, by varying the

[2]ISOLDE - Isotope Separator OnLine DEvice, CERN - European Organization for Nuclear Research, Geneva, Switzerland. http://isolde.web.cern.ch/

[3]ISAC - Isotope Separator and Accelerator, TRIUMF - TRI University Meon Facility: Canada's national laboratory for particle and nuclear physics and accelerator-based science, Vancouver, Canada. http://www.triumf.ca/

density of the material and ε_{rel} by working on the target microstructure and/or isotope element chemistry.

Diffusion and effusion characteristic times, must be in the same order or below the isotope $t_{1/2}$, especially for isotopes in the tens to hundreds of milliseconds range, in order to avoid major losses. Since diffusion has an Arrhenius dependence with the temperature, the reduction of the release times can be achieved by increasing the target temperature, which can bring target material degradation. Shorter release times can also be achieved by reduction of the target material grain sizes and increase of the open porosity [3, 4, 7]. Engineering of the target material microstructure has been done at ISOLDE for SiC [3], CaO [4], UC_x [7] and LaC_2 [9] and multi wall carbon nanotube [10] target materials. In all cases by reducing the grain size and having a large fraction of open porosity, increased released efficiencies and stability over time were obtained.

Nanostructured materials tend to sinter faster than micrometric ones [11], so unless stabilized they have to be operated at lower temperatures. In the case of CaO, the decrease in operation temperature was compensated by the reduction of the diffusion distances (by reduction of the grain size), bringing high yields and stable intensities [4]. To stabilize a nanostructure, one can either dope the material with other elements or introduce a second non-soluble phase which is inert to sintering. This was done for the UC_x target where multi wall carbon nanotubes (MWCNT) were mixed with nanometric UO_2 and heat treated to form UC_x, which sintering is hindered by the presence of MWCNT [5].

1.1. Ti element as a target at ISOL facilities

The titanium element has good spallation cross sections to produce (exotic) neutron deficient Sc, Ca and K isotopes which are interesting for physics studies [12–14]. Titanium has 3 refractory forms which were studied as ISOL materials: Ti metal (melting point, T_m=1668 °C), titanium oxide, TiO_2 (T_m=1843 °C) and titanium carbide, TiC (T_m=3067 °C) [15].

Thin Ti metallic foils of 30 µm are currently used at ISOLDE, in rolls, as a target material with a target thickness, X=16.3 g cm^{-2} on average[4]. Before being rolled and inserted in the Ta target container the foils are embossed, to reduce the contact between the layers avoiding and/or delaying sintering [16]. This target is used to produce neutron deficient beams of Ca, Sc, K and Mg isotopes [17]. Operating the Ti target in a CF_4 atmosphere, molecular beams of CaF and ScF were seen but only at 2-3 and 10 % in intensity when compared with beams of atomic Ca and Sc, respectively [18]. In another Ti foils target, the ratio between CaF and Ca was of 90 % [19], where it is evident that larger variability exists in molecular formation. CaF was also extracted at ISOLDE as ^{38}CaF using a Ti rods target (X=93 g cm^{-2} but in this case the beam was between 10 and 30 % in intensity of ^{38}Ca) [17, 19, 20]. Release studies on Ti, show general fast release of all the studied elements (Mg, Sc, Na, Ca, K; in decreasing order of released fraction) [21–23]. Release studies on Ti metal powder revealed it to be a poor target material due to fast sintering [21]. Nonetheless, during operation, metallic foil targets are known to sinter fast [16] and even melt [18, 19], bringing decreasing isotope yields over time.

Micrometric fibers made of TiO_2 were used at ISOLDE as target material (X=7.2 g cm^{-2}) to produce Ne, Ar and CO beams [17, 24]. However, the produced beams were all below, in intensity when comparing to CaO targets, mainly due to lower production cross sections. The release of K, S, Ar and Cl isotopes from TiO_2 in fiber form has shown to be higher than for TiO_2

[4] Average over 6 Ti targets produced from 2002 to 2016, where 11.1$\leqslant X_{Ti} \leqslant$20.5 g cm^{-2}.

in powder form at 1380 °C [22], whereas no release was seen for either Sc or Mg. The TiO_2 fibers are also reported to better release S and K than the Ti metal foils at 1400 °C [22].

TiC was never used as a target material at ISOLDE, but it was studied in the 70-80's and rendered as a poor release target material [25, 26]. In a release study done at 1800 °C, using 1-50 μm TiC powder, has shown slow release of K [25]. In another attempt, the same TiC was mixed with graphite (1:3 mol, respectively) and the release at 1900 °C improved considerably where Be, K, Ca and Sc could be seen, with the later two specially slowly released [26]. No improvement was obtained for the release of Sc, when using an atmosphere of CF_4 [26], to promote ScF_x molecular formation. Nonetheless, TiC is used in ISAC in TRIUMF to deliver beams of K, Ca, Na, Li, Cl, He, Ne, Ar and O [27]. The target is produced by mixing 1 and 7 μm (1:1) in a water based slurry with plasticizers, surfactant and binder additives which is then slip casted in thin graphite foils and sintered at 1900 °C [28]. The final target material is 50 % dense, 1-10 μm and Ti target thicknesses varies from X_{Ti}=7.6 g cm^{-2} to 29.7 g cm^{-2} [29, 30].

1.2. Previous work

Since nanometric TiC[5] easily sinters at temperatures as low as 1500 °C, sintering hindering of TiC was studied by mixing it with different carbon allotropes [31]. The addition to TiC of graphite, MWCNT or carbon black (CB)[6] in selected quantities resulted, in all cases, a successful stabilization of nanometric TiC, even after 10 h at 1500 °C [31]. The most effective hindering the sintering of TiC was MWCNT, followed by carbon black and finally graphite. Here the carbon allotropes reduce the TiC coordination number and act as an inert, non-soluble and non-sinterable phase, hindering the sintering of TiC.

In another study the sintering of TiC and TiC-50vol.%CB composite (TiC-CB) were studied in more detail through determination of their master sintering curves using dilatometry [32]. An apparent activation energy of 390 kJ mol^{-1} was found for sintering of pure TiC and an higher activation energy of 555 kJ mol^{-1} was found for TiC-CB [32]. The TiC apparent sintering activation energy was in agreement with the ones found in the literature for both sub-micrometric and nanometric TiC. The TiC coordination number reduction due to the presence of CB increases the sintering activation energy in the case of the TiC-CB.

Selected TiC-C nanocomposite samples from [31] were tested up to 1800 °C for 10 h, in another study [33], to further evaluate the stability of nanometric TiC in the composites. In this study, mass losses and phase composition was studied in detail, where the 4.3 - 5.7 wt.% ZrO_2, introduced during co-milling of TiC and carbon allotropes, is studied in terms of interaction with TiC and the carbon allotropes [33]. At high temperatures this contamination transforms into ZrC and solubilizes completely in the TiC at around 1800 °C, bringing an increase of the TiC lattice parameter. The CB in 50 vol.% was found to be the best carbon allotrope hindering the sintering of TiC up to 1800 °C where TiC crystallite sizes of 76 nm were measured.

In this study isotope release properties of selected samples from the previous studies [31, 33] were evaluated and the nanocomposite with the highest isotope released fraction was selected to be integrated in a full target. The production procedure of the selected nanocomposite was upscaled to match the quantities needed to build a full target for ISOLDE. Finally, the prototype target material was successfully operated at ISOLDE and online beam intensities and release

[5] TiC - *Goodfellow* (Ref. LS396999/1), 99.9 % pure, 80-130 nm

[6] Graphite - *Alfa Aesar*, Ref. 40798, 325 mesh, <44 μm; Carbon black - *Orion Engineered Carbons*, *Printex A Pulver*, 40 m^2 g^{-1}, 40 nm primary particle size; MWCNT - *Nanocyl*, Ref. NC3100, >95 % purity, 10 nm diameter, 1.5 μm length

curves were extracted for several elements. Isotope effusion and diffusion release models were applied to further understand this target material release properties.

2. Materials and Methods

2.1. Release studies

The method chosen to study the isotope release consisted in irradiating the material to be studied to produce the isotopes in the bulk of the sample. Then, gamma spectroscopy was used to measure the isotope quantities before and after a certain thermal treatment to check for isotope release [25]. Two nanocomposites and one TiC sample was selected from [33] which characteristics and microstructures can be seen in table 1 and figure 1, respectively. The sample preparation is briefly described ahead, in subsection 2.2, and in detail in [31].

Table 1: Titanium carbide and the nanocomposiste TiC-CNT and TiC-CB characteristics to be used in the release studies. Data extracted from [33]

	TiC	TiC-CNT	TiC-CB
Sample name in [33]	TiCm	75CNTb	50CB
Production heat treatment	1500 °C - 10 h	1500 °C - 10 h	1800 °C - 10 h
Carbon (vol. %)[a]	0	75	50
Density ($g\,cm^{-3}$)	2.33 (52 %)	1.95 (44 %)	1.91 (56 %)
Specific Surface Area[b] ($m^2\,g^{-1}$)	2.6	23.0	16.7
Crystallite size[c] (nm)	107	52	76
Mass losses (%)	6.9	12.3	12.9
Ratio of pores <200 nm[b] (%)	14	86	54
Release studies at (°C)	1500	1500	1740

[a] TiC density $4.93\,g\,cm^{-3}$ [15], MWCNT bulk density from supplier used $0.15\,g\,cm^{-3}$, carbon black density from supplier $1.85\,g\,cm^{-3}$.
[b] Determined from nitrogen adsorption isotherm, see [31, 33] for more.
[c] Determined through X-Ray powder diffraction, see [33] for more.

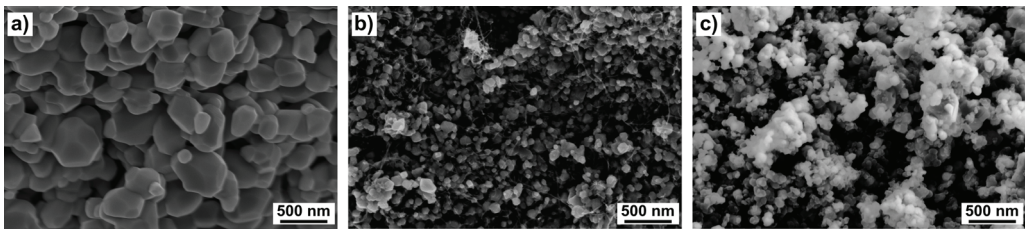

Figure 1: Scanning electron microscopy microstructures of the selected samples: TiC-milled (a), TiC-CNT (b) and TiC-CB (c). Reproduced from [33].

Before the irradiations, simulations had to be conducted using the Monte-Carlo particle transport simulation code FLUKA [34, 35] in order to estimate the isotope inventory, irradiation times and sample cool down times to have acceptable counting rates with minimum human exposure to radiation. The final irradiation conditions were defined: the samples would be irradiated with a total $1 \cdot 10^{15}$ protons and would have a cool down of 24 h in order to be handled safely (ambient

dose equivalent, $H^*(10)$ [μSv] at 10 cm below 100 μSv - see dose rate vs time figure A.4.1 in supplementary materials). The irradiations were conducted using the MEDICIS (Medical Isotopes Collected from ISOLDE) rail conveyor system at ISOLDE-CERN [36]. Since this was the first time such system was used for sample irradiation, a special irradiation stand had to be designed and built (see figure A.4.2 in supplementary materials).

After cooldown, the samples were extracted from the support and taken into the ISOLDE experimental hall to be studied for release properties. Each sample was positioned with a fixed geometry in front of a *Canberra Cryo-Pulse 5 High Purity Germanium Gamma (HPGe)* detector, to acquire a γ-energy spectrum for 90 minutes, in order to identify and quantify the radioisotopes. The samples were then subjected to a defined heat treatment to promote isotope release and a second γ-energy spectrum was acquired. ^{152}Eu and ^{133}Ba sources were used for energy and efficiency calibration of the detector. The isotopes and respective $t_{1/2}$ and γ-ray energies used to follow the release properties of the studied materials can be found in table 2. The results were analyzed with *Genie 2000: Gamma Acquisition & Analysis* v.3.2.1 where isotope peaks were identified, quantified and decay and daughter decay corrected.

Table 2: Isotopes and respective half-lives ($t_{1/2}$), characteristic γ-ray energy (E_γ) and intensity [37] used in the release studies of the different TiC microstructures.

Isotope	$t_{1/2}$	E_γ (keV)	Intensity (%)
^{7}Be	53.22 d	477.6	10.44
^{24}Na	14.96 h	1368.6	99.99
		2754.0	98.72
^{43}K	22.2 h	372.8	87.10
		617.5	80.40
		396.9	11.41
		593.4	10.97
		220.6	4.09
^{44m}Sc	2.44 d	271.1	86.60
		1001.8	1.23
^{47}Ca	4.54 d	1297.1	75.00

The heat treatments were done in a special setup, named *Fast Diffusion Chamber* which allowed for fast heating and cooling ramps up to 1740 °C. This setup is composed of an oven with an automatic shutter and an automatic Z-feedthrough which can rapidly transport samples in and out of the oven, all under a 10^{-3} Pa atmosphere. The feedthrough at its end had a graphite piece specially designed to position the samples to be heat treated. An Al_2O_3 piece, between the graphite piece and the metallic feedthrough was used to thermally isolate the feedthrough. The samples were maintained for 5 minutes at the temperature up to which the properties referred in table 1 are stable. Heating and cooling times were as fast as possible (in the order of 2 minutes) which are essential to limit the isotope release at the defined temperature and time. For statistics, a total of three samples of each material (table 1) was done.

2.2. Target Material Production - Process Upscaling

The TiC-CB composite, which was defined as the best candidate from the release studies, was scaled up in order to produce enough material for a full target. The samples were produced in batches of ≈2 g [31] whereas a target needs 50-70 g of material. The TiC-CB samples were produced by co-milling TiC and CB, in 1:1 volume ratio, in 18 g of isopropanol (IPA) with 0.5 wt.% of polyvinylpirrolidone (PVP) as a dispersant. The co-milling was done in an attrition

mill at 800 rpm for 2 h in an 80 mL grinding bowl with Yttria Stabilized Zirconia (YSZ) grinding balls. After milling, the obtained slurry was dried under vacuum with constant agitation using a rotary evaporator. The obtained powder was deagglomerated and pressed into cylindrical pellets of ≈0.26 g, 12 mm diameter, 1.4 mm thickness at 62 MPa. The pellets were then heat treated at 450 °C under argon to remove the PVP and finally heat treated at 1800 °C in high vacuum for 10 h. The sample procedure details, as well as respective final characteristics after heat treatment at 1800 °C can be found in table 3.

Table 3: Comparison of sample and upscaled material processing and respective main characteristics of the obtained materials after 1800 °C for 10 h.

		Sample	Target
Production	Mass	2.06 g (1.50 g TiC + 0.56 g CB)	48.53 g (34.54 g TiC + 12.98 g CB)
	IPA (0.5 wt.% PVP)	18 g (≈1:9 solids:liquid)	200 g (≈1:4 solids:liquid)
	YSZ balls	138 g (≈1:67 solids:balls)	738 g (≈1:15 solids:balls)
	Mill characteristics	80 ml griding bowl, 800 rpm, 2 h	500 ml griding bowl, 1700 rpm, 2 h
	Pellet	≈0.26 g, 12 mm diam.× 1.4 mm thickness	≈0.50 g, 15 mm diam.× 2.0 mm thickness
Characterization	Density	1.91 g cm^{-3} (56 %)	1.69 g cm^{-3} (50 %)
	Specific Surface Area	16.7 m^2 g^{-1}	16.5 m^2 g^{-1}
	Crystallite size	76 nm	115 nm
	Mass losses	12.9 %	10.5 %
	Ratio of pores <200 nm	54 %	64 %
	Zr wt.%[a]	5.4 %	1.6 %
	MIP Pore size [b](BJH[c])	71 nm (32 nm)	109 nm (47 nm)

[a] Determined by Energy-dispersive X-ray spectroscopy, see [33] for more.
[b] MIP - Mercury Intrusion Porosimetry, see [33] for more.
[c] BJH - Barrett-Joyner-Halenda, the authors of a method to determine pore sizes from nitrogen adsorption isotherms, see [31, 33] for more.

The changed processing parameters from sample to target production are listed and compared in table 3. The powder quantity was increased to a total of 48.53 g from 2.06 g and a different mill with a larger grinding bowl (500 ml) was used. To match the empirically optimized parameters found in previous experiments for this mill, the ratios of solids:liquids and solids:balls were adapted and larger milling speeds (from 800 to 1700 rpm) were used. The pellet size was increased to 15 mm diameter to match ISOLDE requirements and the rest of the production procedure remained unchanged.

The microstructures and characteristics of the final materials obtained from sample and target processing routes can be seen in figures 1c and 2a, respectively, and also in table 3. When comparing the microstructures of figures 2a and 1c and the specific surface areas (a parameter very sensitive to sintering [31–33]) in table 3, one can see that the processing upscale was successful. In the other characteristics there were slight differences as can be seen from table 3. The density was slightly different, from 56 to 50 % which is related with the green body properties obtained during the processing routes. Zr contamination was reduced from 5.4 to 1.6 wt.% which is due to the smaller solids:balls ratio. The smaller %Zr, in the form of ZrO_2, also result in lower mass losses from the reaction with carbon, forming ZrC and releasing CO(g) [33], as seen from the value of 10.5 % which was 12.9 % for the sample (a detailed study of the mass losses in the composites can be found on [33]). The larger crystallite and pore sizes in the target seem to indicate slightly more sintering for the later when comparing with the sample [32]. In previous studies a reduction of the pore ratios below 200 nm was usually related with higher sintering of the microstructures [31, 33]. In this case we see the inverse, where higher crystallite sizes, which indicate sintering, are followed by higher pore ratios <200 nm (64 %). The larger crystallite

sizes could be due to a slightly less homogeneous mixing in the upscaled processing which can bring to a slight increase in the TiC coordination number. Another hypothesis is the that the introduction of ZrC in the crystallite lattice of TiC can be influencing the sintering phenomena.

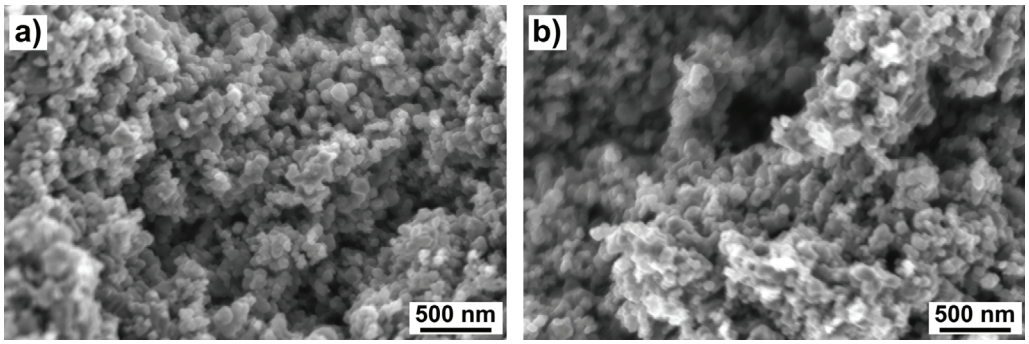

Figure 2: Scanning electron microscopy microstructures obtained for target material heat treated at 1800 (a) and 2000 °C (b).

Since the target was firstly operated at the designed temperature of 1800 °C and later at 2000 °C, further characterizations at 2000 °C were done, which are presented in table 4 and figure 2b. The carbon black effectiveness in hindering the sintering of TiC is further demonstrated by the very similar crystallite sizes (table 4) and microstructures (figure 2) obtained for both temperatures. While there is a small difference in density for both samples, from 50 to 53 %, SSA varies from 16.5 to 14.5 $m^2\,g^{-1}$ and ratio of pores <200 nm increases from 64 to 78 %. While the SSA evolution is expected for higher temperatures, the ratio of pores <200 nm should decrease, as seen in previous studies [31, 33], but 2000 °C sintering temperature was never studied. The higher mass losses are consistent with the favorable thermodynamics at higher temperature to carbon burning as predicted by the Boudouard reaction.

Table 4: Characteristics of the TiC-CB nanocomposite heat treated at 1800 and 2000 °C.

	1800 °C	2000 °C
Density ($g\,cm^{-3}$)	1.69 (50 %)	1.79 (53 %)
SSA ($m^2\,g^{-1}$)	16.5	14.5
Crystallite size (nm)	115	119
Mass losses (%)	10.5	11.2
Ratio of pores <200 nm (%)	64	78

The final target had around 100 pellets of TiC-CB, with a total final mass of 43.96 g which were inserted into a graphite boat. The total target thickness including the boat was of 23.1 $g\,cm^{-2}$, where the Ti thickness was of 8.1 $g\,cm^{-2}$ and carbon from TiC-CB was of 5.9 $g\,cm^{-2}$.

2.3. Online and Offline Prototype Testing

The TiC-CB target prototype was labeled #527, and was assembled with a rhenium surface ion source, a combined Na/Mg mass marker for beam tuning and a $2.2 \cdot 10^{-4}$ $mbar\,l\,s^{-1}$ leak to inject tetrafluormethane, CF_4, to promote molecular beam formation when needed. As usual for all targets operated at ISOLDE, they are firstly tested in an offline separator, for quality control. A mass scan recorded with target at 1800 °C and ion source at 2130 °C up to A=200, can be

found in figure A.4.4 in supplementary materials. A picture of the assembled target and referred components can be found in figure A.4.3 in supplementary materials.

The target was installed at the ISOLDE General Purpose Separator (GPS) frontend, in November 2014 and operated with the ion source at 2050 °C and target at the design temperature, 1800 °C. This target was used to deliver high and stable intensities of ^{37}K to the successful IS527 nuclear physics experiment [14].

The beam intensities and release time-structure after proton pulse were measured using the ISOLDE tapestation [38] which contains a $4\pi\,\beta$ detector. Isotopes of Li, Na and K were measured by varying the target temperatures: 1300, 1600 and 1800 °C while the ion source was kept stable at 2050 °C. Beam intensities were also assessed with the target and ion source at 2000 and 2130 °C, respectively. In these conditions CF_4 was injected into the target unit to promote the release of Ca isotopes in the form of CaF_x molecules.

The release time-structure for an isotope with finite $t_{1/2}$, $P(t)$ or $P_{\lambda_i}(t)$ (where $\lambda_i = \ln 2/t_{1/2}$), can be approximated by a triple exponential time-constant like function [39]:

$$P_{\lambda_i}(t) = \frac{1}{\text{Norm}}(1 - e^{-\lambda_r t})[\alpha e^{-\lambda_f t} + (1-\alpha)e^{-\lambda_s t}] \tag{2}$$

where λ_r [s^{-1}], λ_f [s^{-1}] and λ_s [s^{-1}] are the time constants of the rise, fast fall and slow fall of the pulsed shape curve, α [%] is the weighting factor between the fast and slow fall components and Norm is a normalization factor so $\int_0^\infty P_{\lambda_i}(t)\mathrm{d}t = 1$.

In order to estimate the isotope release efficiency (ε_{rel}) of the new target material the isotope production cross sections were estimated with the ABRABLA07v5 [40] spallation code using $1 \cdot 10^9$ events (see figures A.4.2 and A.4.4 in supplementary materials). The obtained cross sections were then used to calculate the isotope inventory and respective production rates (Y_{Prod}) in the target material [7].

3. Results and Discussion

3.1. Release Studies

The materials for the release studies, were selected in order to have as different as possible microstructures, as can be seen in the figure 1. Since the milling was seen to have a positive influence in the sintering hindering of TiC [31] a sample was selected for release studies and also to serve as a reference for TiC without carbon (TiC in table 1). The two composites which insured the best stabilization of nanometric TiC were selected from previous studies[31, 33]: TiC-CNT and TiC-CB. In terms of characteristics the samples studied were quite different mainly in terms of SSA, crystallite size and ratio of pores <200 nm, as seen in table 1. The temperatures chosen insured that no microstructural evolution would happen during the release studies since the samples were pre-heat treated at temperatures higher or equal of those of the release studies for long times (see table 1).

The released fraction (% of isotopes which were released from the sample during the 5 min heat treatment) was calculated from the isotope activities from the γ-ray spectrum before and after the heat treatment, and the final results can be seen in figure 3a. In this figure the average

[7] The result of the calculation of the cross sections for Ti and C and calculated Y_{Prod} from equation 1, for all the isotopes produced in this target material can be found on supplementary material in figures A.4.2 and A.4.4 and table A.4.1, respectively.

released fraction for each microstructure and each studied element (Be, Na, Mg, K, Sc and Ca) can be seen. The error bars are relative to the error propagation of activity uncertainties over 3 measurements, where lower activities have larger error bars (due to the long half lives and/or lower production cross sections). In figure 3b, TiC-CB is compared to literature values of other release studies done in Ti-based materials [22, 25, 26].

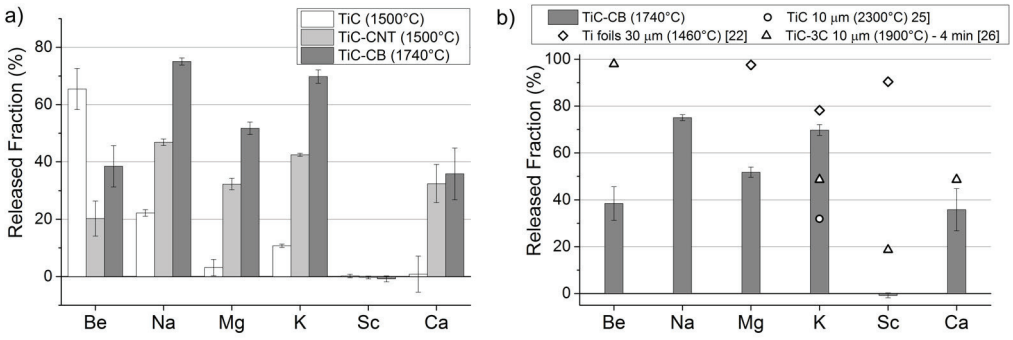

Figure 3: Released fraction for Be, Na, Mg, k, Sc and Ca for three different TiC microstructures at 1500 (TiC and TiC-CNT) and 1740 °C (TiC-CB) (a) and comparison of TiC-CB release fraction with literature [22, 25, 26] values (b).

The Be released fraction, in figure 3a for TiC is a lower estimate, since no Be peak was seen after heat treatment so the detection limit was used. Nonetheless, the Be released fraction, is higher for TiC than for nanocomposites, even for TiC-CB at 1800 °C. This may be due to the presence of carbon in the case of the nanocomposites which can react with Be forming Be_2C (T_m=2127 °C [15]). However in an older study [26] Be is fully released at 1900 °C from a TiC mixed with graphite, 1:3 mol ratio as seen in figure 3b). This difference is either due to the much more reactive carbon used in this study (CB and MWCNT instead of Graphite) or due to the higher temperatures used in the literature.

There is a clear trend for the elements Na, Mg and K in figure 3a where TiC has the lowest released fraction, followed by TiC-CNT and TiC-CB. In here, when comparing TiC and TiC-CNT, where apart from the carbon (MWCNT), the main difference is the crystallite/grain size of TiC (table 1). This result clearly show the influence of the grain size in the release of isotopes. When comparing with TiC-CNT, the release of Na, Mg and K in TiC-CB is higher much probably due to the higher temperature used for the release (1800 °C) for this nanostructure, since both have similar grain sizes. In figure 3b TiC-CB has higher release for K, than other release studies done with TiC in the literature [25, 26]. TiC-CB release of K is very close to the Ti foils in the literature [22], which comes as a very positive result since Ti metalic foils are known to release K very fast both offline and online [17, 22].

In figure 3a, Sc is not released at all from any of the microstructures/temperatures tested, as has been seen before [25, 26]. A small released fraction (20 %) is seen for Sc in TiC-3C in figure 3b at higher temperatures (1900 °C). It is hypothesized in [26] that the release of Sc may be limited by slow in-grain diffusion in TiC, where Sc was very little released even when in the presence of a CF_4 atmosphere. Sc may be as well reacting with the carbon in the TiC matrix forming scandium carbide. Titanium foils are known to release well Ca and Sc both offline [21, 22] (as seen in figure 3b) and online [16, 17].

Ca release is not seen at all for TiC at 1500 °C (figure 3a). The reduction of the TiC grain size

seems to have a large influence on the release of Ca, where in TiC-CNT, at the same temperature the released fraction is more than 30 %. With TiC-CB, even at higher temperatures, contrarily to what has been seen before (for Na, Mg and K) the release stays the same, which may be indicating some trapping of the Ca isotopes within the TiC-CB microstructure.

Due to the higher released fractions of the TiC-CB microstructure of all elements(except Be), this material was chosen to be tested at ISOLDE as a prototype.

3.2. Online Target Characterization

The yields of Li, Na and K isotopes measured at different target temperatures for the TiC-CB target prototype can be found in table 5. In the same table, the current target is compared to other Ti-based target materials at ISOLDE-CERN, $Y_{Ti,ISOLDE}$. In general, when comparing the highest yields obtained from the prototype (at 2000 °C in table 5) to the Ti foils target at ISOLDE [17], the Na and Li yields are higher, while the K yields are lower. The higher yields for Li are mainly due to the presence of carbon in the TiC-CB target which has higher production cross section for Li production than Ti (see cross sections in tables A.4.2 and A.4.4 in supplementary materials). The Na yields in table 5, are higher than for Ti-metal foils, even though Y_{Prod} is estimated to be a factor 2 lower when comparing with the Ti metal foils target due to the lower X_{Ti} (TiC-CB X_{Ti}=8.1 g cm^{-2}, Ti targets X_{Ti}=17.4 g cm^{-2}).

In the case of K, the yields are systematically lower. Even though the Ti metal target yields are higher for K, they are known to rapidly reduce over time due to target material degradation (foil sintering or even melting) [16, 19]. A Ti-foils target operated at ISOLDE in 2016 (#562), at 1450 °C with a tantalum ion source for less than 3 days (65 hours) has shown reduction of the yield by a factor 2.4 for ^{8}Li (from $1.8 \cdot 10^{6}$ to $7.4 \cdot 10^{5}$ μC^{-1}), 4.7 for ^{26}Na (from $2.7 \cdot 10^{6}$ to $6.3 \cdot 10^{5}$ μC^{-1}) and 4.1 for ^{37}K (from $2.3 \cdot 10^{6}$ to $5.6 \cdot 10^{5}$ μC^{-1}). In comparison, for the TiC-CB target, no yield variation was seen for any isotope/element measured, over the course of 5 days, confirmed by measurements on the ISOLDE tape station and by the physics experiment using the target.

When comparing the yields obtained with the ones at ISAC ($Y_{TiC,ISAC}$, in table 5) it can be seen that the yields of Li and Na on the TiC-CB target are systematically higher and in most of the cases more than one order of magnitude, than those at TRIUMF for the same proton current. Since the two targets have similar X_{Ti}, there are only two fundamental differences in terms of microstructure: (i) the size of TiC grains which is 1 to 2 orders of magnitude smaller for TiC-CB and (ii) the nanometric carbon (carbon black) homogeneously mixed with TiC for TiC-CB. The release seems to be enhanced by the reduction of the TiC grain size, as seen for other target materials which microstructure has been engineered in that way [3–5]. K is on the same level as in ISAC and Ca is below, where we believe that the carbon black and/or the small pore size distribution may be hindering the release of these elements.

It should be noted that there are some fundamental differences at ISAC-TRIUMF (comparing to ISOLDE-CERN): higher proton beam proton intensities, slightly lower production cross sections (500 MeVprotons), different target temperature estimation and the presence of radiation enhanced diffusion. Since the interest of this study is the material release efficiency, in order to compare the yields of ISAC-TRIUMF we had to normalize them to the used proton intensities (40 to 70 μC). Production cross sections with the ISAC-TRIUMF's primary proton beam of 500 MeV are up to a factor of 2 lower than those at ISOLDE, for the studied isotopes[8]. ISAC-

[8] See ISOLDE/ISAC cross section ratios for all isotopes on supplementary materials in figure A.4.3 for Ti and figure A.4.3 for C

TRIUMF target temperatures are highly dependent on the beam intensity on the target due to the high proton currents used, where at ISAC-TRIUMF, the TiC target temperatures are estimated to be 1700 °C with 70 μA of beam current and 1430 °C with 40 μA [30]. In any case these temperatures have some a large source of error associated since they are defined in a combination of empirical calibration, beam power deposition calculations and thermal simulations [30]. Finally, radiation enhanced diffusion (RED) is reported at TRIUMF [41, 42], where the yields follow a law with the primary beam intensity (i) between $i^{3/2}$ and i^2 while keeping the temperature constant [41, 42].

Table 5: Summary of the online yields for the studied isotopes on the TiC-CB prototype target, with target temperatures, in target production yield and comparison with ISOLDE [17] and TRIUMF [27] database yields (the later normalized to proton current).

Isotope	$t_{1/2}$	Yield (μC^{-1}) - Target temperature				Y_{Prod} (μC^{-1})	$Y_{Ti,ISOLDE}$ (μC^{-1}) [17]	$Y_{TiC,ISAC}$ (μC^{-1}) [27]
		1300 °C	1600 °C	1800 °C	2000 °C [a]			
^{8}Li	840.3 ms	$9.7 \cdot 10^4$	$8.5 \cdot 10^5$	$1.5 \cdot 10^6$	$6.0 \cdot 10^6$	$1.4 \cdot 10^9$	$1.7 \cdot 10^6$ [c]	$1.2 \cdot 10^5$
^{9}Li	178.3 ms	$1.2 \cdot 10^3$	$3.8 \cdot 10^4$	$3.8 \cdot 10^4$	$3.8 \cdot 10^5$	$1.8 \cdot 10^8$	$3.2 \cdot 10^5$ [b]	
^{20}Na	446 ms	$1.0 \cdot 10^4$	$8.9 \cdot 10^4$	$1.5 \cdot 10^5$	$4.9 \cdot 10^5$	$2.1 \cdot 10^6$	$5.3 \cdot 10^4$ [b]	$1.3 \cdot 10^4$
^{21}Na	22.48 s	$6.6 \cdot 10^6$	$3.6 \cdot 10^7$	$2.0 \cdot 10^7$		$5.0 \cdot 10^7$	$1.5 \cdot 10^7$ [b]	$8.8 \cdot 10^5$
^{25}Na	59.6 s	$1.1 \cdot 10^8$	$2.2 \cdot 10^8$	$2.1 \cdot 10^8$		$2.3 \cdot 10^8$	$8.9 \cdot 10^7$ [b]	$9.0 \cdot 10^5$
^{26}Na	1.07 s	$3.9 \cdot 10^5$	$5.0 \cdot 10^6$	$4.8 \cdot 10^6$	$7.6 \cdot 10^6$	$5.2 \cdot 10^7$	$3.0 \cdot 10^6$ [c]	$3.6 \cdot 10^5$
^{27}Na	301 ms	$2.4 \cdot 10^4$	$2.6 \cdot 10^5$	$6.0 \cdot 10^5$	$6.4 \cdot 10^5$	$1.3 \cdot 10^7$	$1.7 \cdot 10^5$ [b]	$2.8 \cdot 10^4$
^{35}K	190 ms			$3.2 \cdot 10^2$		$1.6 \cdot 10^5$	$8.7 \cdot 10^3$ [b]	$8.8 \cdot 10^1$, $1.1 \cdot 10^2$
^{36}K	342 ms		$3.1 \cdot 10^3$	$6.9 \cdot 10^3$	$8.0 \cdot 10^3$	$4.9 \cdot 10^6$	$9.0 \cdot 10^4$ [b]	$6.1 \cdot 10^3$, $7.3 \cdot 10^3$
^{37}K	1.22 s	$1.8 \cdot 10^4$	$3.9 \cdot 10^5$	$5.3 \cdot 10^5$	$1.1 \cdot 10^6$	$1.0 \cdot 10^8$	$2.3 \cdot 10^6$ [c], $4.9 \cdot 10^6$ [c]	$8.0 \cdot 10^5$, $1.6 \cdot 10^6$
^{46}K	115 s	$1.2 \cdot 10^6$	$2.9 \cdot 10^6$	$6.1 \cdot 10^6$		$5.4 \cdot 10^6$	$1.6 \cdot 10^7$ [b]	$8.3 \cdot 10^4$ [d]
^{47}K	17.5 s		$2.8 \cdot 10^5$	$1.9 \cdot 10^5$	$4.5 \cdot 10^5$	$1.7 \cdot 10^6$	$1.3 \cdot 10^6$ [b]	$4.3 \cdot 10^4$
^{39}CaF	860.7 ms				$1.4 \cdot 10^2$	$1.8 \cdot 10^8$	$1.7 \cdot 10^3$ [b], $6.6 \cdot 10^4$ [b],($2.0 \cdot 10^4$ [e])	$2.3 \cdot 10^3$ ($7.5 \cdot 10^2$ [e])

[a] Ion source at 2130 °C.
[b] ISOLDE old driver beam: CW 600 MeV protons (instead of the present pulsed 1.4 GeV protons).
[c] Measured on targets #529 (2014) and #563 (2016) at the beginning of operation - Ti metal foils with tantalum ion source.
[d] FEBIAD.
[e] Extracted in non molecular form (Ca^+).

The in-target production yields for ISOLDE (Y_{Prod}) are presented in table 5 to compare with the obtained yields. Using equation 1, $\varepsilon_{rel} \cdot \varepsilon_{is}$ was calculated from Y_{Prod}, since the values are already corrected for ε_{transp}, $\varepsilon_{sep} \approx 1$ and the ionization efficiency is not known for each element. The obtained $\varepsilon_{rel} \cdot \varepsilon_{is}$ values for K, Na and Li were plotted vs $t_{1/2}$ for each temperature in figure 4a, b and c, respectively.

ε_{rel} in function of $t_{1/2}$ can be determined by folding $P_{\lambda_i}(t)$ (equation 2) with the exponential decay function ($e^{-\lambda_i t}$ where $\lambda_i = \ln 2/t_{1/2}$), obtaining the release function for an isotope with an infinite $t_{1/2}$, $P_\infty(t)$, and integrating such as [43]:

$$\varepsilon_{rel}(\lambda_i) = \int_0^\infty P_{\lambda_i}(t)\mathrm{d}t = \int_0^\infty P_\infty(t)e^{-\lambda_i t}\mathrm{d}t$$
$$\frac{1}{\mathrm{Norm}}\left(\frac{\alpha_\infty}{\lambda_{r,\infty}+\lambda_i} + \frac{(1-\alpha_\infty)}{\lambda_{s,\infty}+\lambda_i} + \frac{-\alpha_\infty}{\lambda_{f,\infty}+\lambda_{r,\infty}+\lambda_i} + \frac{(\alpha_\infty-1)}{\lambda_{s,\infty}+\lambda_{r,\infty}+\lambda_i}\right) \quad (3)$$

where α_∞, $\lambda_{r,\infty}$, $\lambda_{f,\infty}$, $\lambda_{s,\infty}$ are similar to the parameters obtained on equation 2 but for the $P_\infty(t)$ function. $P_\infty(t)$ is independent from the isotope $t_{1/2}$ and usually describes the release of a chemical element from a specific target and ion source system. In order to obtain $P_\infty(t)$, the release time must be shorter than the $t_{1/2}$ (in other terms $\lambda_s > \lambda_i$), otherwise the isotope decays before it is released and can't describe the complete release time-structure.

The $P_\infty(t)$ was obtained from data which was collected to fit the parameters from equation 3 for ^{25}Na at 1800 and 1600 °C and $\varepsilon_{rel}(t_{1/2})$ was computed and plotted in figure 4b. For the

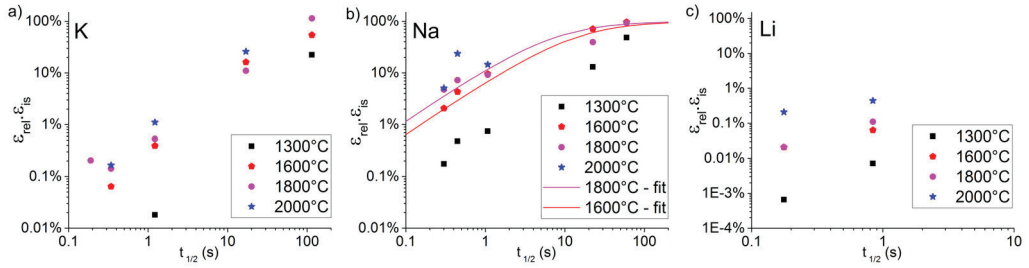

Figure 4: $\varepsilon_{rel} \cdot \varepsilon_{is}$ for K (a), Na (b) and Li (c). Equation 3 parameters for Na in (b) at 1800 °C, α_∞=0.00, $\lambda_{r,\infty}$=92.08 s^{-1}, $\lambda_{f,\infty}$=0.09 s^{-1}, $\lambda_{s,\infty}$=0.09 s^{-1} and for Na at 1600 °C, α_∞=1.00, $\lambda_{r,\infty}$=105.49 s^{-1}, $\lambda_{f,\infty}$=0.05 s^{-1}, $\lambda_{s,\infty}$=0.04 s^{-1}.

other cases (Na at 1300 °C and K), although statistics were high enough to extract a yield, the statistical error is too large to deduce the $P_\infty(t)$ release time structure.

From figure 4 it is evident that for all isotopes there is a large influence of the target temperature on the ε_{rel}, as seen from the values from 1300 to 1600 °C. While for K $\varepsilon_{rel}(t_{1/2})$ from equation 3 could not be obtained, it is however clear that, for short lived isotopes, the release efficiencies are more than one order of magnitude lower than for Na. This is shown in figure 4a and b for ^{37}K ($t_{1/2}$ = 1.22 s), where $\varepsilon_{rel} \cdot \varepsilon_{is}$ = 0.5 %, comparing to ^{26}Na ($t_{1/2}$ = 1.07 s), where $\varepsilon_{rel} \cdot \varepsilon_{is}$ = 9.2 %. For long lived isotopes of Na (^{25}Na - $t_{1/2}$ = 59.6 s) and K (^{47}K - $t_{1/2}$ = 115 s), the $\varepsilon_{rel} \cdot \varepsilon_{is}$ are similar and close to 100 %. This shows that for Na and K the $\varepsilon_{is} \approx$ 100 % which makes $\varepsilon_{rel} \cdot \varepsilon_{is} = \varepsilon_{rel}$ for these cases. For Li the ionization efficiencies are usually much lower [44].

Kirchner [43] has established that for effusion dominated release the log(ε_{rel}) is directly proportionality to the log($t_{1/2}$) while for diffusion dominated release, log(ε_{rel}) has a square root relation with log($t_{1/2}$). Using the 1800 °C K and Na ε_{rel} values (from figures 4a and b, respectively) in a log-log plot the obtained slope for Na was 0.51 while for K was 1.05. These results show that the release of K is controlled by effusion and Na release is controlled by diffusion. Diffusion is normally the controlling mechanism, since effusion is much faster (assuming short element sticking times and limited reactivity [43]). In here, the low K yields and ε_{rel} (compared with Na) are probably explained by long effusion times which are either due to the network of small pores of this target (unlikely, since Na seems to be well released) or due to the reaction of K with TiC or the carbon black, trapping the K or increasing its sticking times. In the release studies of figure 3, K seems to have a similar release to Na, however the release was studied after 5 min of heat treatment which is long enough to release most of the K as shown in figure 3b where ε_{rel} is close to 100 % for longer $t_{1/2}$.

In figure 5 the obtained $P_{\lambda_i}(t)$ curves from equation 2 for ^{37}K, ^{26}Na and ^{8}Li at 1800 °C for TiC-CB are plotted against the $P_{\lambda_i}(t)$ of same isotopes but from a Ti metal foils target at 1450 °C. The isotopes of each element were selected in order to have an $t_{1/2}$ as similar as possible in order to be compared. While for Ti metal foils the release of K is faster and of Li is slower, for TiC-CB there is no change. Also, the TiC-CB release is in general apparently slower, as seen for other nanomaterials [5, 11]. Li, Na, K, in this order, have an increasing radii[9] and reactivity and decreasing boiling point[10]. Ti metal foils exhibit the normal trend where elements with lower

[9]The radii of K is 2.20 Å, Na is 1.80 Å and Li is 1.45 Å [45].

[10]The highest boiling point is the one of Li with 1342 °C followed by Na, 883 °C and K with 759 °C [15].

boiling points are normally faster and easily released. It seems that in TiC-CB the trend is not verified, which is probably related with the carbon black, or the nanometric nature of the target material (larger surface areas bring higher reactivity).

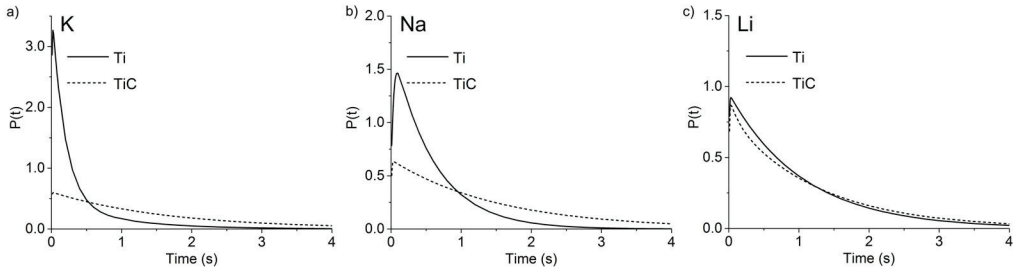

Figure 5: Release profile, $P_{\lambda_i}(t)$, for TiC-CB (1800 °C) and Ti foils (1450 °C) target materials for ^{37}K ($t_{1/2}$ = 1.22 s) (a), ^{26}Na ($t_{1/2}$ = 1.07 s)(b) and ^{8}Li ($t_{1/2}$ = 840.3 ms) (c).

Only when injecting CF_4 in the target, Ca could be detected as ^{39}CaF with $1.4 \cdot 10^2\ \mu C^{-1}$ as seen in table 5. This yield is lower when comparing to other values obtained at ISOLDE and TRIUMF ($Y_{Ti,ISOLDE}$, $Y_{TiC,ISAC}$ in table 5). CaF has been produced before at ISOLDE from a Ti rod target, where CaF was 10 % of the total amount of Ca [19]. Using a Ti foil target, the CaF side band was of 90 % of the total Ca, attributed to the larger surface available of the foils [19]. This is coherent with TRIUMF results and the TiC-CB results (see table 5, since only $_{39}$CaF is detected and not $_{39}$Ca. $\varepsilon_{rel} \cdot \varepsilon_{is}$ is in the order of 10^{-6}, which is extremely low and points to some mechanism hindering the release, such as a chemical reaction. This trend was already seen in the release studies, as referred before. The carbon black may be reacting with the Ca forming CaC_2, a refractory compound with a melting point of 2300 °C [15].

4. Conclusions

Titanium carbide (TiC) engineered nanocomposites developed in previous studies [31, 33] were irradiated and tested for Be, Na, Mg, K, Sc and Ca isotope release at ISOLDE. The release studies revealed that the release from such nanocomposites is higher than for submicrometric TiC for almost all elements. From the two carbon nanocomposites tested, TiC-carbon black and TiC-CNT, the former has shown the highest released fractions, especially for K, at 1800 °C.

Due to the release studies results, the TiC-carbon black material, which presented the higher release, was chosen to be used as a prototype target at ISOLDE and the production procedure was successfully scaled up in order to produce a full target. The final scaled up target material had stable TiC crystallite sizes of 115 nm at 1800 °C and 119 nm at 2000 °C.

TiC-CB target was operated at ISOLDE as a prototype and yields of Li, Na, K and Ca were extracted at target temperatures of 1300, 1600, 1800 and 2000 °C. When comparing with the previous Ti-based targets (Ti metal foils) at ISOLDE and at ISAC-TRIUMF, the proton current normalized yields of Li and especially of Na are higher, while the K yields were on the same level or slightly lower and Ca ones are lower. Ca isotopes were only seen in molecular form (CaF) and with low intensities, where we suspect that the carbon black may be hindering the Ca release by forming CaC_2, a refractory compound.

As seen for other nanomaterials, the release time structure for all isotopes is apparently longer, where for example, Na yields which have longer release time characteristics that Ti metal

targets, but where the yields are higher. Furthermore, the yields of Ti foils target are known to decrease fast over time due to foil sintering and/or melting, which isn't the case for this newly developed Ti-based material. This will result in higher integrated yields over time, particularly for the case of K.

Acknowledgments

The authors would like to acknowledge the MEDICIS collaboration for allowing the use of the rail conveyor system for the irradiations. We would also like to acknowledge Ermano Barbero and Matteo Vagnoni for the design and assembly of essential parts for the irradiations and release studies. We thank the assistance of Camille Lemesre, Ans Pardons and Joachim Vollaire with the safety assessment which was essential in order to proceed with the material irradiations. We would like to acknowledge Carlos Morais for the technical expertise with the scaling up studies as well as Orion Engineered Carbons, S.A. for providing the carbon black used. The author J.P.Ramos would like to acknowledge Uli Köster with the advice and recommendations with the *Genie 2000: Gamma Acquisition & Analysis* software with the analysis of the release studies data, and CERN and EPFL for the doctoral studentship funding.

References

[1] O. Kofoed-Hansen, K. O. Nielsen, Short-Lived Krypton Isotopes and Their Daughter Substances, Physical Review 82 (1) (1951) 96–97. doi:10.1103/PhysRev.82.96.2.

[2] Y. Blumenfeld, T. Nilsson, P. Van Duppen, Facilities and methods for radioactive ion beam production, Physica Scripta T152 (2013) 014023. doi:10.1088/0031-8949/2013/T152/014023.

[3] S. Fernandes, Submicro- and Nano-Structured Porous Materials for Production of High-Intensity Exotic Radioactive Ion Beams, PhD Thesis, École polytechnique fédérale de Lausanne (2010). doi:10.5075/epfl-thesis-4813.

[4] J. Ramos, A. Gottberg, T. Mendonça, C. Seiffert, A. Senos, H. Fynbo, O. Tengblad, J. Briz, M. Lund, G. Koldste, M. Carmona-Gallardo, V. Pesudo, T. Stora, Intense 31–35Ar beams produced with a nanostructured CaO target at ISOLDE, Nuclear Instruments and Methods in Physics Research Section B: Beam Interactions with Materials and Atoms 320 (2014) 83–88. doi:10.1016/j.nimb.2013.12.009.

[5] A. Gottberg, et al., Development and Online Tests of a Nano-Structured Uranium Carbide – MWCNT Composite for the Production of Rare Isotope Beams at ISOLDE-CERN, to be published.

[6] C. Seiffert, Production of radioactive molecular beams for CERN-ISOLDE, PhD Thesis, Technische universitat Darmstad (2015).

[7] A. Gottberg, Target materials for exotic ISOL beams, Nuclear Instruments and Methods in Physics Research Section B: Beam Interactions with Materials and Atomsdoi:10.1016/j.nimb.2016.01.020.

[8] T. Stora, E. Bouquerel, L. Bruno, R. Catherall, S. Fernandes, P. Kasprowicz, J. Lettry, S. Marzari, B. S. N. Singh, E. Noah, L. Penescu, R. Wilfinger, F. D. McDaniel, B. L. Doyle, Oxide Target Designs for High Primary Beam Intensities for Future Radioactive Ion Beam Facilities, in: AIP Conference Proceedings, Vol. 1099, AIP, 2009, pp. 764–768. doi:10.1063/1.3120150.

[9] J. Guillot, et al., LaC2-C nanocomposite targets for the production of neutron-deficient spallation products at CERN-ISOLDE, to be published.

[10] C. Seiffert, et al., Development of radioactive boron beams for CERN-ISOLDE, to be published.

[11] J. Ramos, A. Gottberg, R. Augusto, T. Mendonca, K. Riisager, C. Seiffert, P. Bowen, A. Senos, T. Stora, Target nanomaterials at CERN-ISOLDE: synthesis and release data, Nuclear Instruments and Methods in Physics Research Section B: Beam Interactions with Materials and Atomsdoi:10.1016/j.nimb.2016.03.003.

[12] H. Fynbo, L. Audirac, B. Blank, M. J. García-Borge, G. Canchel, M. Carmona-Gallardo, R. Dominguez-Reyes, L. M. Fraile, H. O. U. Fynbo, D. Galaviz, J. Giovinazzo, S. Hyldegaard, H. B. Jeppesen, J. S. Johansen, A. Jokinen, B. Jonson, O. S. Kirsebom, T. Kurtukian-Nieto, I. Matea, T. Nilsson, G. Nyman, K. Riisager, J. Souin, O. Tengblad, E. Tengborn, J. C. Thomas, J. Ayst, Studies of β-delayed two-proton emission : The cases of ^{31}Ar and ^{35}Ca, Tech. Rep. CERN-INTC-2008-028. INTC-P-248, CERN, Geneva (Apr 2008).
URL `http://cds.cern.ch/record/1100376`

[13] U. Wahl, L. M. Amorim, J. P. Araujo, V. Augustyns, K. Bharuth-Ram, E. David-Bosne, J. G. Correia, A. Costa, P. Miranda, L. M. d. C. Pereira, D. J. Silva, M. R. da Silva, K. Temst, A. Vantomme, Emission channeling lattice location experiments with short-lived isotopes, Tech. Rep. CERN-INTC-2014-001. INTC-P-218-ADD-2, CERN, Geneva (Jan 2014).
URL http://cds.cern.ch/record/1642551

[14] T. Kurtukian-Nieto, Precision measurement of the half-life and branching ratio of the T=1/2 mirror β-decay of 37K, Tech. Rep. CERN-INTC-2014-009. INTC-SR-026, CERN, Geneva (Jan 2014).
URL http://cds.cern.ch/record/1642808

[15] D. R. Lide (Ed.), CRC Handbook of Chemistry and Physics, 90th Edition, CRC Press, 2010.

[16] U. Köster, ISOLDE target and ion source chemistry, Radiochimica Acta 89 (2001) 749. doi:10.1524/ract.2001.89.11-12.749.

[17] ISOLDE Target and Ion Source Development Team, ISOLDE Yield Database.
URL http://test-isolde-yields.web.cern.ch/test-isolde-yields/query_tgt.htm

[18] E. Hagebø, P. Hoff, O. Jonsson, E. Kugler, J. Omtvedt, H. Ravn, K. Steffensen, New production systems at ISOLDE, Nuclear Instruments and Methods in Physics Research Section B: Beam Interactions with Materials and Atoms 70 (1-4) (1992) 165–174. doi:10.1016/0168-583X(92)95927-J.

[19] K. Gustafsson, A. Sandman, Developments of target-ion-source systems at ISOLDE PSB, Diploma thesis, Chalmers University of Technology (1994).

[20] B. Anderson, A. Baldwin, P. Baumann, B. Brown, F. Didierjean, C. Foster, L. Garcia, A. Huck, A. Knipper, R. Madey, D. Manley, G. Marguier, M. Ramdhane, H. Ravn, C. Richard-Serre, G. Walter, J. Watson, Gamow-Teller strength to K38 from the Ar38(p,n) reaction and Ca38(β+) decay, Physical Review C 54 (2) (1996) 602–612. doi:10.1103/PhysRevC.54.602.

[21] T. Bjørnstad, E. Hagebø, P. Hoff, O. Jonsson, E. Kugler, H. Ravn, S. Sundell, B. Vosicki, Recent development of high-temperature metal targets for ISOLDE, Nuclear Instruments and Methods in Physics Research Section B: Beam Interactions with Materials and Atoms 26 (1-3) (1987) 174–182. doi:10.1016/0168-583X(87)90747-6.

[22] A. Joinet, Production de faisceaux d'ions radioactifs chimiquement réactifs par séparation en ligne, PhD Thesis, Universite Paris XI (2003).

[23] K. Peräjärvi, U. Bergmann, V. Fedoseyev, A. Joinet, U. Köster, C. Lau, J. Lettry, H. Ravn, M. Santana-Leitner, Studies of release properties of ISOLDE targets, Nuclear Instruments and Methods in Physics Research Section B: Beam Interactions with Materials and Atoms 204 (2003) 272–277. doi:10.1016/S0168-583X(02)01924-9.

[24] U. Köster, U. Bergmann, D. Carminati, R. Catherall, J. Cederkäll, J. Correia, B. Crepieux, M. Dietrich, K. Elder, V. Fedoseyev, L. Fraile, S. Franchoo, H. Fynbo, U. Georg, T. Giles, A. Joinet, O. Jonsson, R. Kirchner, C. Lau, J. Lettry, H. Maier, V. Mishin, M. Oinonen, K. Peräjärvi, H. Ravn, T. Rinaldi, M. Santana-Leitner, U. Wahl, L. Weissman, Oxide fiber targets at ISOLDE, Nuclear Instruments and Methods in Physics Research Section B: Beam Interactions with Materials and Atoms 204 (2003) 303–313. doi:10.1016/S0168-583X(03)00505-6.

[25] L. Carraz, I. Haldorsen, H. Ravn, M. Skarestad, L. Westgaard, Fast release of nuclear reaction products from refractory matrices, Nuclear Instruments and Methods 148 (2) (1978) 217–230. doi:10.1016/0029-554X(70)90171-0.

[26] P. Hoff, O. Jonsson, E. Kugler, H. Ravn, Release of nuclear reaction products from refractory compounds, Nuclear Instruments and Methods in Physics Research 221 (2) (1984) 313–329. doi:10.1016/0167-5087(84)90002-4.

[27] TRIUMF-ISAC, TRIUMF-ISAC Yield Database.
URL http://mis.triumf.ca/science/planning/yield/target

[28] M. Dombsky, H. V., Method of forming composite ceramic targets, Patent no. US 7682664 B2 (2010).

[29] TRIUMF Annual Report - Scientific Activities, Tech. rep., TRIUMF, Vancouver (2002).

[30] A. Gottberg, personal communication.

[31] J. P. Ramos, A. M. R. Senos, C. M. Fernandes, T. Stora, P. Bowen, Development of a processing route for carbon allotrope-based TiC porous nanocomposites, to be published.

[32] J. Ramos, D. Gueissbühler, A. Senos, T. Stora, P. Bowen, Master sintering curve determination of nanometric TiC and a TiC-carbon black nanocomposite, to be published.

[33] J. P. Ramos, A. M. R. Senos, T. Stora, P. Bowen, Stability of nanometric TiC-carbon composites: effects of carbon allotropes and Zr milling impurities, to be published.

[34] T. Bohlen, F. Cerutti, M. Chin, A. Fasso, A. Ferrari, P. Ortega, A. Mairani, P. Sala, G. Smirnov, V. Vlachoudis, The FLUKA Code: Developments and Challenges for High Energy and Medical Applications, Nuclear Data Sheets 120 (2014) 211–214. doi:10.1016/j.nds.2014.07.049.

[35] A. Ferrari, P. R. Sala, A. Fasso, J. Ranft, FLUKA : A multi-particle transport code, Tech. Rep. October, CERN, Geneva (2005). doi:10.5170/CERN-2005-010.

[36] R. dos Santos Augusto, L. Buehler, Z. Lawson, S. Marzari, M. Stachura, T. Stora, E. CERN-MEDICIS collaboration, CERN-MEDICIS (Medical Isotopes Collected from ISOLDE): A New Facility, Applied Sciences 4 (2) (2014) 265–281. doi:10.3390/app4020265.

[37] Nucleonica GmbH, Nucleonica Nuclear Science Portal (www.nucleonica.com), Karlsruhe (2014).
[38] M. Turrión, M. Eller, R. Catherall, L. Fraile, U. Herman-Izycka, U. Köster, J. Lettry, K. Riisager, T. Stora, Management of ISOLDE yields, Nuclear Instruments and Methods in Physics Research Section B: Beam Interactions with Materials and Atoms 266 (19-20) (2008) 4674–4677. doi:10.1016/j.nimb.2008.05.144.
[39] J. Lettry, R. Catherall, P. Drumm, P. Van Duppen, A. Evensen, G. Focker, A. Jokinen, O. Jonsson, E. Kugler, H. Ravn, Pulse shape of the ISOLDE radioactive ion beams, Nuclear Instruments and Methods in Physics Research Section B: Beam Interactions with Materials and Atoms 126 (1-4) (1997) 130–134. doi:10.1016/S0168-583X(96)01025-7.
[40] A. Kelic, M. V. Ricciardi, K.-H. Schmidt, ABLA07 - towards a complete description of the decay channels of a nuclear system from spontaneous fission to multifragmentation, in: D. Filges, S. Leray, Y. Yariv, A. Mengoni, A. Stanculescu, G. Mank (Eds.), Proceedings of the Joint ICTP-IAEA Advanced Workshop on Model Codes for Spallation Reactions, IAEA INDC(NDS)-530, Vienna, 2009, pp. 181–221. arXiv:0906.4193v1.
[41] M. Dombsky, P. Bricault, P. Schmor, M. Lane, ISAC target operation with high proton currents, Nuclear Instruments and Methods in Physics Research Section B: Beam Interactions with Materials and Atoms 204 (2003) 191–196. doi:10.1016/S0168-583X(02)01902-X.
[42] M. Dombsky, P. Bricault, V. Hanemaayer, Increasing beam currents at the TRIUMF-ISAC Facility; techniques and experiences, Nuclear Physics A 746 (2004) 32–39. doi:10.1016/j.nuclphysa.2004.09.060.
[43] R. Kirchner, On the release and ionization efficiency of catcher-ion-source systems in isotope separation on-line, Nuclear Instruments and Methods in Physics Research Section B: Beam Interactions with Materials and Atoms 70 (1-4) (1992) 186–199. doi:10.1016/0168-583X(92)95930-P.
[44] T. Bjørnstad, E. Hagebø, P. Hoff, O. C. Jonsson, E. Kugler, H. L. Ravn, S. Sundell, B. Vosicki, t. I. Collaboration, Methods for Production of Intense Beams of Unstable Nuclei: New Developments at ISOLDE, Physica Scripta 34 (6A) (1986) 578–590. doi:10.1088/0031-8949/34/6A/013.
[45] J. C. Slater, Atomic Radii in Crystals, The Journal of Chemical Physics 41 (10) (1964) 3199. doi:10.1063/1.1725697.

5.2 Summary of the isotope release properties from TiC-carbon nanocomposites

In figure 5.1 the results obtained in the preliminary TiC release studies (from 1200 to 1450 °C) of section 3.1 are compared with the ones of TiCm (TiC milled) at 1500 °C obtained in the article just presented.

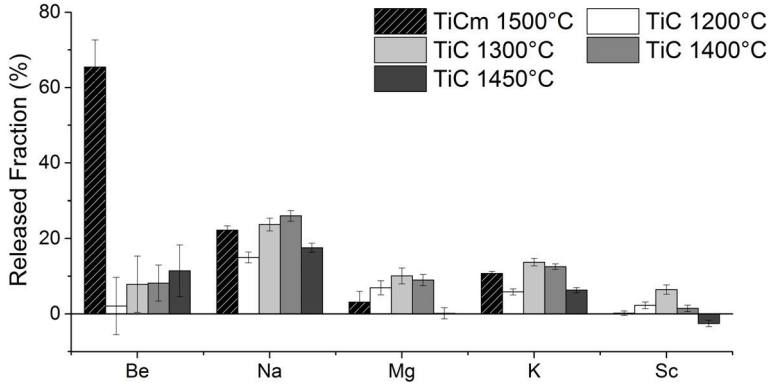

Figure 5.1 – Released fraction for Be, Na, Mg, k, Sc for all the TiC materials used during this work: TiCm 1500 °C corresponds to the one studied in article of section 5.1 and TiC 1200 to 1450 °C correspond to the ones in the preliminary studies of section3.1.

As can be seen the results obtained for TiCm are similar to those obtained in the preliminary studies at higher temperatures (1300-1450 °C), as expected since their microstructures are very similar, except for Mg and Be. Be release seems to be hindered in the case of TiC 1200 to 1450 °C, where it is likely that the presence of TiO_2 may be supplying oxygen to form BeO which has a very high melting point (2578 °C [35]). Furthermore in the release studies of the preliminary studies the sample support was made of Al_2O_3, which could also be a source of oxygen. Regarding the release of Mg we have not enough data to explain the high release of the TiC materials in comparison to TiCm.

For this chapter the main conclusions are:

- TiC milled was selected to be tested at 1500 °C for isotope release to serve as a reference, and TiC-MWCNT and TiC-carbon black were tested at 1500 °C and 1800 °C respectively;
- The release was notably higher for the TiC-carbon black than in the other two cases, where K was almost as high as in the literature values for Ti foils known to have very fast release of this element, Ca release was seen for both nanocomposites contrarily to the TiC and Be was released in smaller quantities due to the presence of carbon;
- TiC-carbon black was selected as the prototype target material to be tested at ISOLDE and the process was successfully upscaled where, relatively to the samples the upscaled material had lower Zr contents and slightly higher crystallite sizes (115 nm instead of 76 nm);
- the difference between the crystallite sizes of the sample and upscaled material is either

due to the processing itself generating a slightly different green body or due to the different percentages of Zr (lower for the upscaled material), showing that Zr may have an influence in the sintering of TiC;

- the prototype material delivered stable beams of Li, Na and K over the full operation time and was tested from 1300 to 2000 °C;
- the yields obtained for Li and Na were higher than previous Ti-foils targets at ISOLDE facility,the K yields were slightly lower than previous targets, and Ca yields were lower. It is hypothesized that this might be due due to reaction with carbon black or due to long effusion times in the case of K and Ca;
- relatively to the ISAC-TRIUMF proton current normalized yields, the protoype yields were all higher with the exception of Ca;
- the release time-structure of all the isotopes in the TiC-carbon black nanocomposite is apparently longer, as seen for all ISOLDE target nanomaterials and are generally, nonetheless of the same level or higher in intensity.

6 Conclusions and outlook

Contents

6.1 Conclusions 149
6.1.1 TiC-carbon nanocomposite development 149
6.1.2 TiC and TiC-carbon black sintering kinetics 150
6.1.3 Isotope release properties from TiC-carbon black nanocomposite . . . 150
6.2 Outlook 151
6.2.1 Future of TiC-based nanocomposites at ISOLDE 152
6.2.2 Modeling of release properties 153

6.1 Conclusions

The ultimate goal for this work was achieved: to develop and test a novel nanostructured Ti-based target material which brought generally high and stable beam intensities to ISOLDE (with the exception of Ca). The work began with nanometric TiO_2 and TiC materials, where TiC was chosen through preliminary sintering and isotope release studied to be further developed. As such, a nanocomposite TiC-C was developed and fully characterized and tested to temperatures as high as 1800 °C to successfully stabilize nanometric titanium carbide. A master sintering curve was determined to study the sintering kinetics of TiC and a TiC-C nanocomposite. At the end selected TiC-C nanocomposites were irradiated and their isotope release was studied in order to determine the best candidate for a target material.

6.1.1 TiC-carbon nanocomposite development

During the preliminary studies of nanometric TiO_2 and TiC materials it was concluded that TiO_2 sinterability was high even at temperatures as low as 1000 °C which limits its application for ISOL target material, where additionally, low isotope release at these temperatures was seen. TiC on the contrary, showed acceptable release of most of the elements studied

(Be, Na, Mg and K where Sc and Ca were not released), even though the structures tested were sub micron and at relatively low temperatures. TiC also revealed low sinterability up to 1450 °C, however the nanometric structure was lost at 1300 °C and TiC was very susceptible to oxidation even under high vacuum atmosphere.

To stabilize nanometric TiC and avoid its oxidation a processing route was developed to produce nanocomposites with graphite, carbon black or MWCNT up to 75 vol.% of carbon. The carbon allotropes addition revealed to be very successful in all three cases where nanometric TiC was stable up to 1500 °C. At this temperature, the most effective carbon allotrope was the TiC-MWCNT where with TiC:C ratio of 10.9 (where in the others was around 2.5), around 60 nm TiC grains were stabilized.

The processing route, which involved attrition milling, had an effect on TiC where the TiC milled, without any carbon addition, had lower sinterability than TiC as-supplied. The processing route chosen (attrition mill) introduced a Zr contamination in the nanocomposites, in the form of ZrO_2 from the milling media. This contamination was discovered to transform into ZrC by reacting with the carbon and solubilize into the TiC, forming $Ti_{(1-x)}Zr_xC$, where at 1800 °C it was totally solubilized. This solubilization was discovered to come with a TiC crystal lattice increase, which seems to be also increased by increasing the C:Ti ratio in the TiC.

The sinterability of the nanocomposites was further assessed at higher temperatures, up to 1800 °C, where in this case the TiC-carbon black nanocomposite was the most effective stabilizing the nanosized TiC. Final crystallite sizes of the TiC in the TiC-CB nanocomposite were 76 nm with a ≈ 50 % density, while in the other two cases TiC crystallite sizes were around 130 nm.

6.1.2 TiC and TiC-carbon black sintering kinetics

Sintering kinetics of the nanometric TiC and the TiC-CB composite were assessed using the master sintering curve, where constant heating rate dilatometry was used. The master sintering curve has never been determined for the TiC material (and also for the TiC-CB). While for the TiC, densities up to 66 % (from 45 %) were reached, the nanocomposite only reached 44 % (from 40 %). The apparent activation energy for TiC was found to be 390 kJ mol^{-1} while for the TiC-carbon black composite was 555 kJ mol^{-1}, which difference is due to the action of the carbon black that reduces the TiC coordination number, reducing its sinterability. Isolating dilatometry sections above 1300 °C and computing the master sintering curve an activation energy of 3.0 MJ was obtained, which has to be confirmed with other experiments or through modeling.

6.1.3 Isotope release properties from TiC-carbon black nanocomposite

Three selected TiC materials from the newly developed TiC-based materials were studied for isotope release: TiC milled (1500 °C), TiC-carbon black (1800 °C) and TiC-MWCNT (at 1500 °C).

The temperatures indicated are the ones at which the nanocomposites were tested for release and correspond those where nanometric TiC (> 100 nm) was stabilized, and TiC milled was used to serve as a reference. TiC-carbon black had the highest release by far for all elements, where K was almost as high as Ti foils values (which are known for fast release), except for Be which release was reduced likely due to the presence of carbon.

The TiC-carbon black was selected as the target material and the processing was upscaled in order to build a full target. The upscaling was successful where the material had the same surface area, morphology and sintering behaviour, with a slightly higher TiC cyrstallite sizes (115 nm instead of the 76 nm and lower Zr contamation.

The target prototype was successfully tested at ISOLDE where a surface ion source was used to ionize alkali and alkaline earth elements produced from this target. Beam intensities and release time-structures were assessed from Li, Na and K isotopes from 1300 to 2000 °C. While the yields on Li and Na were higher than the previously Ti-foils ISOLDE target, the K yields were on the same level and the Ca yields were lower. The lower numbers on K and Ca are hypothesized to be effusion limited, where the carbon black interactions. The nanocomposite TiC-Carbon black target prototype shows the same trend as all the nanometric targets studied so far with apparently longer release time structure but high yields. Furthermore, contrarily to the previous Ti-foils target where the yields decay over time, they were stable for the nanocomposite for the full operation period, where in all cases, except for Ca, the integrated yields over time are higher.

6.2 Outlook

Nanomaterials for ISOL application is a niche research topic where the materials have very specific requirements, rarely found in other research or applications. Having a very porous, fine grained material for very high temperature applications is a nonsubject in the ceramics research, with the exception of a few cases: as is for example high temperature catalysis and ceramic filters for hot gas or liquid metal [139, 140].

Nonetheless nanomaterials for ISOL targets can be in principle deployed in any ISOL facility, where the only limitation might be those facilities with high beam power deposition. Since porous nanomaterials have lower thermal conductivities, this may turn to be an issue where high thermal stresses will be generated that may cause a catastrophic failure of such targets. On the other hand, less dense materials, will also have lower power deposition, so for these facilities further investigations have to be done case by case.

The Li-based refractory blankets for fusion reactors have many similarities with the ISOL targets [141]. The Li-blanket generates heat by absorbing the fast neutrons generated by the fusion reactor in order to heat a coolant in an heat exchanger which is then used to generate electricity. Apart from that, the Lithium blankets has a second function where from the nuclear reaction between the Li and the neutrons, deuterium and tritium are produced, which have

to be extracted from the material. The tritium is the reactor fuel, so extracting it with high efficiency is of high interest. The concepts used in both techniques likely overlap where the nanomaterials release can be of interest for the nuclear fusion materials community, and vice-versa.

By increasing the nanometric TiC volume ratio in the composites, likely higher densities could be reached, where these materials could be used for example on plasma facing materials for future fusion power plants [142] or for ultra-high-temperature ceramics, since nanometric materials densify earlier. Furthermore the obtained master sintering curve for TiC is surely of interest for the tooling and ultra-high-temperature ceramics research communities due to use of TiC in those fields.

The development of materials that enhance the release of radioactive isotopes produced in bulk is also a nonsubject for the nuclear industry, where the release of isotopes is highly undesired, for example in fuel rods. In here, the expertise gathered on the release of isotopes, can probably be used to avoid it and vice-versa. As an hypothetical example, the trapping of certain elements in ISOL targets, as seems to be the case of Ca in the TiC-carbon black target, which is undesirable at ISOLDE, could be desirable for nuclear industry.

Since Ca and K element release seem to be hindered by this target nanomaterial, an improved iteration of the TiC-C composite is described and proposed below, for future use at ISOLDE. Furthermore, modeling the release as is, in the literature, can be improved, especially in terms of microscopic effusion and used to optimize the design of target materials. A small review of the current models present in the literature is done together with suggestions for future work.

6.2.1 Future of TiC-based nanocomposites at ISOLDE

Even though the TiC has already provided a positive outcome to the Ti-based target materials at ISOLDE, with stable beams over time and high intensities of Na, K and Li, the Ca beams could only be extracted with very small intensities. The offline isotope release results reported in the article included on section 5.1 (page 137) indicate that the carbon black might be reacting with Ca, hindering its release, which doesn't seem to happen for the TiC-MWCNT composite.

In order to develop a performing TiC-MWCNT nanocomposite a subsequent thematic was initiated. During the project a novel TiC-MWCNT processing route was designed and the obtained composites were tested for sinterability in terms of shrinkage and mass losses [143]. Further characterization was carried in order to characterize the phase composition, morphology, crystallite size and SSA of the new composites. The processing route was similar to the one developed during the production of the nanometric UC_x [51] (detailed on section 1.3.3, page 30), but with less excess carbon. Therefore, instead of mixing directly TiC with carbon, TiO_2 was used as raw material with MWCNT and thermally treated to form TiC with excess carbon through the TiO_2 carbothermal reduction: $TiO_2 + 4C \rightarrow TiC + C + 2CO$ (g).

The results of this study are very promising (for details see appendix B, on 177), where nanometric TiC (132 nm) in a highly porous (84 %) composite, is stabilized up to 2100 °C and possibly at even higher temperatures. The TiC-carbon black nanocomposite used in the target material had similar crystallite sizes but higher density (50 %) as seen on the article included on the section 5.1 on page 135. If the release efficiency for Ca is high enough, this target may be even able to produce the very exotic ^{35}Ca ($t_{1/2}$ = 25.7 ms) and ^{35}K ($t_{1/2}$ = 190 ms).

6.2.2 Modeling of release properties

As detailed in subsection 1.3.3 (page 30) target nanomaterials have apparently longer release times but with higher beam intensities for short lived isotopes. Modeling of the isotope release properties is complex since many phenomena are involved during the release. The release phenomena starts as soon as the isotopes are thermalized in the bulk of the target material grains after production, until they reach the ion source, which is usually divided into two main processes, diffusion and effusion, introduced in subsection 1.3.1 (page 27).

While diffusion is derived from the heat equations and is well described and treated in the literature [144], that is not the case for effusion, where the large number of variables present make it very difficult to model. Thus effusion is normally simulated [145, 146, 147, 148] or experimentally measured [149, 88], fitted to non-physical parameters or empirically derived [85, 67, 52] and convoluted with diffusion.

Kirchner in 1992 [70] derived the release model ($P_{\mu,\nu}(t)$) convoluting the diffusion delay equation derived for spheres geometry ($P_\mu(t)$) with a one exponential describing effusion ($P_\nu(t)$) - emptying a volume through an orifice:

$$P_\mu(t) = \frac{6\mu}{\pi^2}\sum_{n=1}^{\infty} e^{-\mu n^2 t} \tag{6.1}$$

$$P_\nu(t) = \nu e^{-\nu t} \tag{6.2}$$

$$P_{\mu,\nu}(t) = \int_{t'=0}^{t} P_\mu(t')P_\nu(t-t')\mathrm{d}t' = \begin{cases} \frac{6\mu\nu}{\pi^2}\sum_{n=1}^{\infty}\frac{e^{-\nu t}-e^{-\mu n^2 t}}{\mu n^2-\nu} \\ \\ \frac{6\mu\nu}{\pi^2}\left[te^{-\nu t}+\sum_{n=1}^{\infty}\frac{e^{-\nu t}-e^{-\mu n^2 t}}{\mu n^2-\nu}\right], \quad \text{if} \quad \mu=\nu \end{cases} \tag{6.3}$$

where μ [s^{-1}] and ν [s^{-1}] are the respective diffusion and effusion time constants which have been described in equations 1.6 and 1.7 (pages 28-29). This function is fitted to the P_∞ experimentally obtained release curve. For foils geometry the equation needs to be adapted: the factor 6 becomes 8 and the sum goes from $n = 0$ and μn^2 becomes $\mu(2n+1)^2$, the particle radius, r, in equation 1.6 becomes d, the foil thickness.

From equations 6.1, 6.2 and 6.3, the release efficiency equations were also deduced for the

processes of diffusion and effusion, in a similar way as in equation 3 of the article included on section 5.1 (page 140) [85]:

$$\varepsilon_{rel,\mu}(t_{1/2}) = \int_0^\infty P_\mu(t) e^{-\lambda_i t} \mathrm{d}t = 3\frac{\sqrt{U}\coth\sqrt{U}}{U}, \text{ with } \quad U = \frac{\pi^2 \ln 2}{\mu t_{1/2}} \tag{6.4}$$

$$\varepsilon_{rel,\nu}(t_{1/2}) = \int_0^\infty P_\nu(t) e^{-\lambda_i t} \mathrm{d}t = \frac{\nu}{\nu + \ln 2 / t_{1/2}} \tag{6.5}$$

$$\varepsilon_{rel,\mu,\nu}(t_{1/2}) = \int_0^\infty P_{\mu,\nu}(t) e^{-\lambda_i t} \mathrm{d}t = \varepsilon_{rel,\mu}(t_{1/2}) \cdot \varepsilon_{rel,\nu}(t_{1/2}) = 3\frac{\sqrt{U}\coth\sqrt{U}}{[1 + \ln 2/(\nu t_{1/2})]\, U} \tag{6.6}$$

$P_{\mu,\nu}(t)$ and $\varepsilon_{rel,\mu,\nu}(t_{1/2})$ were plotted in figure 6.1 to study the influence of the diffusion and effusion parameters on the isotope release where, in all cases, effusion is assumed to be faster than diffusion. It should also be noted that, as per definition, all release curves (figures 6.1a and b) have an integral normalized to 1.

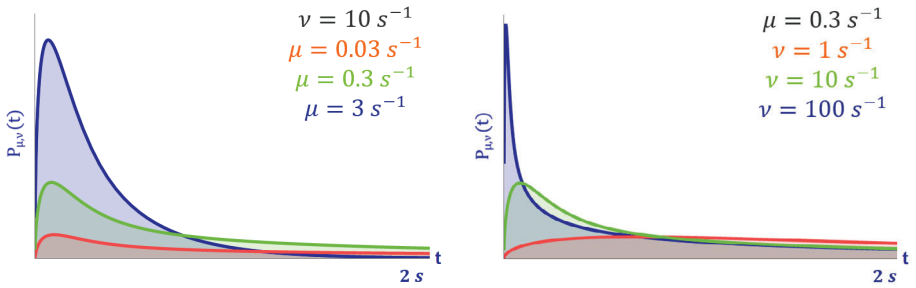

(a) $P_{\mu,\nu}(t)$ for constant effusion and different diffusion time constants.

(b) $P_{\mu,\nu}(t)$ for constant diffusion and different effusion time constants.

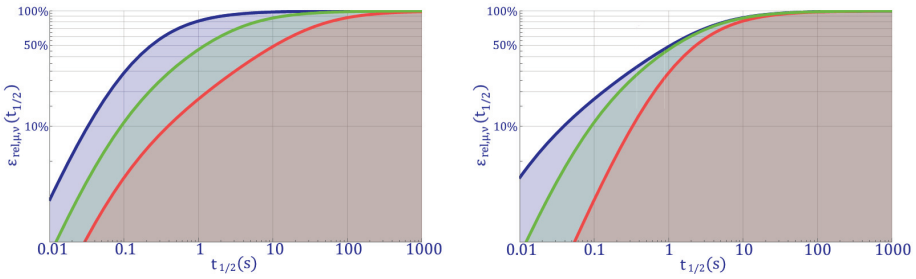

(c) $\varepsilon_{rel,\mu,\nu}(t_{1/2})$ for constant effusion and different diffusion time constants, see (a).

(d) $\varepsilon_{rel,\mu,\nu}(t_{1/2})$ for constant diffusion and different effusion time constants, see (b).

Figure 6.1 – $P_{\mu,\nu}(t)$ and $\varepsilon_{rel,\mu,\nu}(t_{1/2})$ Kirchner model [85] with different effusion and diffusion time constants. μ and ν values are arbitrary.

From figure 6.1a it can be seen by keeping $\nu = 10\,\mathrm{s}^{-1}$ and changing μ by two orders of magnitude (from 0.03 to $3\,\mathrm{s}^{-1}$) - which correspond to an inversely proportional variation of the same magnitude in the grain size (100×) - the release fraction is larger at short times for higher μ, which increases the overall $\varepsilon_{rel,\mu,\nu}(t_{1/2})$, as seen from figure 6.1c. By keeping $\nu = 0.3\,\mathrm{s}^{-1}$) and varying ν by two orders of magnitude (from 1 to $100\,\mathrm{s}^{-1}$), as seen on figure 6.1b the peak of the

release time-structure is shifted in time where at high effusion times, $\varepsilon_{rel,\mu,\nu}(t_{1/2})$ increases for shorter $t1/2$, as represented on 6.1d.

On figure 6.2a the $P_{\mu,\nu}(t) \times e^{-\lambda_i t}$, where $t_{1/2} = 1$ s is plotted with μ and ν arbitrary parameters to reproduce what is seen experimentally for nanomaterials in comparison with standard materials at ISOLDE. As can be seen from figure 6.2a, by assuming a 200 times larger μ and a 30 times smaller ν, with $\mu > \nu$ (where normally $\mu < \nu$), release curves which reproduce the cases shown on figure 1.19c and d (page 33), representative of nanometric and standard ISOLDE materials, respectively. When looking into the $\varepsilon_{rel,\mu,\nu}(t_{1/2})$ generated with the same parameters it doesn't seem to correspond to the experimental data, where nanomaterials in particular, seem to bring approximately the same ratio across a large range of $t_{1/2}$ [50, 51, 54, 49].

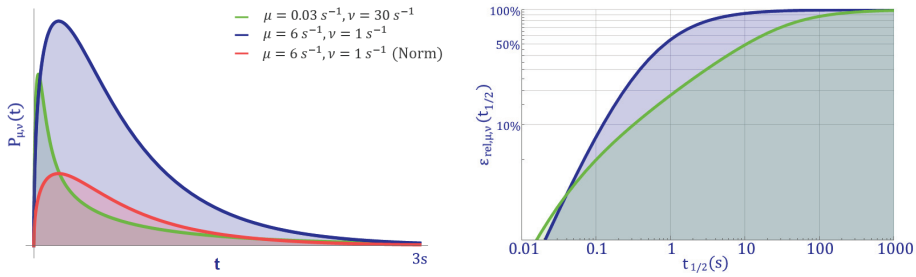

(a) $P_{\mu,\nu}(t)$ (b) $\varepsilon_{rel,\mu,\nu}(t_{1/2})$

Figure 6.2 – Kirchner model $P_{\mu,\nu}(t)$ [85] reproducing the release from nanomaterials ($t_{1/2} =$ 1 s) and respective $\varepsilon_{rel,\mu,\nu}(t_{1/2})$ obtained. Green represents a standard ISOLDE oxide/carbide target, in blue a nanometric target and red the area normalized nanometric target release shape. The μ and ν values are arbitrary and don't represent any real case.

Even though the Kirchner model is appropriate for simple macroscopic geometry targets such as foils [70, 145], this model wouldn't be appropriate to describe the release shape for nanomaterials, however it hints that in nanomaterials it is likely that $\mu > \nu$. In nanomaterials μ is known to be small due to the drastic reduction of target grain size, however it is not possible to reduce grain size without affecting the material porosity. Keeping the material with the same relative density, smaller grains will bring smaller pores which will create a more complex pore network, reducing the mean free path of the particles before colliding with a material surface. One would expect an increase of number of collisions proportional to the grain size reduction, where the former can reach several million of collisions [145].

As discussed above the current effusion phenomena describes relatively well the release from simple geometries such as foil targets or similar for TISS without transfer lines. Nonetheless, the foil target release model has been improved by replacing the Kirchner P_ν with effusion simulated profiles [145, 147, 146]. However, for modeling release from porous materials with grains, an additional step between effusion and diffusion must be added. Diffusion describes already very well the release of isotopes from the moment of production until the atoms reach

the surface of the grain. At this point, the isotope has to effuse through the pore network of the material until it reaches the powder envelope surface (pellet surface or the powder bed surface). From here on, classical effusion can describe the isotope release through the macroscopic spaces of the target container, through the transfer line until it reaches the ion source. This intermediate step, here called microscopic effusion, needs to be assessed and integrated into the general model of release.

An attempt was made to better parametrize effusion empirically by Bouquerel [66], where a double exponential effusion release function was introduced (and later convoluted with diffusion) to better represent the ISOLDE case which has a thick target with a transfer line:

$$P_{v,2}(t) = (1 - e^{-\nu_1 t})e^{-\nu_2 t} \tag{6.7}$$

where ν_1 and ν_2 are the empirical effusion time constants. The final double effusion and diffusion constants release formula has been successfully applied in other works [52, 56].

Attempts to take in consideration the referred microscopic effusion have been made. Leitner [145] has developed a Monte Carlo code, designated RIBO (Radioactive Ion Beam Optimizer) which simulates the release (diffusion, effusion) and ionization. In this code, the microscopic effusion (referred as inter-grain diffusion) is simulated in a limited number of structures - that can be interpolated to get intermediate values - which are then convoluted individually with diffusion and fitted with the release curve. If the result is non satisfactory, the whole process is repeated. This code is usually used to simulate release time-structures where the huge amounts of variables and complexity of TISS make it applicable to very simpler cases, or to simulate the influence of certain parameters on the release [150].

Alyakrinskiy et al. [148] has proposed a similar solution where a similar effusion approach as before was used. In here Knudsen diffusion (which describes diffusion of particles, in low pressure, with mean free path comparable to the pore size [151]) is used to describe microscopic effusion and normal effusion is not simulated, where only one pellet is used for the simulation. In this aproach, the effusion release efficiency is simulated in a randomly packed partially overlapping monodispersed spheres, with 100 % open porosity and multiplied with the diffusion release efficiency, to get the final release efficiency [148]. In here, the release efficiency for a certain element $t_{1/2}$, as a function of grain sizes and porosity is simulated where part of the results are reproduced here for Ar in figure 6.3a and Ga in figure 6.3b [148].

In the study $\tau_s = 0$ s (sticking time) and $\mu = 0.336$ for Ar, while for Ga, $\tau_s = 1.514 \times 10^{-7}$ s and $\mu = 3.55$ [148]. The simulations on figure 6.3 predicted that while for Ar smaller grain sizes bring higher release efficiencies, for Ga it was the inverse. Preliminary data on the release of Ga on nanometric UC_x targets (the same material used in the simulations) have shown a factor 3 to 5 higher yields for Ga isotopes (with $t_{1/2}$ in the order of seconds), when comparing with standard tens of micron targets [51], which disagree with the results presented by Alyakrinskiy et al. The simulation as discussed by the authors assumes that effusion happens only through Knudsen diffusion and no surface diffusion coefficients are taken into consideration, likely

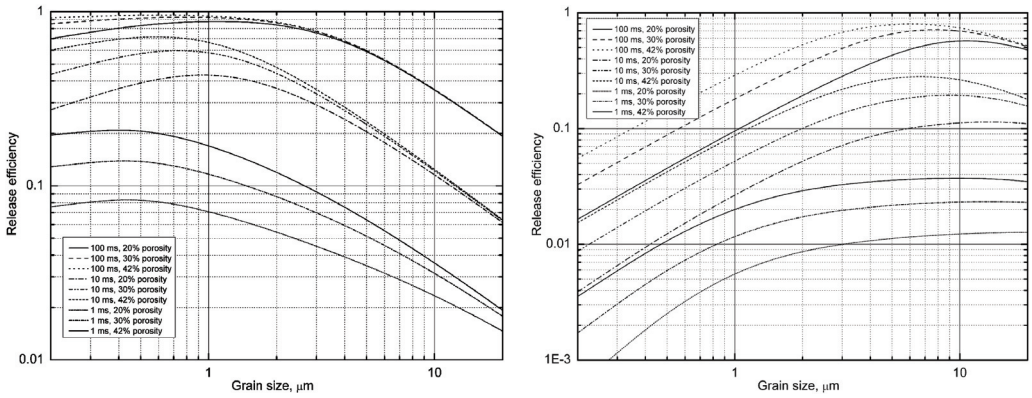

(a) Argon (b) Gallium

Figure 6.3 – Kr and Ga simulated release efficiency as a function of the target grain size. Reproduced from [148].

w

explaining the results obtained for Ga, where in nanomaterials surface diffusion is expected to contribute to the release [148]. Even though the simulation is done for much shorter $t_{1/2}$ than those determined experimentally, it is unlikely that the grain size reduction produces such a drastic reduction of the release efficiencies. The results presented on figure 6.3a are more in line with those obtained experimentally, likely due to the chemical inertness of Ar, which simplifies the simulation.

As another approach, the gas permeability (equivalent to effusion), defined as the ability of a gas to diffuse in a porous structure of a material, is investigated. An experimental setup has been described to measure this parameter for ISOL target materials [149] and an increase of total porosity by 25 % brought up to 2 orders of magnitude increase in the permeability coefficients [88], showing the importance of target porosity. Such type of experiments can be used to assist in the modelling of microscopic effusion.

In summary, there has been effort in the ISOL community to model the release from target materials, even though this is a very complex phenomena. While the diffusion and macroscopic effusion are well studied and modeled, microscopic effusion modelling can still be done. More than 40 years of ISOLDE release data and in-depth characterization of the target materials can be used to refine the models and use them to design and optimize new targets for current and future ISOL facilities.

A Articles supplementary materials

Contents

A.1 Development of a processing route for carbon allotrope-based TiC porous nanocomposites . . . 160

A.1.1 Parameter derivation . . . 160

A.1.2 Composites further characterizations . . . 162

A.2 Stability of nanometric TiC-carbon composites: effects of carbon allotropes and Zr milling impurities . . . 165

A.2.1 Parameter derivation . . . 168

A.3 Master sintering curve determination of nanometric TiC and a TiC-carbon black nanocomposite . . . 169

A.4 Constant isotope release properties measured for an online prototype TiC-carbon nanocomposite target material . . . 170

A.1. Supplementary Materials

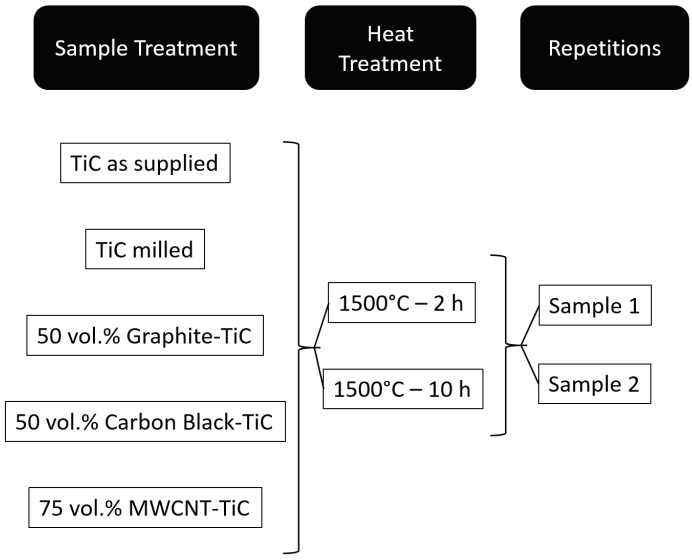

Figure A.1.1: Statistical design used to study through ANOVA analysis of variance, the pore size variation ($\Delta P_s/P_{s,0}$), specific surface area variation ($\Delta S/S_0$) and density variation ($\Delta\rho/\rho_0$) of the materials produced.

A.1.1. Parameter derivation

Calculation of volume ratio of material vs porosity (larger and smaller than 200 nm)

Relative density (ρ_r) is calculated in the following way:

$$\rho_r = \rho/\rho_t \tag{A.1}$$

where ρ_t is the theoretical density of the material and ρ is the geometrical density.

For the composites, the ρ_t of the composites ($\rho_{t,composite}$) was calculated assuming the volume ratios and the respective theoretical densities as shown on table 1:

$$\frac{1}{\rho_{t,composite}} = \frac{m_{C,\%}}{\rho_C} + \frac{m_{TiC,\%}}{\rho_{TiC}} + \frac{m_{ZrO_2/ZrC,\%}}{\rho_{ZrO_2/ZrC}} \tag{A.2}$$

where $m_{C,\%}$, $m_{TiC,\%}$ and $m_{ZrO_2/ZrC,\%}$ correspond to the respective composite component mass ratios and ρ_C, ρ_{TiC} and $\rho_{ZrO_2/ZrC}$ to their densities, where in the case of ρ_C it is either the density graphite, carbon black or MWCNT (non bulk).

Since there are phases changes and mass losses during the thermal treatments the ρ_t changes, since the relative fractions of the composite components change ($m_{C,\%}$, $m_{TiC,\%}$ and $m_{ZrO_2/ZrC,\%}$). To correct for the $ZrO_2 \rightarrow ZrC$ reaction, the ZrO_2 contamination was estimated by XRPD and assumed to convert all to ZrC at high temperatures (16.2% mass losses according to the molecular masses). The carbon mass losses were due to burning of carbon and production of ZrC. Since

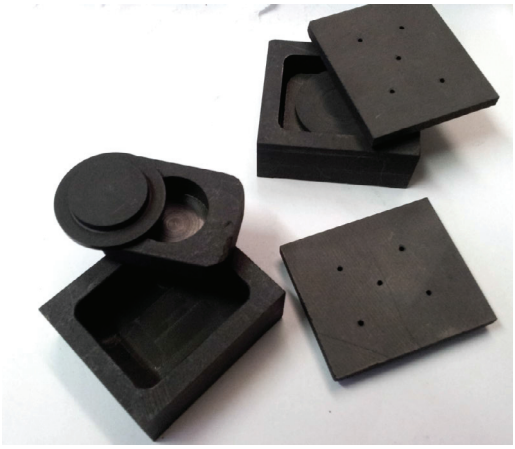

Figure A.1.2: Especially designed double crucibles to avoid sample oxidation in the oven at high temperatures. In the picture, two sets of these crucibles are seen.

TiC also presented mass losses the difference between mass losses of the heat treated TiC and the composites was used to estimate the amount of carbon lost in the composite sample ($[\Delta m/m_0]_{C,\%}$ in wt.%) after thermal treatment:

$$[\Delta m/m_0]_{C,\%} = \frac{[\Delta m/m_0]_{Comp,\%} - [\Delta m/m_0]_{TiC,\%} \times m_{TiC,\%}}{m_{C,\%}} \tag{A.3}$$

where $[\Delta m/m_0]_{Comp,\%}$ and $[\Delta m/m_0]_{TiC,\%}$ are respectively, the experimentally determined composite mass losses and TiC mass losses with the same thermal treatment. From the carbon mass losses and the $ZrO_2 \rightarrow ZrC$ reaction, the $m_{C,\%}$, $m_{TiC,\%}$ and $m_{ZrO_2/ZrC,\%}$ values from equation A.2 were recalculated to determine the $\rho_{t,composite}$ after thermal treatment.

Both corrections of ZrO_2 contamination and carbon losses contribute relatively little to the final values obtained, as both happen in relatively small quantities. In the cases where the ZrO_2 quantities were not determined (the cases in supplementary materials - 25CNT, 50CNT, 75CNT, 25Gr, 25CB, 75CB) the average over all samples was used, 4.6 %.

As for the porosity, the BJH technique, in our case, determined the pore volume below 200 nm ($v_{P,BJH}$) in [$cm^3\ g^{-1}$]. From the ρ_t one can deduce the porosity in [%] below 200 nm ($P_{r,<200\,nm}$), through the following relation:

$$P_{r,<200\,nm} = \frac{v_{P,BJH}}{v_{P,BJH} + \frac{1}{\rho_t}} \tag{A.4}$$

Since the relative total porosity (P_r) and ρ_r (obtained from equation A.1) relation is defined by:

$$P_r = 1 - \rho_r \tag{A.5}$$

then we know the pore size above 200 nm ($P_{r,>200\,nm}$), assuming no closed porosity, can be determined from:

$$P_r = P_{r,>200\,nm} + P_{r,<200\,nm} \tag{A.6}$$

A.1.2. Composites further characterizations

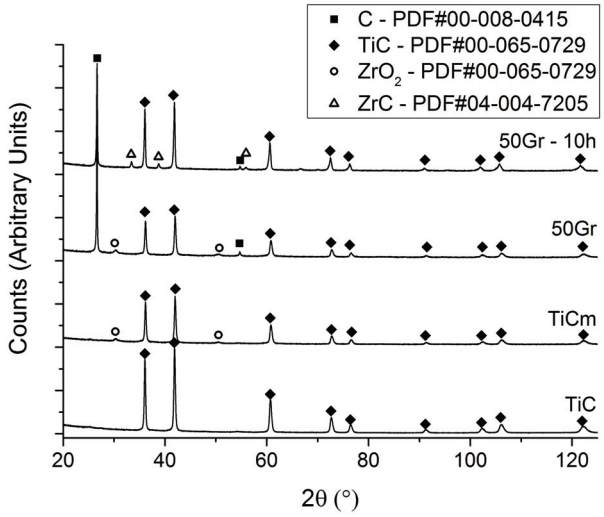

Figure A.1.3: X-ray powder diffraction showing the ZrO_2 contamination and its reduction, exemplified with the 50Gr, into ZrC.

Table A.1.1: Density (ρ), SSA, median pore size (P_S), BJH pore volumes ($v_{P,BJH}$) and mass losses ($\Delta m/m_0$) of 25Gr, 25CB, 75CB, 25CNT, 50CNT and 75CNT as produced and after heat treatments at 1500 °C for 2 and 10 h.

		25Gr	25CB	75CB	25CNT	50CNT	75CNT
ρ (g cm^{-3})	As produced	2.20	1.97	1.18	2.22	2.05	1.68
	1500 °C - 2 h	2.23	2.08	1.19	2.33	2.09	1.93
	1500 °C - 10 h	2.22	2.17	1.21	2.24	2.07	1.91
SSA (m^2 g^{-1})	As produced	30.3	32.4	46.2	32.3	37.1	52.7
	1500 °C - 2 h	8.6	14.1	31.8	3.5	6.3	12.4
	1500 °C - 10 h	8.8	14.0	32.0	2.5	5.7	13.2
P_S (nm)	As produced	26	29	38	25	23	23
	1500 °C - 2 h	38	37	47	38	41	32
	1500 °C - 10 h	44	37	42	41	20	35
$v_{P,BJH}$ (cm^3 g^{-1})	As produced	0.16	0.19	0.30	0.16	0.20	0.27
	1500 °C - 2 h	0.04	0.15	0.37	0.01	0.02	0.09
	1500 °C - 10 h	0.04	0.13	0.26	0.01	0.01	0.05
$\Delta m/m_0$ (%)	1500 °C - 2 h	10.7	11.2	9.0	8.4	11.8	15.7
	1500 °C - 10 h	11.6	12.1	9.2	7.4	12.7	15.5

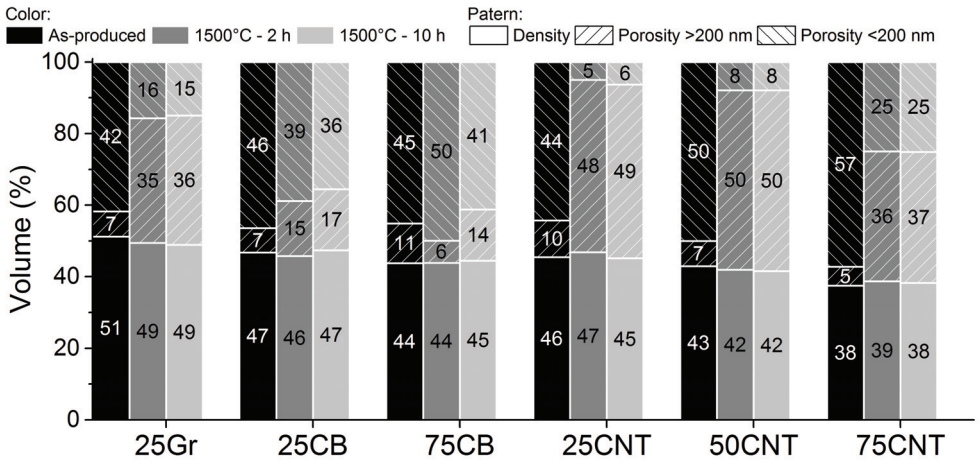

Figure A.1.4: Relative density and porosity ratios (below and above 200 nm) for the TiC, TiCm, 50Gr, 50CB and 75CNTb as produced and heat treated for 2 and 10 h.

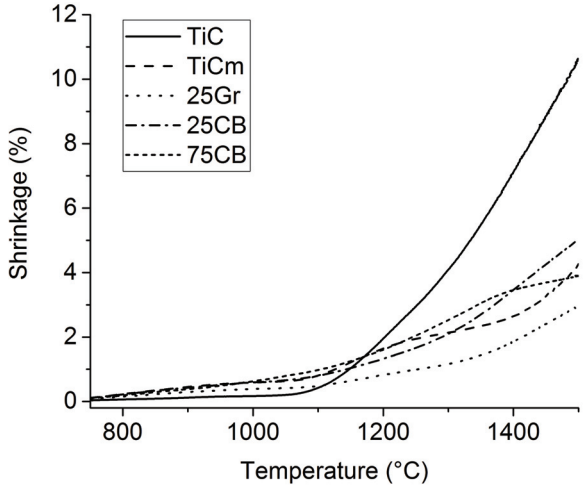

Figure A.1.5: Dilatometry of 25Gr, 25CB and 75CB up to 1500 °C. TiC and TiCm are present for the sake of comparison.

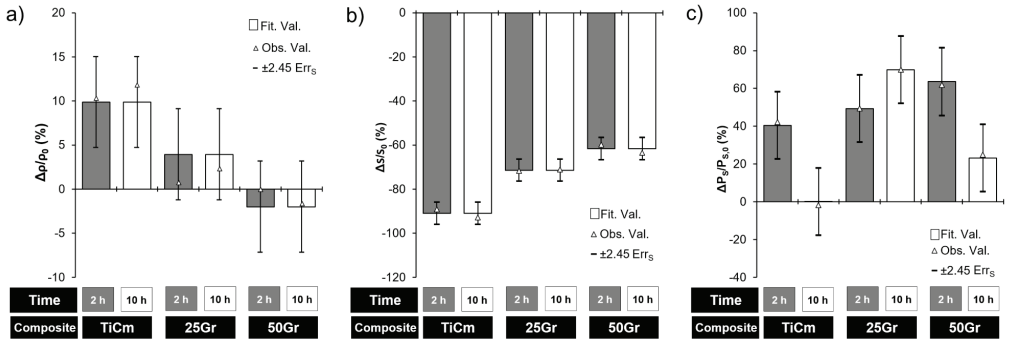

Figure A.1.6: TiCm, 25Gr and 50Gr $\Delta\rho/\rho_0$ (a), $\Delta S/S_0$ (b) and $\Delta P_s/P_{s,0}$ (c) for heat treatments at 1500 °C for 2 and 10 h. The error bars correspond to the standard error of the mean (Err$_S$) - 95 % confidence intervals - for the adjusted values (columns) obtained by ANOVA - analysis of variance.

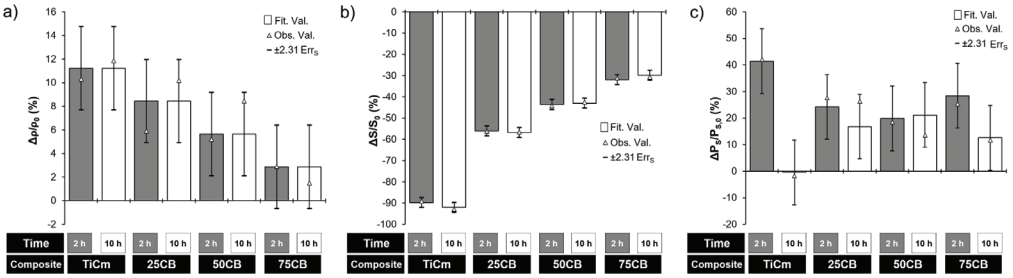

Figure A.1.7: TiCm, 25CB, 50CB and 75CB $\Delta\rho/\rho_0$ (a), $\Delta S/S_0$ (b) and $\Delta P_s/P_{s,0}$ (c) for heat treatments at 1500 °C for 2 and 10 h. The error bars correspond to the standard error of the mean (Err$_S$) - 95 % confidence intervals - for the adjusted values (columns) obtained by ANOVA - analysis of variance.

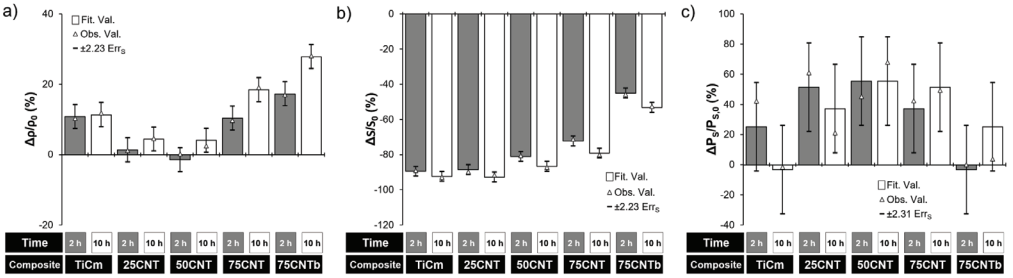

Figure A.1.8: TiCm, 25CNT, 50CNT, 75CNT and 75CNTb $\Delta\rho/\rho_0$ (a), $\Delta S/S_0$ (b) and $\Delta P_s/P_{s,0}$ (c) for heat treatments at 1500 °C for 2 and 10 h. The error bars correspond to the standard error of the mean (Err$_S$) - 95 % confidence intervals - the adjusted values (columns) obtained by ANOVA - analysis of variance.

A.2. Supplementary Materials

Table A.2.1: Characteristics of the raw materials used in this study, where SSA is the specific surface area, P_S is the median pore size, $v_{P,BJH}$ is the pore volume (both determined by BJH) and $D_{v,50}$ is the average particle size.

Characteristic	TiC	Graphite	Carbon Black	MWCNT
Density ($g\,cm^{-3}$)	4.93	2.16	1.85 [a]	2.16 [b] (0.15 [a] - bulk)
Dimensions	80-120 nm[a]	<44 μm [a]	≈40 nm [a]	9.5 nm×1.5 μm [a]
SSA ($m^2\,g^{-1}$)	25.1	2.1	36.9	293.1
G_{BET} - F[c]	48 nm - 6	5.3 μm - 24	88 nm - 6	-
P_S (nm)	41	62	70	38
$v_{P,BJH}$ ($cm^3\,g^{-1}$)	0.07	0.02	0.43	2.70
$D_{v,50}$ (μm)	1.70	33.17	0.46	42.79
A_F [d]	35.4	6.3	5.2	n.a.

[a] Given by supplier.
[b] Graphite density assumed for MWCNT theoretical density.
[c] $G_{BET} = F/(SSA * \rho_t)$, where G_{BET} is the particle size and F is a parameter depending on the shape; $F = 6$ - for spheres; $F = 24$ - for 1:10 flakes [36].
[d] $A_F = D_{v,50}/G_{BET}$ and represents the agglomeration factor [36].

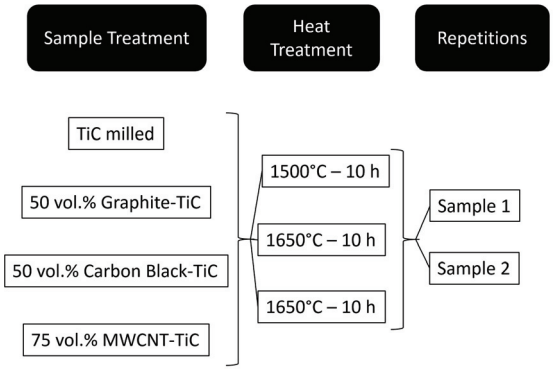

Figure A.2.1: Statistical design used to study through ANOVA analysis of variance, the pore size variation ($\Delta P_s/P_{s,0}$), specific surface area variation ($\Delta S/S_0$) and density variation ($\Delta\rho/\rho_0$) of the materials produced.

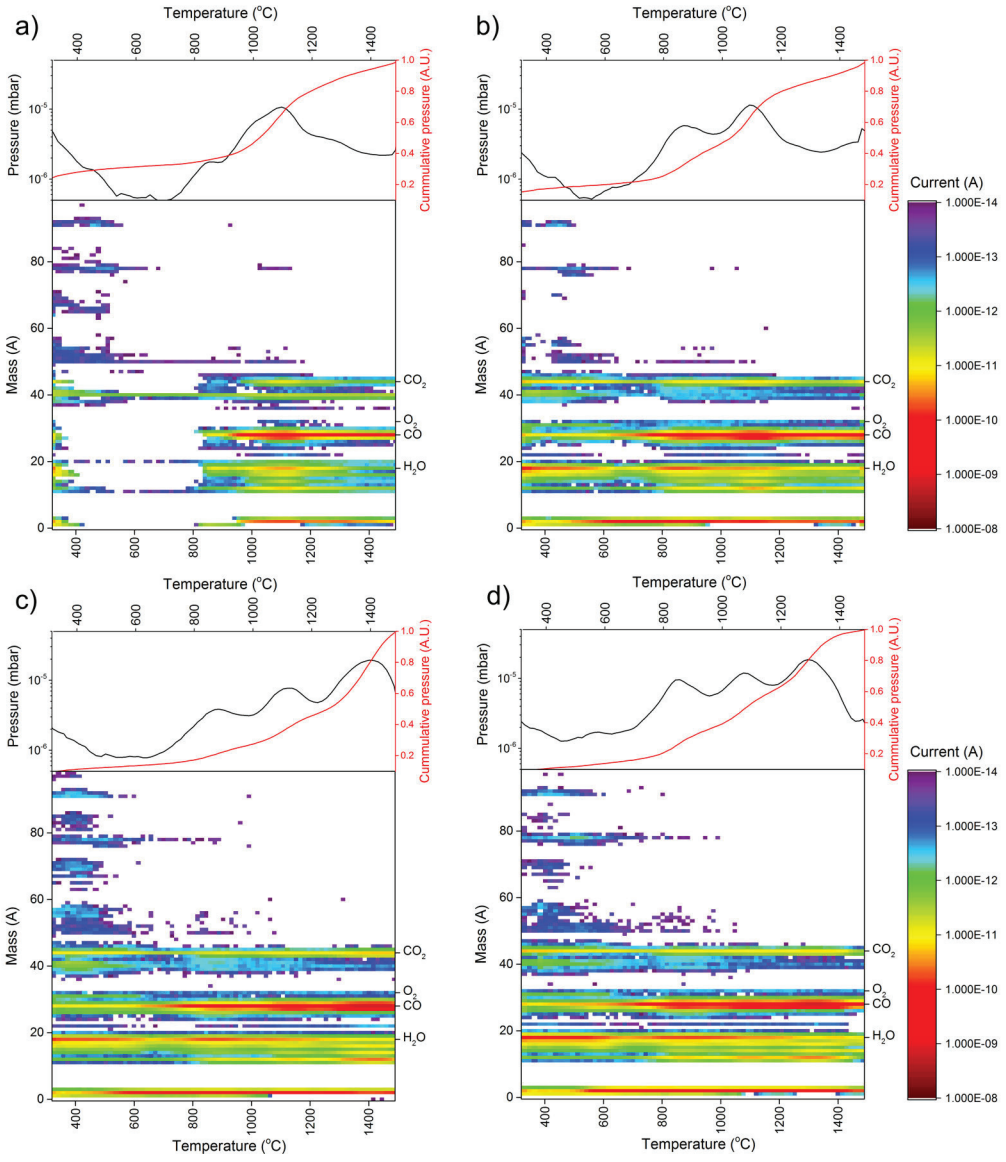

Figure A.2.2: Mass spectrum shown in mass ($1 \leqslant A \leqslant 100$) vs ion current, obtained by residual gas analysis of TiC (a), TiCm (b), 50Gr (c) and 75CNTb (d) from 350 to 1500 °C (bottom) and respective pressure evolution over temperature (top).

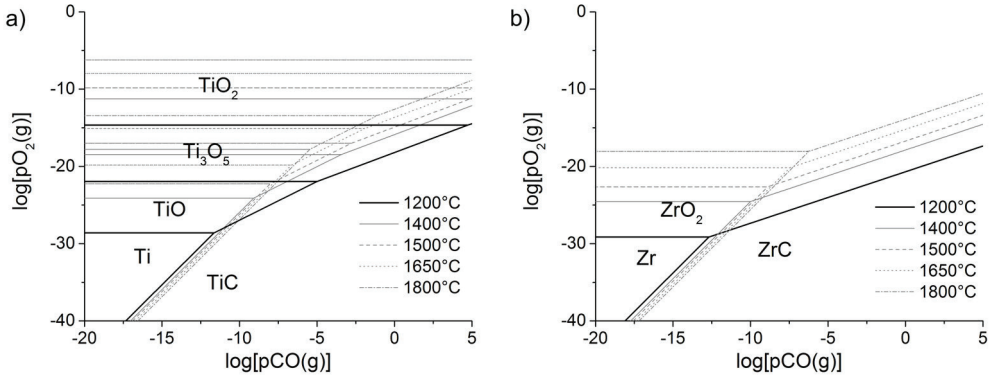

Figure A.2.3: Thermodynamical Ti-C-O (a) and Zr-C-O (b) phase stability diagrams at temperatures from 1200 to 1800 °C.

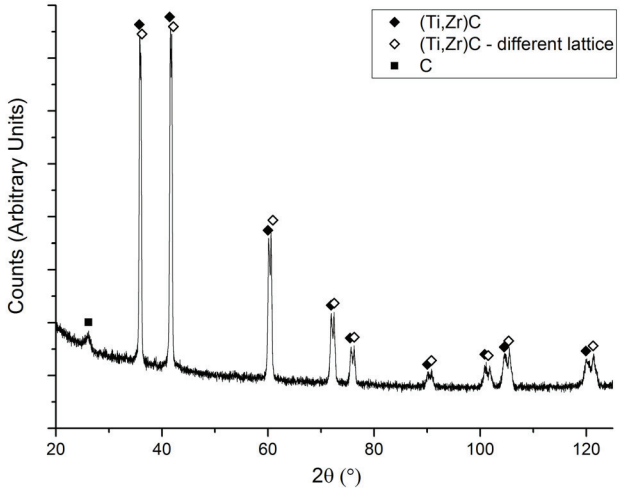

Figure A.2.4: XRPD diffractograms obtained for 50CB heat treated at 1800 °C for 10 h, showing phase segregation.

A.2.1. Parameter derivation

Calculation of volume ratio of material vs porosity (larger and smaller than 200 nm)

(*Reproduced from the supplementary materials of [17]*)

Relative density (ρ_r) is calculated in the following way:

$$\rho_r = \frac{\rho}{\rho_t} \tag{B.1}$$

where ρ_t is the theoretical density of the material and ρ is the geometrical density.

For the composites, the ρ_t of the composites ($\rho_{t,composite}$) was calculated assuming the volume ratios and the respective theoretical densities as shown on table A.2.1:

$$\frac{1}{\rho_{t,composite}} = \frac{m_{C,\%}}{\rho_C} + \frac{m_{TiC,\%}}{\rho_{TiC}} + \frac{m_{ZrO_2/ZrC,\%}}{\rho_{ZrO_2/ZrC}} \tag{B.2}$$

where $m_{C,\%}$, $m_{TiC,\%}$ and $m_{ZrO_2/ZrC,\%}$ correspond to the respective composite component mass ratios and ρ_C, ρ_{TiC} and $\rho_{ZrO_2/ZrC}$ to their densities, where in the case of ρ_C it is either the density graphite, carbon black or MWCNT (non bulk).

Since there are phases changes and mass losses during the thermal treatments the ρ_t changes, since the relative fractions of the composite components change ($m_{C,\%}$, $m_{TiC,\%}$ and $m_{ZrO_2/ZrC,\%}$). To correct for the $ZrO_2 \rightarrow ZrC$ reaction, the ZrO_2 contamination was estimated by XRPD and assumed to convert all to ZrC at high temperatures (16.2% mass losses according to the molecular masses). The carbon mass losses were due to burning of carbon and production of ZrC. Since TiC also presented mass losses the difference between mass losses of the heat treated TiC and the composites was used to estimate the amount of carbon lost in the composite sample ($[\Delta m/m_0]_{C,\%}$ in wt.%) after thermal treatment:

$$[\Delta m/m_0]_{C,\%} = \frac{[\Delta m/m_0]_{Comp,\%} - [\Delta m/m_0]_{TiC,\%} \times m_{TiC,\%}}{m_{C,\%}} \tag{B.3}$$

where $[\Delta m/m_0]_{Comp,\%}$ and $[\Delta m/m_0]_{TiC,\%}$ are respectively, the experimentally determined composite mass losses and TiC mass losses with the same thermal treatment. From the carbon mass losses and the $ZrO_2 \rightarrow ZrC$ reaction, the $m_{C,\%}$, $m_{TiC,\%}$ and $m_{ZrO_2/ZrC,\%}$ values from equation B.2 were recalculated to determine the $\rho_{t,composite}$ after thermal treatment.

Both corrections of ZrO_2 contamination and carbon losses contribute relatively little to the final values obtained, as both happen in relatively small quantities.

As for the porosity, the BJH technique, in our case, determined the pore volume below 200 nm ($v_{P,BJH}$) in [$cm^3\ g^{-1}$]. From the ρ_t one can deduce the relative porosity in [%] below 200 nm ($P_{r,<200\,nm}$), through the following relation:

$$P_{r,<200\,nm} = \frac{v_{P,BJH}}{v_{P,BJH} + \frac{1}{\rho_t}} \tag{B.4}$$

Since the relative total porosity (P_r) and ρ_r (obtained from equation B.1) relation is defined by:

$$P_r = 1 - \rho_r \tag{B.5}$$

then we know the pore size above 200 nm ($P_{r,>200\,nm}$), assuming no closed porosity, can be determined from:

$$P_r = P_{r,>200\,nm} + P_{r,<200\,nm} \tag{B.6}$$

A.3. Supplementary Materials

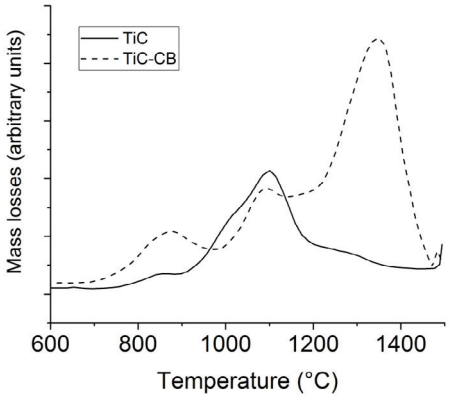

Figure A.3.1: Relative mass losses for TiC and TiC-CB. Reproduced from [8].

A.4. Supplementary Materials

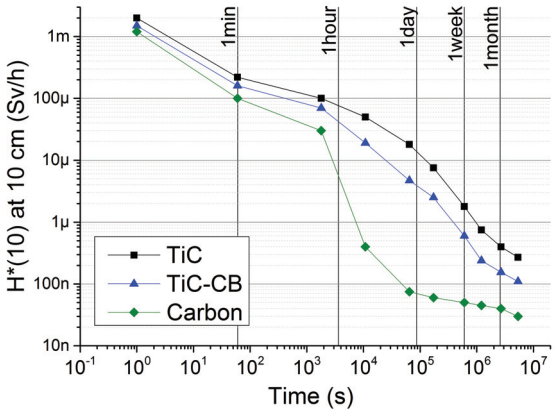

Figure A.4.1: FLUKA [34, 35] simulation which estimates $H^*(10)$ at 10 cm of 3 pellets of 12 mm diameter and 1.5 mm thickness. Irradiation with $1 \cdot 10^{15}$, 1.4 GeV protons. Materials simulated: TiC with theoretical density (4.93 g cm^{-3} [15]), carbon with 2 g cm^{-3} and a mixture of TiC and carbon in 1:1 in volume.

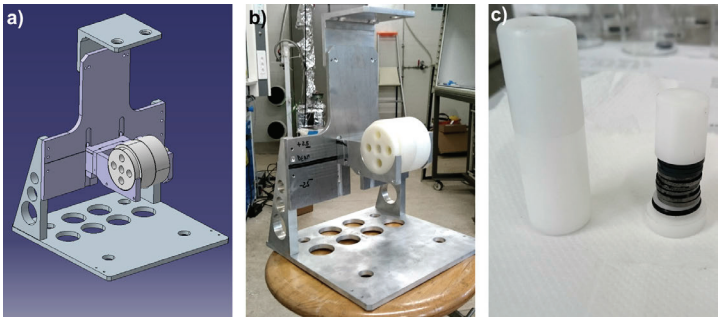

Figure A.4.2: Irradiation stand design in 3D (by Matteo Vagnoni) (a), built (b) and sample tube opened showing the 9 samples for irradiation (c). The sample tube fits in a selected position hole in the white container in (b).

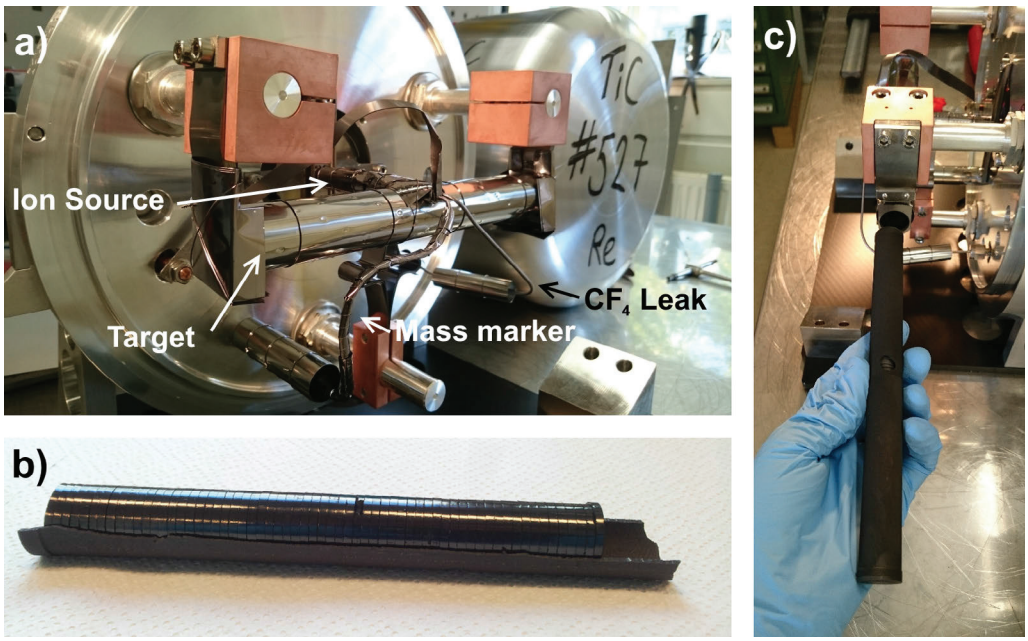

Figure A.4.3: Target unit #527 with target, ion source, mass marker and CF_4 leak identified (a), TiC-CB pellets as-produced (b) and graphite container with TiC-CB pellets ready to be inserted in the target unit oven (c).

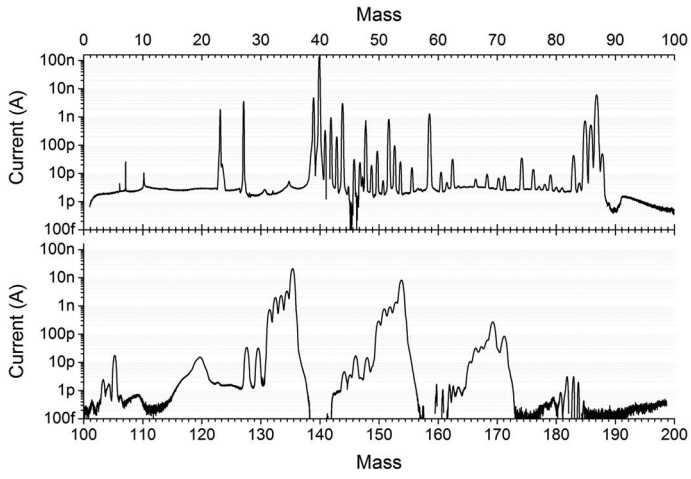

Figure A.4.4: Mass scan of the TiC-CB unit (#527) - target at 1800 °C and Re ion source at 2130 °C.

Table A.4.1: Isotope in-target production yields in the TiC-CB, in μC^{-1}, when bombarding with 1.4 GeV protons. Simulation done with ABRABLA07v5 with $1 \cdot 10^9$ events, accounting for all Ti and C stable isotopes and respective ratios in the target material.

Z/N	0	1	2	3	4	5	6	7	8	9	10	11	12	13	14	15	16	17	18	19	20	21	22	23	24	25	26	27	28
22																		39Ti	40Ti	41Ti	42Ti	43Ti	44Ti	45Ti	46Ti	47Ti	48Ti	49Ti	
																		4.5E+02	4.2E+03	1.9E+05	2.5E+06	6.0E+07	2.1E+09	4.9E+09	1.3E+10	1.3E+10	2.1E+09	8.0E+08	
21																	37Sc	38Sc	39Sc	40Sc	41Sc	42Sc	43Sc	44Sc	45Sc	46Sc	47Sc	48Sc	49Sc	49Sc
																	5.2E+02	7.0E+03	8.6E+04	3.0E+06	4.9E+07	9.0E+08	7.5E+09	1.3E+10	1.9E+10	1.3E+10	1.4E+10	1.1E+09	7.2E+08
20																	35Ca	36Ca	37Ca	38Ca	39Ca	40Ca	41Ca	42Ca	43Ca	44Ca	45Ca	46Ca	47Ca	48Ca
																	1.4E+03	2.2E+04	9.1E+05	1.4E+07	3.0E+08	6.3E+09	1.1E+10	2.3E+10	1.1E+10	2.5E+09	1.6E+09	1.0E+08	4.1E+07
19																	34K	35K	36K	37K	38K	39K	40K	41K	42K	43K	44K	45K	46K	47K
																	1.6E+04	2.7E+05	8.3E+06	1.7E+08	2.5E+09	1.4E+10	1.4E+10	1.3E+10	3.9E+09	2.1E+09	3.9E+08	1.3E+08	9.2E+06	3.0E+06
18													31Ar	32Ar	33Ar	34Ar	35Ar	36Ar	37Ar	38Ar	39Ar	40Ar	41Ar	42Ar	43Ar	44Ar	45Ar	46Ar		
													5.8E+02	2.3E+04	9.2E+05	1.6E+07	4.3E+08	8.8E+09	1.4E+10	2.6E+10	7.0E+09	4.7E+09	7.5E+08	3.1E+08	3.7E-07	1.1E+07	7.1E+05	2.0E+05	
17													36Cl	37Cl	38Cl	39Cl	40Cl	41Cl	42Cl	43Cl	44Cl	45Cl								
													5.8E+03	1.7E+05	6.6E+06	1.6E+08	2.8E+09	1.2E+10	9.6E+09	8.3E+09	2.3E+09	1.1E+09	1.7E+08	5.9E+07	4.9E-06	1.2E+06	6.5E+04	2.3E+04	
16											27S	28S	29S	30S	31S	32S	33S	34S	35S	36S	37S	38S	39S	40S	41S	42S	43S	44S		
											3.1E+02	2.0E+04	5.8E+05	1.2E+07	2.6E+08	4.9E+09	7.9E+09	1.4E+10	4.1E+09	3.6E+09	3.8E+08	1.6E+08	1.9E+07	5.2E+06	3.0E+05	6.9E+04	1.1E+03	1.3E+02	
15											26P		28P	29P	30P	31P	32P	33P	34P	35P	36P	37P	38P	39P	40P	41P		43P	
											1.6E+03		3.0E+06	1.7E+08	1.3E+09	6.6E+09	4.1E+09	4.0E+09	1.0E+09	5.3E+08	6.6E+07	2.3E+07	1.9E+06	6.5E+05	2.5E+04	9.1E+03		3.3E+01	
14									23Si	24Si	25Si	26Si	27Si	28Si	29Si	30Si	31Si	32Si	33Si	34Si	35Si	36Si	37Si	38Si	39Si	40Si				
									1.6E+02	1.0E+04	4.2E+05	3.9E+07	4.4E+08	6.8E+09	5.8E+09	7.8E+09	1.4E+09	1.3E+09	1.3E+08	5.5E+07	5.9E+06	1.6E+06	1.0E+05	1.6E+04	3.7E+02	6.8E+01				
13									21Al	22Al	23Al	24Al	25Al	26Al	27Al	28Al	29Al	30Al	31Al	32Al	33Al	34Al	35Al	36Al	37Al					
									1.6E+03	7.0E+04	1.0E+06	1.7E+07	6.6E+08	2.2E+09	6.2E+09	1.7E+09	1.3E+09	2.9E+08	1.5E+08	1.7E+07	6.0E+06	5.0E+05	2.2E+05	7.5E+03	2.3E+03				
12									20Mg	21Mg	22Mg	23Mg	24Mg	25Mg	26Mg	27Mg	28Mg	29Mg	30Mg	31Mg	32Mg	33Mg	34Mg	35Mg	36Mg					
									8.8E+03	4.4E+05	8.1E+06	1.9E+08	2.1E+09	1.5E+09	1.8E+09	3.1E+08	1.2E+08	1.3E+07	4.4E+06	7.3E+05	1.5E+05	1.5E+04	9.8E+02	3.3E+01	3.3E+01					
11										20Na	21Na	22Na	23Na	24Na	25Na	26Na	27Na	28Na	29Na	30Na	31Na	32Na	33Na							
										3.6E+06	8.7E+07	1.2E+09	2.0E+09	7.6E+08	3.9E+08	9.0E+07	2.2E+07	2.6E+06	4.5E+05	6.9E+04	2.0E+04	5.7E+02								
10								17Ne	18Ne	19Ne	20Ne	21Ne	22Ne	23Ne	24Ne	25Ne	26Ne	27Ne	28Ne	29Ne	30Ne									
								1.1E+05	3.5E+06	6.1E+07	1.5E+09	1.5E+09	1.1E+09	1.5E+08	5.7E+07	6.3E+06	1.1E+06	1.1E+05	1.7E+04	1.2E+03	5.0E+02									
9									17F	18F	19F	20F	21F	22F	23F	24F	25F	26F	27F											
									5.6E+07	5.2E+08	6.9E+08	4.7E+08	2.2E+08	5.2E+07	1.3E+07	1.4E+06	1.5E+05	1.3E+04	1.7E+03											
8						13O	14O	15O	16O	17O	18O	19O	20O	21O	22O	23O	24O													
						8.3E+04	1.1E+07	3.8E+08	2.6E+09	7.5E+08	3.4E+08	6.1E+07	2.6E+07	3.5E+06	7.4E+05	6.1E+04	3.5E+03													
7						12N	13N	14N	15N	16N	17N	18N	19N	20N	21N	22N														
						3.8E+06	2.6E+08	2.6E+09	2.5E+09	2.3E+08	5.1E+07	6.7E+06	1.5E+06	1.7E+05	3.6E+04	1.8E+03	3.3E+01													
6					9C	10C	11C	12C	13C	14C	15C	16C	17C	18C	19C															
					5.4E+07	1.8E+09	2.9E+10	5.1E+09	1.9E+09	5.6E+08	2.2E+07	4.7E+06	2.4E+05	6.8E+04	4.4E+03															
5					8B		10B	11B	12B	13B	14B	15B	17B																	
					4.2E+08		3.0E+10	3.4E+10	3.1E+08	2.0E+07	1.3E+06	1.3E+05		8.4E+02																
4				6Be	7Be		9Be	10Be	11Be	12Be		14Be																		
				2.2E+06	1.1E+10		7.4E+09	4.6E+09	1.1E+07	1.0E+06		3.0E+03																		
3				6Li	7Li		8Li	9Li		11Li	12Li																			
				2.5E+10	1.8E+10	1.4E+09	1.8E+08			1.3E+04	6.8E+01																			
2		3He	4He		6He		8He																							
		5.0E-10	6.6E+11		1.3E+10		2.7E+08																							
1	1H	2H	3H																											
	6.6E+11	2.2E+11	6.9E+10																											

Table A.4.2: Isotope production cross sections for the element Ti, in mb, when bombarding it with 1.4 GeV protons. Simulation done with ABRABLA07v5 with $1 \cdot 10^9$ events, accounting all Ti isotopes and respective ratios.

Z/N	0	1	2	3	4	5	6	7	8	9	10	11	12	13	14	15	16	17	18	19	20	21	22	23	24	25	26	27	28
22																		39Ti	40Ti	41Ti	42Ti	43Ti	44Ti	45Ti	46Ti	47Ti	48Ti	49Ti	
																		7.1E-07	6.6E-06	2.9E-04	3.9E-03	9.5E-02	3.4E+00	7.6E+00	2.0E+01	2.0E+01	3.2E+00	1.2E+00	
21																	37Sc	38Sc	39Sc	40Sc	41Sc	42Sc	43Sc	44Sc	45Sc	46Sc	47Sc	48Sc	49Sc	49Sc
																	8.2E-07	1.1E-05	1.3E-04	4.7E-03	7.7E-02	1.4E+00	1.2E+01	2.0E+01	3.0E+01	2.0E+01	2.1E+01	1.7E+00	1.1E+00
20																	35Ca	36Ca	37Ca	38Ca	39Ca	40Ca	41Ca	42Ca	43Ca	44Ca	45Ca	46Ca	47Ca	48Ca
																	2.2E-06	3.5E-05	1.4E-03	2.2E-02	4.7E-01	9.9E+00	1.7E+01	3.6E+01	1.7E+01	2.0E+01	3.9E+00	2.5E+00	1.6E-01	6.4E-02
19																	34K	35K	36K	37K	38K	39K	40K	41K	42K	43K	44K	45K	46K	47K
																	2.5E-05	4.2E-04	1.3E-02	2.7E-01	3.9E+00	2.2E+01	2.0E+01	6.0E+00	3.3E+00	6.1E-01	2.0E-01	1.4E-02	4.7E-03
18													31Ar	32Ar	33Ar	34Ar	35Ar	36Ar	37Ar	38Ar	39Ar	40Ar	41Ar	42Ar	43Ar	44Ar	45Ar	46Ar		
													9.0E-07	3.6E-05	1.4E-03	2.5E-02	6.7E-01	1.4E+01	2.2E+01	4.0E+01	1.1E+01	7.4E+00	1.2E+00	4.8E-01	5.8E-02	1.7E-02	1.1E-03	3.2E-04	
17													30Cl	31Cl	32Cl	33Cl	34Cl	35Cl	36Cl	37Cl	38Cl	39Cl	40Cl	41Cl	42Cl	43Cl	44Cl	45Cl		
													9.0E-06	2.7E-04	1.0E-02	2.5E-01	3.4E+00	1.9E+01	1.5E+01	1.3E+01	3.6E+00	1.8E+00	2.7E-01	9.2E-02	7.6E-03	1.9E-03	1.0E-04	3.5E-05	
16							27S	28S	29S	30S	31S	32S	33S	34S	35S	36S	37S	38S	39S	40S	41S	42S							
							4.9E-07	3.1E-05	9.1E-04	1.9E-02	4.0E-01	7.7E+00	1.2E+01	2.3E+01	6.4E+00	5.7E+00	6.0E-01	2.5E-01	2.9E-02	8.2E-03	4.8E-04	1.1E-04	1.7E-06	2.1E-07					
15							26P		28P	29P	30P	31P	32P	33P	34P	35P	36P	37P	38P	39P	40P	41P							
							2.5E-06		4.7E-03	2.6E-01	2.1E+00	1.0E+01	6.3E+00	6.2E+00	1.6E+00	8.2E-01	1.0E-01	3.7E-02	3.0E-03	1.0E-03	1.4E-05							
14					23Si	24Si	25Si	26Si	27Si	28Si	29Si	30Si	31Si	32Si	33Si	34Si	35Si	36Si	37Si	38Si	39Si								
					2.5E-07	1.6E-05	6.6E-04	6.1E-02	6.9E-01	1.1E+01	9.1E+00	1.2E+01	2.1E+00	2.0E+00	2.0E-01	8.5E-02	9.2E-03	2.4E-03	1.6E-04	2.5E-05	5.8E-07	1.1E-07							
13					21Al	22Al	23Al	24Al	25Al	26Al	27Al	28Al	29Al	30Al	31Al	32Al	33Al	34Al	35Al	36Al	37Al								
					2.5E-06	1.1E-04	1.6E-03	2.7E-02	1.0E+00	3.4E+00	9.7E+00	2.6E+00	2.1E+00	4.5E-01	2.3E-01	2.7E-02	9.4E-03	7.9E-04	3.5E-04	1.2E-05	3.5E-06							
12					20Mg	21Mg	22Mg	23Mg	24Mg	25Mg	26Mg	27Mg	28Mg	29Mg	30Mg	31Mg	32Mg	33Mg	34Mg	35Mg	36Mg								
					1.4E-05	6.8E-04	1.3E-02	2.9E-01	3.4E+00	2.4E+00	2.8E+00	4.9E-01	1.8E-01	2.0E-02	6.9E-03	1.1E-03	2.3E-04	2.3E-05	1.5E-06	5.2E-08	5.2E-08							
11						20Na	21Na	22Na	23Na	24Na	25Na	26Na	27Na	28Na	29Na	30Na	31Na	32Na	33Na										
						5.6E-03	1.4E-01	1.9E+00	3.2E+00	1.2E+00	6.1E-01	1.4E-01	3.4E-02	4.0E-03	7.1E-04	1.1E-04	3.2E-05	1.1E-06	8.9E-07										
10					17Ne	18Ne	19Ne	20Ne	21Ne	22Ne	23Ne	24Ne	25Ne	26Ne	27Ne	28Ne	29Ne	30Ne											
					1.7E-04	5.5E-03	9.6E-02	2.3E+00	2.4E+00	1.8E+00	2.3E-01	8.9E-02	9.9E-03	1.7E-03	1.8E-04	2.6E-05	1.9E-06	7.9E-07											
9						17F	18F	19F	20F	21F	22F	23F	24F	25F	26F	27F													
						8.7E-02	8.1E-01	1.1E+00	7.4E-01	3.4E-01	8.1E-02	2.1E-02	2.2E-03	2.3E-04	2.0E-05	2.7E-06													
8					13O	14O	15O	16O	17O	18O	19O	20O	21O	22O	23O	24O													
					1.3E-04	1.7E-02	6.0E-01	4.1E+00	1.2E+00	5.3E-01	9.5E-02	4.1E-02	5.4E-03	1.2E-03	9.5E-05	5.4E-06													
7					12N	13N	14N	15N	16N	17N	18N	19N	20N	21N	22N	23N													
					5.9E-03	4.0E-01	4.1E+00	4.0E+00	3.6E-01	7.9E-02	1.0E-02	2.3E-03	2.7E-04	5.7E-05	2.8E-06	5.2E-08													
6			9C	10C	11C	12C	13C	14C	15C	16C	17C	18C	19C																
			3.1E-04	2.2E-02	5.2E-01	7.4E+00	2.9E+00	8.8E-01	3.4E-02	7.4E-03	3.7E-04	1.1E-04	6.8E-06															
5			8B		10B	11B	12B	13B	14B	15B	17B																		
			1.0E-02		1.8E+00	2.1E+00	2.2E-01	3.2E-02	2.0E-03	2.1E-04	1.3E-06																		
4			6Be	7Be	9Be	10Be	11Be	12Be		14Be																			
			1.1E-05	3.2E-01	7.3E-01	3.7E-01	8.5E-03	1.6E-03		4.7E-06																			
3			6Li	7Li	8Li	9Li		11Li	12Li																				
			2.5E+00	1.4E+00	1.9E-01	2.2E-02		2.0E-05	1.1E-07																				
2		3He	4He	6He		8He																							
		2.2E-01	3.8E-02	3.3E+00		6.6E-03																							
1	1H	2H	3H																										
	6.3E+02	1.6E+02	5.3E+01																										

Table A.4.3: Ratio between the isotope production cross sections, in a Ti target, of CERN (1.4 GeV protons) and TRIUMF (500 MeV protons). Simulations done with ABRABLA07v5 with $1 \cdot 10^9$ events, accounting all Ti isotopes and respective ratios. On the table, "only T" and "only C" represents only produced at TRIUMF and only produced at CERN, respectively. However these cases are towards zones with very low production cross sections and subject to high errors.

22																		39Ti	40Ti	41Ti	42Ti	43Ti	44Ti	45Ti	46Ti	47Ti	48Ti	49Ti	
																		0.58	1.77	1.58	1.14	0.91	0.81	0.80	0.79	0.79	0.78	0.78	
21																	37Sc	38Sc	39Sc	40Sc	41Sc	42Sc	43Sc	44Sc	45Sc	46Sc	47Sc	48Sc	49Sc	
																	9.94	0.73	2.06	1.59	1.11	0.94	0.84	0.81	0.80	0.79	0.79	0.78	0.78
20																35Ca	36Ca	37Ca	38Ca	39Ca	40Ca	41Ca	42Ca	43Ca	44Ca	45Ca	46Ca	47Ca	48Ca
																4.51	2.34	2.21	1.69	1.39	1.06	0.98	0.88	0.86	0.82	0.83	0.81	0.82	0.81
19																34K	35K	36K	37K	38K	39K	40K	41K	42K	43K	44K	45K	46K	47K
																2.06	1.97	2.09	1.71	1.46	1.20	1.09	0.99	0.96	0.95	0.97	1.01	1.06	1.08
18														31Ar	32Ar	33Ar	34Ar	35Ar	36Ar	37Ar	38Ar	39Ar	40Ar	41Ar	42Ar	43Ar	44Ar	45Ar	46Ar
														2.73	1.63	2.09	1.97	1.88	1.66	1.54	1.31	1.25	1.13	1.17	1.19	1.34	1.47	1.71	1.70
17														30Cl	31Cl	32Cl	33Cl	34Cl	35Cl	36Cl	37Cl	38Cl	39Cl	40Cl	41Cl	42Cl	43Cl	44Cl	45Cl
														1.96	1.65	1.91	1.93	1.87	1.76	1.70	1.56	1.51	1.48	1.51	1.54	1.84	2.11	3.22	4.72
16													27S	28S	29S	30S	31S	32S	33S	34S	35S	36S	37S	38S	39S	40S	41S	42S	43S	44S
													0.74	1.41	1.81	1.88	1.90	1.87	1.87	1.80	1.79	1.70	1.78	1.82	2.04	1.99	2.55	2.23	4.68	2.00
15													26P		28P	29P	30P	31P	32P	33P	34P	35P	36P	37P	38P	39P	40P	41P	42P	43P
													1.01		1.65	1.83	1.84	1.87	1.87	1.88	1.91	1.95	1.99	2.10	2.33	2.76	2.69	3.32	only T	only C
14												23Si	24Si	25Si	26Si	27Si	28Si	29Si	30Si	31Si	32Si	33Si	34Si	35Si	36Si	37Si	38Si	39Si	40Si	
												0.75	0.99	1.48	1.72	1.74	1.81	1.83	1.86	1.88	1.90	1.99	2.11	2.54	2.29	2.91	2.06	3.74	only C	
13										21Al	22Al	23Al	24Al	25Al	26Al	27Al	28Al	29Al	30Al	31Al	32Al	33Al	34Al	35Al	36Al	37Al				
										1.87	1.41	1.36	1.51	1.65	1.68	1.75	1.77	1.81	1.86	1.93	1.92	1.98	1.93	2.97	2.19	3.10			
12										20Mg	21Mg	22Mg	23Mg	24Mg	25Mg	26Mg	27Mg	28Mg	29Mg	30Mg	31Mg	32Mg	33Mg	34Mg	35Mg	36Mg				
										0.87	1.18	1.38	1.52	1.61	1.64	1.69	1.71	1.73	1.74	1.82	2.35	1.78	3.71	1.84	1.00	only C				
11											20Na	21Na	22Na	23Na	24Na	25Na	26Na	27Na	28Na	29Na	30Na	31Na	32Na	33Na						
											1.33	1.49	1.53	1.56	1.57	1.60	1.61	1.68	1.56	1.39	1.15	1.95	0.68	17.23						
10									17Ne	18Ne	19Ne	20Ne	21Ne	22Ne	23Ne	24Ne	25Ne	26Ne	27Ne	28Ne	29Ne	30Ne								
									1.34	1.35	1.44	1.49	1.49	1.51	1.50	1.50	1.45	1.41	1.64	1.28	1.59	7.62							
9										17F	18F	19F	20F	21F	22F	23F	24F	25F	26F	27F									
										1.40	1.43	1.43	1.40	1.37	1.36	1.37	1.25	1.12	0.85	1.45									
8							13O	14O	15O	16O	17O	18O	19O	20O	21O	22O	23O	24O												
							1.05	1.26	1.37	1.42	1.40	1.34	1.29	1.23	1.18	1.11	1.41	0.44												
7							12N	13N	14N	15N	16N	17N	18N	19N	20N	21N	22N	23N												
							1.13	1.30	1.34	1.36	1.32	1.17	1.09	0.96	0.86	0.81	0.54	0.50												
6				9C	10C	11C	12C	13C	14C	15C	16C	17C	18C	19C	20C															
				1.21	1.14	1.17	1.29	1.29	1.25	1.15	1.03	0.88	0.74	0.95	only T															
5				8B		10B	11B	12B	13B	14B	15B		17B		19B															
				1.11		1.22	1.16	1.11	0.94	0.82	0.66		0.56		only T															
4			6Be	7Be		9Be	10Be	11Be	12Be		14Be		16Be																	
			0.52	1.14		1.22	1.14	1.02	0.88		0.61		only T																	
3				6Li	7Li	8Li	9Li		11Li	12Li																				
				1.28	1.19	1.13	0.98		0.72	0.09																				
2		3He	4He		6He		8He																							
		1.43	1.35		1.28		0.54																							
1	1H	2H	3H																											
	1.33	1.44	1.44																											
Z/N	0	1	2	3	4	5	6	7	8	9	10	11	12	13	14	15	16	17	18	19	20	21	22	23	24	25	26	27	28	

Table A.4.4: Isotope production cross sections in C, in mb, when bombarding it with 1.4 GeV protons. Simulation done with ABRABLA07v5 with $1 \cdot 10^9$ events, accounting both C isotopes and respective ratios.

6				9C	10C	11C	12C	
				2.9E-02	9.7E-01	1.6E+01	2.3E-01	
5				8B		10B	11B	12B
				2.2E-01		1.6E+01	1.8E+01	9.1E-02
4			6Be	7Be		9Be	10Be	11Be
			1.2E-03	5.8E+00		3.8E+00	2.4E+00	3.2E-03
3				6Li	7Li	8Li	9Li	
				1.3E+01	9.2E+00	6.8E-01	9.2E-02	
2		3He	4He		6He		8He	
		1.9E+01	2.3E+02		6.0E+00		1.4E-01	
1	1H	2H	3H					
	1.4E+02	6.7E+01	1.9E+01					
Z/N	0	1	2	3	4	5	6	7

Table A.4.5: Ratio between the isotope production cross sections, in a C target, at CERN (1.4 GeV protons) and at TRIUMF (500 MeV protons). Simulations done with ABRABLA07v5 with $1 \cdot 10^9$ events, accounting for both C isotopes and respective ratios.

6				9C	10C	11C	12C	
				1.20	1.20	1.20	1.19	
5				8B		10B	11B	12B
				1.20		1.20	1.20	1.19
4			6Be	7Be		9Be	10Be	11Be
			1.20	1.20		1.20	1.20	1.19
3				6Li	7Li	8Li	9Li	
				1.20	1.20	1.20	1.19	
2		3He	4He		6He		8He	
		1.20	1.20		1.20		1.20	
1	1H	2H	3H					
	1.20	1.20	1.20					
Z/N	0	1	2	3	4	5	6	7

B TiC-MWCNT - carbothermal reduction from TiO_2 and MWCNT

In order to develop a better quality TiC-MWCNT nanocomposite, a CERN Summer Student Project was submitted and approved by CERN and a graduate student, Silvain Badie, was hired for 2 months and supervised by J.P. Ramos (the thesis author) and T. Stora [143]. In this study a processing route was developed TiC-MWCNT which was produced from the carbothermal reduction of the TiO_2, through the reaction: $TiO_2 + 4C \rightarrow TiC + C + 2CO$ (g). Further characterization was carried after the project concluded in order to characterize the phase composition, morphology, crystallite size and SSA of the new composites, since only densities were determined.

The starting powder was the Sigma Aldrich TiO_2 used[1] in section 3.1, page 62 which was suspended in IPA with a liquid:solid volume ratio of 12 for milling. Systematic milling studies were done in order to find the best milling conditions in a *Fristsch Pulverisette 6* high energy planetary mill in a 250 ml WC grinding bowl with 95 g of WC balls. The final conditions chosen for the milling were 600 rpm for 56 min. MWCNT were suspended in IPA with a liquid:solid volume ratio of 720 (assuming graphite density for MWCNT) and sonicated with agitation for 30 min. After, the milled slurry of TiO_2 was added to the MWCNT suspension and left under agitation and sonication for another hour. The suspension was dried, deagglomerated and dry pressed in cylindrical compacts of 15 mm of diameter and 2 mm of thickness at 111 MPa. The obtained pellets were thermally treated at 1700 and 2100 °C for 1 h and 2100 °C for 15 h in Oven B, to assess thermal stability of the nanocomposite.

After all thermal treatments no more TiO_2 was detected in the XRPD diffractograms, where during the heating ramp the carbothermal reduction was noticed (from the pressure evolution) to start around 1200 °C and finish before 1600 °C. The results for the as produced and thermally treated samples, in terms of SSA, ρ and ρ_r and XRPD determined crystallite size are presented on table B.1 and respective microstructures can be seen on figure B.1.

As it can be seen, from table B.1 there is a large reduction of SSA from the as produced material

[1] Another TiO_2 raw material was tried, but yielded very similar results, which are not presented here. For more information refer to [143]

Table B.1 – SSA, density and XRPD crystallite size of the as produced samples and thermally treated at 1700 °C for 1 h and at 2100 °C for 1 and 15 h.

Sample	SSA $m^2 g^{-1}$	ρ (ρ_r) [a] $g cm^{-3}$	Crystallite size nm	$\Delta m/m_0$ %
As produced	138.9	0.71 (23 %)	22	
1700 °C - 1 h	81.8	0.65 (16 %)	121	43.5
2100 °C - 1 h	75.0	0.66 (16 %)	102	43.0
2100 °C - 15 h	62.9	0.66 (16 %)	132	43.8

[a] Assuming theoretical density of 4.93 $g cm^{-3}$ for TiC [35] and graphite density, 2.16 $g cm^{-3}$ [35], for MWCNT.

to the 1700 °C thermal treatment, likely due to the consumption of C from CNT to form TiC. There are SSA changes during the heat treatments at 2100 °C (1 and 15 h) but they are not drastic, where XRDP crystallite size is also not changing much (table B.1).

Furthermore the mass losses of ≈ 43 – 44 %, seen on table B.1 for the thermally treated samples, are matching the predicted mass losses for the carbothermal reduction of TiO_2 into TiC, which is 43.8 %. The relative densities on table B.1 were calculated are very low (16 %), and completely stable at high temperatures. The stability of the nanometric TiC is also seen on the SEM pictures of figure B.1b, c and d, where in all thermal treatments there is barely any significant change in the TiC.

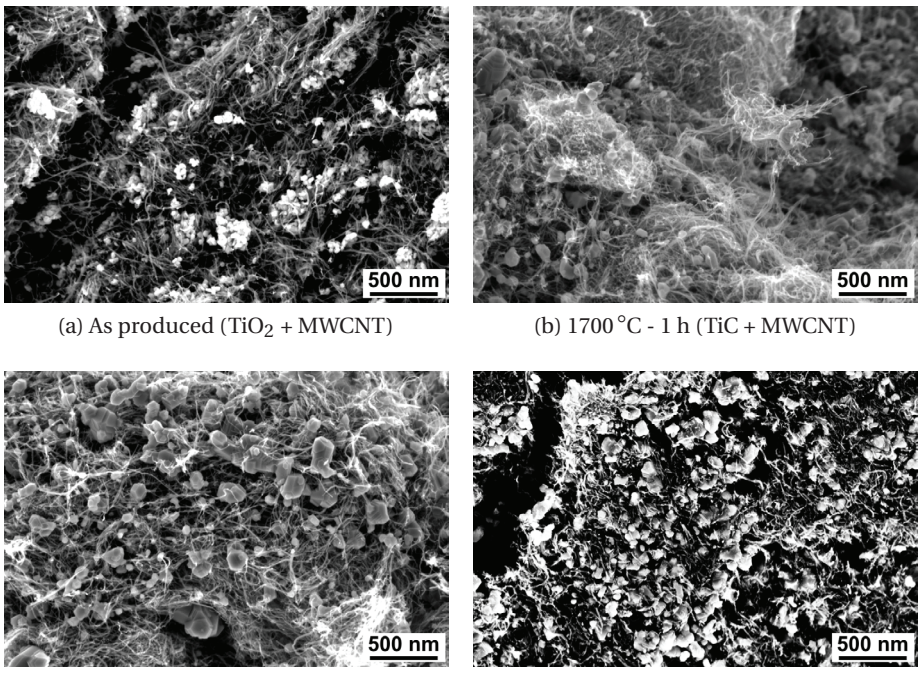

(a) As produced (TiO_2 + MWCNT) (b) 1700 °C - 1 h (TiC + MWCNT)

(c) 2100 °C - 1 h (TiC + MWCNT) (d) 2100 °C - 15 h (TiC + MWCNT)

Figure B.1 – SEM microstructures of the as produced TiO_2 + MWCNT and resulting microstructures after thermal treatments (TiC + MWCNT) at 1700 °C and at 2100 °C for 1 h and 15 h.

The results from this study are very promising, where nanometric TiC is stabilized up to 2100 °C and very likely also at even higher temperatures. As seen from the article included in the section 3.3, table 3 (page 102), the 75CNTb thermally treated 1800 °C for 10 h has an SSA of 12.0 $m^2 g^{-1}$ and a density of 2.70 $g cm^{-3}$. The much lower density can be very beneficial for effusion due to the larger mean free path for the isotopes. However due to lower density the mass of Ti target thickness will also be lower, which will reduce the Y_{Prod}. But as described in 1.3.3 (30), nanomaterials have often lower target thicknesses but bring higher yields, thus this material needs to be tested online. In any case this target will be able to operate at higher temperatures which can bring increases in the yields due to the Arrhenius dependence of diffusion and effusion on temperature - equations 1.5 (page 27) and 1.8 (page 29), respectivelly.

Bibliography

[1] Nucleonica GmbH, Karlsruhe Nuclide Chart Online, KNCO++, Nucleonica Nuclear Science Portal (www.nucleonica.com), Version 3.0.65.0001, Karlsruhe (2014).

[2] International Union of Pure and Applied Chemistry, IUPAC is naming the four new elements nihonium, moscovium, tennessine, and oganesson (Jun 2016).
URL https://iupac.org/iupac-is-naming-the-four-new-elements-nihonium-moscovium-tennessine-and-oganesson/

[3] R. A. Serway, C. J. Moses, C. A. Moyer, Modern Physics, 3rd Edition, Thompson Learning, Belmont, 2005.

[4] CERN, About CERN, Accessed on 19-08-2016.
URL http://www.cern.ch/about

[5] ISOLDE-CERN, The ISOLDE facility website, Accessed on 19-08-2016.
URL http://isolde.web.cern.ch

[6] M. Borge, Highlights of the ISOLDE facility and the HIE-ISOLDE project, Nuclear Instruments and Methods in Physics Research Section B: Beam Interactions with Materials and Atoms 376 (2016) 408–412. doi:10.1016/j.nimb.2015.12.048.

[7] G. Friedlander, J. W. Kennedy, E. S. Macias, J. M. Miller, Nuclear and Radiochemistry, 3rd Edition, John Wiley & Sons, New York, 1981.

[8] G. R. Gilmore, Practical Gamma-ray Spectrometry, 2nd Edition, John Wiley & Sons, Ltd., Warrington, UK, 2008.

[9] M. Huyse, The Why and How of Radioactive-Beam Research, in: J. Al-Khalili, E. Roeckl (Eds.), The Euroschool Lectures on Physics with Exotic Beams, Vol. I, Vol. 651 of Lecture Notes in Physics, Springer Berlin Heidelberg, Berlin, Heidelberg, 2004, Ch. 651, pp. 1–32. doi:10.1007/978-3-540-44490-9_1.

[10] Y. Blumenfeld, T. Nilsson, P. Van Duppen, Facilities and methods for radioactive ion beam production, Physica Scripta T152 (2013) 014023. doi:10.1088/0031-8949/2013/T152/014023.

[11] B. Jonson, K. Riisager, The ISOLDE facility, Scholarpedia 5 (7) (2010) 9742, revision #90796. doi:10.4249/scholarpedia.9742.

[12] U. Wahl, Materials science and biophysics applications at the ISOLDE radioactive ion beam facility, Nuclear Instruments and Methods in Physics Research Section B: Beam Interactions with Materials and Atoms 269 (24) (2011) 3014–3020. doi:10.1016/j.nimb.2011.04.082.

[13] W. Chou, Spallation Neutron Source and Other High Intensity Proton Sources, in: A. W. Chao, H. O. Moser, Z. Zhao (Eds.), Accelerator Physics, Technology and Applications - Selected Lectures of OCPA International Accelerator School 2002, Singapore, World Scientific Publishing Co. Pte. Ltd., Toh Tuck, 2004, pp. 231–255.

[14] J. Wei, H. Chen, Y. Chen, Y. Chen, Y. Chi, C. Deng, H. Dong, L. Dong, S. Fang, J. Feng, S. Fu, L. He, W. He, Y. Heng, K. Huang, X. Jia, W. Kang, X. Kong, J. Li, T. Liang, G. Lin, Z. Liu, H. Ouyang, Q. Qin, H. Qu, C. Shi, H. Sun, J. Tang, J. Tao, C. Wang, F. Wang, D. Wang, Q. Wang, S. Wang, T. Wei, J. Xi, T. Xu, Z. Xu, W. Yin, X. Yin, J. Zhang, Z. Zhang, Z. Zhang, M. Zhou, T. Zhu, China Spallation Neutron Source: Design, R&D, and outlook, Nuclear Instruments and Methods in Physics Research, Section A: Accelerators, Spectrometers, Detectors and Associated Equipment 600 (1) (2009) 10–13. doi:10.1016/j.nima.2008.11.017.

[15] P. V. Duppen, Isotope Separation On Line and Post Acceleration, The Euroschool Lectures on Physics with Exotic Beams, Vol. II 700 (2006) 37–77. doi:10.1007/3-540-33787-3_2.

[16] M. Thoennessen, Fusion-Evaporation Reactions, in: The Discovery of Isotopes, Springer International Publishing, Cham, 2016, pp. 197–226. doi:10.1007/978-3-319-31763-2_11.

[17] O. Kofoed-Hansen, K. O. Nielsen, Short-lived krypton isotopes and their daughter substances [41], Physical Review 82 (1) (1951) 96–97. doi:10.1103/PhysRev.82.96.2.

[18] M. Borge, M. Kowalska, T. Stora, Motivations to receive a 2 GeV proton beam at ISOLDE / HIE-ISOLDE: Impact on radioisotope beam availability and physics program, Tech. rep., CERN, Geneva, ISOLDE and neutron Time-of-Flight Experiments Committee; INTC (2012).
URL https://cds.cern.ch/record/1482729?ln=en

[19] P. Jardin, O. Bajeat, P. Delahaye, M. Dubois, R. Frigot, V. Kuchi, C. Leboucher, L. Maunoury, New target ion source systems at GANIL/SPIRAL1: Prospective, Nuclear Instruments and Methods in Physics Research Section B: Beam Interactions with Materials and Atoms 376 (2016) 64–67. doi:10.1016/j.nimb.2016.03.020.

[20] A. Gottberg, Target materials for exotic ISOL beams, Nuclear Instruments and Methods in Physics Research Section B: Beam Interactions with Materials and Atomsdoi:10.1016/j.nimb.2016.01.020.

[21] H. J. Woo, B. H. Kang, K. Tshoo, C. S. Seo, W. Hwang, Y. H. Park, J. W. Yoon, S. H. Yoo, Y. K. Kim, D. Y. Jang, Overview of the ISOL facility for the RISP, Journal of the Korean Physical Society 66 (3) (2015) 443–448. doi:10.3938/jkps.66.443.

[22] E. Kugler, The ISOLDE facility, Hyperfine Interactions 129 (2000) 23–42. doi:10.1023/A:1012603025802.

[23] F. Wienholtz, D. Beck, K. Blaum, C. Borgmann, M. Breitenfeldt, R. B. Cakirli, S. George, F. Herfurth, J. D. Holt, M. Kowalska, S. Kreim, D. Lunney, V. Manea, J. Menéndez, D. Neidherr, M. Rosenbusch, L. Schweikhard, a. Schwenk, J. Simonis, J. Stanja, R. N. Wolf, K. Zuber, Masses of exotic calcium isotopes pin down nuclear forces., Nature 498 (7454) (2013) 346–9. doi:10.1038/nature12226.

[24] S. Rothe, a. N. Andreyev, S. Antalic, a. Borschevsky, L. Capponi, T. E. Cocolios, H. De Witte, E. Eliav, D. V. Fedorov, V. N. Fedosseev, D. a. Fink, S. Fritzsche, L. Ghys, M. Huyse, N. Imai, U. Kaldor, Y. Kudryavtsev, U. Köster, J. F. W. Lane, J. Lassen, V. Liberati, K. M. Lynch, B. a. Marsh, K. Nishio, D. Pauwels, V. Pershina, L. Popescu, T. J. Procter, D. Radulov, S. Raeder, M. M. Rajabali, E. Rapisarda, R. E. Rossel, K. Sandhu, M. D. Seliverstov, a. M. Sjödin, P. Van den Bergh, P. Van Duppen, M. Venhart, Y. Wakabayashi, K. D. a. Wendt, Measurement of the first ionization potential of astatine by laser ionization spectroscopy., Nature communications 4 (May) (2013) 1835. doi:10.1038/ncomms2819.

[25] L. P. Gaffney, P. A. Butler, M. Scheck, A. B. Hayes, F. Wenander, M. Albers, B. Bastin, C. Bauer, A. Blazhev, S. Bönig, N. Bree, J. Cederkäll, T. Chupp, D. Cline, T. E. Cocolios, T. Davinson, H. De Witte, J. Diriken, T. Grahn, A. Herzan, M. Huyse, D. G. Jenkins, D. T. Joss, N. Kesteloot, J. Konki, M. Kowalczyk, T. Kröll, E. Kwan, R. Lutter, K. Moschner, P. Napiorkowski, J. Pakarinen, M. Pfeiffer, D. Radeck, P. Reiter, K. Reynders, S. V. Rigby, L. M. Robledo, M. Rudigier, S. Sambi, M. Seidlitz, B. Siebeck, T. Stora, P. Thoele, P. Van Duppen, M. J. Vermeulen, M. von Schmid, D. Voulot, N. Warr, K. Wimmer, K. Wrzosek-Lipska, C. Y. Wu, M. Zielinska, Studies of pear-shaped nuclei using accelerated radioactive beams., Nature 497 (7448) (2013) 199–204. doi:10.1038/nature12073.
URL http://dx.doi.org/10.1038/nature12073

[26] Y. Kadi, Y. Blumenfeld, R. Catherall, W. D. Venturini, M. J. G. Borge, M. Huyse, P. V. Duppen, HIE-ISOLDE: The future of radioactive beam physics at CERN, in: Challenges and Goals for Accelerators in the XXI Century, WORLD SCIENTIFIC, 2016, pp. 585–610. doi:10.1142/9789814436403_0031.

[27] R. dos Santos Augusto, L. Buehler, Z. Lawson, S. Marzari, M. Stachura, T. Stora, E. CERN-MEDICIS collaboration, CERN-MEDICIS (Medical Isotopes Collected from ISOLDE): A New Facility, Applied Sciences 4 (2) (2014) 265–281. doi:10.3390/app4020265.

[28] R. Catherall, J. Lettry, S. Gilardoni, U. Köster, Radioactive ion beams produced by neutron-induced fission at ISOLDE, Nuclear Instruments and Methods in Physics Research Section B: Beam Interactions with Materials and Atoms 204 (2003) 235–239. doi:10.1016/S0168-583X(02)01915-8.

[29] R. Luis, J. G. Marques, T. Stora, P. Vaz, L. Zanini, Optimization studies of the CERN-ISOLDE neutron converter and fission target system, The European Physical Journal A 48 (6) (2012) 90. doi:10.1140/epja/i2012-12090-9.

[30] A. Gottberg, T. Mendonca, R. Luis, J. Ramos, C. Seiffert, S. Cimmino, S. Marzari, B. Crepieux, V. Manea, R. Wolf, F. Wienholtz, S. Kreim, V. Fedosseev, B. Marsh, S. Rothe, P. Vaz, J. Marques, T. Stora, Experimental tests of an advanced proton-to-neutron converter at ISOLDE-CERN, Nuclear Instruments and Methods in Physics Research Section B: Beam Interactions with Materials and Atoms 336 (2014) 143–148. doi:10.1016/j.nimb.2014.04.026.

[31] T. Stora, E. Bouquerel, L. Bruno, R. Catherall, S. Fernandes, P. Kasprowicz, J. Lettry, S. Marzari, B. S. N. Singh, E. Noah, L. Penescu, R. Wilfinger, F. D. McDaniel, B. L. Doyle, Oxide Target Designs for High Primary Beam Intensities for Future Radioactive Ion Beam Facilities, in: AIP Conference Proceedings, Vol. 1099, AIP, 2009, pp. 764–768. doi:10.1063/1.3120150.

[32] A. Kjelberg, G. Rudstam, The ISOLDE isotope separator on-line facility at CERN, Tech. rep., CERN, Geneva (1970). doi:10.5170/CERN-1970-003.

[33] U. Köster, ISOLDE target and ion source chemistry, Radiochimica Acta 89 (2001) 749. doi:10.1524/ract.2001.89.11-12.749.
URL http://www.oldenbourg-link.com/doi/abs/10.1524/ract.2001.89.11-12.749

[34] ISOLDE-CERN, ISOLDE Yield Database.
URL http://test-isolde-yields.web.cern.ch/test-isolde-yields/query{_}tgt.htm

[35] D. R. Lide (Ed.), CRC Handbook of Chemistry and Physics, 90th Edition, CRC Press, 2010.

[36] J. Lettry, R. Catherall, G. Cyvoct, P. Drumm, A. Evensen, M. Lindroos, O. Jonsson, E. Kugler, J. Obert, J. Putaux, J. Sauvage, K. Schindl, H. Ravn, E. Wildner, Release from ISOLDE molten metal targets under pulsed proton beam conditions, Nuclear Instruments and Methods in Physics Research Section B: Beam Interactions with Materials and Atoms 126 (1-4) (1997) 170–175. doi:10.1016/S0168-583X(96)01088-9.

[37] H. Ravn, S. Sundell, L. Westgaard, New Molten-Metal Targets for ISOLDE, in: G. Anderson, G. Holmen (Eds.), Proceedings of the 8th International EMIS Conference on Low Energy Ion Accelerators and Mass Separators, Goteborg, Sweden, 1973, pp. 432–444.
URL https://cds.cern.ch/record/286598?ln=en

[38] T. M. Mendonça, R. Hodak, V. Ghetta, M. Allibert, D. Heuer, E. Noah, S. Cimmino, M. Delonca, A. Gottberg, M. Kronberger, J. P. J. Ramos, C. Seiffert, T. Stora, T. Mendonca, Production and release of ISOL beams from molten fluoride salt targets, Nuclear Instruments and Methods in Physics Research Section B: Beam Interactions with Materials and Atoms 329 (2014) 1–5. doi:10.1016/j.nimb.2014.03.003.

[39] M. Maiti, K. Ghosh, T. M. Mendonça, T. Stora, S. Lahiri, Comparison on the production of radionuclides in 1.4 GeV proton irradiated LBE targets of different thickness, Journal of Radioanalytical and Nuclear Chemistry 302 (2) (2014) 1003–1011. doi:10.1007/s10967-014-3636-6.

[40] E. Hagebø, P. Hoff, O. Jonsson, E. Kugler, J. Omtvedt, H. Ravn, K. Steffensen, New production systems at ISOLDE, Nuclear Instruments and Methods in Physics Research Section B: Beam Interactions with Materials and Atoms 70 (1-4) (1992) 165–174. doi:10.1016/0168-583X(92)95927-J.

[41] T. Bjørnstad, E. Hagebø, P. Hoff, O. Jonsson, E. Kugler, H. Ravn, S. Sundell, B. Vosicki, Recent development of high-temperature metal targets for ISOLDE, Nuclear Instruments and Methods in Physics Research Section B: Beam Interactions with Materials and Atoms 26 (1-3) (1987) 174–182. doi:10.1016/0168-583X(87)90747-6.

[42] U. Bergmann, L. Axelsson, J. Bennett, M. Borge, R. Catherall, P. Drumm, V. Fedoseyev, C. Forssén, L. Fraile, H. Fynbo, U. Georg, T. Giles, S. Grévy, P. Hornshøj, B. Jonson, O. Jonsson, U. Köster, J. Lettry, K. Markenroth, F. Marqués, V. Mishin, I. Mukha, T. Nilsson, G. Nyman, A. Oberstedt, H. Ravn, K. Riisager, G. Schrieder, V. Sebastian, H. Simon, O. Tengblad, F. Wenander, K. Wilhelmsen Rolander, Light exotic isotopes: recent beam developments and physics applications at ISOLDE, Nuclear Physics A 701 (1-4) (2002) 363–368. doi:10.1016/S0375-9474(01)01611-6.

[43] C. Seiffert, Production of radioactive molecular beams for CERN-ISOLDE, PhD Thesis, Technische universitat Darmstad (2015).
URL https://cds.cern.ch/record/2064456

[44] C. Seiffert, et al., Development of radioactive boron beams for CERN-ISOLDE, in preparation.

[45] J. Guillot, Synthèses et caractérisations de pastilles de carbure de lanthane, Tech. rep., INSTN/CERN-ISOLDE, Orsay/Geneva (2014).

[46] C. Guillot, et al., LaC_2-C nanocomposite targets for the production of neutron-deficient spallation products at CERN-ISOLDE, in preparation.

[47] L. Biasetto, P. Zanonato, S. Carturan, P. Di Bernardo, P. Colombo, A. Andrighetto, G. Prete, Lanthanum carbide-based porous materials from carburization of lanthanum oxide and lanthanum oxalate mixtures, Journal of Nuclear Materials 378 (2) (2008) 180–187. doi:10.1016/j.jnucmat.2008.06.016.

[48] T. Bjørnstad, E. Hagebø, P. Hoff, O. C. Jonsson, E. Kugler, H. L. Ravn, S. Sundell, B. Vosicki, t. I. Collaboration, Methods for Production of Intense Beams of Unstable Nuclei: New Developments at ISOLDE, Physica Scripta 34 (6A) (1986) 578–590. doi:10.1088/0031-8949/34/6A/013.

[49] S. Fernandes, Submicro- and Nano-Structured Porous Materials for Production of High-Intensity Exotic Radioactive Ion Beams, PhD Thesis, École polytechnique fédérale de Lausanne (2010). doi:10.5075/epfl-thesis-4813.
URL https://cds.cern.ch/record/1312950

[50] T. Stora, Recent developments of target and ion sources to produce ISOL beams, Nuclear Instruments and Methods in Physics Research, Section B: Beam Interactions with Materials and Atoms 317 (PART B) (2013) 402–410. doi:10.1016/j.nimb.2013.07.024.

[51] A. Gottberg, et al., Development and Online Tests of a Nano-Structured Uranium Carbide - MWCNT Composite for the Production of Rare Isotope Beams at ISOLDE-CERN, in preparation.

[52] T. Stora, E. Noah, R. Hodak, T. Y. Hirsh, M. Hass, V. Kumar, K. Singh, S. Vaintraub, P. Delahaye, H. Franberg-Delahaye, M.-G. Saint-Laurent, G. Lhersonneau, A high intensity 6He beam for the β-beam neutrino oscillation facility, EPL (Europhysics Letters) 98 (3) (2012) 32001. doi:10.1209/0295-5075/98/32001.

[53] H. Ravn, R. Catherall, J. Barker, P. Drumm, A. Evensen, E. Hagebø, P. Hoff, O. Jonsson, E. Kugler, J. Lettry, K. Steffensen, O. Tengblad, Bunched release of gases from oxide targets, Nuclear Instruments and Methods in Physics Research Section B: Beam Interactions with Materials and Atoms 126 (1-4) (1997) 176–181. doi:10.1016/S0168-583X(96)01091-9.

[54] J. Ramos, A. Gottberg, T. Mendonça, C. Seiffert, A. Senos, H. Fynbo, O. Tengblad, J. Briz, M. Lund, G. Koldste, M. Carmona-Gallardo, V. Pesudo, T. Stora, Intense 31–35Ar beams produced with a nanostructured CaO target at ISOLDE, Nuclear Instruments and Methods in Physics Research Section B: Beam Interactions with Materials and Atoms 320 (2014) 83–88. doi:10.1016/j.nimb.2013.12.009.

[55] J. Ramos, C. Fernandes, T. Stora, A. Senos, Sintering kinetics of nanometric calcium oxide in vacuum atmosphere, Ceramics International 41 (6) (2015) 8093–8099. doi:10.1016/j.ceramint.2015.03.007.

[56] J. Ramos, Materials Characterization Report #2 - Target #476a - Y_2O_3, Tech. rep., CERN, Geneva (2012).
URL https://edms.cern.ch/document/1245219/1

[57] J. Ramos, A. Gottberg, R. Augusto, T. Mendonca, K. Riisager, C. Seiffert, P. Bowen, A. Senos, T. Stora, Target nanomaterials at CERN-ISOLDE: synthesis and release data, Nuclear Instruments and Methods in Physics Research Section B: Beam Interactions with Materials and Atoms 376 (2016) 81–85. doi:10.1016/j.nimb.2016.03.003.

[58] U. Köster, U. Bergmann, D. Carminati, R. Catherall, J. Cederkäll, J. Correia, B. Crepieux, M. Dietrich, K. Elder, V. Fedoseyev, L. Fraile, S. Franchoo, H. Fynbo, U. Georg, T. Giles, A. Joinet, O. Jonsson, R. Kirchner, C. Lau, J. Lettry, H. Maier, V. Mishin, M. Oinonen,

K. Peräjärvi, H. Ravn, T. Rinaldi, M. Santana-Leitner, U. Wahl, L. Weissman, Oxide fiber targets at ISOLDE, Nuclear Instruments and Methods in Physics Research Section B: Beam Interactions with Materials and Atoms 204 (2003) 303–313. doi:10.1016/S0168-583X(03)00505-6.

[59] J. Lettry, R. Catherall, P. Drumm, P. Van Duppen, A. Evensen, G. Focker, A. Jokinen, O. Jonsson, E. Kugler, H. Ravn, Pulse shape of the ISOLDE radioactive ion beams, Nuclear Instruments and Methods in Physics Research Section B: Beam Interactions with Materials and Atoms 126 (1-4) (1997) 130–134. doi:10.1016/S0168-583X(96)01025-7.

[60] M. Delonca, Development of new target concepts for proton beams at CERN/ISOLDE, PhD Thesis, Université de Technologie Belfort-Montbéliard (2015).
URL https://cds.cern.ch/record/2230047

[61] T. Stora, S. Fernandes, S. Mathot, P. Bowen, Nanostructured Target for Isotope Production, Patent no. WO 2010/034364 A1, World Intellectual Property Organization (2010).

[62] P. Hoff, O. Jonsson, E. Kugler, H. Ravn, Release of nuclear reaction products from refractory compounds, Nuclear Instruments and Methods in Physics Research 221 (2) (1984) 313–329. doi:10.1016/0167-5087(84)90002-4.

[63] G. J. Dienes, A. C. Damask, Radiation Enhanced Diffusion in Solids, Journal of Applied Physics 29 (12) (1958) 1713. doi:10.1063/1.1723032.

[64] M. Dombsky, P. Bricault, P. Schmor, M. Lane, ISAC target operation with high proton currents, Nuclear Instruments and Methods in Physics Research Section B: Beam Interactions with Materials and Atoms 204 (2003) 191–196. doi:10.1016/S0168-583X(02)01902-X.

[65] M. Dombsky, P. Bricault, V. Hanemaayer, Increasing beam currents at the TRIUMF-ISAC Facility; techniques and experiences, Nuclear Physics A 746 (2004) 32–39. doi:10.1016/j.nuclphysa.2004.09.060.

[66] E. Bouquerel, R. Catherall, M. Eller, J. Lettry, S. Marzari, T. Stora, Beam purification by selective trapping in the transfer line of an ISOL target unit, Nuclear Instruments and Methods in Physics Research Section B: Beam Interactions with Materials and Atoms 266 (19-20) (2008) 4298–4302. doi:10.1016/j.nimb.2008.05.060.

[67] E. Bouquerel, Atomic Beam Merging and Suppression of Alkali Contaminants in Multi Body High Power Targets: Design and Test of Target and Ion Source Prototypes at ISOLDE, PhD Thesis, Université Paris XI, CERN-THESIS-2010-057 (2009).
URL http://cds.cern.ch/record/1259908

[68] T. Stora, Radioactive Ion Sources, in: R. Bailey (Ed.), CAS - CERN Accelerator School, Ion Sources, Senec, Slovakia, 2013, pp. 331–349. doi:10.5170/CERN-2013-007.

[69] M. Kronberger, A. Gottberg, T. Mendonca, J. P. J. Ramos, C. Seiffert, P. Suominen, T. Stora, G. Alexander, T. M. Mendonça, Production of molecular sideband radioisotope beams at CERN-ISOLDE using a Helicon-type plasma ion source, Nuclear Instruments and Methods in Physics Research Section B: Beam Interactions with Materials and Atoms 317 (2013) 438–441. doi:10.1016/j.nimb.2013.07.032.

[70] R. Kirchner, On the thermoionization in hot cavities, Nuclear Instruments and Methods in Physics Research Section A: Accelerators, Spectrometers, Detectors and Associated Equipment 292 (2) (1990) 203–208. doi:10.1016/0168-9002(90)90377-I.

[71] U. Köster, Resonance ionization laser ion sources, Nuclear Physics A 701 (1-4) (2002) 441–451. doi:10.1016/S0375-9474(01)01625-6.

[72] M. Menna, R. Catherall, J. Lettry, E. Noah, T. Stora, R&D for the development of negative ion beams of halogens, Nuclear Instruments and Methods in Physics Research Section B: Beam Interactions with Materials and Atoms 266 (19-20) (2008) 4391–4393. doi:10.1016/j.nimb.2008.05.064.

[73] S. Rothe, T. Day Goodacre, D. Fedorov, V. Fedosseev, B. Marsh, P. Molkanov, R. Rossel, M. Seliverstov, M. Veinhard, K. Wendt, Laser ion beam production at CERN-ISOLDE: New features – More possibilities, Nuclear Instruments and Methods in Physics Research Section B: Beam Interactions with Materials and Atoms 376 (2016) 91–96. doi:10.1016/j.nimb.2016.02.024.

[74] D. Fink, S. Richter, B. Bastin, K. Blaum, R. Catherall, T. Cocolios, D. Fedorov, V. Fedosseev, K. Flanagan, L. Ghys, A. Gottberg, N. Imai, T. Kron, N. Lecesne, K. Lynch, B. Marsh, T. Mendonca, D. Pauwels, E. Rapisarda, J. Ramos, R. Rossel, S. Rothe, M. Seliverstov, M. Sjödin, T. Stora, C. Van Beveren, K. Wendt, First application of the Laser Ion Source and Trap (LIST) for on-line experiments at ISOLDE, Nuclear Instruments and Methods in Physics Research Section B: Beam Interactions with Materials and Atoms 317 (2013) 417–421. doi:10.1016/j.nimb.2013.06.039.

[75] D. Fink, S. Richter, K. Blaum, R. Catherall, B. Crepieux, V. Fedosseev, A. Gottberg, T. Kron, B. Marsh, C. Mattolat, S. Raeder, R. Rossel, S. Rothe, F. Schwellnus, M. Seliverstov, M. Sjödin, T. Stora, P. Suominen, K. Wendt, On-line implementation and first operation of the Laser Ion Source and Trap at ISOLDE/CERN, Nuclear Instruments and Methods in Physics Research Section B: Beam Interactions with Materials and Atoms 344 (2015) 83–95. doi:10.1016/j.nimb.2014.12.007.

[76] S. Rothe, R. Catherall, B. Crepieux, T. Day Goodacre, V. Fedosseev, T. Giles, B. Marsh, J. Ramos, R. Rossel, Advances in surface ion suppression from RILIS: Towards the Time-of-Flight Laser Ion Source (ToF-LIS), Nuclear Instruments and Methods in Physics Research Section B: Beam Interactions with Materials and Atoms 376 (2016) 86–90. doi:10.1016/j.nimb.2016.02.060.

[77] R. Kirchner, E. Roeckl, Investigation of small-volume gaseous discharge ion sources for isotope separation on-line, Nuclear Instruments and Methods 131 (2) (1975) 371–374. doi:10.1016/0029-554X(75)90342-0.

[78] L. Penescu, R. Catherall, J. Lettry, T. Stora, Development of high efficiency Versatile Arc Discharge Ion Source at CERN ISOLDE., The Review of scientific instruments 81 (2) (2010) 02A906. doi:10.1063/1.3271245.

[79] T. Day Goodacre, J. Billowes, R. Catherall, T. Cocolios, B. Crepieux, D. Fedorov, V. Fedosseev, L. Gaffney, T. Giles, A. Gottberg, K. Lynch, B. Marsh, T. Mendonça, J. Ramos, R. Rossel, S. Rothe, S. Sels, C. Sotty, T. Stora, C. Van Beveren, M. Veinhard, Blurring the boundaries between ion sources: The application of the RILIS inside a FEBIAD type ion source at ISOLDE, Nuclear Instruments and Methods in Physics Research Section B: Beam Interactions with Materials and Atoms 376 (2016) 39–45. doi:10.1016/j.nimb.2016.03.005.

[80] T. Bohlen, F. Cerutti, M. Chin, A. Fasso, A. Ferrari, P. Ortega, A. Mairani, P. Sala, G. Smirnov, V. Vlachoudis, The FLUKA Code: Developments and Challenges for High Energy and Medical Applications, Nuclear Data Sheets 120 (2014) 211–214. doi:10.1016/j.nds.2014.07.049.

[81] A. Ferrari, A. Sala, Paola R. Fasso, J. Ranft, FLUKA : A multi-particle transport code, Tech. Rep. October, CERN, Geneva (2005). doi:10.5170/CERN-2005-010.

[82] J.-J. Gaimard, K.-H. Schmidt, A reexamination of the abrasion-ablation model for the description of the nuclear fragmentation reaction, Nuclear Physics A 531 (3-4) (1991) 709–745. doi:10.1016/0375-9474(91)90748-U.

[83] A. Kelic, M. V. Ricciardi, K.-H. Schmidt, ABLA07 - towards a complete description of the decay channels of a nuclear system from spontaneous fission to multifragmentation, in: D. Filges, S. Leray, Y. Yariv, A. Mengoni, A. Stanculescu, G. Mank (Eds.), Proceedings of the Joint ICTP-IAEA Advanced Workshop on Model Codes for Spallation Reactions, IAEA INDC(NDS)-530, Vienna, 2009, pp. 181–221. arXiv:0906.4193v1.

[84] L. Carraz, I. Haldorsen, H. Ravn, M. Skarestad, L. Westgaard, Fast release of nuclear reaction products from refractory matrices, Nuclear Instruments and Methods 148 (2) (1978) 217–230. doi:10.1016/0029-554X(70)90171-0.

[85] R. Kirchner, On the release and ionization efficiency of catcher-ion-source systems in isotope separation on-line, Nuclear Instruments and Methods in Physics Research Section B: Beam Interactions with Materials and Atoms 70 (1-4) (1992) 186–199. doi:10.1016/0168-583X(92)95930-P.

[86] G. Alton, J.-C. Bilheux, A. McMillan, A new method for infiltration coating complex geometry matrices with compound materials for ISOL production target applications,

Nuclear Instruments and Methods in Physics Research Section A: Accelerators, Spectrometers, Detectors and Associated Equipment 521 (1) (2004) 108–125. doi:10.1016/j.nima.2003.11.405.

[87] M. Czapski, T. Stora, C. Tardivat, S. Deville, R. Santos Augusto, J. Leloup, F. Bouville, R. Fernandes Luis, Porous silicon carbide and aluminum oxide with unidirectional open porosity as model target materials for radioisotope beam production, Nuclear Instruments and Methods in Physics Research, Section B: Beam Interactions with Materials and Atoms 317 (PART B) (2013) 385–388. doi:10.1016/j.nimb.2013.08.022.

[88] S. Corradetti, L. Biasetto, M. Innocentini, S. Carturan, P. Colombo, A. Andrighetto, Use of polymeric fibers to increase gas permeability of lanthanum carbide based targets for nuclear physics applications, Ceramics International 42 (15) (2016) 17764–17772. doi:10.1016/j.ceramint.2016.08.104.

[89] L. Biasetto, S. Carturan, G. Maggioni, P. Zanonato, P. D. Bernardo, P. Colombo, A. Andrighetto, G. Prete, Fabrication of mesoporous and high specific surface area lanthanum carbide–carbon nanotube composites, Journal of Nuclear Materials 385 (3) (2009) 582–590. doi:10.1016/j.jnucmat.2009.01.035.

[90] S.-J. L. Kang, Sintering: Densification, Grain Growth and Microstructure, 1st Edition, Elsevier B.V., Oxford, 2005.

[91] M. N. Rahaman, Ceramic Processing and Sintering, Marcel Dekker, 2003.

[92] R. L. Coble, Sintering Crystalline Solids. I. Intermediate and Final State Diffusion Models, Journal of Applied Physics 32 (5) (1961) 787. doi:10.1063/1.1736107.

[93] R. M. German, Z. A. Munir, Surface Area Reduction During Isothermal Sintering, Journal of the American Ceramic Society 59 (9-10) (1976) 379–383. doi:10.1111/j.1151-2916.1976.tb09500.x.
URL http://doi.wiley.com/10.1111/j.1151-2916.1976.tb09500.x

[94] C. Greskovich, K. W. Lay, Grain Growth in Very Porous Al2O3 Compacts, Journal of the American Ceramic Society 55 (3) (1972) 142–146. doi:10.1111/j.1151-2916.1972.tb11238.x.

[95] L. C. D. Jonghe, M. N. Rahaman, Sintering of Ceramics, in: S. Somiya, F. Aldinger, N. Claussen, R. M. Spriggs, K. Uchino, K. Koumoto, M. Kaneno (Eds.), Handbook of Advanced Ceramics, Volume I: Materials Science, Elsevier, Academic Press, 2003, Ch. Chapter 4, pp. 187–264. doi:10.1016/B978-012654640-8/50006-7.

[96] L. De Jonghe, M. Rahaman, C. Hsueh, Transient stresses in bimodal compacts during sintering, Acta Metallurgica 34 (7) (1986) 1467–1471. doi:10.1016/0001-6160(86)90034-9.

[97] J. D. French, M. P. Harmer, H. M. Chan, G. A. Miller, Coarsening-Resistant Dual-Phase Interprenetrating Microstructures, Journal of the American Ceramic Society 73 (8) (1990) 2508–2510. doi:10.1111/j.1151-2916.1990.tb07621.x.

[98] Z. Yan, C. L. Martin, O. Guillon, D. Bouvard, Effect of size and homogeneity of rigid inclusions on the sintering of composites, Scripta Materialia 69 (4) (2013) 327–330. doi:10.1016/j.scriptamat.2013.05.013.

[99] M. W. Weiser, L. C. De Jonghe, Inclusion Size and Sintering of Composite Powders, Journal of the American Ceramic Society 71 (3) (1988) C–125–C–127. doi:10.1111/j.1151-2916.1988.tb05030.x.

[100] L. Olmos, C. L. Martin, D. Bouvard, Sintering of mixtures of powders: Experiments and modelling, Powder Technology 190 (1-2) (2009) 134–140. doi:10.1016/j.powtec.2008.04.057.

[101] E. A. Aitken, Some comments regarding sintering characteristics in a radiation environment, in: Symposium on Radiation Effects in Refractory Fuel Compounds, American Society for Testing and Materials, Philadelphia, 1961, pp. 123–130.

[102] R. Smoluchowski, Radiation Sintering of Lunar Dust, Science 150 (3699) (1965) 1025–1026. doi:10.1126/science.150.3699.1025.

[103] A. C. Damask, Radiation sintering, Radiation Effects 1 (2) (1969) 95–100. doi:10.1080/00337576908235479.

[104] H. Jain, O. Parkash, M. Y. Xu, Sintering of a Ceramic at Very Low Temperatures, Journal of the American Ceramic Society 72 (11) (1989) 2176–2177. doi:10.1111/j.1151-2916.1989.tb06052.x.

[105] S. Fernandes, R. Bruetsch, R. Catherall, F. Groeschel, I. Guenther-Leopold, J. Lettry, E. Manfrin, S. Marzari, E. Noah, S. Sgobba, T. Stora, L. Zanini, Microstructure evolution of nanostructured and submicrometric porous refractory ceramics induced by a continuous high-energy proton beam, Journal of Nuclear Materials 416 (1-2) (2011) 99–110. doi:10.1016/j.jnucmat.2011.02.048.

[106] G. Ackland, Controlling Radiation Damage, Science 327 (5973) (2010) 1587–1588. doi:10.1126/science.1188088.

[107] X. M. Bai, A. F. Voter, R. G. Hoagland, M. Nastasi, B. P. Uberuaga, Efficient Annealing of Radiation Damage Near Grain Boundaries via Interstitial Emission, Science 327 (5973) (2010) 1631–1634. doi:10.1126/science.1183723.

[108] Attrition mills, Metal Powder Report 51 (5) (1996) 58. doi:10.1016/S0026-0657(96)93248-8.

[109] L. Y. Sadler, D. A. Stanley, D. R. Brooks, Attrition mill operating characteristics, Powder Technology 12 (1) (1975) 19–28. doi:10.1016/0032-5910(75)85004-2.

[110] K. Shinohara, B. Golman, T. Uchiyama, M. Otani, Fine-grinding characteristics of hard materials by attrition mill, Powder Technology 103 (3) (1999) 292–296. doi:10.1016/S0032-5910(99)00042-X.

[111] L. Michalski, K. Eckersdorf, J. Kucharski, J. McGhee, Temperature measurement, 2nd Edition, John Wiley & Sons, Ltd., Chichester, England, 2001.

[112] E. de Hoffmann, V. Stroobant, Mass Spectrometry, 3rd Edition, John Wiley & Sons, Ltd., Chichester, England, 2007.

[113] Pfeiffer Vacuum GmbH, Vacuum Technology Book (Pfeiffer Catalog) (2013).
URL https://www.pfeiffer-vacuum.com/en/downloads/vacuum-technology-book/

[114] H. G. Merkus, Particle Size Measurements, Vol. 17 of Particle Technology Series, Springer Netherlands, Dordrecht, 2009. doi:10.1007/978-1-4020-9016-5.

[115] J. B. Condon, Surface Area and Porosity Determinations by Physisorption - Measurements and Theory, 1st Edition, Elsevier B.V., Radarweg, 2006.

[116] J. Rouquerol, D. Avnir, C. W. Fairbridge, D. H. Everett, J. M. Haynes, N. Pernicone, J. D. F. Ramsay, K. S. W. Sing, K. K. Unger, Recommendations for the characterization of porous solids (Technical Report), Pure and Applied Chemistry 66 (8) (1994) 1739–1758. doi:10.1351/pac199466081739.

[117] Q. Instruments, Nova Operations Manual - High Speed Gas Sorption Analyzer Version 11.02 - P/N 05069 Rev S, Tech. rep., CERN, Boynton Beach, USA (2009).

[118] S. Brunauer, P. Emmett, E. Teller, Adsorption of Gases in Multimolecular Layers, Journal of the American Chemical Society 60 (2) (1938) 309–319. doi:10.1021/ja01269a023.

[119] E. P. Barrett, L. G. Joyner, P. P. Halenda, The Determination of Pore Volume and Area Distributions in Porous Substances. I. Computations from Nitrogen Isotherms, Journal of the American Chemical Society 73 (1) (1951) 373–380. doi:10.1021/ja01145a126.

[120] J. I. Goldstein, D. E. Newbury, P. Echlin, D. C. Joy, C. E. Lyman, E. Lifshin, L. Sawyer, J. R. Michael, Scanning Electron Microscopy and X-ray Microanalysis, 3rd Edition, Springer US, Boston, MA, 2003. doi:10.1007/978-1-4615-0215-9.

[121] D. Drouin, A. R. Couture, D. Joly, X. Tastet, V. Aimez, R. Gauvin, CASINO V2.42—A Fast and Easy-to-use Modeling Tool for Scanning Electron Microscopy and Microanalysis Users, Scanning 29 (3) (2007) 92–101. doi:10.1002/sca.20000.

[122] H. Giesche, Mercury Porosimetry: A General (Practical) Overview, Particle & Particle Systems Characterization 23 (1) (2006) 9–19. doi:10.1002/ppsc.200601009.
URL http://doi.wiley.com/10.1002/ppsc.200601009

[123] N. Hearn, R. Hooton, Sample mass and dimension effects on mercury intrusion porosimetry results, Cement and Concrete Research 22 (5) (1992) 970–980. doi:10.1016/0008-8846(92)90121-B.

[124] V. K. Pecharsky, P. Y. Zavalij, Fundamentals of Powder Diffraction and Structural Chracterization of Materials, 1st Edition, Springer, 2003.

[125] P. Scherrer, Bestimmung der Grösse und der inneren Struktur von Kolloidteilchen mittels Röntgensrahlen (Determination of the size and internal structure of colloidal particles using X-rays), Nachrichten von der Königlichten Gesellschaft der Wissenschaften zu Göttingen. Mathematisch-physikalische Klasse aus der Jahre 1918 (1918) 98–100, (German).

[126] J. I. Langford, A. J. C. Wilson, Scherrer after sixty years: A survey and some new results in the determination of crystallite size, Journal of Applied Crystallography 11 (2) (1978) 102–113. doi:10.1107/S0021889878012844.

[127] J. Langford, The Use of the Voigt Function in Determining Microstructural Properties from Diffraction Data by means of Pattern Decomposition, in: E. Prince, J. Stalick (Eds.), Proceedings of the international conference Accuracy in Powder Diffraction II - NIST Special Publication 846, NIST, NIST, Gaithersburg, 1992, pp. 110–126.

[128] G. Williamson, W. Hall, X-ray line broadening from filed aluminium and wolfram, Acta Metallurgica 1 (1) (1953) 22–31. doi:10.1016/0001-6160(53)90006-6.

[129] A. Albinati, B. T. M. Willis, The Rietveld method, in: International Tables for Crystallography, Vol. C, International Union of Crystallography, Chester, England, 2006, pp. 710–712. doi:10.1107/97809553602060000614.

[130] R. A. Young, The Rietveld Method, Oxford University Press Inc., New York, USA, 1993.

[131] T. Degen, M. Sadki, E. Bron, U. König, G. Nénert, The HighScore suite, Powder Diffraction 29 (S2) (2014) S13–S18. doi:10.1017/S0885715614000840.

[132] G. F. Knoll, Radiation Detection and Measurement, 4th Edition, John Wiley & Sons, Ltd., Hoboken, USA, 2011.

[133] D. A. H. Hanaor, C. C. Sorrell, Review of the anatase to rutile phase transformation, Journal of Materials Science 46 (4) (2011) 855–874. doi:10.1007/s10853-010-5113-0.

[134] K.-N. P. Kumar, K. Keizer, A. J. Burggraaf, T. Okubo, H. Nagamoto, S. Morooka, Densification of nanostructured titania assisted by a phase transformation, Nature 358 (6381) (1992) 48–51. doi:10.1038/358048a0.

[135] Y.-H. Zhang, A. Reller, Phase transformation and grain growth of doped nanosized titania, Materials Science and Engineering: C 19 (1-2) (2002) 323–326. doi:10.1016/S0928-4931(01)00409-X.

[136] K. Peräjärvi, U. Bergmann, V. Fedoseyev, A. Joinet, U. Köster, C. Lau, J. Lettry, H. Ravn, M. Santana-Leitner, Studies of release properties of ISOLDE targets, Nuclear Instruments and Methods in Physics Research Section B: Beam Interactions with Materials and Atoms 204 (2003) 272–277. doi:10.1016/S0168-583X(02)01924-9.

[137] D. C. Montgomery, Design and Analysis of Experiments, 8th Edition, John Wiley & Sons, Inc., 2012.

[138] V. Pouchly, K. Maca, Z. Shen, Two-stage master sintering curve applied to two-step sintering of oxide ceramics, Journal of the European Ceramic Society 33 (12) (2013) 2275–2283. doi:10.1016/j.jeurceramsoc.2013.01.020.

[139] S. G. Rudisill, Z. Wang, A. Stein, Maintaining the Structure of Templated Porous Materials for Reactive and High-Temperature Applications, Langmuir 28 (19) (2012) 7310–7324. doi:10.1021/la300517g.

[140] M. D. M. Innocentini, W. S. Chacon, J. R. Coury, A. Dey, N. Kayal, O. Chakrabarti, High-temperature permeability of porous silicon carbide for hot gas cleaning applications, in: Proceedings of the 12th Conference of the European Ceramic Society – ECerS XII, Vol. 1, Stockholm, Sweden, 2011, pp. 4–7.

[141] P. Gierszewski, M. D. Donne, H. Kawamura, M. Tillack, Ceramic pebble bed development for fusion blankets, Fusion Engineering and Design 27 (C) (1995) 167–178. doi:10.1016/0920-3796(95)90124-8.

[142] J. M. Ramos-Fernández, M. Martínez-Escandell, F. Rodríguez-Reinoso, Production of nanoTiC-graphite composites using Ti-doped self-sintering carbon mesophase powder, Journal of the European Ceramic Society 33 (3) (2013) 583–591. doi:10.1016/j.jeurceramsoc.2012.09.019.

[143] S. Badie, Engineering a novel material: Nanometric titanium carbide particles in a matrix of carbon nanotubes, Tech. rep., CERN, Geneva, CERN-STUDENTS-Note-2015-027 (2015).
URL https://cds.cern.ch/record/2043845?ln=en

[144] J. Crank, The mathematics of diffusion, 2nd Edition, Clarendon Press, Oxford, 1975.

[145] M. S. Leitner, H. Ravn, F. C. Tavares, A Monte Carlo code to optimize the production of radioactive ion beams by the ISOL technique, PhD Thesis, Technical University of Catalonia (UPC) (2005).
URL http://cds.cern.ch/record/905537

[146] L. Egoriti, S. Boeckx, L. Ghys, D. Houngbo, L. Popescu, Analytical model for release calculations in solid thin-foils ISOL targets, Nuclear Instruments and Methods in Physics Research Section A: Accelerators, Spectrometers, Detectors and Associated Equipment 832 (June 2016) (2016) 202–207. arXiv:1606.06485, doi:10.1016/j.nima.2016.06.106.

[147] B. Mustapha, J. Nolen, Optimization of ISOL targets based on Monte-Carlo simulations of ion release curves, Nuclear Instruments and Methods in Physics Research Section B: Beam Interactions with Materials and Atoms 204 (2003) 286–292. doi:10.1016/S0168-583X(02)01926-2.
URL http://linkinghub.elsevier.com/retrieve/pii/S0168583X02019262

[148] O. Alyakrinskiy, K. Gubin, P. Martyshkin, L. Tecchio, Influence of grain size and porosity on the release of radioactive isotopes from target materials with high open porosity, Nuclear Instruments and Methods in Physics Research Section B: Beam Interactions with Materials and Atoms 267 (15) (2009) 2554–2558. doi:10.1016/j.nimb.2009.05.050.

[149] L. Biasetto, M. Innocentini, W. Chacon, S. Corradetti, S. Carturan, P. Colombo, A. Andrighetto, Gas permeability of lanthanum oxycarbide targets for the SPES project, Journal of Nuclear Materials 440 (1-3) (2013) 70–80. doi:10.1016/j.jnucmat.2013.04.038.

[150] M. Barbui, A. Andrighetto, C. Antonucci, L. Biasetto, S. Carturan, F. Cervellera, S. Cevolani, M. Cinausero, P. Colombo, A. Dainelli, P. Di Bernardo, M. Giacchini, F. Gramegna, M. Lollo, G. Maggioni, M. Manzolaro, G. Meneghetti, C. Petrovich, L. Piga, G. Prete, M. Re, V. Rizzi, D. Stracener, M. Tonezzer, D. Zafiropoulos, P. Zanonato, Calculations and first results obtained with a SiC prototype of the SPES direct target, Nuclear Instruments and Methods in Physics Research Section B: Beam Interactions with Materials and Atoms 266 (19-20) (2008) 4289–4293. doi:10.1016/j.nimb.2008.05.049.

[151] R. M. A. Roque-Malherbe, Adsorption and Diffusion in Nanoporous Materials, CRC Press, Puerto-Rico, 2007.

europass Curriculum vitae

PERSONAL INFORMATION

João Pedro FERNANDES PINTO RAMOS

joao.pedro.ramos@cern.ch
http://www.joaopedroramos.com

Sex Male | Date of birth 26/02/1987 | Nationality Portuguese

WORK EXPERIENCE

10/2016–Present — **Senior Fellow (Post-doc)**

CERN - European Organization for Nuclear Research, Geneva (Switzerland)

Main project: optimization of the ISOLDE neutron converter/target geometry using FLUKA and ANSYS simulation codes, in an international collaboration: TRIUMF (Canada) and SCK (Belgium). Other responsibilities: ISOLDE target operation and beam characterization, UC2-CNT nanocomposite development, general materials characterization studies.

10/2012–09/2016 — **Doctoral Student/Assistant**

CERN - European Organization for Nuclear Research, Geneva (Switzerland)

1st three years financed by CERN, 4th year financed by École polytechnique fédérale de Lausanne, EPFL.

- Main project: PhD thesis (see *Education and Training*)
- Collaboration in the development of (nanocomposite) target materials and ion sources for radioactive ion beam production, in particular uranium carbide-multi wall carbon nanotubes nanocomposite - see more in *Publications list*
- Operation of the radioactive ion beam production facility, ISOLDE at CERN, for beam quality control (intensity, time-structure, purity, ion source and target tuning) and prototype testing
- Supervision of students, material characterization responsibilities and expertise: x-ray powder diffraction, scanning electron microscopy and nitrogen adsorption.

04/2011–09/2012 — **Engineer Trainee**

CERN - European Organization for Nuclear Research, Geneva (Switzerland)

Position financed by the Portuguese Science and Technology Foundation and CERN.

- Main project: master thesis (see *Education and Training*)
- Responsible for oxide/carbide target materials characterizations;
- Collaboration in other target and ion source development projects - see *Publications list*
- Operation of the radioactive ion beam production facility, ISOLDE at CERN, for beam quality control (intensity, time-structure, purity, ion source and target tuning) and prototype testing

EDUCATION AND TRAINING

09/2012–01/2017 — **PhD in Materials Science and Engineering** — EQF level 8

École polytechnique fédérale de Lausanne, Lausanne (Switzerland)

Thesis: "*Titanium carbide-carbon porous nanocomposite materials for radioactive ion beam production: processing, sintering and isotope release properties*".

- Development of porous TiC-C nanocomposites stable up to 2000 °C, under high energy proton irradiation for radioactive ion beam production at CERN-ISOLDE
- Co-supervision and teaching experience acquired
- Collaboration with Universidade de Aveiro (Portugal);

© European Union, 2002-2016 | http://europass.cedefop.europa.eu

- Main courses: design and analysis of experiments in materials science and engineering, effects of radiation on materials, powder characterization and dispersion, scanning electron microscopy techniques
- PhD thesis nominated for EPFL doctoral prize

09/2009–02/2012

Master's Degree in Materials Engineering

EQF level 7

University of Aveiro, Aveiro (Portugal)

Master thesis: "*Effect of Calcium Oxide Microstructure on the Diffusion of Isotopes*" with the supervision of Prof. Ana Senos (University of Aveiro) and Dr. Thierry Stora (CERN), grade of 19 in 20 (final masters grade 16 in 20).

- Industry oriented masters degree: Human Resources Management, Quality Management, Introduction to Marketing, Environmental Systems Management, Industrial Installation Practices, Metallurgical, Polymer and Ceramics Industrial Technologies, Instrumentation and Automatic Control, Thermal Treatments, Advanced Processing of Materials.

09/2005–06/2009

Degree in Materials Engineering

EQF level 6

University of Aveiro, Aveiro (Portugal)

Materials Characterization, Phase Diagrams, Solids Structures, Microstructural Development, Solid State Reactions, Recycling and New Products, Corrosion and Materials Protection, Physical Chemistry of Polymers, Organic Chemistry, Operations Management, Computer-Assisted Design and Manufacture, Technical Design.

- Final project: "*Study of Belite and Sulfobelite Clinkers*" with Prof. João A. Labrincha, grade 16 in 20 (final degree grade 13 in 20).

PERSONAL SKILLS

Mother tongue(s) Portuguese

Other language(s)

	UNDERSTANDING		SPEAKING		WRITING
	Listening	Reading	Spoken interaction	Spoken production	
English	C1	C2	C1	C1	C1
French	A2	B1	A2	A1	A2

Levels: A1 and A2: Basic user - B1 and B2: Independent user - C1 and C2: Proficient user
Common European Framework of Reference for Languages

Communication skills Leadership and team spirit, good oral communication, organized, quick learner,clear writer and flexible adapting to change. Experience in project/event organization/management.

Job-related skills Design of experiments both in terms of statistical relevance and hardware, safety trained (radioprotection, cryogenics, high voltage electrical installations, nanoparticles), ISOLDE facility operation (target, ion source and beam diagnostics), radioactivity techniques (gamma spectrometry and beta detection).

Materials characterization hands-on practice: nitrogen adorption (mesoporosity, surface area), X-ray powder diffraction (crystallite size, Rietveld refinement), laser diffraction particle size distribution, scanning electron microscopy (with energy dispersive X-ray spectroscopy), residual gas analysis, mercury intrusion porosimetry.

Experience working with (high) vacuum, very high temperature ovens (up to 2300 °C) and beam manipulation.

Digital competence Data analysis (Excel, Mathematica and Origin); typesetting (Word and LaTex), simulation software (ABRABLA, SRIM, CASINO and HSC Chemistry), website building (Wordpres), advanced software and hardware computer user.

ADDITIONAL INFORMATION

Publications list

- A. Fenta, et al., "The 68m Cu/ 68 Cu isotope as a new probe for hyperfine studies: The nuclear moments", EPL 116 (6) (2016)
- S. Rothe, et al., "Advances in surface ion suppression from RILIS: Towards the Time-of-Flight Laser Ion Source (ToF-LIS)", NIMB 376 (2016), 86-90
- T.D. Goodacre, et al., "Blurring the boundaries between ion sources: The application of the RILIS inside a FEBIAD type ion source at ISOLDE", NIMB 376 (2016), 39-45
- J.P. Ramos, et al., "Target nanomaterials at CERN-ISOLDE: synthesis and release data", NIMB 379 (2016), 81-85
- J.P. Ramos, et al., "Sintering kinetics of nanometric calcium oxide in vacuum atmosphere", Ceram. Int. 41 (2015), 8093-8099
- A. Gottberg, et al.,"Experimental tests of an advanced proton-to-neutron converter at ISOLDE-CERN", NIMB 336 (2014), 143-148
- T.M. Mendonca, et al.,"Production and release of ISOL beams from molten fluoride salt targets", NIMB 329 (2014), 1-5
- J.P. Ramos, et al., "Intense 31-35Ar beams produced with nanostructured CaO target at ISOLDE", NIMB 320 (2014), 83-88
- M. Kronberger, et al. "Production of molecular sideband radioisotope beams at CERN-ISOLDE using a Helicon-type plasma ion source", NIMB 317 (2013), 438-441
- D.A. Fink, et al., "First application of the Laser Ion Source and Trap (LIST) for on-line experiments at ISOLDE", NIMB 317 (2013), 417-421

Conferences and Talks

Total of 4 invited talks for seminars/workshops in CERN (Switzerland), Universidade de Aveiro (Portugal), and GANIL (France).

Accepted talks and posters in prestigious conferences: ECERS 2015 (Toledo, Spain), E-MRS 2014 Fall Meeting (Warsaw, Poland), ISOLDE Workshop and Users meeting 2011 (Geneva, Switzerland), EMIS 2015 (Michigan, USA), EURORIB'2012 (Padova, Italy) and others.

Full list of publications/(invited) talks/posters in www.joaopedroramos.com/publications.

Honours and awards

- PhD thesis recommended for the EPFL yearly doctoral prize
- Best Young Speaker Award, 2015, ISOLDE Workshop and Users Meeting 2015
- TNT Express Portugal Award 2010, Quality Management group monograph, University of Aveiro, 2nd Place.

Volunteer/Associative Positions

President of Caritas Group of Gafanha da Nazaré for 3 years, coordinator of Materials Students Association of Students' Union of University of Aveiro for 2 years, Scout for 14 years performing tasks of team leader and treasurer and others.

Hobbies

Traveling, cardiovascular sports practice (running and biking), team based strategic computer games (Heroes of the Storm, Overwatch)

© European Union, 2002-2016 | http://europass.cedefop.europa.eu